The Evolution of Galaxies in the Early Universe with the Next Generation of Telescopes

Rohan Gadiyar Varadaraj

St Anne's College

University of Oxford

A thesis submitted for the degree of

Doctor of Philosophy

Hilary 2025

DECLARATION

The work presented in this thesis was undertaken in the Sub-department of Astrophysics at the University of Oxford between October 2021 and March 2025, under the supervision of Professor Matthew Jarvis and Dr Rebecca Bowler. I declare that no part of this thesis has been accepted, or is currently being submitted, for any degree or diploma or certificate or any other qualification in this University or elsewhere. Except where otherwise stated, or where reference is made to the work of others, the work in this thesis is entirely my own.

The chapters in this thesis are based on papers I have led which are either already published or will soon be submitted for publication.

Chapter 2 is based on Varadaraj R. G., Bowler R. A. A., Jarvis M. J., Adams N. J., Häußler B., 2023, MNRAS, 524, 4586. The brown dwarf number density models used in Section 2.3.4 were provided by Rebecca Bowler.

Chapter 3 is based on Varadaraj et al., in preparation. This work will be circulated within the *Euclid* Consortium before being submitted for publication. The *JWST* COSMOS-Web imaging used in this chapter was reduced by Nathan Adams, and the brown dwarf number density models used in Section 3.3.6 were provided by Rebecca Bowler.

Chapter 4 is based on Varadaraj R. G., Bowler R. A. A., Jarvis M. J., Adams N. J., Choustikov N., Koekemoer A. M., Carnall A. C., McLeod, D. J., Dunlop, J. S., Donnan, C. T., and Grogin, N. A., 2024, MNRAS, 533, 3724. The *JWST* data used in this chapter were reduced by Koekemoer A. M., Carnall A. C., McLeod, D. J., Dunlop, J. S., Donnan, C. T., and Grogin, N. A. along with members of the PRIMER team (https://primer-jwst.github.io/team.html).

Rohan Gadiyar Varadaraj — July 23, 2025

Acknowledgements

It feels surreal to reach the end of the DPhil, and after writing only the first sentence I'm already feeling quite emotional.

First, I want to thank my supervisors, Rebecca and Matt. Thank you for teaching me so much and giving me the opportunity to follow my dream. Honestly, my experience with you has been nothing short of amazing. I also want to thank my entire research group for being the best colleagues I could have asked for. Catherine, Imogen, and Anastasia – I really treasure the advice you've given me over the last few years. A special thanks goes to my predecessor, Nathan, for doing all the hard stuff before me, and my undergraduate mentor, Elizabeth, whose encouragement gave me the confidence to pursue a PhD. Natalia, Shruti, and Andreea – thank you for being great friends to work with. I have learned so much from each of you. Thanks to the year above, in particular Madalina, Alex, and Casey, for being chaotic guiding stars throughout the DPhil, giving my year group fantastic reason to procrastinate with quizzes, and helping massively with my impostor syndrome. A big thank you to Ashling, who made me feel so welcome when I was a nervous new starter, along with Leanne and Lawrence, for running the department and being the nicest people in the world. Also, thank you to Jonathan for running Glamdring and teaching me extremely basic command line prompts.

Thank you to my officemates, Phil, Fergus, Matthew, James, David, and Haochuan, for providing constant entertainment and support, especially during my toughest moments. I hope we will be friends forever, reminiscing on this time when we are much older.

A big thanks to my matcha boys, the leg day people, and more recently the Sunday morning bouldering gang. A massive thanks to the students and postdocs who I have almost never had a scientific discussion with during lunch, coffee and cake, and at the pub. Conversations with you have made me laugh so much. In some ways, all of you have made this DPhil, the hardest challenge of my life, the easiest thing I've ever done. A massive thank you to the astro band, Pat and the Roche Lobes, for their encouragement and for giving me the profound experience of playing live music for the first time.

Thank you to Luke, Aaron, Robin, and all the PhD students I met in Perth/Boorloo for taking care of me. My time with you was one of my happiest.

To all my housemates along the way, thank you for giving me a home. Owen, thank you for giving me all of my Thanksgiving experiences. Karan, thank you for being the first person I met here and acting out my intrusive thoughts. Erkan, thank you for being the best chaos in my life, for being a close friend, and for finally respecting me as a professional photographer. Sophie, thank you for showing me the magic of frozen grapes. Charlotte, thank you for being the cosiest person to live with, and for always being a shoulder to lean on. Arjang, whilst our time together was short, I learned so much about life from you. Same with you Blanca, one of the kindest souls on Earth. Arti - thank you for being one of my best friends. You've been there for me so much, and I've loved gymming with you, climbing with you, and living with you. Same with you Zed, I'm so happy I can be friends with you - keep it swanging. My life in Oxford has also been made great by the many friends I made during my time here - thank you to Fergus, Edith, Sid, Bea, Ryan, Emma, Shivani, Clara, everyone who rowed for our (at the time) terrible St Anne's Boat Club, and many more.

Thank you also to friends before Oxford - Sam, James, and Ryan from the Shire, and my Ashley Lodge Probation Centre friends from Warwick, for supporting me even back when all of this was just a dream of mine.

I am deeply grateful to my parents, my *Amma* and *Anna*, and my sister, Mallika, for their unwavering, unconditional love and support throughout my entire education and for encouraging my love of astronomy. None of this would have been possible without you. *Amma* – one of my earliest memories is seeing a picture of Jupiter in a book you got me as a kid. Thanks for kickstarting all this. *Anna* – through my toughest times, you've always known the right thing to say. Thanks for being my role model. Malliku – thanks for your iconic midnight grape and cheese slice gremlin activities.

Anjali - you've seen this whole thing play out from the start. Thank you for being my best friend, my explorer, for always believing in me, and for teaching me so much about myself. I love you, and I can't wait to see where our adventures take us next.

Finally, thank you to my grandfather, my *Ajja*, a remarkably selfless man who worked tirelessly to support those around him through significant hardship, always placing his family's happiness above his own. While the university I attended mattered far less to me than the subject of my PhD, it was his dream to see his grandchild study at Oxford. He would often ask if I would try to go one day. He

didn't quite get to see it happen, but I am incredibly proud that I could make his dream come true by studying at one of the best universities in the world.

Ajja, I dedicate this thesis to you.

Abstract

In this thesis, I present results on the statistical properties of luminous star-forming galaxies in the early Universe, spanning the first two billion years of cosmic time. I combine deep, degree-scale optical and near-infrared imaging from the latest ground-based surveys with next-generation observatories - *Euclid*, which provides deep, degree-scale space-based near-infrared imaging for the first time, and *JWST*, which delivers unrivalled depth and resolution in the near-infrared and infrared. With this unique combination, I place strong constraints on the number densities and size-scaling relations of the first galaxies.

First, by combining imaging from the VISTA telescope with deep ground-based optical surveys, infrared imaging from *Spitzer*/IRAC, and early data from *Euclid*, I construct a sample of galaxy candidates at redshift $6.5 < z < 7.5$ spanning a rest-UV absolute magnitude range of $-23.5 \leq M_{\rm UV} \leq -20.2$. These sources represent some of the most luminous and massive galaxies at this epoch. After accounting for brown dwarf contamination through a careful SED-fitting analysis, I find that the rest-frame UV luminosity function at $z \simeq 7$ is best described by a double-power law, showing an excess relative to a Schechter function at absolute rest-UV magnitudes $M_{\rm UV} \lesssim -22.5$ and evolving slowly from $z \simeq 8$. This suggests that luminous galaxies at this epoch are not yet significantly affected by dust obscuration or mass quenching, and that active galactic nuclei do not contribute significantly to the luminosity function until very bright magnitudes ($M_{\rm UV} < -24$).

I then measure the size-scaling relations of 1,668 luminous galaxies at $z \simeq 3-5$ using the *JWST* PRIMER survey. These sources were selected from ground-based, seeing-dominated imaging, presenting an unbiased sampling of the morphology and size distributions of luminous sources. I find a build-up of large ($R_e > 2$ kpc) galaxies at $z = 3$ relative to $z = 4-5$, a redshift-dependent size evolution leading to larger mean sizes at $z = 3$, and an increase in the intrinsic scatter of the size-mass relations towards lower redshift. These results suggest that by $z = 3$, some galaxies have undergone dissipative processes such as mergers and gas accretion, allowing for the formation of rare, larger galaxies. However, the majority of galaxies remain compact over this redshift range, with a typical (modal) size of $\bar{R}_e = 0.7-0.9$ kpc. Finally, I find that the size-mass and size-luminosity relations are consistent with predictions from simulations such as Illustris and FLARES, providing evidence for centrally concentrated star formation in the most massive galaxies at high redshift.

Contents

List of Abbreviations

ΛCDM . . . . Λ Cold Dark Matter

ACS . . . . . Advanced Camera for Surveys

AGN . . . . . Active Galactic Nucleus

ALMA . . . . Atacama Large Millimeter/submillimeter Array

BAGPIPES . Bayesian Analysis of Galaxies for Physical Inference and Parameter EStimation

BD . . . . . Brown Dwarf

BIC . . . . . Bayesian Information Criterion

CANDELS . . Cosmic Assembly Near-Infrared Deep Extragalactic Legacy Survey

CCD . . . . . Charged Coupled Device

CDFS . . . . . *Chandra* Deep Field South

CDS . . . . . Cosmic Dawn Survey

CEERS . . . . Cosmic Evolution Early Release Science Survey

CFHT(LS) . . Canada-France-Hawaii Telescope (Legacy Survey)

CGM . . . . . Circumgalactic Medium

COSMOS . . . Cosmic Evolution Survey

CSFH . . . . . Constant Star Formation History

DEVILS . . . . Deep Extragalactic VIsible Legacy Survey

DM . . . . . Dark Matter

DPL . . . . . Double Power Law

DR . . . . . Data Release

EAF . . . . . *Euclid* Auxiliary Field

ECDF-S . . . . Extended *Chandra* Deep Field South

EDF . . . . . *Euclid* Deep Field

EoR . . . . . Epoch of Reionisation

ERO . . . . . Early Release Observations

EWS . . . . . *Euclid* Wide Survey

FLARES . . . First Light And Reionisation Epoch Simulations

FRESCO . . . First Reionization Epoch Spectroscopically Complete Observations

FWHM . . . . Full Width at Half Maximum

GOLDRUSH . Great Optically Luminous Dropout Research Using Subaru HSC

GOODS . . . . Great Observatories Deep Survey

HMF . . . . . Halo Mass Function

HSC . . . . . Hyper-Suprime Cam

IMF . . . . . Initial Mass Function

IGM . . . . . Intergalactic Medium

ISM . . . . . Interstellar Medium

IRAC . . . . . Infrared Array Camera

JADES . . . . *JWST* Advanced Deep Extragalactic Survey

JELS . . . . . *JWST* Emission Line Survey

JWST . . . . . James Webb Space Telescope

LAE . . . . . Lyman-α Emitter

LBG . . . . . Lyman-Break Galaxy

LF . . . . . Luminosity Function

LSST . . . . . Legacy Survey of Space and Time

Ly$\boldsymbol{\alpha}$ . . . . . Lyman-α

MIRI . . . . . Mid Infrared Instrument

MOONS . . . Multi-Object Optical and Near-infrared Spectrograph

NICMOS . . . Near Infrared Camera and Multi-Object Spectrometer

NIR . . . . . Near Infrared

NIRCam . . . Near Infrared Camera

NIRSpec . . . Near Infrared Spectrograph

NISP . . . . . Near-Infrared Spectrometer and Photometer

PAH . . . . . Polyaromatic Hydrocarbon

PFS . . . . . Prime Focus Spectrograph

PSF . . . . . Point Spread Function
PRIMER . . . Public Release IMaging for Extragalactic Research
PV . . . . . Performance Verification
REBELS . . . Reionisation Era Bright Emission Line Survey
SED . . . . . Spectral Energy Distribution
SEDS . . . . . *Spitzer* Extended Deep Survey
SERVS . . . . *Spitzer* Extragalactic Representative Volume Survey
SFG . . . . . Star-Forming Galaxy
SFH . . . . . Star Formation History
SFR . . . . . Star Formation Rate
SMACS . . . . Southern MAssive Cluster Survey
SMBH . . . . . Supermassive Black Hole
SPS . . . . . Stellar Population Synthesis
SSP . . . . . Simple Stellar Population
SSP . . . . . Subaru Strategic Program
UDS . . . . . Ultra-Deep Survey
UKIRT . . . . United Kingdom Infrared Telescope
UV . . . . . Ultraviolet
VIDEO . . . . VISTA Deep Extragalactic Observations
VIS . . . . . Visible Camera
VISTA . . . . Visible and Near-infrared Survey Telescope for Astronomy
VLT . . . . . Very Large Telescope
VOICE . . . . VST Optical Imaging of the CDFS and ES1 Fields
VST . . . . . VLT Survey Telescope
WFC3 . . . . . Wide Field Camera 3
XMM-LSS . . *XMM-Newton* Large-Scale Structure

This is it! The moment we should have trained for!

—Turanga Leela, Futurama

1 Introduction

Contents

For thousands of years, humans have looked up at the sky and sought to develop a theory explaining the origins of the Universe and our place within it. The prehistoric monument of Newgrange in County Meath, Ireland, indicates that as early as 3200 BCE during the Neolithic Period, our ancestors were tracking the solar year, evidenced by sunlight flooding the central chamber on the winter solstice (Brennan, 1982). Around 5 millennia later, William Herschel proposed that our galaxy, the Milky Way, was a flattened disk composed of stars, star clusters, and nebulae (Herschel, 1785). Although Herschel speculated that some nebulae might be 'Island Universes' external to the Milky Way, it was not until 1925 that Edwin Hubble, using the well-known relationship between the luminosity and pulsation period of Cepheid variable stars, demonstrated that the Andromeda (M31) and Triangulum (M33) nebulae were in fact galaxies beyond our own (Hubble, 1925). The known Universe was revealed to be far more expansive than previously imagined, and this profound result marked the birth of Extragalactic Astronomy. Today, a hundred years after this discovery, the field has progressed immensely. Hubble's work culminated in a study showing that the universe was expanding (Hubble, 1929). Since then, astronomers have discovered quasars powered by supermassive black holes (Schmidt, 1963), inferred the existence of dark matter (Rubin and Ford, 1970), and most recently discovered galaxies at redshift $z = 14$, corresponding to only 300 million years (Myr) after the Big Bang (Carniani et al., 2024).

In high-redshift astronomy, we observe the distant Universe in order to seek answers to fundamental questions: When did the first galaxies form, and what were their properties? What are the physical mechanisms governing the growth and evolution of these galaxies? This thesis presents new results from my research on some of the most luminous galaxies to exist during the first 2 Gyr of the Universe. I begin by providing an overview of the conditions in the early Universe and exploring how the earliest galaxies formed and evolved.

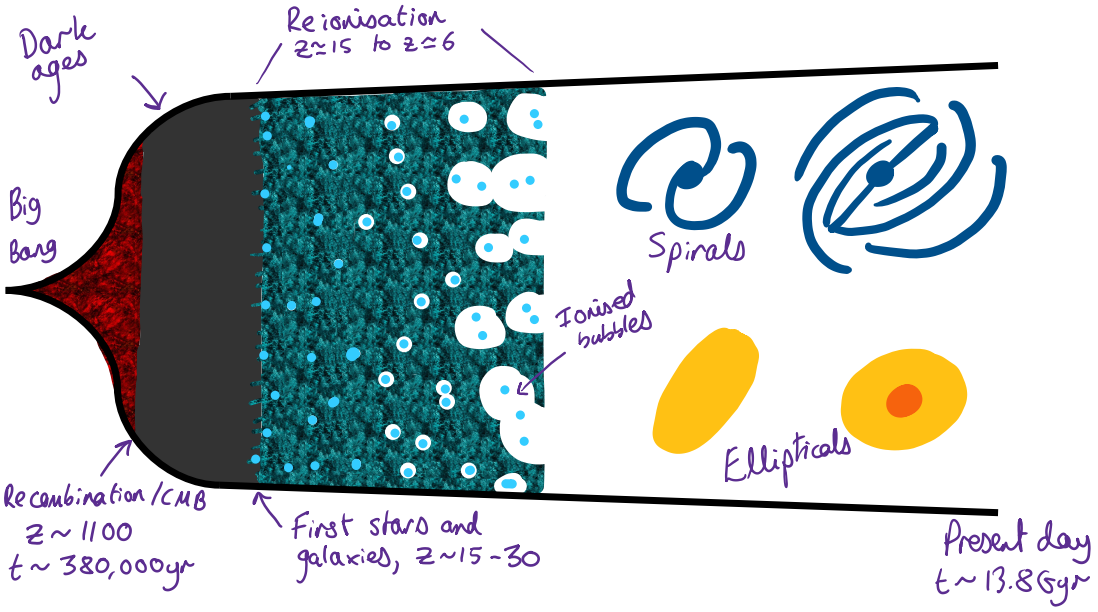

Figure 1.1: A sketch of the history of the Universe. Time increases from left to right, and correspondingly redshift decreases along this axis. Some key moments shown include recombination at $z \simeq 1100$, formation of the first stars at $z \sim 30$, and reionization ending around $z \sim 6 - 7$.

1.1 History of the Universe

The Universe has undergone significant evolution since the Big Bang. Observations of the Universe across the electromagnetic spectrum have allowed us to split its complicated evolution into several key stages. Here, I outline some key stages in the history of the Universe. I show a sketch of this timeline in Fig. 1.1.

1. **Prior to recombination**, during the first $\sim 380,000$ years after the Big Bang, the Universe was hot ($T > 3000$ K) and filled with an ionised plasma (free protons and electrons) and photons. The mean free path of photons was short, meaning they could not propagate freely without being scattered by a free electron. This renders the first epoch of the Universe opaque to direct electromagnetic observations, limiting what we can learn about it.

2. As the Universe expanded it diluted the hot plasma, cooling it ($T \propto 1 + z$ where z is the redshift) enough to allow for the **recombination** of free protons and electrons into primarily neutral hydrogen and helium (Peebles, 1968).

This corresponds to a redshift of $z = 1090$, or $\sim 380,000$ years after the Big Bang, when the Universe reached a temperature of $T \sim 3000$ K. After this, photons could stream freely through the Universe. We observe these earliest photons from recombination as the 'Cosmic Microwave Background' (McKellar, 1940; Penzias and Wilson, 1965), which today has a temperature of $T_{\rm CMB} = 2.73$ K (Fixsen, 2009).

3. After this, the Universe entered the **Dark Ages**. The distribution of matter was not completely uniform — small overdensities existed thanks to quantum fluctations that were expanded by a factor of 10^{26} due to a rapid acceleration of the Universe in the first 10^{-36} seconds (Guth, 1981). These overdensities began to coalesce under the force of gravitation, forming the first haloes of dark and baryonic matter (Press and Schechter, 1974). These initial structures would seed what is now the gas-rich cosmic web, with galaxy clusters sitting in the overdensities.

4. Once the gas within the first dark matter halos becomes dense enough, it cools via rotational and vibrational excitation of H_2 through collisions with other particles, allowing it to condense, eventually igniting nuclear fusion and forming the Universe's first stars. These stars form from pristine, metal-free gas—where metals (elements heavier than helium) would otherwise facilitate cooling, leading to the formation of extremely massive and luminous stars (Bromm et al., 1999; Abel et al., 2002). These stars emit intense ultraviolet (UV) radiation, live short, energetic lives, and rapidly enrich their surroundings with metals, enabling the formation of the stars we observe today. Over time, these first stars, along with the galaxies they inhabit, initiate the reionization of neutral hydrogen (requiring UV photons corresponding to $E \geq 13.6$ eV) in the intergalactic medium (IGM), marking the transition known as the **Epoch of Reionization (EoR)**. The epoch during which these first galaxies formed is known as **Cosmic Dawn**. Bubbles of ionised hydrogen surrounded the first ionising sources, and expanding until they coalesced to form a predominantly

reionised IGM. The midpoint of the EoR is thought to be at a redshift $z \simeq 7.82$ (~ 650 Myr after the Big Bang, Planck Collaboration et al., 2020), with the full timeline still being uncertain but thought to have started between $z \sim 10 - 30$ (depending on when the first stars and galaxies formed) and finished by about $z \simeq 6 - 7$ (Barkana and Loeb, 2001; Robertson, 2022). There is debate surrounding the nature of the reionising sources - whilst thought to be dominated by faint galaxies, rare, luminous galaxies (Naidu et al., 2020) or extremely rare, ultra-luminous quasars (Madau, 1995) may also contribute.

5. After the EoR, the cosmic star formation rate density (solar masses formed per year per cubic comoving megaparsec) continued to increase, reaching a peak at $z \sim 1 - 3$ (~ 3 Gyr after the Big Bang), increasing by a factor $\gtrsim 10$ from $z \simeq 7$ ($\simeq 750$ Myr after the Big Bang). This period is called **Cosmic Noon**. Galaxies also undergo significant morphological evolution, growing in size and forming structures such as disks, bars, bulges, spiral arms, developing into a 'Hubble sequence' of spirals and ellipticals (Oesch et al., 2010b; Conselice, 2014) that we see in the local Universe.

This thesis examines the properties of luminous galaxies at redshift $z \simeq 3 - 7$. In order to study galaxies during the EoR and into Cosmic Noon, it is essential that we are able to accurately measure their distances and sizes.

1.2 Distance scales in an expanding universe

Hubble (1929) showed that the recessional velocity of galaxies is proportional to their distance from the observer, providing the first evidence for expansion. This is known as Hubble's law. To measure the properties of the first galaxies, this thesis first requires an understanding of distance, size, and volume measures in an expanding Universe. An important equation in cosmology is the Friedmann equation, which describes this expansion. A key observation of the Universe is that it is homogeneous (the same everywhere) and isotropic (there is no preferred direction) on the largest physical scales ($\gtrsim 100$ Mpc). Using this, we can consider

the Universe as being filled with a uniform expanding medium with density ρ. I also introduce comoving coordinates, a coordinate system which scale with the expansion of the Universe. I relate the real separation r and the comoving separation x by $r = a(t)x$, where $a(t)$ is the scale factor, a quantity which describes how the size of the Universe changes over time due to expansion. The standard form of the Friedmann equation is then given by

$$\left(\frac{\dot{a}}{a}\right)^2 = \frac{8\pi G}{3}\rho - \frac{kc^2}{a^2} \tag{1.1}$$

where c is the speed of light, G is the gravitational constant, and k is some constant describing the curvature of the Universe: $k > 0$ corresponds to a closed universe, $k = 0$ corresponds to a flat universe, and $k < 0$ corresponds to a hyperbolic open universe.

We can now use the Friedmann equation to understand Hubble's law, namely that the recessional velocity of a galaxy, v, is related to its distance from the observer, d, by $v = H_0 d$, where H_0 is the Hubble constant (Hubble, 1929). In an expanding Universe, $v = dr/dt = (\dot{r}/r)r = (\dot{a}/a)r$, where we used the definition of the comoving position $r = a(t)x$. Thus we can equate these two forms to find that

$$H = \frac{\dot{a}}{a}. \tag{1.2}$$

Substituting into the Friedmann equation (1.2), we find an expression for the time-evolving Hubble parameter:

$$H^2(t) = \frac{8\pi G}{3}\rho(t) - \frac{kc^2}{a^2(t)}. \tag{1.3}$$

Note that it is possible to separately derive the fluid equation, which describes the time evolution of ρ (Liddle, 2003).

Our best model for the evolution of the Universe is called ΛCDM, where Λ is the cosmological constant introduced by Einstein and refers to dark energy driving the expansion of the Universe, and CDM is Cold Dark Matter, which forms the dark-matter haloes where structure formation in the Universe takes place. This model depends on some key physical constants, which for the purpose of this thesis I will assume as

$$\Omega_{\rm m} = 0.3,\ \Omega_\Lambda = 0.7,\ H_0 = 70\ {\rm km\ s^{-1}\ Mpc^{-1}} \tag{1.4}$$

where Ω is the fraction of the total energy density contained in each of baryonic and dark matter ($\Omega_{\rm m}$) and dark energy (Ω_Λ). Note that $\Omega_{\rm total} = \Omega_{\rm m} + \Omega_\Lambda = 1$ corresponds to a flat Universe. Setting $k = 0$, it is possible to derive the Friedmann equation for ΛCDM:

$$\left(\frac{\dot{a}}{a}\right)^2 = H_0^2 \left(\Omega_{\rm m} \frac{a_0^3}{a^3} + \Omega_\Lambda\right). \tag{1.5}$$

This tells us that before dark-energy dominated the energy density of the Universe, its evolution was governed by baryonic and dark matter, which decelerated the expansion. However, in the dark-energy-dominated era since $z \sim 0.5$, the influence of matter has weakened, leading to the observed accelerating expansion of the Universe.

Since galaxies are receding away from us, we find that the wavelength at which we observe some feature (such as a spectral line) is observed is related to the rest-frame wavelength $\lambda_{\rm rest}$ by

$$\lambda_{\rm obs} = (1 + z)\ \lambda_{\rm rest} \tag{1.6}$$

where z is the redshift. Note that this redshift is the cosmological redshift, caused by the expansion of the Universe, and distinct from Doppler redshift by peculiar motion and gravitational redshift. The redshift in an expanding Universe is given by

$$1 + z = \frac{a_{\rm obs}(t)}{a_{\rm emit}(t)} \tag{1.7}$$

where we used the recasting of Hubble's law in terms of the scale factor.

Due to the speed of light c being fixed in all frames of reference, one can observe the Universe at earlier epochs by observing it at greater distances and making use of the redshift relation in Equation 1.7. However, in the above expanding ΛCDM cosmology, the notion of distance is complicated. In general relativity, we unite space and time coordinates into space-time coordinates (Wald, 1984). Events are thus described by a set of four coordinates, (x, y, z, t). The spacetime interval ds between two infinitesimally close spacetime events in a flat, static (Minkowski) space is given by

$$ds^2 = -c^2 dt^2 + dx^2 + dy^2 + dz^2 \tag{1.8}$$

where c is the speed of light. If we allow different types of curvature with $k \in [-1, 0, +1]$, account for the expansion of the Universe with $a(t)$, use the homogeneity of the Universe, and move to spherical polar spatial coordinates, we arrive at the Robertson-Walker metric:

$$ds^2 = -c^2dt^2 + a^2(t)\left[\frac{dr^2}{1-kr^2} + r^2(d\theta^2 + \sin^2\theta d\phi^2)\right]. \tag{1.9}$$

For completeness, the Friedmann equation can be recovered from Einstein's field equations under this metric.

1.2.1 Cosmological redshift

We are now equipped to understand how certain properties, such as distance, size, and luminosity, depend on the cosmological model. Firstly, under the Robertson-Walker metric, it is possible to re-derive the cosmological redshift described in Equation 1.7. This redshift will be critical, since it will be used as a proxy for distance to galaxies. Light propagates along null spacetime intervals, giving $ds = 0$. From the Roberston-Walker metric, it is possible to derive

$$\frac{\lambda_{\rm obs}}{\lambda_{\rm emit}} = \frac{a(t_{\rm obs})}{a(t_{\rm emit})}. \tag{1.10}$$

From this we define the redshift as

$$1 + z \coloneqq \frac{a(t_{\rm obs})}{a(t_{\rm emit})}. \tag{1.11}$$

I will use this redshift to describe time and distances to distant objects. In particular, an object at redshift z refers to a distance such that the light is redshifted by a factor of $1+z$, and a time when the Universe was a factor $1/(1+z)$ smaller. In this thesis I study galaxies at $z \simeq 3-7$. Under the ΛCDM cosmological model, this corresponds to between roughly 750 Myr and 2 Gyr after the Big Bang.

1.2.2 The luminosity distance

On cosmological scales, the inverse square law cannot be used to calculate distances to objects since the expansion of the Universe further dilutes the photons detected by an observer in two ways:

- Photons lose energy proportional to $1+z$ as they are redshifted.
- The observer receives less photons proportional to $1+z$.

The luminosity distance D_L is critical for computing the absolute magnitude of objects from their apparent magnitudes by accounting for this dilution.

Suppose that an object has a luminosity L, defined as the energy emitted per second. The radiation flux density received by an observer, S, is defined as the energy received per unit area per second. Then for a static Universe, $D_L^2 \coloneqq L/4\pi S$, and so at the current time one would observe a flux $S = L/4\pi r_0^2$. However, by incorporating the two effects due to the expansion, the received flux

$$S = \frac{L}{4\pi a_0^2 r_0^2 (1+z)^2}. \tag{1.12}$$

This means the luminosity distance is $D_L = a_0 r_0 (1+z)$, recalling that r_0 is a comoving distance.

The above luminosity is actually the bolometric luminosity, integrated across all wavelengths. In practice, we observe distant galaxies in photometric filters sensitive only to a particular range of wavelengths. Given the redshift, the apparent magnitude (observed magnitude of an object) can be converted into the absolute magnitude (the apparent magnitude of an object if it were viewed from 10 pc away, providing a measure of intrinsic luminosity), taking into account the $(1+z)$ band-stretching of the continuum. In high-redshift astronomy, these magnitudes are typically defined via the AB magnitude system (Oke and Gunn, 1983). This system is defined with a zeropoint of 3631 Jy, such that given a flux density in Jy, the apparent monochromatic AB magnitude is given by $m_{\rm AB} = -2.5\log_{10}(f_\nu/3631\ {\rm Jy})$. If the flux is given in cgs units of erg s^{-1} cm^2 Hz^{-1}, then $m_{\rm AB} = -2.5\log_{10}(f_\nu) - 48.6$. However, we must pay attention to the rest-frame wavelengths probed by the filter used: for example, suppose that light is emitted by a galaxy at a wavelength $\lambda_{\rm emit} = 0.125\mu$m. If this galaxy is at redshift z = 7, we observe the light in the near-infrared (NIR) at $\lambda_{\rm obs} = 1\mu$m. An additional 'K-correction' which depends on the colour (or intrinsic spectral shape) of a source should be introduced that

accounts for the mismatch of the filter profile de-redshifted to the rest-frame of the galaxy and the desired luminosity band.

1.2.3 The angular diameter distance

A quantity of interest is the size of galaxies in the distant Universe, since this can be used as a probe of their growth and evolution. The angular diameter distance relates the angle of an object on the sky with its physical extent at its redshift. Suppose that an object along the line of sight has a physical diameter l. Then the angular diameter distance D_A is given by $D_A = l/\sin\theta \approx l/\theta$ using the small-angle approximation, certainly valid in astronomical and cosmological contexts. Returning to the Robertson-Walker metric (Equation 1.9), if the object is at a comoving radial distance r_0, and the object is aligned in the direction θ, then $l = ds = r_0 a(t_{\rm emit}) d\theta$. The observer then sees an angular size

$$d\theta = \frac{l}{r_0 a(t_{\rm emit})} = \frac{l(1+z)}{a_0 r_0}. \tag{1.13}$$

The angular diameter distance is thus given by

$$D_A = \frac{a_0 r_0}{1+z}. \tag{1.14}$$

The angular diameter distance has a peculiar consequence. For nearby galaxies ($z \ll 1$), D_A is essentially the same as the physical distance, and objects shrink as they move further away. However, at $z \gtrsim 1$, $a_0 r_0$ remains finite, whereas light continues to be redshifted. This means as $z \to \infty$, $D_A \to 0$. Objects thus begin to appear larger as they move farther away (Liddle, 2003). This property of the Universe permits size measurements of the first galaxies. For example, $D_A(z = 7) = 1078$ Mpc. This means that if we observe a galaxy with an angular diameter of 1 arcsec, it has a physical size of ~ 5.2 kpc. Compare this with a lower redshift: $D_A(z = 0.4) = 1100$ Mpc, which would give an object with an angular diameter of 1 arcsec a similar physical size. The angular diameter distance and the corresponding angular size of an object with a diameter of 5 kpc, both as a function of redshift, are shown in Fig. 1.2.

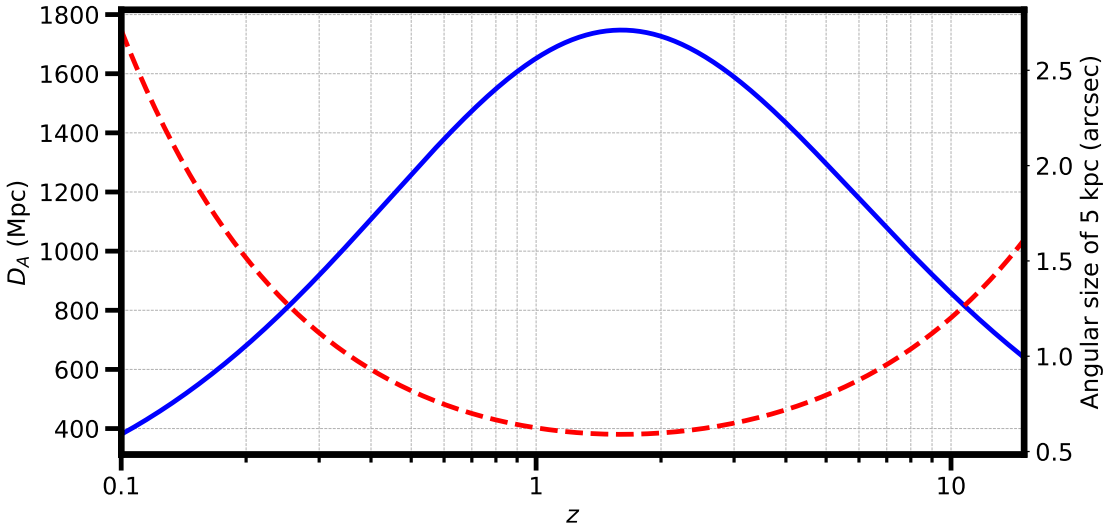

Figure 1.2: The angular diameter distance D_A as a function of redshift z, shown by the blue solid line. Also shown is the angular size of an object with a physical diameter of 5 kpc, given by 5 kpc/$\mathrm{D_A}$ in the small angle approximation, shown by the red dashed line. Due to the expanding Universe, galaxies of a fixed size at $z \gtrsim 2$ begin to appear larger as they move further away.

Additionally, if galaxies are resolved at high redshift, several of the above cosmological effects contribute to a reduction in their observed surface brightness. First, each photon is redshifted, reducing its energy by a factor of $(1+z)^{-1}$. Second, due to time dilation, the rate at which photons arrive is also reduced by a factor of $(1+z)^{-1}$. Finally, distant objects emitted their light when they were closer and had a larger angular size on the sky, spreading the light over a larger angular area by a factor of $(1+z)^2$. This leads to an effect called cosmological surface brightness dimming, where the surface brightness (flux per unit solid angle) of a source is proportional to $(1+z)^{-4}$.

1.2.4 The comoving volume

From the Robertson-Walker metric (Equation 1.9), a volume element corresponding to a cube of sides dr, $d\theta$ and $d\phi$ is given by

$$dV = \frac{a^3(t)dr}{\sqrt{1-kr^2}} r^2 d\theta \sin(\theta) d\phi \tag{1.15}$$

This volume scales with the expansion of the Universe – $dV \propto a^3(t)$. A more useful notion for galaxy evolution is the comoving volume element dV_C, given by

$$dV_C = \frac{c}{H_0} \frac{(1+z)^2 D_A^2}{\sqrt{\Omega_M (1+z)^3 + \Omega_\Lambda}} d\omega dz. \tag{1.16}$$

where $d\omega = \sin\theta d\theta d\phi$ (Peebles, 1993). The comoving volume keeps the number count constant for a non-evolving population, allowing for the removal of cosmological effects when exploring the evolution of a galaxy population density with redshift.

1.3 Formation of the first galaxies

As discussed in Section 1.1, the distribution of matter during the Dark Ages was not completely uniform – small overdensities existed. These overdensities began to coalesce under the force of gravity, forming the first haloes of dark and baryonic matter (Press and Schechter, 1974). In this Section, I outline steps for forming the first stars and galaxies in the Universe, occurring within these first dark matter haloes. In Fig. 1.3 I show a diagram of these galaxy formation steps.

1.3.1 The first stars

Stars form when gas falling into the halo is able to cool sufficiently to fragment and become dense enough to start nuclear fusion. In the local Universe, gas can cool efficiently via emission lines of 'metals' (elements heavier than helium) in the interstellar medium (ISM). These metals are produced by previous generations of stars. However, the first stars formed from primordial hydrogen and helium gas, meaning that metals were not yet available for metal line cooling. Their formation relied on cooling by molecular hydrogen (H_2). When the cooling time scale is much faster than the dynamical time scale of the gas cloud, it collapses (Rees and Ostriker, 1977; Silk, 1977), and since H_2 cooling is more inefficient than metal line cooling, the gas cloud can reach much higher temperatures and densities before collapsing. The very first stars, called Population III, may have therefore been extremely massive with $M \simeq 10^2 - 10^3 M_\odot$, perhaps even reaching $10^4 M_\odot$ in extreme cases where significant fragmentation of gas clouds does not occur (Bromm et al.,

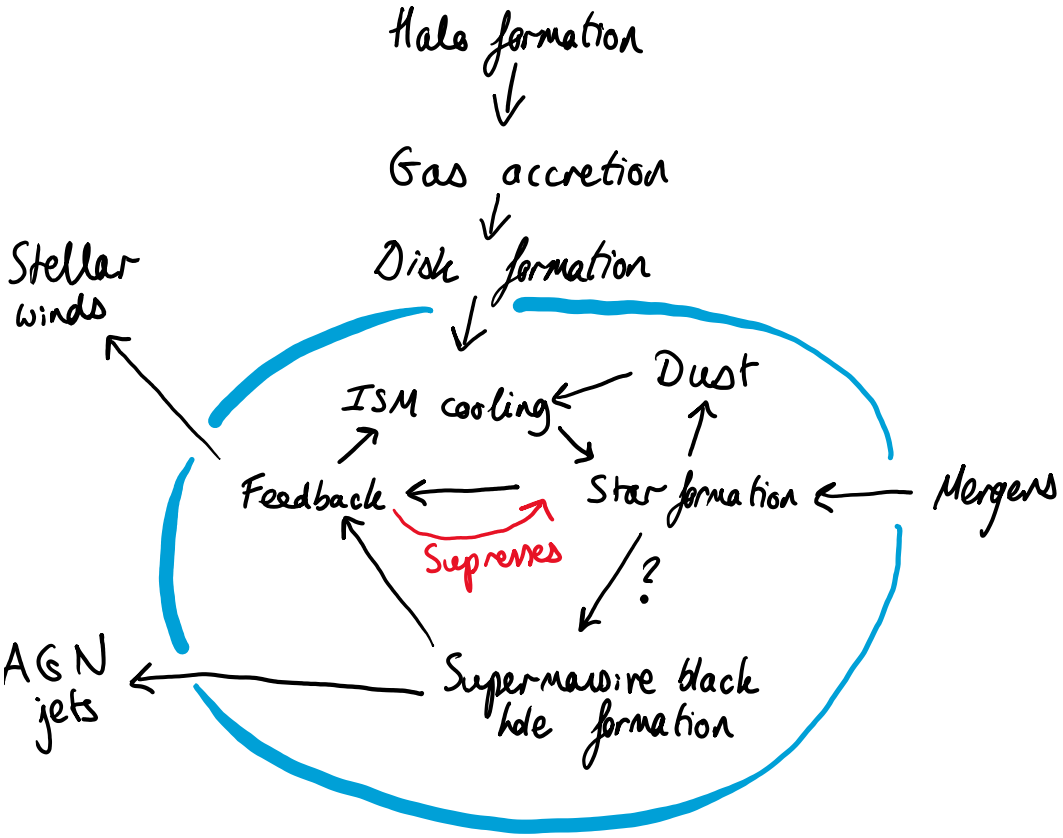

Figure 1.3: Flow chart of the steps in galaxy formation, adapted from Loeb and Furlanetto (2013). First a dark matter halo forms, accreting gas. This gas then settles into a rotationally supported disk, with its size governed by the host dark matter halo. Once the gas cools sufficiently, star formation begins, and stellar feedback can eject material in the ISM via galactic winds. Cooling and feedback provides self-regulation within the ISM. Dust is also produced by supernovae and stellar winds. Mergers can induce star formation, and dense stellar clusters might provide one pathway for the formation of SMBHs. SMBHs can become active by building luminous accretion disks, leading to the suppression of star formation and the launching of jets.

1999). These first stars would then live very rapid lives, very quickly enriching the surrounding ISM with metals, allowing for the formation of typical stars observed in the local Universe. The extreme UV radiation outputted by Population III stars would have allowed for the reionisation of their surrounding neutral gas (e.g. Wyithe and Loeb, 2003) and dense clusters provide one possible pathway for the formation of supermassive black holes at high redshift (e.g. Devecchi and Volonteri, 2009; Bañados et al., 2018)

1.3.2 A simple disk formation model

Eventually, the gas that has fallen into a halo cools enough to contract and become supported by its own angular momentum. This angular momentum provides the means for the galaxy to develop a regular morphology via disk formation. The angular momentum J of a halo with mass M_h and total energy E are often related via a dimensionless spin parameter λ, given by

$$\lambda \coloneqq J|E|^{1/2}G^{-1}M_h^{5/2}. \tag{1.17}$$

This spin parameter roughly represents the ratio of the rotation speed of the halo to the maximal value beyond which it would be disrupted (Fall and Efstathiou, 1980; Mo et al., 1998; Bullock et al., 2001). Now that the gas has settled into a rotationally supported disk, it has a mass that is some fraction m_d of the halo mass M_h, and angular momentum j_d which is some fraction of the halo angular momentum J. For an isothermal profile for the dark matter halo, neglecting self-gravitation of the gas disk, and assuming an exponential surface density profile given by $\Sigma(R) = \Sigma_0 \exp(-R/R_d)$ where R_d is the disk scale radius, then it can be shown that

$$R_d = \frac{1}{\sqrt{2}} \left(\frac{j_d}{m_d} \right) \lambda r_{\text{vir}} \tag{1.18}$$

where r_{vir} is the virial radius of the dark matter halo, and it is thought that this distribution does not change with time (Bullock et al., 2001). The size of the disk is therefore proportional to the spin parameter of the halo and the specific angular momentum of the galaxy, which depends on the halo mass. This

means that under this model, the distribution of galaxy sizes is determined by the distribution of spin parameters and dark-matter halo masses (Barkana and Loeb, 2000). Warren et al. (1992) showed via numerical simulations that the spin parameter follows a log-normal distribution,

$$p(\lambda)d\lambda = \frac{1}{\sigma_\lambda\sqrt{2\pi}} \exp\left[\frac{\ln^2(\lambda/\bar{\lambda})}{2\sigma_\lambda^2}\right] \frac{d\lambda}{\lambda} \tag{1.19}$$

which immediately predicts that galaxy sizes should be log-normally distributed, under this simple model. It also makes predictions about how disk sizes should scale with redshift – for a halo with fixed circular velocity, the disk sizes should scale with redshift as $R_d \propto (1+z)^{-1}$. Additionally, since $r_{\rm vir} \propto H(z)^{-2/3}$, and $H(z) \propto (1+z)^{-1}$ in a matter-dominated Universe at $z \gg 1$, for a fixed halo mass we expect $R_d \propto (1+z)^{-1.5}$. Measuring galaxy sizes across redshift, with some attempt to hold either the halo circular velocity or mass constant, provides an additional test of the disk formation model. An assumption of this model is that the disks form in isolation, without merging or interacting with other galaxies, and without any internal feedback.

1.3.3 Star formation

Once the gas has cooled and collapsed within star-forming galaxies, widespread star formation can begin. A key quantity of interest to both observers and theorists is the star formation efficiency–the effectiveness with which a galaxy converts gas into stars. In the local Universe, the Kennicutt-Schmidt relation states that the star formation rate surface density is related to the gas surface density as $\Sigma_* \propto \Sigma_{\rm gas}^{1.4}$ (Schmidt, 1959; Kennicutt, 1998). Whether this holds at high redshift, at lower metallicity with higher galaxy gas fractions, is not immediately clear. Galaxies at $z \sim 1-4$ follow a Kennicutt-Schmidt relation, but with differing slopes and normalisations indicating higher efficiency (Genzel et al., 2010; Tacconi et al., 2013; Tacconi et al., 2018). This may be caused by a more turbulent and clumpy distribution of gas at high redshift (Dekel et al., 2009a), possibly leading to bursty star formation (Sun et al., 2023).

1.3.4 Gas accretion and mergers

Galaxies are regions of the Universe where material accreted into a dark matter halo has been transformed into stars, metals, dust, and black holes. Through this transformation of infalling gas, galaxies undergo complex physics restricting or encouraging star formation, including feedback, jets, winds, and mergers. The mass growth of early proto-galaxies is first driven by gas accretion, providing the fuel for star formation. The filamentary structure of the Cosmic Web provides the means for cold gas accretion, and at high redshift, dark matter haloes are able to accrete gas more rapidly than at low redshift (Neistein et al., 2006). Mergers provide an alternate pathway for mass growth. They are often split into major mergers, where the mass ratio of the two galaxies is less than 1:3, and minor mergers, where the mass ratio is greater than 1:3 (e.g. Conselice, 2014, although the precise choice of mass ratio can vary). In minor mergers, the less massive galaxy usually does not cause a major perturbation in the more massive galaxy's structure. Major mergers are often more violent, resulting in a descendant galaxy whose morphology is unlike that of both parents. In the local Universe, it is thought that elliptical galaxies are formed by major mergers between spiral galaxies. Mergers can induce gravitational tides which disrupt the gas within galaxies. This causes the gas to collide via shocks, which can result in 'starbursts' – widespread star formation over short timescales (Cox et al., 2008). At high redshift, large fractions of galaxies often exhibit irregular morphologies, which may be indicative of merging behaviour (Kartaltepe et al., 2023). It may be the case that such starbursts are important for rapidly building the very luminous galaxies we see in the early Universe (Mason et al., 2023).

1.3.5 Black holes

It is thought that most galaxies host a supermassive black hole (SMBH) at their centre (Magorrian et al., 1998), and supermassive black holes have been discovered at high redshift (e.g. Bañados et al., 2018). They are too massive to have only accreted material at the Eddington-limited rate to grow such large masses at early cosmic time if starting from a stellar remnant black hole, thus requiring massive

seed black holes at very high redshift, super-Eddington accretion or mergers. One scenario discussed earlier was the formation of large seed black holes from Population III stellar clusters. Other potential seeds include direct collapse black holes, formed from gas collapsing directly into black holes with $M \sim 10^5 - 10^6\ M_\odot$ at $z \sim 15$ (e.g. Regan and Haehnelt, 2009) and primordial black holes formed before recombination during the radiation-dominated era of the Universe at $z \gtrsim 1100$ (e.g. Hawking, 1971). An active galactic nucleus (AGN) is a galaxy containing a SMBH which is actively accreting matter, leading to an accretion disk with Eddington ratio exceeding a limit of $L_{\rm AGN}/L_{\rm Edd} > 10^{-5}$ (although this exact limit can vary), where $L_{\rm AGN}$ is the bolometric luminosity of the SMBH and $L_{\rm Edd}$ is the Eddington luminosity, the maximum luminosity before radiation-driven winds blow apart the accretion disk (see Netzer, 2015, for a review). AGN are also capable of launching jets, leading to some of the largest astrophysical structures in the Universe (Oei et al., 2022).

1.3.6 Feedback processes

Massive stars and supermassive black holes have a profound impact on their host galaxy via feedback mechanisms, playing a major role in galaxy evolution by regulating the ISM and producing 'quenched' galaxies with very little to no star formation and red colours.

Supernovae are the cataclysmic final stage of massive stars and some binary star systems experiencing accretion from one star to another. Supernovae are energetic enough to cause shock heating of the ISM, rendering star formation inefficient, and drive strong galactic winds capable of expelling gas from galaxies, with the outflow rate surpassing the star formation rate of the galaxy. In fact, simulations have shown that the mass outflow rate can be as high as $10 - 20$ times the star formation rate (Hopkins et al., 2012). Supernova feedback preferentially impacts low-mass galaxies, resulting in dwarf galaxies with irregular morphologies, patchy star-forming regions (if ongoing) and hot bubbles in the ISM (e.g. Governato et al., 2010).

AGN are also capable of significantly impacting their host galaxies. The velocity of accreted material in the accretion disk around a SMBH follows a strong gradient,

causing friction and leading to the emission of gravitational potential energy as light. These accretion disks can have luminosities higher than the host galaxy since they can convert mass to light much more efficiently than star formation ($L_{\rm AGN} \sim 0.1\dot{m}c^2$, compared to $L_* < 10^{-2}\dot{m}c^2$ for nuclear fusion). AGN that completely outshine their host galaxy are known as quasars (Schmidt, 1963). Radiation from the accretion disk is also capable of stopping star formation by limiting the cooling of the ISM, preventing the collapse of gas into protostars (Bower et al., 2006). Radiation from the accretion disk can also drive outflows of ionised gas and dust (Laha et al., 2021). AGN are also capable of launching polar jets caused by twisting of magnetic fields from both the black hole and the accretion disk. These jets cause shocks and heat the ISM, leading to reduced star formation efficiency (Blandford et al., 2019). AGN feedback predominantly affects high-mass galaxies, which are capable of sustaining the growth of their supermassive black holes. It is believed that galaxies that exceed a certain quenching mass threshold experience strong suppression of star formation due to feedback mechanisms (Peng et al., 2010), with AGN feedback being a potential driver of this process. I discuss AGN feedback further in Section 1.6.

1.3.7 Dust

An additional major component of galaxies, along with gas, stars, and black holes, is dust. Produced in stellar outflows and explosive ejecta, dust undergoes a variety of physical processes that affect its properties (Dwek, 1998). Dust is effective at absorbing short-wavelength light (e.g. in the rest-frame UV) and re-emitting it at infrared and submillimetre wavelengths. It is therefore effective at *obscuring* star formation - in order to measure total star formation, one needs to observe the rest-UV light from dust-free regions, as well as long-wavelength light from dusty regions. In fact, dust-obscured star formation contributes more than half of the total star formation in the Universe at $1 < z < 4$ (Zavala et al., 2021). The production of dust in galaxies at high redshift marks a key threshold where the ISM has become enriched enough to produce carbonaceous grains of material. I discuss the role of dust at high redshift further in Section 1.6.

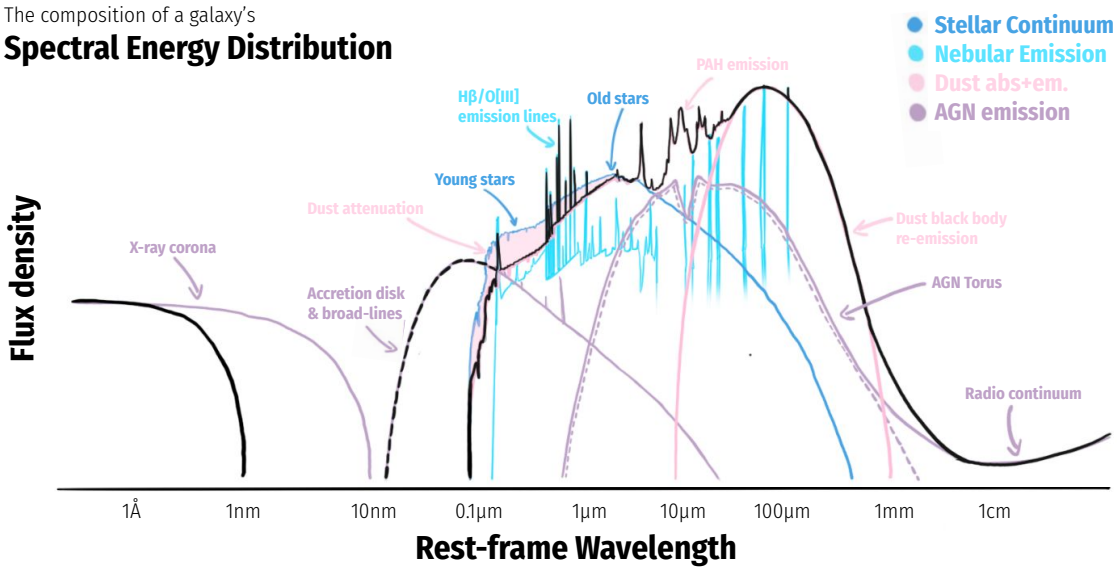

Figure 1.4: Panchromatic SED of a galaxy, showing the contributions from the stellar continuum, nebular and dust emission, and dust absorption and emission. Reproduced from Iyer et al. (2025).

1.4 The spectral energy distribution of a galaxy

The light produced by a galaxy as a function of wavelength, or its spectral energy distribution (SED), encodes a wealth of information regarding the past and current state of a galaxy. Fitting of a model SED to data provides a method for inferring properties such as stellar masses, star formation rates and histories, metallicities, dust content, and the properties of the interstellar gas.

1.4.1 Components of the SED

A galaxy SED is a combination of flux from all the components outlined in the previous section: stars (stellar emission), gas in the ISM (nebular emission), black holes (AGN emission), and dust absorption and emission.

In Fig. 1.4, I show a schematic of the panchromatic SED of a galaxy, reproduced from Iyer et al. (2025). Focusing first on the stellar continuum, the UV emission of galaxies is dominated by young stars. These are O- and B-spectral-type stars, which are very massive ($M \sim 3-60\ M_{\odot}$) and short-lived ($t \sim 1-400$ Myr). Strong rest-UV emission is therefore thought to be tracing star formation on scales of $10 - 100$ Myr

(see for example fig. 2 of Madau and Dickinson, 2014); correspondingly, if a galaxy does not have recent or ongoing star formation, it will not have significant rest-UV continuum flux. Note also the difference in UV flux between the stellar continuum and the pink curve showing the attenuated SED in Fig. 1.4 – dust attenuation significantly impacts the slope of the UV continuum, acting to redden it. Another strong feature that can be observed in the SED is the Lyman limit at 912Å. Photons blueward of this limit are capable of ionising hydrogen from the ground state. Since young UV-luminous stars usually still reside within the neutral hydrogen (HI) gas they initially formed from, emission of these photons is suppressed. However, if there are large amounts of star formation or intense starbursts, then strong winds can blow holes into the neutral hydrogen, allowing these ionising photons to escape into the circumgalactic medium (CGM) and intergalactic medium (IGM) (Heckman et al., 2001). Measuring the escape fraction of these photons, $f_{\rm esc}$, is critical at high redshift because they are responsible for the reionisation of the neutral hydrogen gas in the entire Universe left over after recombination at $z = 1100$ (e.g. Madau et al., 1999).

The Balmer break that occurs at 3650Å can be best seen as a jump in Fig. 1.4 just blueward of 1μm. This is caused by the ionisation of hydrogen atoms from the $n = 2$ level, and is strongest for A-type stars which peak in temperature at around $10,000$ K and have lifetimes of $t \sim 1$ Gyr. The strength of the Balmer break is, therefore, a good tracer of the age of the stellar population. There is also an additional break at 4000 Å due to absorption by calcium, carbon, and nitrogen in stellar atmospheres. This probes yet older stellar populations than the Balmer break, in particular populations comprised of G- and K-type stars whose lifetimes can be up to 17 Gyr. Redwards of this break is the optical continuum. Note that optical light is not as strongly attenuated by dust as UV light. Since less massive older stars usually dominate in number over young, short-lived, luminous stars, this flux is usually associated with the older stellar population of the galaxy and is therefore used to trace the stellar mass of the source. However, intense star formation can lead to strong nebular emission lines, produced by the recombination of ionised atoms in the ISM. These lines include Hα λ6563, Hβ λ4861 [OII] $\lambda\lambda 3726, 3729$,

[OIII] $\lambda\lambda 4959, 5007$, [SII] $\lambda\lambda 6716, 6731$, and [NII] $\lambda 6583$ (Charlot and Longhetti, 2001). Measurements of these lines with spectroscopy provide a probe of the gas phase (e.g. electron temperature and density) of the ISM (Cameron et al., 2023). However, in broadband photometry at $z > 6$, it can be difficult to distinguish strong nebular emission from a strong Balmer break (Stark et al., 2013).

There are also UV emission lines that provide insight into the ionising properties of galaxies. Of high importance is the Lyman-α (Lyα) line, caused by resonant scattering and recombination of hydrogen as the electron drops from the $n = 2$ to $n = 1$ energy level. This line not only traces ionised hydrogen (HII) regions and AGN activity, but also ionised gas in the CGM around galaxies (Ouchi et al., 2020).

In the mid-infrared at $\sim 10\mu$m the polycyclic aromatic hydrocarbon (PAH) features can be seen. PAHs account for $\lesssim 15\%$ of carbon in the ISM and can be used as a tracer of star formation (e.g. Shipley et al., 2016) and to probe highly obscured AGN (e.g. Donnan et al., 2023b).

Dust emission dominates the far-infrared and sub-millimetre wavelengths of the galaxy SED, as it re-emits light from rest-UV and optical wavelengths. The formation, growth and destruction of dust is poorly understood (Schneider and Maiolino, 2024). An example of a formation pathway is in supernovae (first seen in SN 1987A, Kozasa et al., 1989) and subsequent growth by accretion of monomers in the ISM. In Fig. 1.5, I show examples of dust attenuation laws. The shape of the attenuation curve and the presence of a bump may depend on the dust grain composition, star-dust geometry, and turbulence within galaxies (Salim and Narayanan, 2020). Measuring dust attenuation curves at high redshift is therefore key to understanding the evolution of dust through cosmic time.

1.4.2 SED fitting

In practice, it is not possible with current instruments to obtain the full galaxy SED via spectroscopy. Photometry uses charged coupled devices (CCDs) to quantify the total light received from astronomical bodies within the wavelength range of a broadband photometric filter, and is generally faster than spectroscopy over large

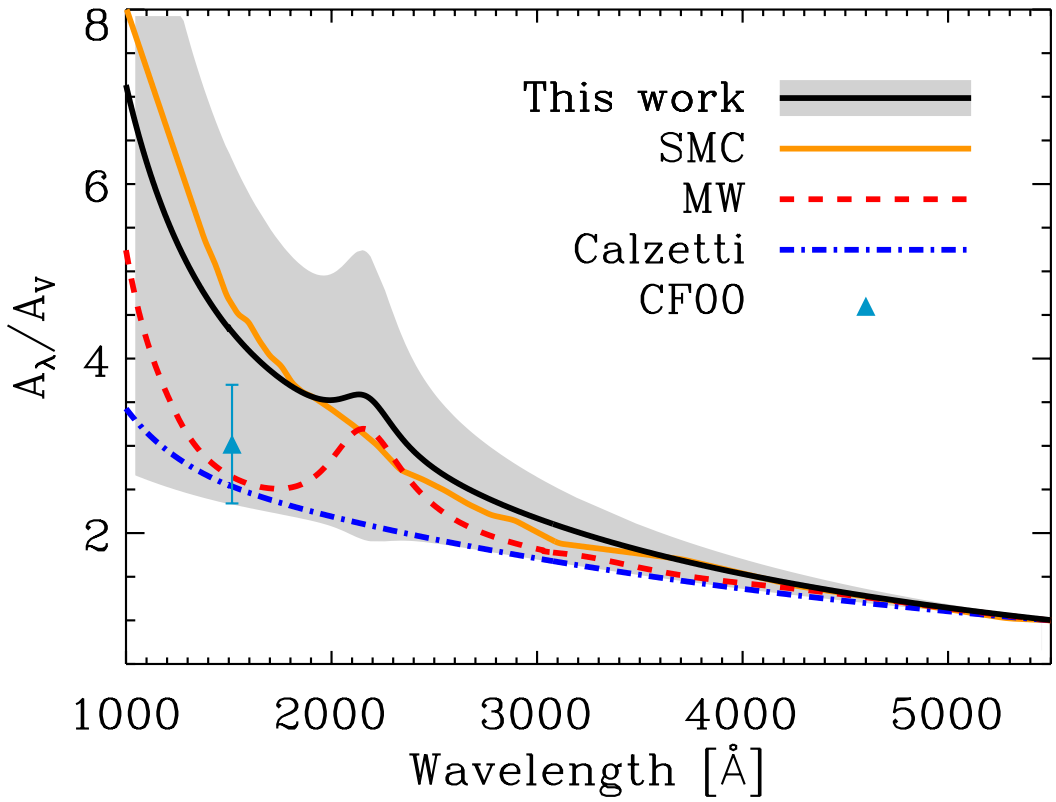

Figure 1.5: Dust attenuation curves of galaxies in the local Universe, reproduced from Salim et al. (2018). Also shown are the dust attenuation curves for the Small Magellanic Cloud, the Milky Way, and the Calzetti et al. (2000) law based on starburst galaxies. The attenuation is stronger at shorter wavelengths, and can show a characteristic bump at 2175Å thought to be caused by carbanaceous dust grains, in particular PAHs (Li and Draine, 2001).

areas. Photometry thus provides a coarse sampling of the underlying SED across a wide wavelength range. Astronomers therefore use SED fitting codes to infer the underlying SED and to then measure the physical properties of galaxies.

The creation of an SED model is shown in Fig. 1.6. The general process is as follows: first, a simple stellar population (SSP) model is generated, which describes the time evolution of a single coeval population of stars which relies on some input initial mass function (IMF), isochrones, and stellar spectra templates (Conroy, 2013). The IMF determines the mass distribution of a newly formed SSP. Common choices include those of Salpeter (1955), Kroupa (2001) and Chabrier (2003). However, measurements of galaxies at high redshift showing signs of being dominated by

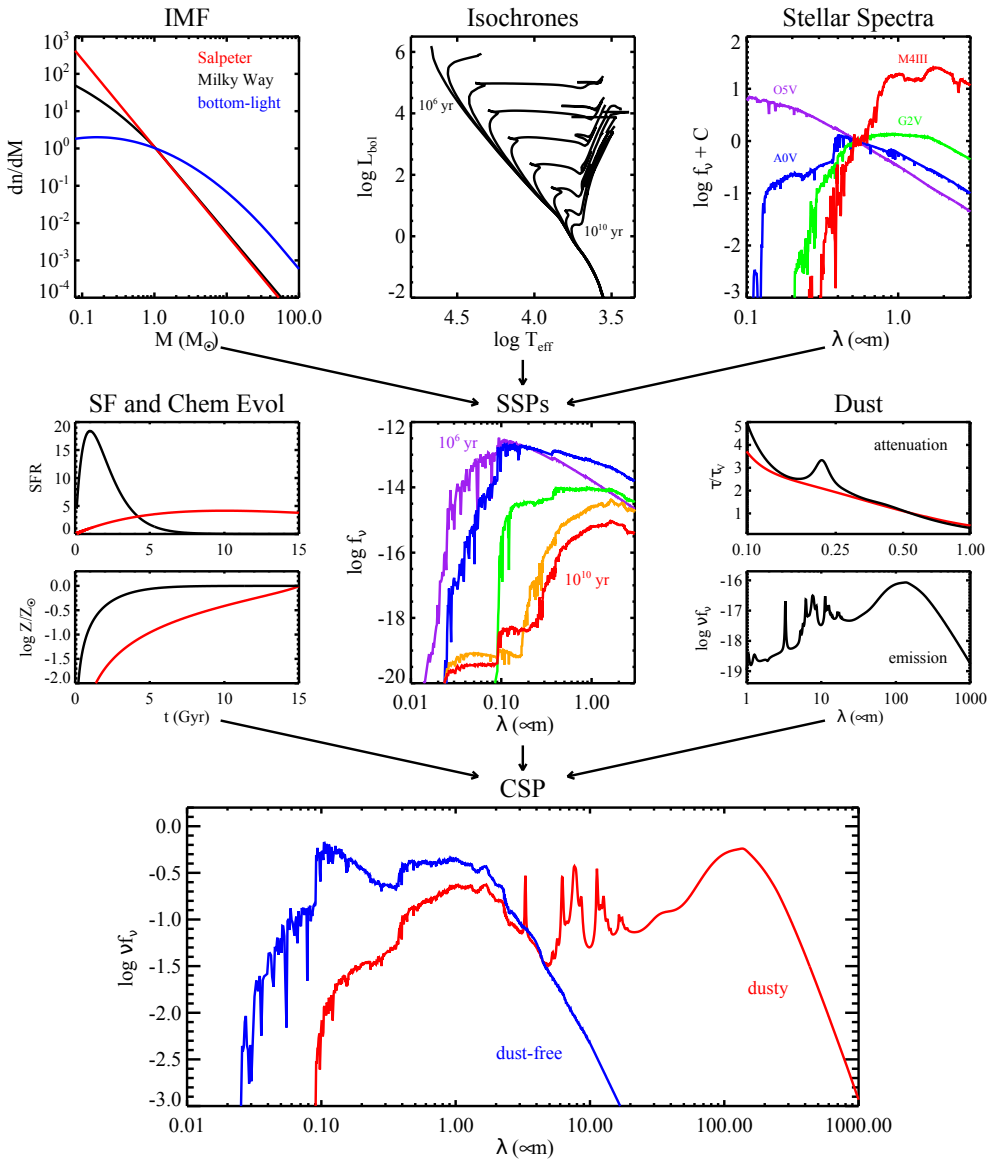

Figure 1.6: The ingredients of an SED model, reproduced from Conroy (2013). In the top row, a single stellar population is created based on an input initial mass function, isochrones governing their time evolution, and template stellar spectra. These simple stellar populations are then populated according to some star formation history, with some dust absorption/emission and chemical evolution, to produce the final SED shown in the bottom.

nebular emission may suggest a top-heavy IMF, where larger abundances of massive stars are formed (Cameron et al., 2024). Isochrones determine the luminosity and temperature of a star as a function of time. Stellar population synthesis (SPS) models then generate composite stellar populations by populating SSPs according to some star formation history. Commonly used SPS models include Bruzual and Charlot (2003) and Stanway and Eldridge (2018), the latter of which accounts for binary star systems. Additional effects such as dust attenuation, chemical evolution, IGM absorption, and gas-phase properties leading to nebular emission lines are then also included to produce the final SED model. In particular, nebular emission requires detailed modelling of the physics of ionised gases (e.g. CLOUDY, Ferland et al., 1998). IGM absorption by neutral hydrogen gas along the line of sight is usually prescribed according to Madau (1995), although more recent updated analytic models produce some systematic offsets (Inoue et al., 2014). Dust absorption and emission often assume energy balance, with absorbed UV and optical light being re-emitted by PAHs and blackbody emission at some dust temperature (da Cunha et al., 2008). The best fitting SED to a set of photometric measurements is then found by minimising the χ^2 statistic across a set of model SEDs (e.g. LePhare, Arnouts et al., 1999; Ilbert et al., 2006) or by exploring a parameter space restricted by some set of priors (e.g. BAGPIPES, Carnall et al., 2018).

1.4.3 Degeneracies in SED fitting

One challenge facing the SED fitting method is that some physical parameters can be degenerate for a given set of input data. For example, age and metallicity can be degenerate – at a fixed stellar temperature, higher metallicity results in redder colours. However, age also reddens the SED by the effect it has on isochrones (Worthey, 1994). In addition, age and dust are degenerate if only UV to NIR photometry is available (Papovich et al., 2001). This creates a triplet of age-dust-metallicity degeneracy, leading to large uncertainties on estimated physical parameters. Additionally, in broadband photometry (such as with *Spitzer*/IRAC at high redshift), it is difficult to distinguish between strong rest-optical continuum

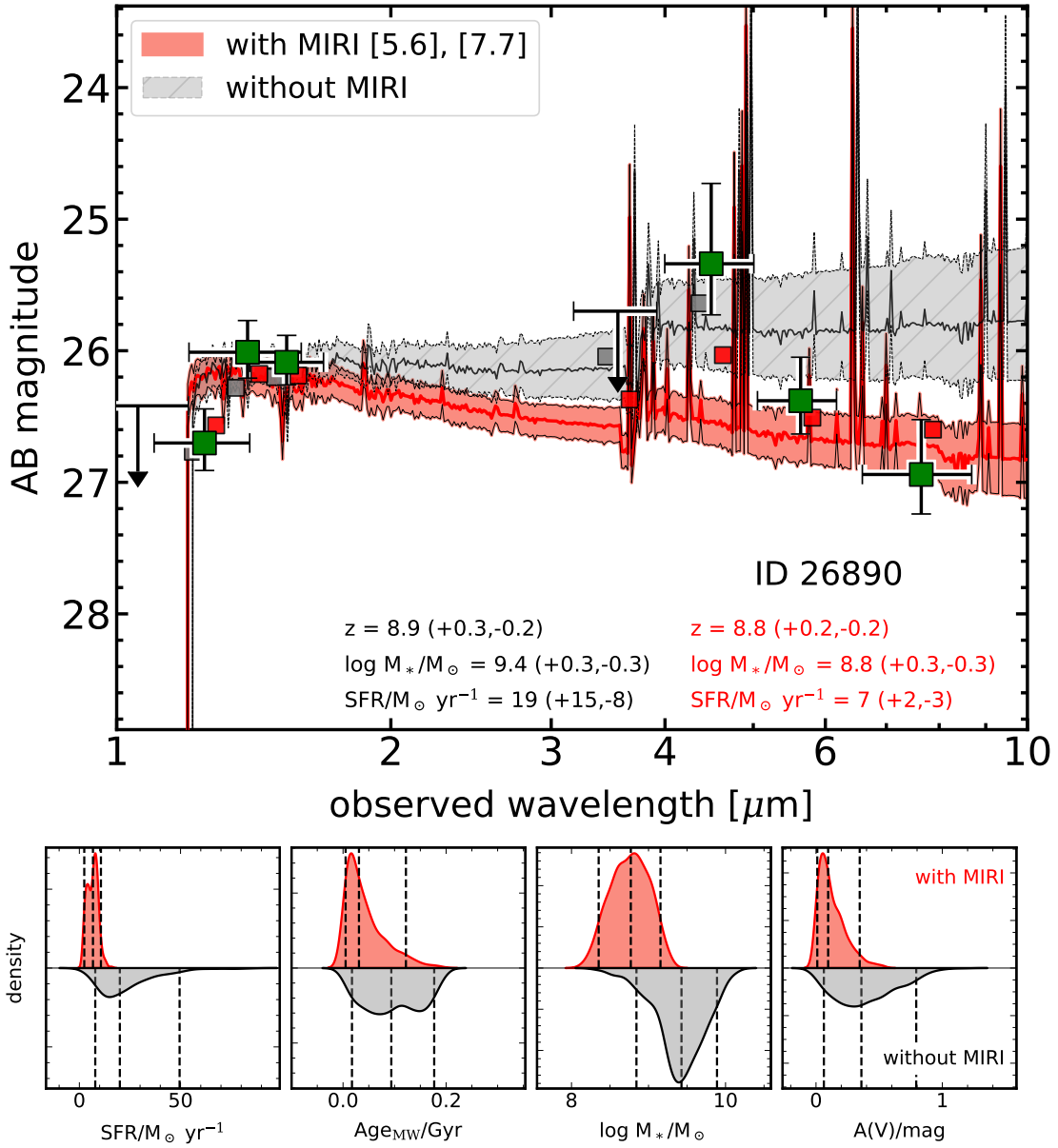

Figure 1.7: Top: SED fitting of a galaxy at $z = 8.8$ with MIRI (gray) and without MIRI (red). The green points show the *Hubble*, *Spitzer*/IRAC and *JWST*/MIRI photometry, and the gray and red points are model photometry. **Bottom:** inferred properties of the galaxies (SFR, age, stellar mass and dust attenuation) with/without MIRI. The dashed lines represent the 5th, 50th and 95th percentiles. Reproduced from Papovich et al. (2023).

emission from older stellar populations and nebular emission. Far-infrared observations help constrain dust temperature and mass, and spectroscopic measurements of emission and absorption lines constrain metallicity, allowing for improvements to be made on estimates of properties such as the SFR. In Fig. 1.7, I show the

SED fitting of a galaxy at $z = 8.8$ with and without *JWST* Mid Infrared Camera (MIRI) photometry at 5.6μm and 7.7μm. The inferred properties with MIRI change significantly – the SFR, stellar mass and dust attenuation are much lower since, in the absence of MIRI data, SED models cannot distinguish whether the red rest-frame UV and optical colours are a result of dust attenuation, older stellar populations, or strong emission lines (or all of them). In this case, the fits including MIRI photometry are dominated in the rest-optical by strong nebular emission.

Not only can physical parameters of galaxies be degenerate, but entire classes of galaxies and even objects within the Milky Way can all have very similar photometry with completely different underlying SEDs. To disentangle these cases, one must use enough photometric filters covering a significant portion of the electromagnetic spectrum, alongside a robust understanding of the different astrophysical populations that can produce similar observations. One topic I will explore in this thesis is distinguishing between the similar photometry that is seen for brown dwarfs within the Milky Way, dusty galaxies at $z \sim 1 - 2$ with a strong Balmer break, and star-forming galaxies at $z > 6$.

1.5 Observing the first galaxies

In the previous sections, I discussed the formation of galaxies, the components of their SEDs, and the use of SED fitting to infer galaxy properties. Before embarking on the search for high-redshift galaxies, there is one more important feature of their observed SEDs to consider, imprinted as light travels from the galaxy towards our observatories. As discussed earlier, the Lyman limit at 912Å corresponds to the hydrogen ionisation energy. Similarly, the transition between the $n = 2$ and $n = 1$ energy levels of hydrogen corresponds to a wavelength of 1216Å, known as the Lyman-α transition. If neutral hydrogen clouds lie along the line of sight, they absorb flux corresponding to the Lyman-α transition (Gunn and Peterson, 1965; Becker et al., 2001). This absorption occurs at the rest-frame wavelength of the intervening gas cloud, leading to a feature known as the Lyman-α forest. This is characterised by a series of spectral absorption lines, with the redshifting of

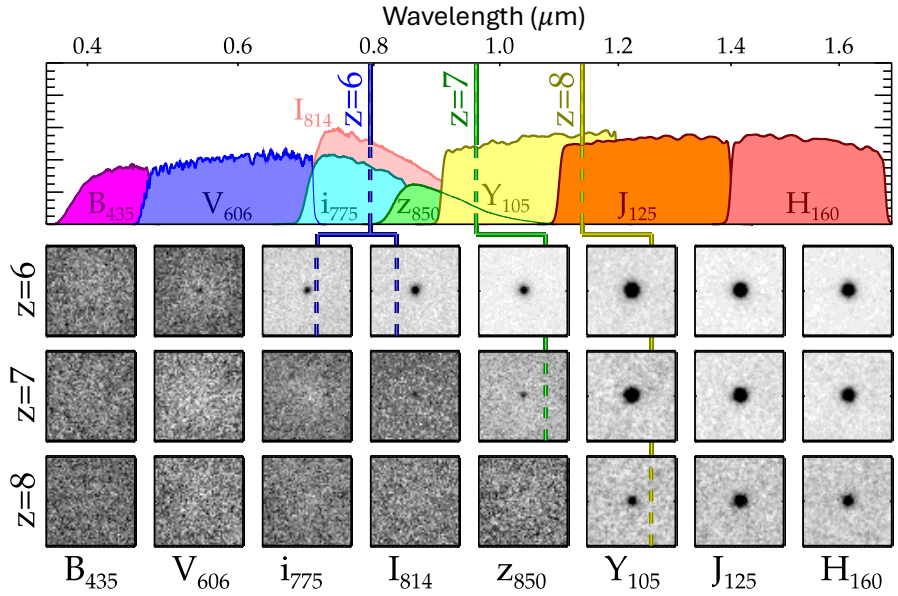

Figure 1.8: *Hubble* filter response curves (top) used to find galaxies at $z \geq 6$ with the Lyman-break technique. The bottom rows show the postage stamps of candidate galaxies at $z = 6, 7, 8$. Reproduced from Finkelstein et al. (2015).

light causing the absorption features to appear at progressively longer wavelengths (redward of the Lyman-α line in the rest-frame of the galaxy). As redshift increases, the density of HI clouds grows, and by $z \gtrsim 6$, the IGM becomes completely neutral. This implies that at higher redshift, the Lyman-α forest thickens and eventually causes nearly complete absorption of light with wavelengths shorter than 1216Å. As a result, the Lyman limit becomes unobservable, and the most prominent feature imprinted on the galaxy SED is the strong Lyman-α break at 1216Å. The Lyman break, observed at $\lambda = 1216(1 + z_{\text{source}})$Å is the primary feature used to search for high-redshift galaxies (although note that galaxies at $z \sim 3$ still have flux between $\lambda_{\text{rest}} = 912 - 1216$Å). Galaxies with this feature are called Lyman-break galaxies (LBGs).

1.5.1 The Lyman-break technique

The power of the Lyman break lies in its ability to be observed in broadband photometry. The colour of LBGs in two filters bracketing the Lyman break should show a strong red colour, and should also have relatively flat colours in two filters

which probe the rest-frame UV continuum. Guhathakurta et al. (1990) used UBR filters (centred at 3600Å, 4500Å, and 6500Å respectively) to find sources with a red $U-B$ colour and blue $B-R$ colour, placing constraints on the number density of galaxies at $z \gtrsim 3$. Steidel et al. (1996) then validated this technique by spectroscopically confirming candidate LBGs at $z \sim 3$ identified with this colour-colour method. LBGs are also often referred to as 'dropout' galaxies, since they 'drop out' of shorter wavelength filters due to IGM absorption, only appearing in longer wavelength filters redwards of the break. An example of the Lyman break technique to select galaxies at $z \geq 6$ with *Hubble* filters is shown in Fig. 1.8.

1.5.2 Overview of previous searches

Hubble

The *Hubble* Deep Field (Williams et al., 1996), taken in 1995 with the Wide Field and Planetary Camera 2 and shown in Fig. 1.9, marked a significant step forward in the search for the first galaxies. By 'burning a hole in the sky' (Loeb and Furlanetto, 2013) over the course of ten days in an area of 5.3 arcmin^2 in filters covering $\lambda \simeq 0.3-0.8\mu$m, this survey of the extragalactic sky contained faint galaxies out to $z \sim 6$. Subsequent *Hubble* fields included the Ultra Deep Field and the Great Observatories Deep Survey (GOODS)-North and -South fields with the Near Infrared Camera and Multi-Object Spectrometer (NICMOS) and from the Advanced Camera for Surveys (ACS) instruments. These fields provided constraints on the number densities of very faint galaxies out to $z = 6$ (e.g. Bunker et al., 2003; Bunker et al., 2004; Giavalisco et al., 2004; Stanway et al., 2004; Beckwith et al., 2006; Bouwens et al., 2006; Oesch et al., 2007). The installation of Wide Field Camera 3 (WFC3) in 2009 included NIR filters (shown in Fig. 1.8), extending the wavelength range of *Hubble* to 1.7μm. This allowed for the identification of galaxies at $z \gtrsim 7$ whose Lyman break is redshifted to $\lambda \gtrsim 1\mu$m. Imaging campaigns with WFC3 included that of existing *Hubble* fields (e.g. Windhorst et al., 2011; Koekemoer et al., 2013; Ellis et al., 2013) as well as the Cosmic Assembly Near-Infrared Deep Extragalactic Legacy Survey (CANDELS, Grogin et al., 2011; Koekemoer et al., 2011). This lead

Figure 1.9: The *Hubble* Deep Field (Williams et al., 1996). Covering 5.3 arcmin^2, this image provided a glimpse into Cosmic Dawn by imaging galaxies out to $z = 6$. Credit: R. Williams (STScI), the *Hubble* Deep Field Team and NASA/ESA.

to the identification of galaxy candidates out to redshifts as high as $z = 8 - 11$ (Bunker et al., 2010; Bouwens et al., 2011; Oesch et al., 2012a; Ellis et al., 2013). Grism observations of the luminous galaxy GN-z11 in GOODS-North confirmed the existence of galaxies as early as 400 Myr after the Big Bang (Oesch et al., 2016). However, *Hubble* was unable to probe beyond $z \simeq 12$, where the Lyman-break redshifts beyond the $F160W$ filter. Deep *Hubble* imaging across the optical and NIR now covers more than 1100 arcmin^2, and this has culminated in studies on galaxy evolution covering $z \simeq 2 - 9$ (e.g. Bouwens et al., 2021; Bouwens et al., 2022b).

Ground-based telescopes

During the 2000s and 2010s, while *Hubble* made significant breakthroughs, ground-based imaging also saw remarkable progress, enabling the study of a different population of LBGs. Ground-based telescopes such as Subaru and the UK Infrared Telescope (UKIRT) provided degree-scale imaging at optical and NIR wavelengths, although to depths $\sim 1-2$ mag shallower than *Hubble* (Kashikawa et al., 2004; Lawrence et al., 2007). However, these wide areas were crucial for constraining the number densities of bright sources (e.g. Iye et al., 2006; McLure et al., 2009), which are much rarer than the galaxies discovered with *Hubble*. More recently, the installation of the Hyper-Suprime Cam (HSC) on Subaru with its *grizy* filter set (Miyazaki et al., 2012; Aihara et al., 2022), along with deep near-infrared surveys from VISTA (UltraVISTA and the VISTA Deep Extragalactic Observations (VIDEO) survey, McCracken et al., 2012; Jarvis et al., 2013, respectively) have together imaged > 10 deg^2, leading to the discovery of the most luminous LBGs, AGN and quasars over the redshift range $z \simeq 2-10$ (Bowler et al., 2012; Bowler et al., 2014; Ono et al., 2018; Stefanon et al., 2019; Bowler et al., 2020; Harikane et al., 2022b; Adams et al., 2023b; Donnan et al., 2023a). Ground-based studies have greatly benefitted from *Spitzer*/IRAC imaging at 3.6μm and 4.5μm (Mauduit et al., 2012; Ashby et al., 2013; Euclid Collaboration et al., 2022b), providing access to the rest-optical continuum and probing nebular emission at $z > 6$, aiding in the SED fitting for the determination of galaxy properties. However, similarly to *Hubble*, ground-based studies have also been limited to $z \simeq 10-13$, although some ultra-high redshift candidates identified as $J-$ and $H-$band dropouts (Bowler et al., 2020; Harikane et al., 2022a) have demanded spectroscopic follow-up.

JWST

The long-awaited launch of *JWST* at the end of 2021 marked the beginning of a revolution in high-redshift astronomy. Its instruments cover the 0.9–28μm range and provide a sensitivity at least three times higher than *Hubble* in the NIR with the Near Infrared Camera (NIRCam, Rieke et al., 2023) and ten to a hundred times

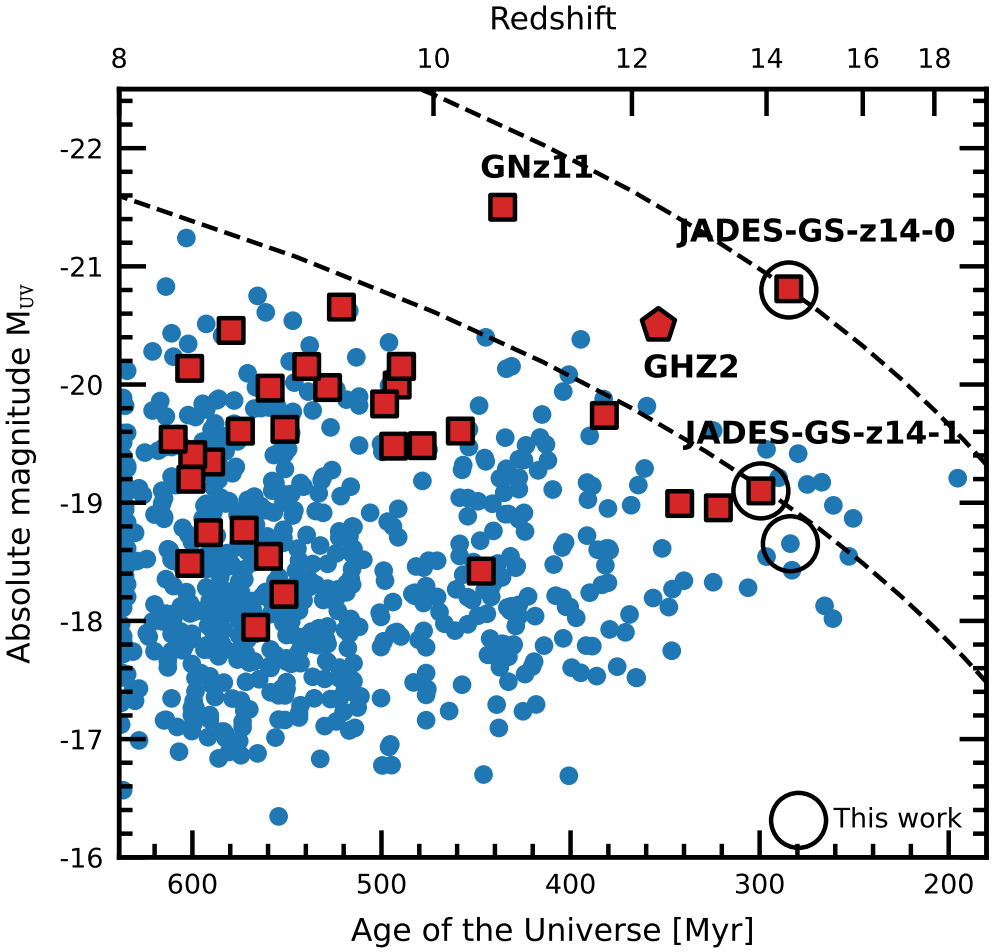

Figure 1.10: *JWST* galaxy candidates (blue dots) and spectroscopically confirmed galaxies (red squares) as a function of their redshift z (and corresponding age of the Universe) and absolute magnitude $M_{\rm UV}$ in the rest-frame UV (computed using Equation 1.21). Reproduced from Carniani et al. (2024).

higher than *Spitzer* with with the Mid-Infrared Instrument (MIRI, Wright et al., 2023) at $\lambda > 5\mu$m (see fig. 7 in Rigby et al., 2023). *JWST* provides the capability to construct statistical samples of galaxies at $z > 10$ with wavelength coverage beyond the corresponding Lyman break at $\lambda > 1.3\mu$m. The *JWST* Early Release Observations (EROs, Pontoppidan et al., 2022) in the SMACS 0723 field enabled the rapid discovery of galaxy candidates at $z > 9$ using the NIRCam instrument, which spans $0.9 - 4.4\mu$m. This was achieved by searching for $F090W$ dropouts (Adams et al., 2023a; Atek et al., 2023b), though initial challenges with zeropoint and flux calibration complicated the process. Next came Early Release Science campaigns

such as GLASS (Merlin et al., 2022), covering 7 arcmin^2 with NIRCam and leading to the identification of two particularly luminous candidate galaxies at $z = 10.6$ and $z = 12.2$ (Castellano et al., 2022; Naidu et al., 2022), the latter of which was later confirmed spectroscopically with the NIRSpec instrument (Castellano et al., 2024). *JWST* spectroscopy has also revealed contamination in ultra-high redshift samples. For example, some $J-$ and $H-$band dropouts identified in Bowler et al. (2020) and Harikane et al. (2022a) were revealed to be galaxies at $z \simeq 3-4$ with a Balmer break and scattering of photometry mimicking a strong Lyman break (Harikane et al., 2025). Additionally, an early, extremely luminous candidate at $z \simeq 16$ (Donnan et al., 2023a) was later revealed to be a dusty emission line galaxy at $z = 4.9$ again mimicking a Lyman break and flat rest-UV continuum (Arrabal Haro et al., 2023).

Over the past three years, several *JWST* surveys have been conducted, including purely photometric campaigns as well as those that combine photometry with spectroscopy–both untargeted grism and targeted spectroscopy. These include JADES (which provided a spectrum of GN-z11, revealing several low- and high-ionisation emission lines, Eisenstein et al., 2023; Bunker et al., 2023; Bunker et al., 2024), UNCOVER (Bezanson et al., 2024), PRIMER (Dunlop et al., 2021), FRESCO (providing NIRCam/grism observations of the [OIII] and Hβ nebular emission lines at $z \simeq 7-9$, Oesch et al., 2023), GLIMPSE (utilising lensing fields to obtain ultra-deep imaging, Atek et al., 2023a) and COSMOS-Web (Casey et al., 2023). All of these surveys cover tens to hundreds of arcmin^2, apart from COSMOS-Web, which is the largest area *JWST* programme to date, covering 0.5 deg^2. A key observing strategy of many of these surveys has been to re-observe key *Hubble* fields, providing a wealth of ancillary data to use with *JWST*. These surveys have led to the discovery of hundreds of galaxy candidates at $z > 10$. Additionally, the NIRSpec instrument has provided a significant increase in the redshift record, with two galaxies confirmed at $z \simeq 14$ (Carniani et al., 2024). In Fig. 1.10 I show *JWST* galaxy candidates and spectroscopically confirmed galaxies as functions of their redshift (and corresponding age of the Universe) and absolute magnitude in the rest-frame UV ($M_{\rm UV}$, computed using Equation 1.21).

1.6 The luminosity function

With sufficiently large samples of high-redshift galaxies, one can infer statistical properties that are sensitive to the physical processes governing their evolution. A key statistic for understanding galaxy evolution is the luminosity function (LF), which describes the number density of galaxies as a function of luminosity (usually in units mag^{-1} Mpc^{-3}). By applying Equation 1.16 for the comoving volume, we remove the effect of cosmic expansion, allowing us to track how the galaxy number density evolves with redshift. This evolution provides insight into the physical mechanisms driving the evolution of the first galaxies. In the local Universe, the galaxy LF follows a Schechter function (Schechter, 1976) given by

$$\Phi(L) = \frac{\Phi^*}{L^*}\left(\frac{L}{L^*}\right)^{\alpha} e^{-L/L^*} \tag{1.20}$$

where $\Phi(L)$ is the number density at luminosity L, Φ^* is the normalisation of the distribution, L^* is the characteristic luminosity, and α is a power-law slope. This function tells us that faint galaxies follow a power-law distribution, followed by an exponential decline in the bright end beyond L^*. Luminosity functions are measured across the electromagnetic spectrum.

1.6.1 Observations of the rest-frame UV LF

The rest-frame UV LF probes mainly the unobscured SFR in star-forming galaxies. It is often expressed in terms of the absolute UV magnitude, M_{UV}, usually measured based on the apparent magnitude near $\lambda_{\text{rest frame}} = 1450 - 1500$Å (either from a photometric filter which covers this wavelength range or from the best-fit SED). The luminosity distance D_L (see Section 1.2.2) is used to compute the rest-frame UV absolute magnitude, given by

$$M_{\mathrm{UV}} = m - 5\log_{10}(D_L/10) + K(z) \tag{1.21}$$

where m is the apparent magnitude, the luminosity distance D_L is expressed in parsecs, and the final term is the K-correction (Hogg et al., 2002). For this thesis, the K-correction is given by $K(z) = 2.5\log_{10}(1+z)$. Since this form of K-correction

depends on the observed wavelength exactly matching the rest-frame at 1500Å, the apparent magnitude m used to compute $M_{\rm UV}$ is measured by placing a top-hat filter at 1500Å with width 100Å on the best-fit SED in the rest-frame.

The Schechter function has provided good fits to observations of the rest-frame UV LF at $z \geq 6$ with *Hubble* down to $M_{\rm UV} \simeq -17$ (e.g. Oesch et al., 2012b; McLure et al., 2013; Finkelstein et al., 2015; McLeod et al., 2016; Bouwens et al., 2021). Results suggested a smooth evolution in the LF at $z \gtrsim 4$. The number density of luminous $M_{\rm UV} \simeq -21$ galaxies declined more rapidly than faint $M_{\rm UV} \simeq -17$ galaxies, driven largely by a decrease in the normalisation Φ^* with redshift, a steepening in the faint-end slope α, and little evolution in M^*. However, in the latest study conducted by Bouwens et al. (2021), the *Hubble* imaging only covered 1136 arcmin^2, providing relatively weak constraints on the LF at $M_{\rm UV} \lesssim -21$ due to a lack of area.

The degree-scale ground-based imaging campaigns outlined in Section 1.5.2 provided the means to constrain the number densities of rare luminous galaxies at high redshift. The first determinations of the $z \simeq 7$ UV LF with degree-scale surveys showed an excess of bright galaxies compared to the Schechter function at $M_{\rm UV} \lesssim -21.5$, with a double power law (DPL) fit preferred (Capak et al., 2011; Bowler et al., 2012; Bowler et al., 2014, see Fig. 1.11). The double-power law can be written as

$$\Phi(L) = \left(\frac{\Phi^*}{L^*}\right) \frac{1}{(L/L^*)^{\alpha} + (L/L^*)^{\beta}} \tag{1.22}$$

where Φ^* and L^* are as before, with α and β controlling the faint- and bright-end power law slopes respectively. This is usually recast in terms of magnitude;

$$\Phi(M) = \frac{\Phi^*}{10^{0.4(\alpha+1)(M-M^*)} + 10^{0.4(\beta+1)(M-M^*)}} \tag{1.23}$$

where M^* is the characteristic magnitude, marking the transition from the faint end to the bright end. The DPL form has also been identified in optical-only studies from the Hyper-Suprime Cam GOLDRUSH program (Ono et al., 2018; Harikane et al., 2022b), and the bright-end excess appears to continue to $z \simeq 10$ (Stefanon et al., 2019; Bowler et al., 2020), in contrast to *Hubble* findings of a relatively rapid decline in $M_{\rm UV} \simeq -21$ galaxies at $z \gtrsim 4$. Additionally, there is evidence that

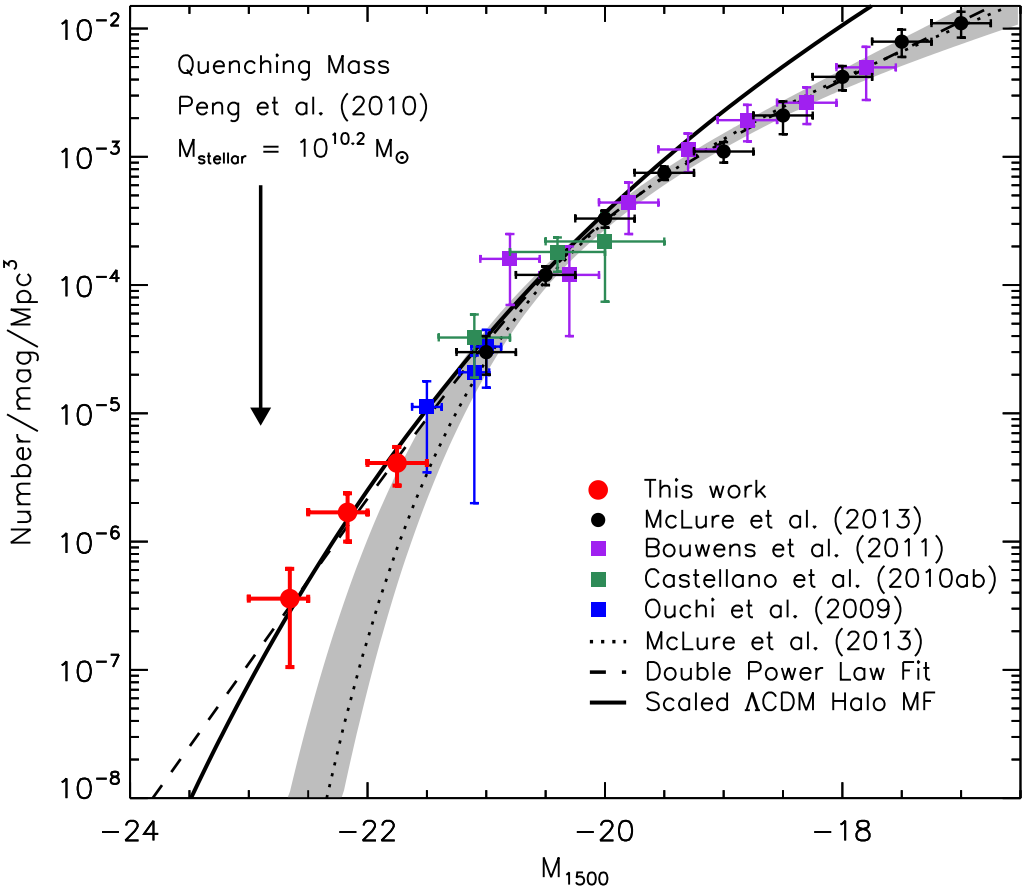

Figure 1.11: The rest-frame UV LF at $z = 7$, reproduced from Bowler et al. (2014). The LF shows an excess to the Schechter function (dotted line), with a double-power law fit (dashed line) preferred. This functional form is more akin to the shape of the halo mass function (solid line). Bowler et al. (2014) suggest that at this epoch, galaxies are only just reaching the critical quenching mass (Peng et al., 2010), meaning their growth has not yet been significantly suppressed.

whatever mechanism causes quenching of luminous galaxies has a rapid onset, with a clear steepening of the bright-end slope found to occur in just 400 Myr between $z = 7$ and $z = 5$ (Bowler et al., 2015; Adams et al., 2023b).

JWST has now extended measurements of the rest-UV LF to $z = 14$, corresponding to just 300 Myr after the Big Bang. Studies have constructed samples spanning $-22 < M_{\rm UV} < -17$ at $z = 8 - 12$ and find a slow evolution over the redshift range due to an abundance of luminous ($M_{\rm UV} \simeq -21$) galaxies (e.g. Naidu et al., 2022; Finkelstein et al., 2022; Donnan et al., 2024; Chemerynska et al., 2024; McLeod et al., 2024; Adams et al., 2024). This slow evolution is unexpected if one

assumes a constant star formation efficiency, with the expectation that galaxies with $M_{\rm UV} < -17$ should be very rare at $z \gtrsim 10$ (Oesch et al., 2018; Stark et al., 2025). Although constraints are still limited due to the effect of cosmic variance (see e.g. Willott et al., 2024) and the limited volume of *JWST* surveys so far (limiting samples at $M_{\rm UV} < -21$), the abundance of galaxies out to $z = 14$ has required a revised understanding of galaxy physics in the early Universe. Wide-area programmes such as COSMOS-Web (Casey et al., 2023) or SAPPHIRES (Egami et al., 2024) will also help address the lack of volume.

1.6.2 Theoretical interpretation

The LF provides a link to the dark-matter haloes within which galaxies reside. This is because star formation efficiency is expected to depend strongly on halo mass (e.g. Vale and Ostriker, 2006; Behroozi et al., 2013; Wechsler and Tinker, 2018), although the relation betwen the rest-UV LF and the halo mass function (HMF) is likely to be non-trivial given that rest-UV observations trace recent star formation. At low-redshift, feedback processes within galaxies suppresses star formation, leading to Schechter function fits to the LF which lie in defecit to the HMF (see the dashed line in Fig. 1.11 relative to the scaled HMF). Bouwens et al. (2021) find that the Schechter function provides a good fit to the rest-UV LF over $z = 2 - 9$, suggesting that the evolution in the rest-UV LF is driven by an evolution in the halo mass function with no evolution in star formation efficiency. However, the excess in the bright end at $z \geq 6$ seen in ground-based studies more closely follows the functional form of the HMF (e.g. Moster et al., 2010). This suggests a lack of quenching in luminous galaxies at high-redshift, allowing for higher number densities.

Simulations and theoretical studies provide one method of understanding number densities in the bright end. While at lower redshifts the steep decline in luminous/massive galaxies (e.g. Yang et al., 2009) can be attributed to mass quenching (Peng et al., 2010), dust attenuation (or lack thereof) is predicted to be the more significant effect in shaping the UV LF at high redshifts (e.g. Cai et al., 2014; Vijayan et al., 2021; Mauerhofer and Dayal, 2023). Large-volume simulations such as

FLARES (Lovell et al., 2021) predict a rapid dust accumulation between $z = 8 - 9$, whereas Donnan et al. (2025) have found tentative evidence for a gradual increase in dust attenuation from $z = 12.5$ to $z = 6$, at a fixed stellar mass. Additionally, as AGN begin to grow and turn on in the early Universe, energetic feedback from their accretion disk may suppress star formation in massive galaxies (e.g. Bower et al., 2012; Davé et al., 2019; Lovell et al., 2023). While quasars at $z \simeq 7$ are extremely rare (e.g. Mortlock et al., 2011; Bañados et al., 2018; Wang et al., 2021), the quasar LF appears to rapidly increase to lower redshifts, which leads to the faint end of the AGN LF being comparable to the bright end of the star-forming galaxy LF around $M_{\rm UV} \simeq -23$ at $z \simeq 5$ (Cano-Díaz et al., 2012; Adams et al., 2023b; Harikane et al., 2022b). Bowler et al. (2014) suggest that at $z \simeq 7$, luminous galaxies have not yet reached the mass threshold required to undergo quenching (see Fig. 1.11). By determining the functional form of the luminosity function at different redshifts, the onset of potential quenching and/or dust obscuration can be investigated.

At even higher redshift probed by *JWST*, the abundance of galaxies with $M_{\rm UV} = -21$ out to $z \simeq 14$ also demands a theoretical interpretation. Some studies have suggested enhanced star formation efficiency can be attained by shielding star-forming clouds from the feedback of earlier stellar populations (e.g. Dekel et al., 2023). Top-heavy IMFs provide an alternate means to rapidly produce luminous galaxies (e.g. Hutter et al., 2025). Bursty star formation, causing rest-UV variability, may also lead to temporary up-scattering of galaxy luminosities (e.g. Sun et al., 2023; Mason et al., 2023; Shen et al., 2023). However, the simplest explanation may be provided by a assuming a non-evolving halo-mass dependent galaxy-formation efficiency in line with local observations (Donnan et al., 2025).

1.6.3 Dust and AGN feedback

The impact of dust obscuration and AGN feedback is particularly important for the LF at $z = 7$, which I will measure in Chapters 2 and 3. Here, I briefly outline our current observational understanding of both processes at high redshift.

Recent studies are beginning to reveal the significance of dust in early galaxies (e.g., Bowler et al., 2022; Inami et al., 2022; Algera et al., 2023) and are placing constraints on dust properties at $z > 5$ using sub-millimetre observations from ALMA (e.g., Bouwens et al., 2022a; Inami et al., 2022; Sommovigo et al., 2022). Numerous works have demonstrated that $z \simeq 7$ LBGs can host substantial dust reservoirs and exhibit significant dust obscuration (e.g. Bowler et al., 2024; Algera et al., 2025). This growing evidence appears to be in tension with the observed excess of rest-UV-luminous galaxies in ground-based imaging. However, this discrepancy arises because optical and near-infrared studies primarily trace unobscured star formation, whereas sub-millimetre observations are required to detect obscured star formation through dust emission. Many luminous galaxies at $z \simeq 7$ display clumpy rest-UV morphologies, with dust emission often offset from the unobscured star-forming regions (Hashimoto et al., 2019; Bowler et al., 2022). At $z = 4 - 6$, resolved SED fitting of star-forming galaxies further reveals complex morphologies, with reddened rest-UV slopes coinciding with dust continuum detections (Lines et al., 2024). While obscured star formation is therefore already well established by $z = 7$, the effect of dust on the rest-UV LF is primarily through attenuation, which reddens the rest-UV continuum slopes of galaxies, making them more difficult to detect in optical and NIR surveys that rely on rest-UV emission.

As discussed in the previous section, AGN are capable of suppressing star formation in massive galaxies. Although the population of quasars declines rapidly from $z = 6$ to $z = 7$ (e.g. Matsuoka et al., 2023), *JWST* has revealed a potential population of faint, low-mass AGN which could play a significant role in galaxy evolution. Little Red Dots (Matthee et al., 2024) are a population of objects discovered at $z > 4$ with compact sizes and broad Hα emission lines, indicating an actively accreting SMBH (Harikane et al., 2023b; Greene et al., 2024) and potentially in place as early as $z \simeq 10$ (Fujimoto et al., 2024). These sources have number densities an order of magnitude higher than extrapolations of the quasar LF to fainter magnitudes, and modelling of the SFH of such sources has revealed quenching episodes (Kokorev et al., 2024), providing evidence for AGN quenching

at $z > 5$. In the massive, bright-end population of AGN, luminous obscured SMBHs have been discovered in massive galaxies at $z \simeq 7$ (Fujimoto et al., 2022; Endsley et al., 2023). The discovery of a blazar (a quasar with a relativistic jet directed towards the observer) at $z \simeq 7$ (Bañados et al., 2025) indicates the presence of AGN jets and feedback during the EoR. The discovery of these extremely rare sources at $z \simeq 7$ suggests we are witnessing the very beginnings of quenching by AGN feedback, as these systems may be the progenitors of galaxies which have experienced mass quenching at lower redshift.

1.6.4 The cosmic star formation rate density

The integral of the rest-UV LF represents the unobscured cosmic star formation rate density $\rho_{\rm SFR}$, usually integrated down to some minimum luminosity. This quantity is important as a measure for how the Universe converts baryons from gas into stars, and places constraints on the ability of faint galaxies to reionise the Universe at $z > 6$. Additionally, $\rho_{\rm SFR}$ is important for understanding reionisation. It can be used to estimate how many ionising photons are produced by the galaxy population for a given ionising photon prodution rate and escape fraction (e.g. Wyithe et al., 2010; Yung et al., 2020). The Madau-Lilly diagram shows that $\rho_{\rm SFR}$ increased to a peak at $z \sim 2$, and has been declining since (Lilly et al., 1996; Madau and Dickinson, 2014). However, results from *JWST* have found some evidence for an excess in $\rho_{\rm SFR}$ at $z > 10$ (see Fig. 1.12) relative to a constant star formation efficiency over cosmic time, argued for by *Hubble* studies (e.g. Oesch et al., 2012a; Ishigaki et al., 2015; Oesch et al., 2018). Similarly to the slow evolution in the LF out to $z = 14$, this observation requires an alternate explanation. Harikane et al. (2023a) suggest that this could be caused by unaccounted-for AGN activity, a lack of suppression of star formation by UV radiation in low-mass haloes, or a top-heavy IMF possibly including population III stars. However, again, Donnan et al. (2025) argue that observations can be explained by a non-evolving halo-mass-dependent galaxy formation efficiency.

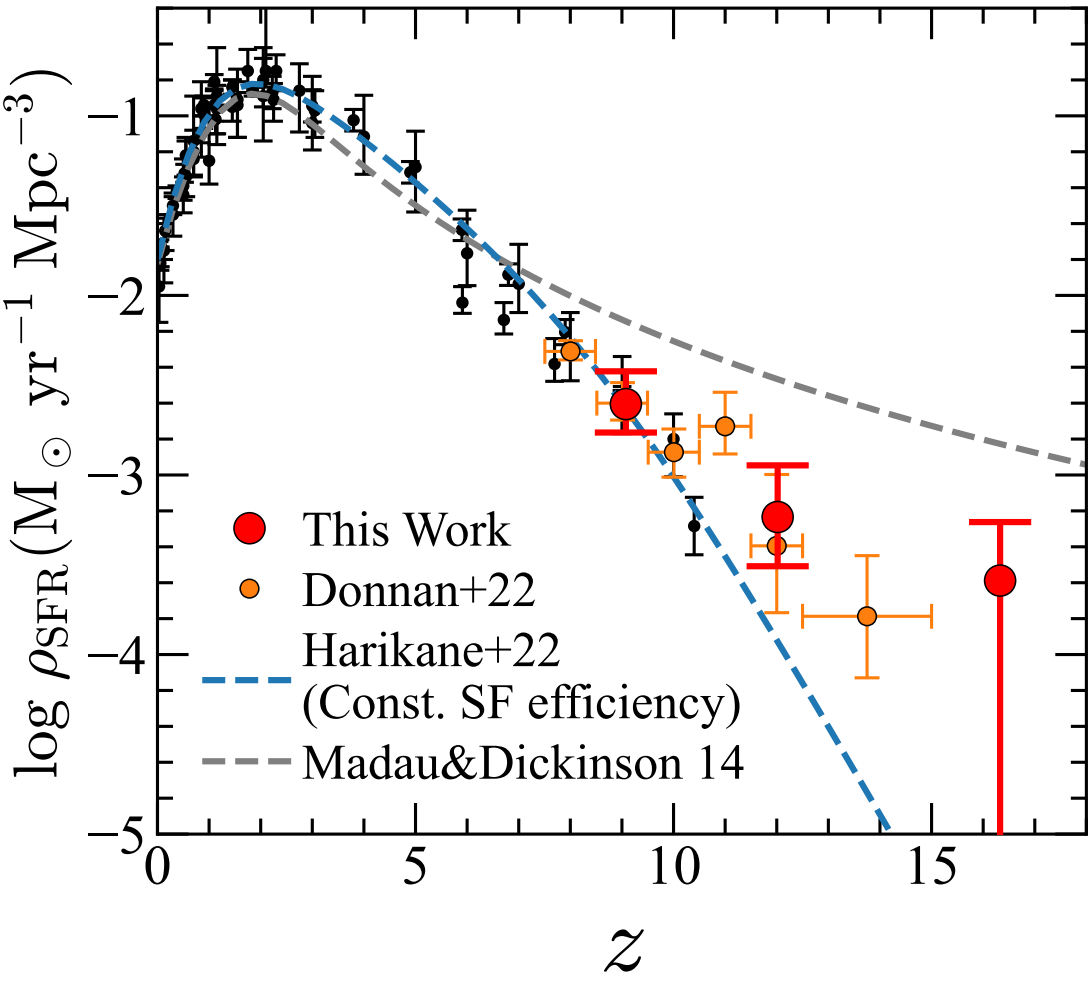

Figure 1.12: The cosmic star formation rate density, $\rho_{\rm SFR}$, as a funtion of redshift, measured with *JWST* at $z \geq 8$ (red and orange points). The blue dashed line indicates the expected evolution for a constant star formation efficiency. The gray dashed line shows an extrapolation from Madau and Dickinson (2014). Reproduced from Harikane et al. (2023a).

1.6.5 *Euclid*

Euclid is a European Space Agency medium-class mission (Euclid Collaboration et al., 2024a). It was launched in July 2023 and is equipped with a 1.2m primary mirror. The primary mission of *Euclid* is to measure the nature of dark matter and dark energy via weak lensing and clustering. However, a major component of the mission is the legacy science possible with the telescope. The Visible Camera (VIS, Euclid Collaboration et al., 2024b) instrument on *Euclid* features a high resolution (0.16″) optical filter, I_E, equivalent to the combination of the ground-

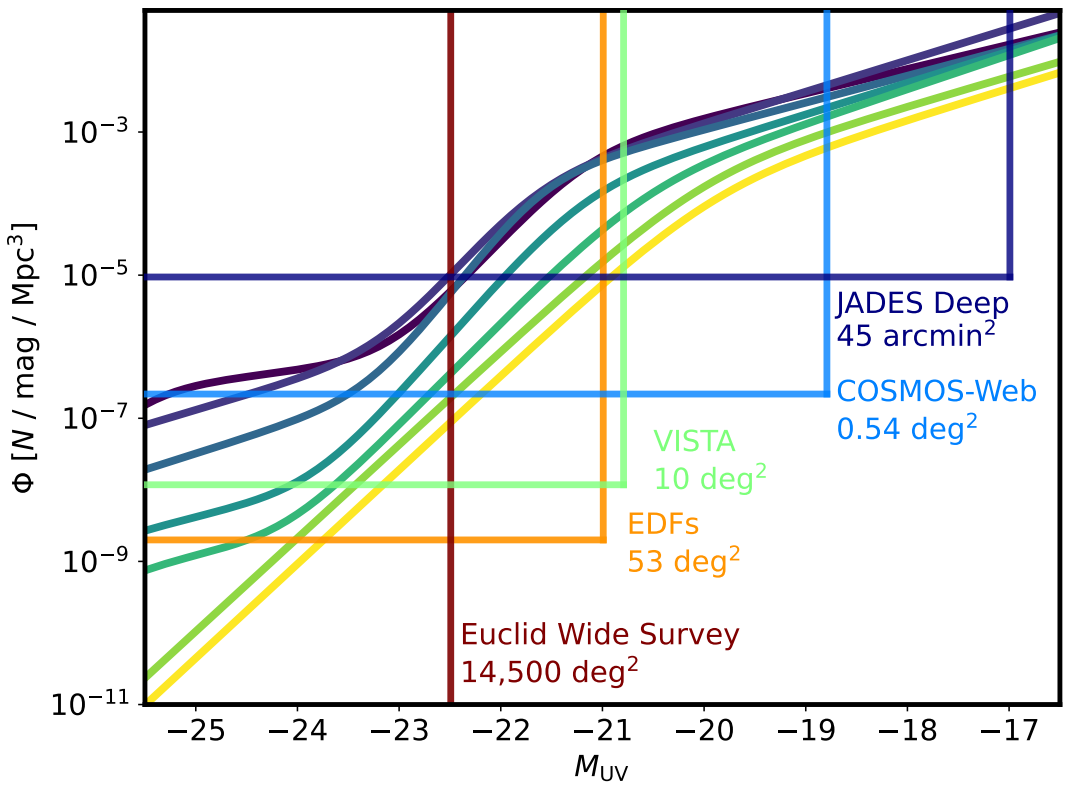

Figure 1.13: The rest-UV LFs over $z = 3 - 9$, compiled from Adams et al. (2023b), Bowler et al. (2015), Schindler et al. (2023), Bowler et al. (2017), Matsuoka et al. (2023), and Donnan et al. (2023a). The boxes indicate the volume probed at $z = 7$ by JADES Deep (Eisenstein et al., 2023), COSMOS-Web (Casey et al., 2023) surveys, UltraVISTA + VIDEO (McCracken et al., 2012; Jarvis et al., 2013), the *Euclid* Deep Fields (EDFs) and the *Euclid* Wide Survey (Euclid Collaboration et al., 2024a).

based *riz* filters. The Near-Infrared Spectrometer and Photometer (NISP, Euclid Collaboration et al., 2024c) features three near-infrared filters, Y_E, J_E and H_E. The field of view of *Euclid* is ~ 0.55 deg^2, and will eventually map out 14000 deg^2 of the extragalactic sky, reaching NISP depths of 24.5 mag as part of the *Euclid* Wide Survey (EWS). It will also obtain 53 deg^2 of deep imaging in the *Euclid* Deep Fields (EDFs), reaching NISP depths of ~ 26 mag. Fig. 1.13 shows rest-UV LFs over the redshift range $z = 3 - 9$. In addition to this, boxes have been drawn that indicate the LF volume probed by two *JWST* surveys (JADES and COSMOS-Web), UltraVISTA + VIDEO, as well as EDFs and the EWS. Clearly *Euclid* will be instrumental in discovering large samples of $L > L^*$ galaxies, whereas the power of *JWST* lies in identifying $L < L^*$ galaxies with photometry and spectroscopy.

Euclid measurements of the bright end of the rest-UV LF will therefore strongly complement *JWST* observations by discovering 1000s of luminous galaxies at $z \sim 7$ with $M_{\rm UV} < -21$ (Bowler et al., 2017). These sources will be ideal for follow-up with the Multi-Object Optical and Near-infrared Spectrograph on the VLT (MOONS, Cirasuolo et al., 2020; Maiolino et al., 2020) and Prime Focus Spectrograph on Subaru (PFS, Tamura et al., 2016), allowing for novel reionisation and clustering studies in the EoR, which were not possible before.

1.7 Galaxy sizes

The LF is an unresolved galaxy statistic that does not require knowledge of the structure or morphology of the galaxies in the sample (unless one wants to treat multiple components as separate galaxies, Bowler et al., 2017; Harikane et al., 2025). However, galaxy structure and morphology are fundamental properties through which galaxy evolution can be measured (see Conselice, 2014, for a review). Resolving galaxy structure at high redshift with ground-based telescopes is difficult, since imaging is seeing-dominated; that is, imaging is degraded due to turbulence in the atmosphere. In particular, at $z = 3 - 7$, a galaxy with a diameter of 2 kpc has an angular size of $\theta < 0.5$ arcsec, smaller than the seeing of, for example, the VISTA telescope at $\sim$ 0.8 arcsec.

A common parametrisation for the intensity profile of a disk galaxy is the Sérsic profile, given by

$$I(R) = I_e \exp\left(-b_n \left[\left(\frac{R}{R_e}\right)^{1/n} - 1\right]\right) \tag{1.24}$$

where R_e is the half-light radius (the radius which contains half the total light of the galaxy), also called the effective radius, I_e is the intensity at R_e, n is the Sérsic index, and b_n is a normalising function dependent on n. Profiles with Sérsic index $n = 1$ correspond to an exponential disk, which provides a good fit to spiral galaxies, and $n = 4$ corresponds to the de Vaucouleurs profile seen for elliptical galaxies. As discussed in Section 1.3.2, simple disk formation models provide predictions on the evolution of galaxy size and the distribution of sizes, depending on whether

galaxy sizes are determined by their host dark-matter haloes. These predictions were that sizes should evolve according to $(1+z)^n$ for some value of n, and that sizes at a given epoch should follow a log-normal distribution. However, this model assumes galaxies form in isolation, which is certainly not the case. In fact, galaxy sizes also trace feedback processes. For example, in the local Universe, quiescent galaxies follow a steeper size-mass relation than star-forming galaxies (SFGs, van der Wel et al., 2014). Stellar feedback can also lead to steep size-luminosity relations for faint galaxies (Kawamata et al., 2018).

Some complications in studying galaxy size include the fact that different size measurements are available (e.g. the Petrosian radius and non-parametric size measurements), and Sérsic fitting is not appropriate for galaxies with irregular morphology. Additionally, simulations often used particle-based and non-parametric size measurements (Costantin et al., 2023; Katz et al., 2023) making direct comparisons difficult.

1.7.1 Rest-frame UV sizes

Space-based telescopes such as *Hubble* do not suffer from atmospheric seeing, providing a clear view of galaxy morphology. A key finding was that high-redshift galaxies are usually compact or clumpy in their rest-UV emission (probing recent star formation), with signs of inside-out mass growth (e.g. Ferguson et al., 2004; Trujillo et al., 2006; Mosleh et al., 2011; Oesch et al., 2010a; Law et al., 2012; Grazian et al., 2012; van der Wel et al., 2014; Shibuya et al., 2015; Whitney et al., 2019). Furthermore, at fixed luminosity, across $z = 0-8$ galaxy sizes evolved roughly as $R_e \propto (1+z)^{-1}$, consistent with galaxy sizes being governed by the angular momentum of their host dark-matter halo. However, rest-frame optical-wavelength morphologies, tracing the older stellar population and therefore earlier disk formation, were only observable out to $z \simeq 3$ with *Hubble*. This limited the comparison between young and old stellar populations in high-redshift galaxies, and prevented a comparison of rest-optical sizes at high-redshift with our observations of galaxy morphology in the local Universe.

1.7.2 Rest-frame optical sizes

The infrared coverage of *JWST* and its unparalleled resolution has opened the window to the first simultaneous view rest-UV *and* rest-optical light at $z \gtrsim 3$ (e.g. Ferreira et al., 2023; Kartaltepe et al., 2023; Leethochawalit et al., 2023a; Ormerod et al., 2024) revealing early mass assembly and a significant fraction of disk galaxies (30-50 per cent) at $z > 4$. Additionally, galaxies have been found to be very compact at $z > 5$ (e.g. $R_e \simeq 0.2$ kpc at $z = 6.5 - 9.5$ Ono et al., 2024), indicating high star formation rate surface densities. The first spatially resolved rest-optical imaging of galaxies at $z > 5$ also revealed that, unlike at lower redshift where blue star-forming structures surround an older, redder central component (e.g. Wuyts et al., 2012), the rest-optical morphologies of high-redshift galaxies can be just as clumpy as their rest-UV counterparts, with no clear evidence for centrally concentrated older stellar populations (e.g. Ono et al., 2024; Sun et al., 2024). This suggests that galaxies at these epochs are still in an early phase of the inside-out growth model seen with *Hubble*. In Fig. 1.14 I show the rest-optical size-redshift evolution determined by Ormerod et al. (2024) over $z = 1 - 8$.

In addition to early *JWST* size measurements, simulations have made predictions for size-scaling relations measured with *JWST*. In the First Light And Reionization Epoch Simulations (FLARES, Lovell et al., 2021), Roper et al. (2022) find intrinsically negative size-luminosity relations. At $z = 5 - 10$, the inclusion of dust attenuation predicts observed size-luminosity relations with increasingly positive slopes at shorter wavelengths, building on similar predictions by Marshall et al. (2022). Costantin et al. (2023) also simulate CEERS observations with Illustris TNG50 (Pillepich et al., 2019) at $z = 3-6$ and predict a size-redshift evolution in the rest-optical consistent with fixed circular velocity of DM haloes, as well as negative observed size-mass relations with wavelength at $z = 5 - 6$. Both Roper et al. (2022) and Costantin et al. (2023) explain their findings by requiring massive galaxies to undergo episodes of centrally concentrated star formation, leading to small sizes at high mass and high dust attenuation in the cores of massive galaxies. In Chapter 4 I will explore the use of both parametric and non-parametric sizes to compare directly

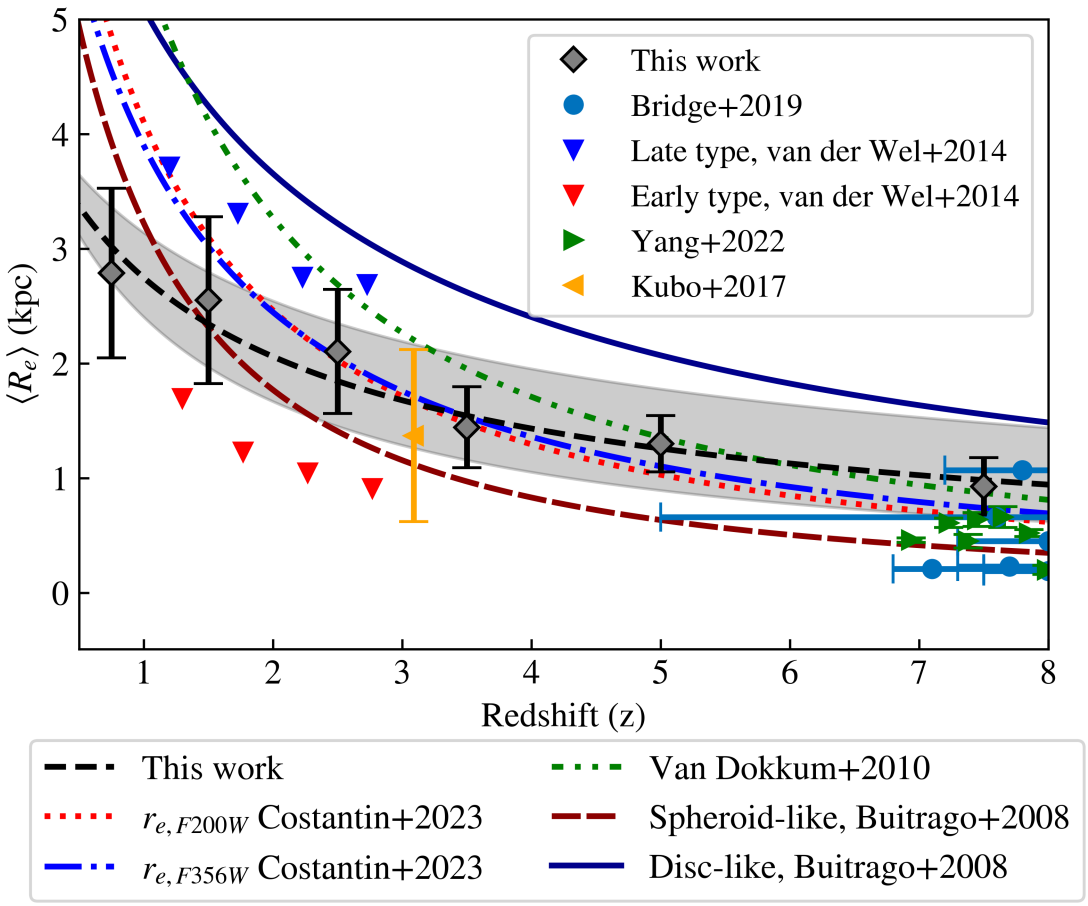

Figure 1.14: The rest-frame optical size-redshift evolution of galaxies, reproduced from Ormerod et al. (2024). Galaxies stay compact at $z > 4$ before growing rapidly in size. Note that the strength of the evolution, given by β in $R_e \propto (1+z)^{\beta}$, differs for different galaxy types, as shown by the different lines.

predictions from the FLARES and Illustris simulations. Additionally, *JWST*-selected studies tend to probe low-mass galaxies. By combining ground-selected samples with *JWST*, I will extend these analyses to the high-mass end.

1.8 Outline of thesis

In this thesis, I use deep optical and NIR imaging from state-of-the-art ground-based telescopes, combined with imaging from next-generation space-based telescopes such as *Euclid* and *JWST*, to understand the astrophysics and evolution of the most luminous galaxies in the first 2 Gyr of the Universe. The following chapters are based on papers that I have written which are published or will be submitted for

publication. In Chapter 2 I measure the bright end of the rest-UV LF at $z \simeq 7$ using 8.2 deg^2 of deep optical+NIR imaging. I show that brown dwarf contamination is a significant issue facing searches for bright galaxies at $z \simeq 7$, and confirm the DPL function form of the rest-UV LF, indicating a lack of mass quenching and/or dust obscuration in the bright end at this epoch. In Chapter 3, I extend the analysis from Chapter 2 to imaging in a smaller 1.7 deg^2 area, but reaching depths roughly one magnitude deeper. I combine ground-based NIR imaging with photometry from *Euclid*, which is able to probe wavelengths inaccessible from the ground due to atmospheric absorption. I show that *Euclid* is powerful for constructing clean samples of LBGs at $z \simeq 7$, providing a robust measurement of the rest-UV LF across three magnitudes when combined with results from Chapter 2. My results show that the gentle DPL decline seen in Chapter 2 continues down to the knee of the LF, in excellent agreement with faint-end *Hubble* studies. I also discuss the prospect of using the higher resolution of *Euclid* to remove brown dwarfs as point sources in future studies, and present a Lyman-α emitter candidate identified through the unique combination of Subaru, VISTA and *Euclid* filters. In Chapter 4 I move to studying the resolved properties of bright LBGs at $z \simeq 3-5$. I measure the size-scaling relations of $1,668$ ground-selected LBGs with *JWST*. Since the sample is selected from seeing-dominated data, this chapter presents an unbiased sampling of the morphology and size distributions of luminous sources. I measure the size distributions in redshift bins at $z = 3, 4, 5$, the size-redshift evolution, as well as the size-mass and size-luminosity relations. The size measurement methods I choose allows for a direct comparison with simulations, providing evidence for centrally concentrated star formation in the most massive galaxies at high redshift. Finally, in Chapter 5 I summarise my results and present potential directions for future work based on the results of this thesis. All magnitudes in this thesis are reported in the AB system (Oke and Gunn, 1983).

I'm sciencing as fast as I can!

—The Professor, Futurama

2

The bright end of the galaxy luminosity function at $z \simeq 7$ from the VISTA VIDEO survey

Contents

2.1 Introduction

Observing the formation and evolution of galaxies at very high-redshifts is vital for understanding the build-up of early structures and all subsequent galaxy evolution to the present day. The Lyman-break technique has been used successfully for over three decades to search for high-redshift galaxies (Guhathakurta et al., 1990; Steidel et al., 1996) via the redshifted Lyman-α break at $\lambda_{\rm rest} = 1216$Å, by utilizing the strong spectral break that appears at the wavelength of the Lyman-α line due to absorption by the IGM along the line of sight. The selection of high-redshift ($z \geq 7$) LBGs has been revolutionised thanks to the unparalleled near-infrared capabilities of *JWST*. Early results have identified and spectroscopically confirmed galaxies in the range $z = 10.6$–13.1 (e.g. Curtis-Lake et al., 2023; Bunker et al., 2023; Arrabal Haro et al., 2023) and rest-frame optical spectroscopy has revealed the gas phase properties for the first time (e.g. Fujimoto et al., 2023; Cameron et al., 2023; Curti et al., 2023). One surprising result from the first samples of galaxy candidates found by *JWST* has been the discovery of an unexpected number of luminous ($M_{\rm UV} \sim -21$) sources at $z > 8$ (e.g. Naidu et al., 2022; Finkelstein et al., 2022) that have challenged models of galaxy formation (Ferrara et al., 2023).

Galaxies form and reside within dark matter halos, and the LF (recalling that this is just number density as a function of brightness) provides a connection to the dark-matter halo-mass function and early galaxy formation since galaxy formation efficiency has a strong dependency on halo mass (e.g. Vale and Ostriker, 2006; Behroozi et al., 2013; Wechsler and Tinker, 2018). This makes the LF a key measurement in galaxy evolution. As at $z \gtrsim 6$ LBGs are typically selected and studied in the NIR, which provides access to the rest-frame UV emission from young stars, many studies have derived the rest-frame UV LF from photometric

samples at $z > 4$ (e.g. McLure et al., 2013; Finkelstein et al., 2015; Stefanon et al., 2019; Bouwens et al., 2021). The shape of the UV LF gives insight into feedback properties within galaxies and ionising properties of galaxies in the early Universe (e.g. Benson et al., 2003; McLure et al., 2010; Bradley et al., 2012; Bowler et al., 2015). A common form used to fit the rest-frame UV LF in the local Universe is the Schechter function (Schechter, 1976), $\phi(L)dL = \phi^*(L/L^*)^\alpha e^{-L/L^*} d(L/L^*)$, where α is the faint end slope, L^* is the characteristic luminosity and ϕ^* is the density normalisation. The faint end follows a power law and a rapid decline is seen in the bright end, necessitating an exponential cut-off beyond the knee at L^*. This suggests the growth of the brightest, most massive galaxies is quenched in lower redshift LBG samples (e.g. van der Burg et al., 2010; Stevans et al., 2018; Adams et al., 2023b), since the dark matter halo mass function has a shallower high-mass slope and is more akin to a double power law. Probing the bright end of the rest-frame UV LF requires galaxy searches to be conducted in degree-scale surveys, since the number density of bright objects declines rapidly. For example, LBGs at $z \simeq 7$ have a surface density of a few per square degree at $M_{\rm UV} < -22$ (Bowler et al., 2014). The widest survey fields imaged by *Hubble* only cover 1136 arcmin^2 (e.g. Bouwens et al., 2021), proving only weak constraints on the LF at $M_{\rm UV} \lesssim -21$. Prior to the launch of space missions capable of imaging a wide area (e.g. *Euclid* and *Roman*), ground-based NIR surveys provide the only insight into the number density of the very bright galaxy population at $z > 6$. The first determinations of the $z \simeq 7$ UV LF with degree-scale surveys showed an excess of bright galaxies compared to the commonly used Schechter function, with a double power law (DPL) fit preferred (Bowler et al., 2012; Bowler et al., 2014). The DPL form has also been identified in optical-only studies from the Hyper-Suprime Cam GOLDRUSH program (Ono et al., 2018; Harikane et al., 2022b). This bright end excess appears to continue out to $z \simeq 10$ (Stefanon et al., 2019; Bowler et al., 2020). Again, as discussed in Section 1.6, there is evidence that the mechanism causing the Schechter function form at lower redshift has a rapid onset in the 400 Myrs between $z = 7$ and $z = 5$ seen as a rapid steepening of the bright end (Bowler et al., 2015; Adams et al., 2023b)

Interestingly, many simulations do not predict *intrinsic* UV LFs with a DPL shape at $z > 5$, with a steeper bright-end only appearing after the addition of significant dust obscuration (see compilation in Bowler et al., 2015; Cai et al., 2014). While at lower redshifts the steep decline in luminous/massive galaxies (e.g. Yang et al., 2009) can be attributed to mass quenching (Peng et al., 2010), attenuation or a lack of attenuation is predicted to be the more significant effect in shaping the rest-UV LF at high redshifts (e.g. Cai et al., 2014; Vijayan et al., 2021). As discussed in Section 1.6.2, energetic feedback from AGN accretion disks may suppress star formation in massive galaxies. Additionally, due to the rapid evolution of the quasar LF, the faint end of the AGN LF is comparable to the bright end of the galaxy LF at $M_{\rm UV} \simeq -23$ by $z \simeq 5$ (Cano-Díaz et al., 2012; Adams et al., 2023b; Harikane et al., 2022b). By determining the functional form of the luminosity function at different redshifts, the onset of potential quenching and/or dust obscuration can be investigated. Comparison of the bright end of the galaxy UV LF with simulations, plus follow-up observations with *JWST* and ALMA, can then uncover the dominant mechanism responsible for the shape of the UV LF.

A key step in searching for $z \simeq 7$ galaxies is the removal of red, dusty galaxies at $z \sim 1-2$ and cool Galactic M, L and T dwarf stars (e.g. Stanway et al., 2008; Bowler et al., 2015) which have photometry that can mimic a Lyman break. The selection of robust samples requires the use of deep optical, NIR and *Spitzer* Infrared Array Camera (IRAC) photometry via a colour-colour selection or spectral energy distribution (SED) fitting (e.g. Bowler et al., 2014; Bouwens et al., 2022a). In this work we conduct a search for $z \simeq 7$ galaxies within the VISTA VIDEO XMM-LSS and ECDF-S fields. Crucially, these fields are covered by a range of deep multi-wavelength data including the optical, red optical and NIR filters extending to 2.2 μm (and up to 5 μm with *Spitzer*/IRAC data) allowing the robust removal of contaminant populations. This work comprises the largest ground-based optical+NIR search for $z \simeq 7$ galaxies to date, providing the most robust constraints on the bright-end of the rest-frame UV LF prior to the launch of wide-area space missions.

This chapter is structured as follows. In Section 2.2 we outline the multi-wavelength datasets, and in Section 2.3 we present the selection process of our $z \simeq 7$ LBG sample. We present our candidate $z \simeq 7$ galaxies and their properties in Section 2.4, and in Section 2.5 we measure the rest-frame UV LF at $z \simeq 7$ and present our results. We discuss contamination and potential contribution by AGN in Section 2.6. We then present our conclusions in Section 2.7. In Appendices A, B and C we present SED fitting and postage stamps of all candidate objects, present an alternate calculation of the UV LF at $z \simeq 7$ using a more inclusive sample, and show the SED fitting of an object with unusual photometry identified as part of the selection.

2.2 Data

In this study we use multi-wavelength data across two fields, XMM-LSS and ECDF-S. These fields are selected for their coverage by the VISTA Deep Extragalactic Observations (VIDEO) survey in the near-infrared $YJHK_s$ bands (Jarvis et al., 2013), in addition to having overlapping deep optical data. We use the final data release of the VISTA VIDEO survey, which is now publicly available[1]. The VIDEO data in the ELAIS-S1 field is not included due to a current lack of deep optical imaging, particularly in the red optical bands around the expected position of the Lyman break. The total overlapping optical and NIR area used in this work covers 8.22 deg^2. The field footprints are shown in Fig. 2.1. The optical and NIR bands are used for SED fitting, and *Spitzer*/Infrared Array Camera (IRAC) imaging in the mid-infrared is used to remove low-redshift dusty interlopers (see Section 2.3.4).

2.2.1 XMM-LSS

The VIDEO data are split into three VISTA pointings, or tiles (XMM1, 2, 3), of 1.5 deg^2 each as shown in Fig. 2.1. Optical data are taken from the Data Release 3 of the Hyper Suprime-Cam Subaru Strategic Program (HSC-SSP, Aihara et al., 2022). XMM1 contains an 'ultradeep' HSC pointing with longer exposure than the 'deep' pointings. The DR3 data provide an increase in 5σ depth of $\sim 0.1 - 0.7$ mag

[1] http://www-astro.physics.ox.ac.uk/~video/public/Home

on DR2 (Aihara et al., 2019). HSC-SSP also provides two narrow bands, NB816 and NB921, near the expected position of the Lyman break at $z \simeq 7$. This can aid in reducing errors on photometric redshifts. In addition, imaging from the *Spitzer* Extragalactic Representative Volume Survey (SERVS, Mauduit et al., 2012) is used along with the deeper *Spitzer* Extended Deep Survey (SEDS, Ashby et al., 2013) where available. The area containing overlapping VIDEO and HSC data is 4.33 deg^2, accounting for masking of bright stars and artefacts such as stellar ghosts.

2.2.2 ECDF-S

Similarly to XMM-LSS, the VIDEO images in ECDF-S are split into three tiles (CDFS1, 2, 3) of 1.5 deg^2 each as shown in Fig. 2.1. Optical data is comprised of ancillary HSC data compiled by Ni et al. (2019), in the form of four pointings in *G, I* and *Z* and a central single pointing of the *R*-band. The HSC data are a combination of different observation conditions, leading to poor seeing in the *I*- and *Z*-bands. The full width at half maximum (FWHM) of the point spread function (PSF) varies by 0.1 arcsec across the field in these bands (see Section 2.2.4). Furthermore, there is poor coverage in the *R*-band. We therefore complement the HSC data with optical data from VST Optical Imaging of the CDFS and ES1 fields (VOICE, Vaccari et al., 2016), covering 4 deg^2. *Spitzer*/IRAC imaging is taken from the Cosmic Dawn Survey (CDS, Euclid Collaboration et al., 2022b). The area containing overlapping VIDEO, HSC and VOICE data is 3.89 deg^2.

2.2.3 Image processing and depths

The astrometry of the VIDEO data is matched to *Gaia* (Gaia Collaboration et al., 2018). If not already matched to *Gaia*, all other auxiliary data was shifted into this frame using SCAMP (Bertin, 2006), and the pixel scale was matched using SWARP (Bertin et al., 2002). The 5σ depths were computed across the images to determine flux uncertainties. Circular apertures with a 2 arcsec diameter were placed on empty regions of the image. For the *Spitzer*/IRAC data we use a 2.8 arcsec diameter aperture to account for the poorer resolution. The SEGMENTATION map produced

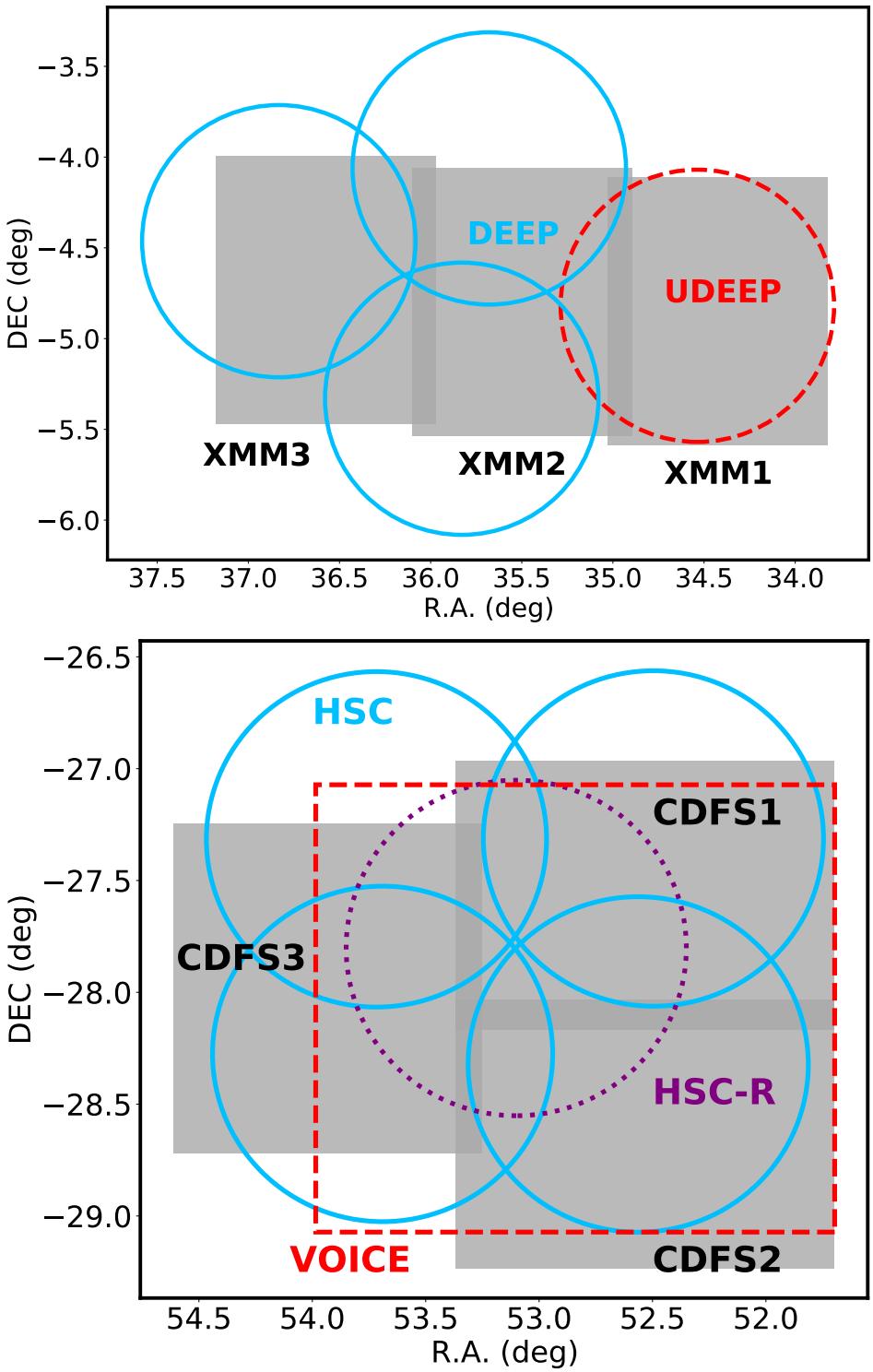

Figure 2.1: XMM-LSS footprint (top) and ECDF-S footprint (bottom). The VIDEO tiles are shown in grey and the HSC pointings in blue circles. In ECDF-S, the VOICE pointing is shown as a dashed red square. The central HSC-R pointing is shown as a dotted purple circle. In XMM-LSS, the ultradeep HSC pointing is shown as a dashed red circle.

Table 2.1: The 5σ limiting magnitudes for each band used in this work, in each VISTA VIDEO tile (see Fig. 2.1). The local depths were measured by placing 2 arcsec diameter circular apertures on empty regions of the images. The depth quoted here is the mode of these local depths. IRAC depths were measured in 2.8 arcsec diameter circular apertures to account for the poorer resolution. The first section shows bands from VST. The second section shows bands from HSC. The third section shows bands from VISTA. The final section shows bands from *Spitzer*/IRAC.

Filter	XMM1	XMM2	XMM3	CDFS1	CDFS2	CDFS3
u	-	-	-	25.5	25.6	25.4
g	-	-	-	26.0	25.9	26.0
r	-	-	-	26.0	26.0	26.0
i	-	-	-	24.6	24.8	24.7
G	27.6	27.1	27.1	26.5	26.2	26.4
R	27.1	26.6	26.5	25.5	25.5	25.5
I	26.9	26.2	26.2	25.6	25.5	25.5
NB0816	26.0	25.4	25.4	-	-	-
Z	26.5	25.9	25.9	25.1	24.8	24.8
NB0921	26.0	25.3	25.4	-	-	-
y	25.6	24.7	24.7	-	-	-
Y	25.2	25.1	25.2	25.2	25.1	25.3
J	24.7	24.7	24.7	24.6	24.9	24.6
Y+J	25.3	25.3	25.3	25.3	25.3	25.2
H	24.2	24.3	24.3	24.1	24.2	24.1
K_s	23.8	23.9	23.9	23.8	23.7	23.7
3.6μm	24.3	24.3	24.4	25.0	24.9	24.9
4.5μm	24.1	24.1	24.1	24.8	24.8	24.8

by SExtractor (Bertin and Arnouts, 1996) was used to avoid foreground objects. To measure the standard deviation of the fluxes, the median absolute deviation (MAD) was used. This is more robust to outliers than Gaussian fitting, and is given by MAD = median(|flux − median|), with $\sigma = 1.4826 \times$ MAD. Local depth maps in each image were produced by splitting the image into local regions with a size determined by taking the closest 300 apertures to each point. The global depths were taken as the mode of these local depths and are reported in Table 2.1.

Table 2.2: Values of parameters used when running SExtractor in dual image mode.

Parameter	Value
DETECT_MINAREA	3
DETECT_THRESH	1.4
ANALYSIS_THRESH	1.4
DEBLEND_NTHRESH	32
DEBLEND_MINCONT	0.0001
BACK_SIZE	64
BACK_FILTERSIZE	9
BACKPHOTO_TYPE	LOCAL
BACKPHOTO_THICK	24

2.2.4 Catalogue creation

At $z \simeq 7$, the Lyman break will cause objects to drop out of either the Z, y or Y bands. The VIDEO-Y band is deeper than the HSC-y band (see Table 2.1), hence we produced fiducial catalogues by running SExtractor in dual image mode on a $Y + J$ stacked image parameters used are provided in Table 2.2). This probes the rest-frame UV ($\sim$ 1500Å) at $z \simeq 7$. The photometry was performed in 2 arcsec diameter apertures, which encloses 70-80% of the total flux of a point source. This provides high signal-to-noise whilst balancing against the need for a large aperture correction. For the *Spitzer*/IRAC photometry, 2.8 arcsec diameter apertures were used to account for the broader PSF.

Since fluxes are measured in fixed apertures, the measurement must be corrected to a total flux by accounting for light beyond the aperture using the shape of the PSF. The FWHM of the Y-band imaging is 0.8 arcsec. However, as mentioned in Section 2.2.2, in ECDF-S the FWHM of the PSF varies markedly (by up to 0.1 arcsec) across the field for the $I-$ and $Z-$bands. We thus used PSFEx (Bertin, 2011) to generate a local PSF model to aperture correct our photometry by splitting each tile into a 10×10 grid. For our analysis we only considered regions where VOICE, HSC and VIDEO data overlap (see Fig. 2.1). Bright stars and regions of low signal-to-noise at the edges of the VISTA VIDEO tiles are masked.

2.3 Galaxy selection

The selection of robust $z \simeq 7$ candidates required several steps, which we detail in this section and present an overview of in Table 2.3.

2.3.1 Initial selection

The $Y + J$ selected catalogues contained $1,814,513$ and $1,846,027$ objects in XMM-LSS and ECDF-S respectively. Objects without overlapping VOICE+HSC+VIDEO imaging are removed, shown as the 'remove missing data' step in Table 2.3. Bright objects were selected by requiring detections at $> 5\sigma$ significance in $Y + J$ for XMM-LSS. In the ECDF-S data, a 5σ cut was insufficient because Z is ~ 1 mag shallower than Y (see Table 2.1), making it challenging to select drop-out objects. We therefore applied a brighter 8σ cut in ECDF-S, corresponding to ~ 0.5 mag brighter than the 5σ cut in XMM-LSS.

We then require $< 2\sigma$ significance (i.e. a non-detection) in bands bluewards of and including i/I. In ECDF-S the HSC R-band is not used for this due to its poor coverage and because r is deeper by 0.5 mag. Similarly, the i-band is not used for this since HSC-I is $\gtrsim 0.7$ mag deeper (see Table 2.1). The $u-$band is also not used due to its significantly shallower depth. Note that all of these bands are later included for SED fitting in Section 2.3.2. The results of these steps on reducing the sample are shown in Table 2.3.

Table 2.3: The results of our selection in XMM-LSS (top) and ECDF-S (bottom). The left column describes the selection step and the right column shows the number of objects remaining after this step. SED fitting is used to find candidates with photometric redshifts $z > 6$ and remove low-redshift interlopers, and visual checks are used to remove artefacts. The objects remaining after the removal of brown dwarfs is the final number of candidate galaxies in each field.

Selection step	Objects remaining
XMM-LSS	
Initial catalogue	1814513
Remove missing data	1707431
5σ $Y + J$ cut	807190
$< 2\sigma$ in I	11821
$< 2\sigma$ in R	3398
$< 2\sigma$ in G	3217
SED fitting: $z > 6$	307
Visual selection	121
Dusty $z \sim 1 - 2$ galaxies	97
Brown dwarf removal	22
ECDF-S	
Initial catalogue	1846027
Remove missing data	1291653
8σ $Y + J$ cut	428695
$< 2\sigma$ in I	2859
$< 2\sigma$ in r	1504
$< 2\sigma$ in g	1427
$< 2\sigma$ in G	1390
SED fitting: $z > 6$	186
Visual selection	70
Dusty $z \sim 1 - 2$ galaxies	61
Brown dwarf removal	6

Table 2.4: The photometry of sources in our final $z \simeq 7$ sample. The top section shows objects in XMM-LSS, and the bottom section shows objects in ECDF-S. Objects are ordered by their photometric redshift. The first column shows the object ID, and the next two columns show the coordinates of the candidate. The remaining columns show the photometry in the bands available in each field. We require a $< 2\sigma$ detections bluewards of and including the i/I-bands, so we only present bands redwards of this. The photometry is measured in a 2.0 arcsec diameter circular aperture apart from the *Spitzer*/IRAC bands where 2.8 arcsec diameter apertures are used to account for the broader PSF. The photometry is corrected to a total flux assuming a point-source correction. If the measured flux is $< 2\sigma$ we present an upper limit. Objects with confused *Spitzer*/IRAC photometry are marked with an asterisk.

ID	RA	DEC	Z	NB921	y	Y	J	H	Ks	[3.6]	[4.5]
VIDEO_z7_1*	02:22:56.06	-05:28:00.37	$26.3^{+0.5}_{-0.3}$	$24.9^{+0.2}_{-0.2}$	$25.3^{+0.6}_{-0.4}$	$24.7^{+0.2}_{-0.2}$	$24.4^{+0.2}_{-0.2}$	$24.9^{+0.7}_{-0.4}$	$23.7^{+0.2}_{-0.2}$	$22.2^{+0.1}_{-0.1}$	$22.0^{+0.1}_{-0.1}$
VIDEO_z7_2	02:25:51.03	-04:03:16.98	$26.3^{+0.7}_{-0.4}$	$25.5^{+0.4}_{-0.3}$	$25.1^{+0.7}_{-0.4}$	$24.5^{+0.2}_{-0.2}$	$24.5^{+0.3}_{-0.2}$	$24.3^{+0.4}_{-0.3}$	> 24.1	$23.4^{+0.2}_{-0.2}$	$23.7^{+0.3}_{-0.2}$
VIDEO_z7_3	02:26:39.93	-04:01:09.51	$26.3^{+0.5}_{-0.4}$	$24.9^{+0.2}_{-0.1}$	$24.6^{+0.3}_{-0.2}$	$24.4^{+0.2}_{-0.1}$	$24.0^{+0.2}_{-0.2}$	$24.4^{+0.4}_{-0.3}$	> 24.2	$23.3^{+0.2}_{-0.2}$	$23.8^{+0.2}_{-0.2}$
VIDEO_z7_4	02:27:38.62	-04:51:36.34	> 26.2	$25.2^{+0.2}_{-0.2}$	> 24.6	$24.7^{+0.2}_{-0.2}$	$25.0^{+0.5}_{-0.4}$	$24.9^{+0.7}_{-0.4}$	> 24.2	$23.5^{+0.2}_{-0.2}$	$23.5^{+0.2}_{-0.2}$
VIDEO_z7_5*	02:26:30.02	-04:20:32.23	> 26.2	$25.9^{+0.5}_{-0.3}$	$24.8^{+0.4}_{-0.3}$	$24.4^{+0.2}_{-0.2}$	$24.4^{+0.3}_{-0.2}$	$24.2^{+0.4}_{-0.3}$	$24.2^{+0.5}_{-0.3}$	$21.8^{+0.2}_{-0.2}$	$21.8^{+0.2}_{-0.2}$
VIDEO_z7_6	02:16:32.44	-05:30:05.82	> 25.9	$24.9^{+0.2}_{-0.2}$	$24.6^{+0.2}_{-0.2}$	$24.7^{+0.2}_{-0.2}$	> 24.6	> 24.1	$24.3^{+0.5}_{-0.4}$	$24.5^{+0.3}_{-0.2}$	> 25.1
VIDEO_z7_7	02:27:30.78	-04:25:12.11	$26.4^{+0.4}_{-0.3}$	$24.7^{+0.1}_{-0.1}$	$24.6^{+0.3}_{-0.2}$	$24.5^{+0.1}_{-0.1}$	$25.2^{+0.5}_{-0.3}$	$24.4^{+0.4}_{-0.3}$	> 23.9	$23.8^{+0.3}_{-0.2}$	$24.2^{+0.6}_{-0.4}$
VIDEO_z7_8	02:22:05.84	-04:54:10.85	> 26.0	> 25.5	$25.0^{+0.6}_{-0.4}$	$24.6^{+0.2}_{-0.2}$	$24.8^{+0.4}_{-0.3}$	> 24.4	$24.4^{+0.5}_{-0.4}$	$23.9^{+0.3}_{-0.2}$	> 24.4
VIDEO_z7_9	02:23:47.30	-05:21:25.49	$25.4^{+0.2}_{-0.2}$	$25.0^{+0.2}_{-0.2}$	$24.4^{+0.2}_{-0.2}$	$24.5^{+0.1}_{-0.1}$	$24.3^{+0.2}_{-0.2}$	$24.3^{+0.3}_{-0.3}$	$24.3^{+0.5}_{-0.3}$	$22.9^{+0.1}_{-0.1}$	$23.2^{+0.1}_{-0.1}$
VIDEO_z7_10*	02:16:36.51	-04:54:50.62	> 26.8	> 26.4	$24.9^{+0.2}_{-0.2}$	$24.8^{+0.3}_{-0.2}$	$24.6^{+0.3}_{-0.2}$	$24.7^{+0.6}_{-0.4}$	$24.3^{+0.6}_{-0.4}$	$22.1^{+0.2}_{-0.2}$	$22.2^{+0.2}_{-0.2}$
VIDEO_z7_11	02:24:59.99	-04:43:54.27	> 26.6	> 26.0	$24.7^{+0.3}_{-0.2}$	$24.7^{+0.3}_{-0.2}$	$24.9^{+0.4}_{-0.3}$	$24.7^{+0.4}_{-0.3}$	> 24.2	$23.6^{+0.2}_{-0.2}$	> 24.3
VIDEO_z7_12*	02:17:00.07	-04:12:26.78	> 26.6	> 26.6	$25.1^{+0.2}_{-0.2}$	$24.8^{+0.2}_{-0.2}$	$25.3^{+0.6}_{-0.4}$	> 24.7	> 23.8	$23.6^{+0.2}_{-0.2}$	$24.4^{+0.3}_{-0.2}$
VIDEO_z7_13	02:25:17.59	-04:38:54.33	> 26.2	> 25.4	$24.8^{+0.4}_{-0.3}$	$24.7^{+0.2}_{-0.1}$	$24.7^{+0.3}_{-0.2}$	$24.6^{+0.4}_{-0.3}$	$24.7^{+0.6}_{-0.4}$	> 24.0	$24.0^{+0.4}_{-0.3}$
VIDEO_z7_14	02:27:37.26	-04:10:52.04	> 26.6	> 25.8	$25.2^{+0.5}_{-0.3}$	$24.8^{+0.2}_{-0.2}$	$25.2^{+0.6}_{-0.4}$	$25.0^{+0.7}_{-0.4}$	$24.7^{+0.7}_{-0.4}$	> 24.6	> 24.2
VIDEO_z7_15	02:21:29.47	-05:15:27.24	> 26.5	> 25.7	$25.5^{+0.6}_{-0.4}$	$25.2^{+0.3}_{-0.2}$	$25.3^{+0.4}_{-0.3}$	> 24.5	> 24.2	> 24.1	> 23.8

ID	RA	DEC	Z	NB921	y	Y	J	H	Ks	[3.6]	[4.5]
VIDEO_z7_16	02:22:27.88	-05:13:41.40	> 26.5	> 25.9	$25.5^{+0.7}_{-0.4}$	$24.9^{+0.2}_{-0.2}$	> 25.1	$25.1^{+0.6}_{-0.4}$	> 24.6	> 24.6	> 24.3
VIDEO_z7_17	02:25:30.47	-05:18:01.46	> 26.6	> 25.5	$25.3^{+0.7}_{-0.4}$	$24.9^{+0.2}_{-0.2}$	$25.2^{+0.4}_{-0.3}$	> 24.6	> 24.2	> 24.0	> 24.5
VIDEO_z7_18	02:21:16.56	-04:33:20.28	> 26.7	> 25.8	$25.2^{+0.3}_{-0.2}$	$24.4^{+0.1}_{-0.1}$	$24.6^{+0.2}_{-0.2}$	$24.3^{+0.3}_{-0.2}$	$24.6^{+0.6}_{-0.4}$	$22.6^{+0.2}_{-0.2}$	$23.1^{+0.2}_{-0.2}$
VIDEO_z7_19	02:18:06.79	-04:25:30.56	> 27.1	> 26.5	$25.3^{+0.2}_{-0.2}$	$24.7^{+0.2}_{-0.2}$	$25.0^{+0.4}_{-0.3}$	> 24.7	> 24.3	$24.9^{+0.4}_{-0.3}$	> 24.3
VIDEO_z7_20	02:15:31.44	-05:09:07.95	> 26.6	> 26.4	$25.1^{+0.3}_{-0.2}$	$24.6^{+0.2}_{-0.2}$	$24.7^{+0.4}_{-0.3}$	$24.6^{+0.7}_{-0.4}$	> 24.0	$24.1^{+0.2}_{-0.2}$	$25.0^{+0.5}_{-0.3}$
VIDEO_z7_21*	02:26:46.18	-04:59:53.51	> 26.4	> 25.7	> 24.5	$24.6^{+0.2}_{-0.1}$	$24.5^{+0.3}_{-0.2}$	$24.5^{+0.4}_{-0.3}$	$24.4^{+0.6}_{-0.4}$	$24.1^{+0.4}_{-0.3}$	$23.4^{+0.2}_{-0.2}$
VIDEO_z7_22*	02:16:25.10	-04:57:38.56	> 27.2	> 26.2	$26.5^{+0.7}_{-0.4}$	$24.7^{+0.2}_{-0.2}$	$24.1^{+0.2}_{-0.1}$	$24.1^{+0.2}_{-0.2}$	$23.6^{+0.3}_{-0.2}$	$23.1^{+0.2}_{-0.2}$	$22.9^{+0.2}_{-0.2}$
VIDEO_z7_23*	03:30:17.50	-28:14:20.71	> 25.1	-	-	$24.3^{+0.1}_{-0.1}$	$24.4^{+0.2}_{-0.2}$	$24.5^{+0.4}_{-0.3}$	$23.7^{+0.3}_{-0.2}$	$22.7^{+0.2}_{-0.2}$	$22.5^{+0.2}_{-0.2}$
VIDEO_z7_24*	03:35:19.41	-27:49:32.15	> 25.3	-	-	$24.3^{+0.1}_{-0.1}$	$24.6^{+0.3}_{-0.2}$	$24.9^{+0.7}_{-0.4}$	> 24.0	> 24.8	$24.8^{+0.5}_{-0.3}$
VIDEO_z7_25	03:34:44.08	-28:02:51.72	> 25.5	-	-	$24.2^{+0.1}_{-0.1}$	$23.7^{+0.1}_{-0.1}$	$23.2^{+0.1}_{-0.1}$	$22.8^{+0.1}_{-0.1}$	$22.5^{+0.2}_{-0.2}$	$22.4^{+0.2}_{-0.2}$
VIDEO_z7_26	03:28:29.28	-27:59:28.38	> 25.5	-	-	$24.5^{+0.1}_{-0.1}$	$24.2^{+0.2}_{-0.1}$	$23.5^{+0.1}_{-0.1}$	$23.1^{+0.1}_{-0.1}$	$22.4^{+0.2}_{-0.2}$	$22.1^{+0.2}_{-0.2}$
VIDEO_z7_27	03:30:42.79	-27:17:30.39	> 25.6	-	-	$24.2^{+0.1}_{-0.1}$	$24.3^{+0.2}_{-0.2}$	$24.7^{+0.6}_{-0.4}$	$23.4^{+0.2}_{-0.2}$	$23.8^{+0.2}_{-0.2}$	$24.3^{+0.2}_{-0.2}$
VIDEO_z7_28	03:34:29.33	-28:13:00.47	> 25.1	-	-	$24.1^{+0.1}_{-0.1}$	$23.5^{+0.1}_{-0.1}$	$24.4^{+0.5}_{-0.3}$	$24.2^{+0.4}_{-0.3}$	$23.7^{+0.2}_{-0.2}$	$22.4^{+0.2}_{-0.2}$

2.3.2 SED fitting and photometric redshifts

We make use of all available bands to select Lyman break galaxies at $z \simeq 7$ by using a SED fitting analysis. SED fitting is done using LePhare (Arnouts et al., 1999; Ilbert et al., 2006), which works by minimising χ^2 to find the best-fitting redshift and galaxy templates. The redshift was allowed to vary between $z = 0 - 9$. Bruzual and Charlot (2003) stellar population models were used with metallicities of $Z = [0.2, 0.4, 1.0]\ Z_{\odot}$. The star-formation histories explored were constant, instantaneous bursts and exponentially declining with timescales in the range $\tau = 0.05 - 10$ Gyr. Stellar population ages could range from 10 Myr to 13.8 Gyr, limited by the age of the Universe at a given redshift. Dust reddening was prescribed by the Calzetti et al. (2000) dust law, with attenuation in the range $0.0 \leq A_V \leq 4.0$ to allow for very dusty low-redshift interlopers. A Chabrier (2003) initial mass function is assumed, and absorption by the IGM was applied according to Madau (1995). *Spitzer*/IRAC photometry was not used initially to determine the photometric redshifts of objects due to the larger uncertainties and high rates of confusion due to a larger PSF. Instead, we included the IRAC photometry (when unconfused) for a separate check for low-redshift interlopers (see Section 2.3.4).

Lyman-α emission can increase the photometric redshift of objects by $\Delta z \sim 0.5$ (Bowler et al., 2014) due to the addition of flux to the broadband. This is accounted for by simultaneously fitting Bruzual and Charlot (2003) templates which have lines of equivalent widths 0 Å $\leq \mathrm{EW}_0 \leq$ 240 Å added . To do this, the continuum level was measured from the mean flux between 1250Å and 1300Å. Note that by restricting 0Å $\leq \mathrm{EW}_0$, we are ignoring negative equivalent widths, which are possible for damped Lyman-α systems and damping wings (e.g. see Wolfe et al., 2005). The photometric redshift constraints from this Lyman-α analysis are stronger in XMM-LSS due to many overlapping filters around the expected position of the Lyman break, and due to the availability of narrowband filters that can very precisely pick out excess flux due to an emission line. The photometric redshifts are highly degenerate in ECDF-S due to the gap between Z and Y.

Candidates were first required to have their best fitting solution at $z > 6$. The fits then had to be sufficiently good, defined as $\chi^2 < 11.3$ (12.9) for XMM-LSS (ECDF-S). These values correspond to 2σ significance given 5 (6) degrees of freedom. We also required that the high-redshift solution was better than the low-redshift solution by a threshold $\Delta\chi^2 > 4$, which corresponds to a 2σ significance. This removes 2910 objects in XMM-LSS and 1204 in ECDF-S, leaving 307 and 186 objects respectively.

2.3.3 Visual selection

We conducted a visual selection of the remaining objects to remove artefacts that appear as good high-redshift candidates in the photometry, primarily in the form of crosstalk in VIDEO images and diffraction spikes. Crosstalk is an artefact produced in the readout from the VIRCAM instrument on VISTA that produces ghost images at multiples of 128 pixels in the native scale from bright stars (Bowler et al., 2017). Optical stacked postage stamp images are created to check for low-level optical flux that would indicate a low-redshift galaxy. The bands used for the optical stack are required to have similar 5σ depths, leading to a GRI stack in XMM-LSS and a $grGI$ stack in ECDF-S. Single-band detections are also removed. This step removes 186 objects in XMM-LSS and 116 in ECDF-S, leaving 121 and 70 objects respectively.

Two objects in XMM-LSS (VIDEO_z7_8 and VIDEO_z7_12) appeared to have low-level flux in their optical stacks. This optical flux is offset from the position of the object in the $Y + J$ detection filter by > 1 arcsec, suggesting the optical flux originates from a foreground object and hence we retain them. One object (ID 1610530, RA 02:27:12.04, DEC -04:32:05.05) appeared to be remarkably bright at $M_{\rm UV} \simeq -24.4$, but a marginal detection at 3.6μm around 2 mag fainter than in K_s and a non-detection at 4.5μm resulted in very unusual photometry that passed our selection criterion. For such a rest-UV bright high-redshift object, we would expect much brighter *Spitzer*/IRAC flux. We checked for this object in J-band imaging from the overlapping WIRCam Deep Survey (WIRDS, Bielby et al., 2012), where it was not present. However, a fainter object closely separated to the south is visible. This object is thus likely either a VIDEO artefact or a transient,

supported by the faint 3.6μm detection. The SED fitting and postage stamp images of this object are presented in Appendix C.

2.3.4 Removing contaminants

Dusty galaxies at $z \sim 1-2$ with Balmer breaks masquerading as Lyman breaks form one class of contaminant. These galaxies tend to have much redder continuum slopes than galaxies at $z \simeq 7$, as observed in the NIR. We use SED fitting with the *Spitzer*/IRAC bands to test for dusty low-redshift galaxies. If the SED fitting has a low-redshift solution that is preferred to the high-redshift solution when IRAC is included, the object is rejected if the IRAC photometry is unconfused. This step removes 24 objects in XMM-LSS and 9 objects in ECDF-S, leaving 97 and 61 objects respectively.

M, L and T brown dwarf (BD) stars comprise a major contaminant in high-redshift searches around a magnitude $m_{\rm AB} \sim 25$ where their number density in extragalactic surveys peaks (Ryan et al., 2011). They have intrinsically red optical to NIR colours with heavy molecular spectral absorption complexes (e.g. Cushing et al., 2008; Marley et al., 2021). The removal of BDs must be done carefully since peaks in their SEDs can line up with the ground-based $YJHK_s$ filters, mimicking a flat NIR colour. We fit our photometry with stellar templates taken from the SpeX prism library (Burgasser, 2014). The u, G, g, R and r bands are excluded from the SED fitting since the templates do not contain any information at these wavelengths. The $\chi^2_{\rm BD}$ values are then compared to $\chi^2_{\rm galaxy}$ values, also fitted without these filters. In Bowler et al. (2015), a simulation of brown dwarfs in the Milky Way shows that removing objects with good brown dwarf fits at $\chi^2_{\rm BD} < 10$ decreases the contamination rate to essentially zero. We therefore retain those high-redshift candidates which have $\chi^2_{\rm BD} > 10$. This step removes around 80% of objects (see Table 2.3) compared to around 20% in Bowler et al. (2015). To understand this discrepancy, we use a similar model to Bowler et al. (2015) (provided by Rebecca Bowler) to compute the expected number of brown dwarfs in our fields, assuming a Galactic scale-height of 300 pc. Considering magnitudes down to the 5σ (8σ)

depths in XMM-LSS (ECDF-S), we expect 480 and 220 dwarf stars respectively. Restricting this to the most common stellar types found by our initial SED fitting, we expect 146 and 76 dwarf stars respectively. We do not predict the exact number of dwarf stars because the Galactic scale-height is highly uncertain, with estimates varying between 300 pc (Ryan et al., 2017) and 400 pc (Sorahana et al., 2019). The difference in the fraction of sources cut between this work and Bowler et al. (2015) can thus be attributed to a higher LBG number density at the fainter magnitudes and lower redshift probed by their work ($-22.7 \leq M_{\rm UV} \leq -20.5$ at $z = 6$), coupled with higher brown dwarf densities at brighter magnitudes probed by this work.

Bowler et al. (2015) state that keeping objects with $\chi^2_{\rm BD} > 10$ likely removes some genuine high-redshift galaxies, and they account for this with a completeness correction. We note that many of our candidates with $\chi^2_{\rm BD} < 10$ have a significantly better fitting high-redshift galaxy template. In an attempt to be complete to genuine $z \simeq 7$ galaxies that may be removed from our primary robust sample due to being fit well as BDs, we conducted a more inclusive BD cut which retains these potential $z \simeq 7$ galaxies, and is described in Appendix A.

2.3.5 SED fitting with BAGPIPES

We repeat SED fitting on the final sample with Bayesian Analysis of Galaxies for Physical Inference and Parameter EStimation (BAGPIPES, Carnall et al., 2018) to compare photometric redshifts with LePhare and determine physical parameters such as stellar masses. The advantage of BAGPIPES is the implementation of grids of nebular emission line models based on input stellar population models. We used a fiducial constant star formation history (SFH) model. The time since star formation switched on varies between the start of the Universe and the redshift being considered. We adopt a uniform prior on the redshift, $0 \leq z \leq 9$, and the ionization parameter, $-4 \leq \log U \leq -2$. The metallicity is fixed at $Z = 0.2 Z_{\odot}$. Fixing of the metallicity at a value $Z < Z_{\odot}$ is motivated by recent spectroscopic measurements at $z \gtrsim 7$ that suggest galaxies tend to be metal-poor (e.g. Curtis-Lake et al., 2023; Langeroodi et al., 2023; Matthee et al., 2023; Fujimoto et al., 2023). We also

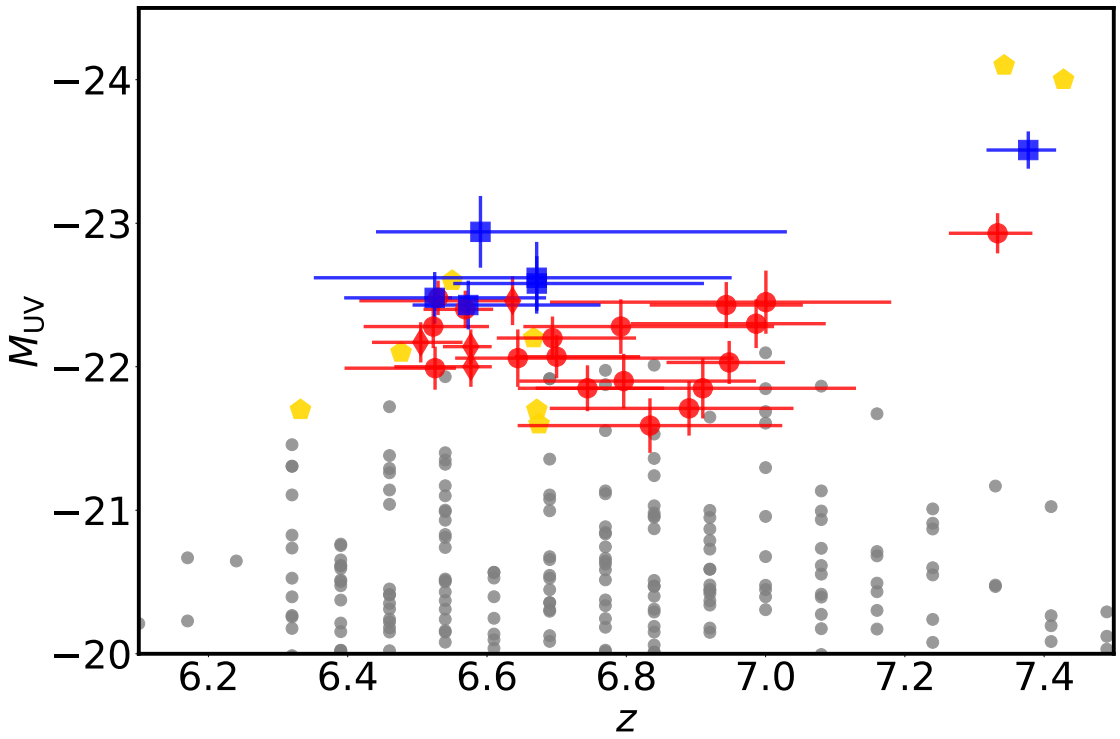

Figure 2.2: Rest-frame absolute UV magnitudes of the 28 LBGs in our sample against their photometric redshifts as measured by LePhare. Candidates from XMM-LSS are shown as red circles, and those with a Lyman-α best-fitting SED are shown as red diamonds. Candidates from ECDF-S are shown as blue squares. The grey circles are candidate galaxies from Bouwens et al. (2021), which uses *Hubble* data. The yellow pentagons show the high-redshift solution of SED fitting on objects from Harikane et al. (2022b) crossmatched with our catalogues.

restrict the dust attenuation to the range $0 \leq A_V \leq 0.5$, limiting it to the largest attenuation we measure with LePhare (VIDEO_z7_25 and VIDEO_z7_26, shown in Table 2.5). If we do not restrict the range of A_V, large values occur for the objects with the most massive stellar masses: $A_V \gtrsim 1$ when $\log_{10}(M/M_\odot) \gtrsim 11$. This is because dust extinction is degenerate with age (since we have fixed metallicity), so large values are a consequence of the constant SFH model rather than being a realistic estimate of the dust emission (e.g. Inami et al., 2022; Ferrara et al., 2023).

2.4 The final sample

The final sample consists of 28 objects, with photometry presented in Table 2.4. The results of SED fitting and properties of objects (e.g. photometric redshift,

$M_{\rm UV}$, dust attenuation) are shown in Table 2.5. Of the 22 primary candidates in XMM-LSS, 18 are newly identified. Five are within the ultradeep HSC pointing, and four have a best-fitting template which includes Lyman-α emission (and have $z_{\rm No\ Ly\alpha} < 6.5$). The best-fitting rest-frame equivalent widths for these objects are noted in Table 2.5. In ECDF-S, all candidates are presented here for the first time. One object in ECDF-S had a best-fitting Lyman-α template, but was rejected due to having a good low-redshift fit. Therefore, all Lyα objects lie in XMM-LSS. The absolute UV magnitudes, $M_{\rm UV}$, are computed by placing a top-hat filter at 1500Å with width 100Å on the rest-frame best-fitting SED. The sample has a mean redshift $\bar{z} = 6.74$, and spans nearly 2 magnitudes in the rest-UV, $-23.5 \leq M_{\rm UV} \leq -21.6$. The distribution of photometric redshifts against UV absolute magnitude, split by field, is shown in Fig. 2.2. Candidates in ECDF-S are brighter on average than those in XMM-LSS simply by nature of the different selection thresholds that we imposed because of the shallower optical data available in this field. Uncertainties on the photometric redshifts tend to be lower in XMM-LSS compared to ECDF-S due to the proximity and overlap between Z, NB921, y and Y around the Lyman break. The grey points in Fig. 2.2 are candidate galaxies from Bouwens et al. (2021), which uses 1136 square arcminutes of *Hubble* imaging to derive the rest-UV LF at $z \simeq 7$. Their brightest candidate is $M_{\rm UV} \simeq -22.1$. Only 10 of our candidates are fainter than this, showing that these ground-based data better probe the bright-end of the rest-UV LF.

Table 2.5: The 28 LBG candidates in XMM-LSS (top) and ECDF-S (bottom), ordered by photometric redshift as in Table 2.4. The first column shows the object ID. The next four columns show properties of the high-redshift solution: photometric redshift, absolute magnitude in a top-hat filter at 1500Å with width 100Å, dust attenuation, and χ^2 value as derived by LePhare. The next two columns show the secondary photometric redshift and χ^2. The following two columns show the stellar type for fitting to standard MLT brown dwarf spectra, and $\chi^2_{\rm BD}$. The next two columns show the equivalent width for objects that have a best-fitting SED with Lyman-α emission. The final three columns show properties derived from SED fitting with BAGPIPES, namely the photometric redshift $z_{\rm BP}$, dust attenuation $A_{V,\ \rm BP}$ and stellar mass. Objects with IRAC non-detections have upper limits for their stellar masses. Object IDs marked with an asterisk have confused IRAC photometry, meaning stellar mass estimates may be overestimated. Object IDs marked with superscripts 1 and 2 have been previously identified in Bouwens et al. (2022a) and Endsley et al. (2021b) respectively.

ID	z	$M_{\rm UV}$ / mag	A_V / mag	χ^2	$z_{\rm gal2}$	$\chi^2_{\rm gal2}$	Stellar Type	$\chi^2_{\rm BD}$	EW$_0$ / Å	$z_{\rm BP}$	$A_{V,\ \rm BP}$ / mag	$\log_{10}(M_\star/M_\odot)$
VIDEO_z7_1*	$6.50^{+0.07}_{-0.06}$	-22.2 ± 0.1	0.2	11.9	1.3	18.4	M8	18.2	40	$6.43^{+0.05}_{-0.06}$	$0.41^{+0.07}_{-0.13}$	$10.31^{+0.17}_{-0.32}$
VIDEO_z7_2	$6.52^{+0.08}_{-0.10}$	-22.3 ± 0.2	0.0	11.3	1.2	36.8	T3	15.8		$6.53^{+0.03}_{-0.04}$	$0.32^{+0.12}_{-0.15}$	$10.20^{+0.15}_{-0.18}$
VIDEO_z7_3	$6.53^{+0.02}_{-0.02}$	-22.5 ± 0.1	0.2	5.4	1.3	42.8	M8	27.7		$6.49^{+0.03}_{-0.05}$	$0.27^{+0.15}_{-0.17}$	$10.17^{+0.24}_{-0.33}$
VIDEO_z7_4	$6.53^{+0.03}_{-0.13}$	-22.0 ± 0.2	0.2	7.1	1.3	31.6	T3	23.2		$6.48^{+0.04}_{-0.06}$	$0.42^{+0.06}_{-0.10}$	$10.28^{+0.11}_{-0.15}$
VIDEO_z7_5	$6.57^{+0.04}_{-0.06}$	-22.4 ± 0.1	0.0	6.3	1.5	21.9	T3	12.5		$6.57^{+0.25}_{-0.02}$	$0.32^{+0.14}_{-0.18}$	$10.24^{+0.21}_{-0.28}$
VIDEO_z7_6[1]	$6.58^{+0.03}_{-0.12}$	-22.0 ± 0.1	0.0	7.9	1.3	46.2	M8	31.0	50	$6.46^{+0.04}_{-0.07}$	$0.05^{+0.07}_{-0.03}$	$9.12^{+0.29}_{-0.26}$
VIDEO_z7_7	$6.58^{+0.02}_{-0.04}$	-22.1 ± 0.1	0.0	8.0	1.3	74.9	M8	65.5	50	$6.44^{+0.03}_{-0.04}$	$0.17^{+0.17}_{-0.12}$	$10.03^{+0.22}_{-0.37}$
VIDEO_z7_8	$6.64^{+0.31}_{-0.08}$	-22.1 ± 0.2	0.0	4.4	1.45	16.5	M6	14.2		$6.73^{+0.18}_{-0.13}$	$0.22^{+0.18}_{-0.15}$	$10.04^{+0.23}_{-0.34}$
VIDEO_z7_9	$6.64^{+0.01}_{-0.22}$	-22.5 ± 0.2	0.0	4.1	1.25	23.5	M8	17.7	240	$6.30^{+0.05}_{-0.05}$	$0.47^{+0.02}_{-0.04}$	$10.55^{+0.05}_{-0.08}$
VIDEO_z7_10[2*]	$6.69^{+0.12}_{-0.07}$	-22.2 ± 0.2	0.2	3.4	1.35	40.4	T4	25.2		$6.74^{+0.10}_{-0.10}$	$0.46^{+0.03}_{-0.07}$	$10.51^{+0.09}_{-0.13}$
VIDEO_z7_11	$6.70^{+0.12}_{-0.06}$	-22.1 ± 0.2	0.0	2.7	1.5	26.9	T8	20.4		$6.70^{+0.11}_{-0.07}$	$0.18^{+0.17}_{-0.13}$	$9.93^{+0.25}_{-0.34}$
VIDEO_z7_12*	$6.74^{+0.12}_{-0.10}$	-21.8 ± 0.2	0.0	8.6	1.5	30.0	M6	33.9		$6.68^{+0.10}_{-0.06}$	$0.23^{+0.16}_{-0.13}$	$9.94^{+0.16}_{-0.18}$
VIDEO_z7_13	$6.79^{+0.22}_{-0.14}$	-22.3 ± 0.2	0.2	8.6	1.5	54.0	T8	25.9		$6.83^{+0.15}_{-0.17}$	$0.13^{+0.16}_{-0.09}$	$9.80^{+0.24}_{-0.34}$
VIDEO_z7_14	$6.80^{+0.19}_{-0.15}$	-21.9 ± 0.2	0.0	7.8	1.5	28.2	T8	18.9		$6.79^{+0.13}_{-0.13}$	$0.25^{+0.17}_{-0.17}$	< 9.90

ID	z	$M_{\rm UV}$ / mag	A_V / mag	χ^2	$z_{\rm gal2}$	$\chi^2_{\rm gal2}$	Stellar Type	$\chi^2_{\rm BD}$	$\rm EW_0$ / Å	$z_{\rm BP}$	$A_{V,\ \rm BP}$ / mag	$\log_{10}(M_\star/M_\odot)$
VIDEO_z7_15	$6.83^{+0.19}_{-0.18}$	-21.6 ± 0.2	0.0	4.7	1.5	24.4	T8	12.7		$6.77^{+0.19}_{-0.13}$	$0.18^{+0.20}_{-0.14}$	< 9.70
VIDEO_z7_16	$6.89^{+0.15}_{-0.20}$	-21.7 ± 0.2	0.0	8.0	1.5	31.8	T8	23.5		$6.79^{+0.14}_{-0.14}$	$0.10^{+0.13}_{-0.07}$	< 9.32
VIDEO_z7_17	$6.91^{+0.22}_{-0.24}$	-21.8 ± 0.2	0.0	7.8	1.15	35.1	T8	16.9		$6.79^{+0.15}_{-0.12}$	$0.12^{+0.13}_{-0.09}$	< 9.35
VIDEO_z7_18	$6.94^{+0.12}_{-0.10}$	-22.4 ± 0.2	0.0	6.3	1.5	45.4	T3	23.6		$6.86^{+0.11}_{-0.11}$	$0.44^{+0.04}_{-0.09}$	$10.52^{+0.10}_{-0.14}$
VIDEO_z7_19	$6.95^{+0.08}_{-0.09}$	-22.0 ± 0.2	0.0	9.4	1.25	88.2	T8	35.9		$6.76^{+0.11}_{-0.09}$	$0.08^{+0.11}_{-0.05}$	$9.40^{+0.28}_{-0.32}$
VIDEO_z7_20	$6.99^{+0.09}_{-0.18}$	-22.3 ± 0.2	0.0	3.7	1.45	38.7	T8	16.0		$6.78^{+0.10}_{-0.11}$	$0.14^{+0.15}_{-0.09}$	$9.55^{+0.24}_{-0.35}$
VIDEO_z7_21[1*]	$7.00^{+0.18}_{-0.31}$	-22.5 ± 0.2	0.1	4.5	1.5	41.8	T8	17.5		$7.00^{+0.10}_{-0.15}$	$0.25^{+0.14}_{-0.14}$	$10.18^{+0.14}_{-0.19}$
VIDEO_z7_22[1*]	$7.33^{+0.06}_{-0.07}$	-22.9 ± 0.1	0.0	11.4	1.6	33.6	T1	14.5		$7.29^{+0.06}_{-0.06}$	$0.40^{+0.07}_{-0.10}$	$10.59^{+0.11}_{-0.13}$
VIDEO_z7_23*	$6.52^{+0.16}_{-0.13}$	-22.5 ± 0.2	0.0	6.7	1.45	12.2	M6	14.7		$6.49^{+0.19}_{-0.12}$	$0.45^{+0.03}_{-0.07}$	$10.61^{+0.09}_{-0.13}$
VIDEO_z7_24*	$6.57^{+0.2}_{-0.08}$	-22.4 ± 0.2	0.0	8.3	1.45	17.7	M7	19.7		$6.71^{+0.25}_{-0.21}$	$0.04^{+0.06}_{-0.03}$	$9.18^{+0.22}_{-0.20}$
VIDEO_z7_25	$6.59^{+0.44}_{-0.15}$	-22.9 ± 0.3	0.5	4.0	1.25	14.6	L8	13.5		$7.31^{+0.05}_{-0.05}$	$0.46^{+0.03}_{-0.06}$	$10.92^{+0.08}_{-0.14}$
VIDEO_z7_26	$6.67^{+0.28}_{-0.32}$	-22.6 ± 0.3	0.5	4.0	1.5	8.7	L8	14.7		$7.30^{+0.05}_{-0.06}$	$0.48^{+0.02}_{-0.03}$	$10.86^{+0.06}_{-0.09}$
VIDEO_z7_27	$6.67^{+0.24}_{-0.12}$	-22.6 ± 0.2	0.0	5.6	1.45	29.4	M8	29.7		$6.79^{+0.15}_{-0.12}$	$0.20^{+0.18}_{-0.14}$	$9.70^{+0.21}_{-0.31}$
VIDEO_z7_28	$7.38^{+0.03}_{-0.06}$	-23.5 ± 0.1	0.0	9.9	1.5	77.7	T8	11.1		$7.24^{+0.06}_{-0.09}$	$0.09^{+0.14}_{-0.07}$	$9.93^{+0.26}_{-0.50}$

The SED fitting and stamps of a candidate galaxy from each field is shown in Fig. 2.3. The SED fitting and stamps for all candidates in this work are shown in Appendix B. The [3.6] and [4.5] *Spitzer*/IRAC bands can be contaminated by nebular emission lines at $z > 6.5$ (primarily Hα, Hβ, [O II] and [O III]). The [3.6] - [4.5] colour will accordingly change with redshift as these lines move through the filters (Smit et al., 2014; Smit et al., 2015). By accounting for nebular emission during SED fitting, we can obtain more precise photometric redshifts. An interesting example is the brightest object in our sample, VIDEO_z7_28, which has a red IRAC colour of $[3.6] - [4.5] = 1.3 \pm 0.4$ and a photometric redshift of $z = 7.38^{+0.03}_{-0.06}$. Bowler et al. (2020) extend the expected IRAC colours derived by Smit et al. (2014) out to higher redshifts, predicting that galaxies with strong Hβ+[OIII] emission ($\mathrm{EW}_0 = 500 - 2000$Å) can have colours as high as $[3.6] - [4.5] \simeq 1.0$ at $z \simeq 7.5$, in agreement with our photometry for this object. As we discuss later in Section 2.4.1, we show that several previous $z \sim 7$ candidates at around $z = 7.4$ are likely to be BDs. VIDEO_z7_28 passes our selection criterion with the BD fit showing $\chi^2_{\mathrm{BD}} = 11.1$. It is slightly extended in the data with a FWHM of 1.5 arcsec in comparison to the PSF of the Y-band (FWHM of 0.8 arcsec). However, we cannot fully rule out a BD solution for this source, and further follow-up will be required to confirm this extremely luminous LBG.

2.4.1 Comparison to previous work

The Reionisation Era Bright Emission Line Survey (REBELS, Bouwens et al., 2022a) is a search for bright $z > 6.5$ galaxies in XMM-LSS and COSMOS, with the aim of following up these galaxies with the Atacama Large Millimeter/submillimeter Array (ALMA). Within XMM-LSS they make use of VIDEO (Jarvis et al., 2013), the UKIDSS Ultra Deep Survey (UDS, Lawrence et al., 2007), and optical data from HSC-SSP DR2 and the Canada-France Hawaii Telescope Legacy Survey (CFHTLS) D1 field (Erben et al., 2009). Of the 40 REBELS objects, 15 are in XMM-LSS and we recover three out of four that are bright enough to meet our 5σ $Y + J$ cut, namely REBELS-01 (VIDEO_z7_22), REBELS-02 (VIDEO_z7_6) and

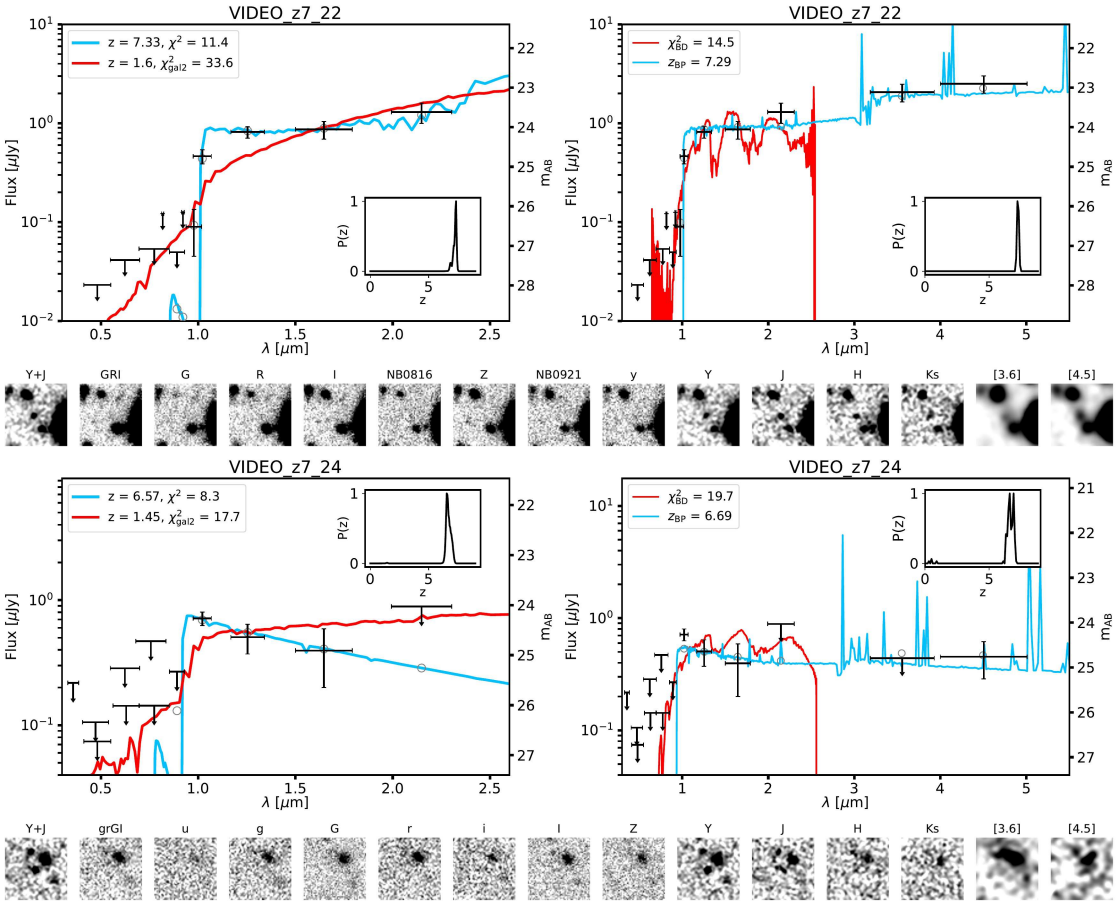

Figure 2.3: Two example candidate galaxies in XMM-LSS (top object, VIDEO_z7_22) and ECDF-S (bottom object, VIDEO_z7_24). For each object, the black points in both plots are the measured photometry, with non-detections replaced by 2σ upper limits. **Top Left:** SED fitting with LePhare. The blue curve shows the best-fitting high-redshift solution, and grey circles are its model photometry. The red curve shows the low-redshift solution. The legend shows the redshift and χ^2 value of each solution. The wavelength range of this plot is limited to $\lambda \simeq 2.5\mu$m to focus on the Lyman break and rest-UV continuum. The inset black curve shows the redshift probability distribution. **Top Right:** best-fitting BD template (red) along with the best-fit BAGPIPES galaxy fit (blue curve). The chi-squared value for the brown dawrf fit, $\chi^2_{\rm BD}$, is computed without IRAC and without bands bluewards of i/I. The grey circles show the model photometry of the BAGPIPES solution. The legend shows $\chi^2_{\rm BD}$ and the redshift of the BAGPIPES solution, $z_{\rm BP}$. This plot extends out to $\lambda > 5\mu$m to show the *Spitzer*/IRAC photometry and the nebular emission component of the fit. The inset black curve is the redshift probability distribution found by BAGPIPES. **Bottom:** 10 arcsec $\times$ 10 arcsec postage stamps of the object in the filters used.

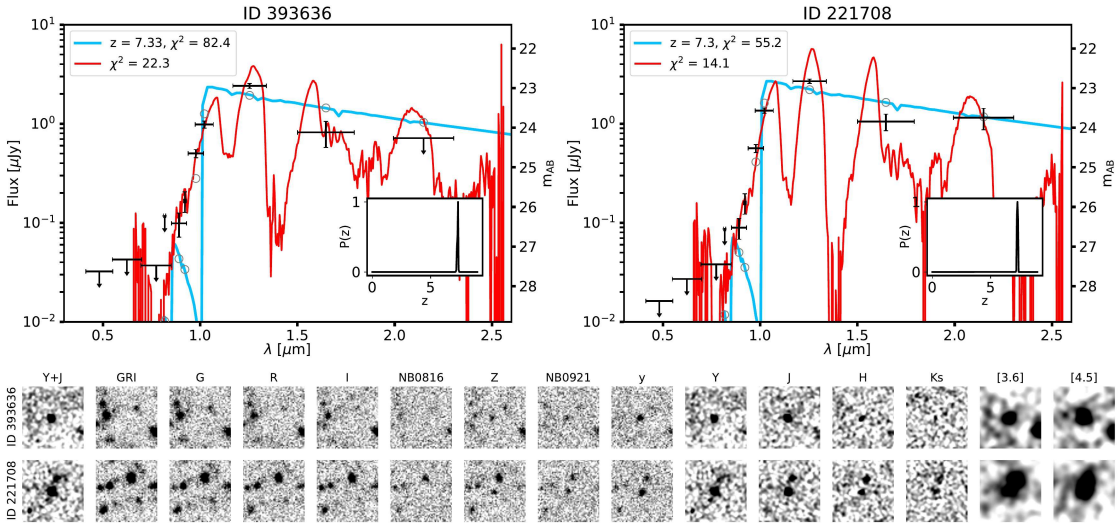

Figure 2.4: Top: SED fitting of the two brightest GOLDRUSH objects in XMM-LSS that overlap with our selection, ID 393636 (left) and ID 221708 (right). The black points are the measured photometry, with non-detections replaced by 2σ upper limits. The dwarf star SED is shown in red, and the high-redshift solution in blue. The grey circles are the model photometry for the high-redshift solution. Inset is the redshift probability distribution for the galaxy fit. The legend shows the redshift of the galaxy template and χ^2 values. Both objects have preferred brown-dwarf fits and poor galaxy fits: the rising slope in the blue end of the brown dwarf SED and the drop in flux at 1.6μm are captured by the optical and $YJHK_s$ bands respectively. **Bottom:** 10 arcsec $\times$ 10 arcsec postage stamps each object. From left to right we have: the detection filter $Y + J$, the optical stack used to check for low-level flux in each field, and the filters available for objects in each field ordered by increasing wavelength, as in Fig. 2.3.

REBELS-14 (VIDEO_z7_21). REBELS-10 is not recovered due to blending with a foreground object. VIDEO_z7_21 and VIDEO_z7_22 are spectroscopically confirmed at $z = 7.084$ and $z = 7.177$ respectively (Bouwens et al., 2022a), in agreement with our photometric redshifts. The difference in objects selected is due to deeper UDS data used by REBELS. By making use of the UDS data they are able to select fainter candidates, and their selection also identifies candidates at $z > 7.5$.

Great Optically Luminous Dropout Research Using HSC (GOLDRUSH, Harikane et al., 2022b) uses HSC-SSP DR2 data ($GRIZy$) to search for LBGs at $z = 4 - 7$. This survey covers 20.2 deg^2 to depths comparable to the 'deep' and 'ultradeep' regions of XMM-LSS outlined in Section 2.2.1. There are eight objects that overlap with our XMM-LSS data, all in the 'ultradeep' HSC pointing. Three out of eight of these objects are recovered in our 5σ $Y + J$ cut. We find that the two brightest ob-

jects recovered at 5σ in $Y + J$ have preferred brown dwarf fits, with poor galaxy fits. The SED fits for these objects are shown in Fig. 2.4. These objects have coordinates (RA 02:18:11.39 DEC -05:29:56.55) and (RA 02:17:00.95 DEC -04:40:35.14). The third object (RA 02:19:40.78 DEC -05:13:53.76)[2] recovered at 5σ in $Y + J$ appears to have low-level optical flux, best seen in a GRI stack, due to confusion with a nearby foreground object. Our SED fitting is also used on the remaining five objects that do not satisfy the 5σ $Y + J$ cut. Of these, two objects have $z_{\rm phot} < 6.5$, and three objects have $z_{\rm phot} > 6.5$. This appears to give a fiducial contamination rate of ~ 50 per cent, but because we find brown dwarf fits for their brightest objects, it may be the case that their brightest bins are more significantly contaminated. We show the photometric redshifts of the $z \geq 6$ solutions of SED fitting and resulting absolute UV magnitudes $M_{\rm UV}$ for these objects in Fig. 2.2. The high-redshift solution for the two brown dwarfs places them at $z \simeq 7.4$ with extremely bright absolute UV magnitudes of $M_{\rm UV} \simeq -24$. The remainder of the objects are fainter, similar to the bulk of our sample. Contamination of the Harikane et al. (2022b) sample, and the impact on the derived bright end of the UV LF, is discussed further in Section 2.6.1.

Endsley et al. (2021b) select galaxies at $z = 6.63 - 6.83$ using overlapping data from HSC-SSP DR2, VIDEO and the UDS. They search in XMM1 and COSMOS, finding 9 objects in XMM1. XMM1-313310 in their study corresponds to VIDEO_z7_10 in this work. We find $z_{\rm phot} = 6.72$, agreeing with their redshift range. XMM1-418672 in their study exists in our initial catalogue, but has $\chi^2 = 15.3$ so is rejected since it fails the $\chi^2 < 11.3$ cut in XMM-LSS. The other 7 objects were selected by Endsley et al. (2021b) in the deeper UDS data, so are not recovered in this work.

2.4.2 Physical properties with BAGPIPES

Table 2.5 shows the results of our BAGPIPES fitting. All photometric redshifts measured by BAGPIPES agree with those measured by LePhare apart from objects VIDEO_z7_25 and VIDEO_z7_26 in ECDF-S, which agree within 2σ, due to

[2]These have IDs 37484833881991283, 37485130234754131 and 37484567594038420 respectively in the Harikane et al. (2022b) catalogue.

degeneracies in best-fitting redshift because of the gap between the Z and Y bands. IRAC detections probe the rest-frame optical, providing improved estimates of stellar masses. Measured stellar masses of the galaxies with unconfused *Spitzer*/IRAC photometry are in the range $9.1 \leq \log_{10}(M_\star/M_\odot) \leq 10.9$, with a mean stellar mass of $\log_{10}(M_\star/M_\odot) = 10.0$. Our stellar mass for VIDEO_z7_22 agrees with that found by Bouwens et al. (2022a), but our stellar mass for VIDEO_z7_21 is an order of magnitude higher than theirs. This is because *Spitzer*/IRAC bands for this object are confused, leading to boosted flux due to the foreground object to the north. Bouwens et al. (2022a) apply neighbour subtraction to their IRAC photometry, which we do not do. Consequently, we mark objects that are confused in their *Spitzer*/IRAC photometry with an asterisk in Table 2.5, indicating that these objects may have overestimated stellar masses. We also show confused IRAC photometry in green and with dashed error bars in the SED fitting plots for all candidates in Appendix B. Nearly half (10/23) of our galaxies with unconfused IRAC photometry have stellar masses $\log_{10}(M_\star/M_\odot) > 10$, suggesting that these galaxies represent some of the most massive galaxies at this epoch (compared to e.g. Bowler et al., 2014; Bouwens et al., 2022a; Labbé et al., 2023a). The lower end of our derived stellar masses are more uncertain because the rate of *Spitzer*/IRAC non-detections increases for $\log_{10}(M_\star/M_\odot) \lesssim 9.4$, meaning we cannot directly measure the rest-frame optical emission. Our masses are therefore upper limits.

Further issues arise in estimating stellar masses at these redshifts since it is difficult to tell if there is nebular emission (primarily [OIII] + Hβ) contaminating the IRAC photometry, outshining the stellar continuum and masking contributions from the older stellar population. Since we have fixed metallicity, this results in a degeneracy between age and dust attenuation. Whitler et al. (2023) have shown that properties derived from SED fitting depend on the SFH used. The dependence is strongest for derived age and weakest for stellar mass. This can be somewhat remedied by restricting the redshift range and using narrowband and intermediate band photometry to compute more precise photometric redshifts (Endsley et al., 2021b), limiting nebular emission to only one of the two *Spitzer*/IRAC bands

and leaving the other free from contamination. Despite this contamination of the IRAC bands, we find that BAGPIPES provides reasonable estimates of the stellar masses in comparison to those derived by excluding contaminated bands entirely (e.g. Bowler et al., 2018).

2.5 The rest-frame UV luminosity function

We use the LBG candidates found in our selection to determine the UV LF at $z \simeq 7$. The $1/V_{\rm max}$ method is used to compute points on the LF (Schmidt, 1968), where $V_{\rm max}$ is the maximum comoving volume a galaxy can occupy and still be included in our survey. The maximum redshift $z_{\rm max}$ is determined by redshifting the galaxy in steps of $\Delta z = 0.01$ until it no longer satisfies the 5σ (8σ) detection threshold in $Y + J$ in XMM-LSS (ECDF-S). $V_{\rm max}$ is then the comoving volume between $z = 6.5$ and $z = z_{\rm max}$. The UV LF is then calculated as

$$\Phi(M)d\log(M) = \frac{1}{\Delta M}\sum_{i}^{N}\frac{1}{C(M_i, z_i)}\frac{1}{V_{{\rm max},i}}\ , \tag{2.1}$$

where ΔM is the width of the magnitude bin and $C(M_i, z_i)$ is a completeness correction, which depends on the magnitude and redshift of the object. Poissonian errors are given by

$$\delta\Phi(M) = \frac{1}{\Delta M}\sqrt{\sum_{i}^{N}\left(\frac{1}{V_{{\rm max},i}}\right)^2} \tag{2.2}$$

following Adams et al. (2023b). Bin widths $\Delta M_{\rm UV} = 0.75$ are chosen for all bins to maximise the number of galaxies in each bin. The bins are centred at $M_{\rm UV} = -22.175, -22.925$ and -23.675. These bins contain 21, 4 and 1 galaxies respectively. The brightest bin only contains VIDEO_z7_28, so the binning is also chosen to ensure this object is roughly in the centre of the bin. The faintest bin was chosen to ensure we are significantly brighter than where our sample becomes incomplete, as discussed in Section 2.5.1. We compute an upper limit on the number density of galaxies at $M_{\rm UV} = -24.425$ with bin width $\Delta M = 0.75$. This is calculated by $1/V/\Delta M$, where V is the volume probed by our survey at $6.5 \leq z \leq 7.5$.

2.5.1 Completeness correction

The focus of this work is the bright end of the rest-frame UV LF. We expect that the brightest bins are close to complete (excluding area lost due to foreground objects) in a 5σ $Y+J$ selection since they are much brighter than the detection threshold ($> 8\sigma$ at $M_{\rm UV} \lesssim -22.4$). We estimate the completeness of our initial selection (see Section 2.3.1) by comparing the number of objects per square degree as a function of apparent magnitude in $Y+J$ in XMM-LSS and ECDF-S with the 'ultradeep' stripes from the UltraVISTA Survey (McCracken et al., 2012) in COSMOS, reaching 5σ depths of 26.3 in $Y+J$ in the ultradeep stripes, ~ 1 mag deeper than VIDEO. We find, as expected, that our $Y+J$ selection is 95 per cent complete by $M_{\rm UV} = -21.8$, so we choose our faintest bin to cut off at this absolute UV magnitude. This excludes two candidates from the LF calculation, VIDEO_z7_15 and VIDEO_z7_16.

SED fitting is in general more complete than a colour-colour selection (e.g. Adams et al., 2020), motivating its use in this work. To ensure our SED fitting selection is not overly conservative, we test the completeness of our SED fitting by estimating the fraction of genuine high-redshift galaxies incorrectly cut by our selection as a function of absolute UV magnitude and redshift. The values of $M_{\rm UV}$ used reaches one magnitude below the 5σ limit of each of our fields to account for up-scattering of objects into the sample. We use BAGPIPES to generate $z = 6-8$ SEDs with ages varying between 50 Myr to 700 Myr (or the age of the Universe at a given redshift). We vary the dust attenuation between 0 - 0.5 mag and fix the metallicity at $0.2Z_{\odot}$. We generate 26,000 galaxies for ECDF-S and each of XMM-LSS 'deep' and 'ultradeep'. Mock photometry in the available bands is generated by perturbing the model photometry using local depths within each field. SED fitting is performed on a catalogue of mock objects, where we apply the χ^2 cuts outlined in Sections 2.3.2 and 2.3.4. The completeness is then the fraction of galaxies recovered in each magnitude-redshift bin. We report the median completeness values for each LF bin in Table 2.6.

Table 2.6: The rest-UV luminosity function points at $z \simeq 7$ derived from the sample presented in this work. The first two columns show the absolute UV magnitude of the bin and the number of galaxies in the bin. All bins have a width of 0.75 mag. The third column shows the comoving number density of galaxies. The final column shows the median completeness in the bin.

Bin / mag	$n_{\rm gal}$	ϕ / mag / Mpc^3	Completeness
-22.175	21	$2.70 \pm 0.66 \times 10^{-6}$	0.63
-22.925	4	$2.81 \pm 1.54 \times 10^{-7}$	0.76
-23.675	1	$2.37 \pm 2.50 \times 10^{-8}$	0.79
-24.425	0	$< 2.07 \times 10^{-8}$	-

2.5.2 Cosmic variance

Galaxy surveys are a discrete sampling of the large scale structure of the Universe. Substructures such as voids and filaments can thus impact measurements of the LF if the dimensions of the survey are small. This effect has come to be known as 'Cosmic Variance'. We make use of the Trenti and Stiavelli (2008) calculator to estimate additional uncertainties due to this. We find that the Poisson errors dominate: cosmic variance contributes just 7.1 per cent to the brightest bin at $M_{\rm UV} \simeq -23.7$, going down to a 5.7 per cent contribution to our faintest bin at $M_{\rm UV} \simeq -22.2$. We include these contributions in our LF errors by adding them in quadrature.

2.5.3 Results

In this section we present our binned rest-frame UV LF measurement at $z \simeq 7$ and compare to measurements and best-fitting functions from other studies. In Fig. 2.5 we show the measurement of the rest-frame UV LF at $z \simeq 7$ from this work. The values of each bin are reported in Table 2.6.

Comparison of binned LF points

We compare our measurement of the $z \simeq 7$ UV LF to current wide-area studies from Harikane et al. (2022b) and Bowler et al. (2017), and add studies of the faint end using *Hubble* from McLure et al. (2013), Finkelstein et al. (2015) and Bouwens et al. (2021). Bowler et al. (2017) do not probe as bright as this work because they were

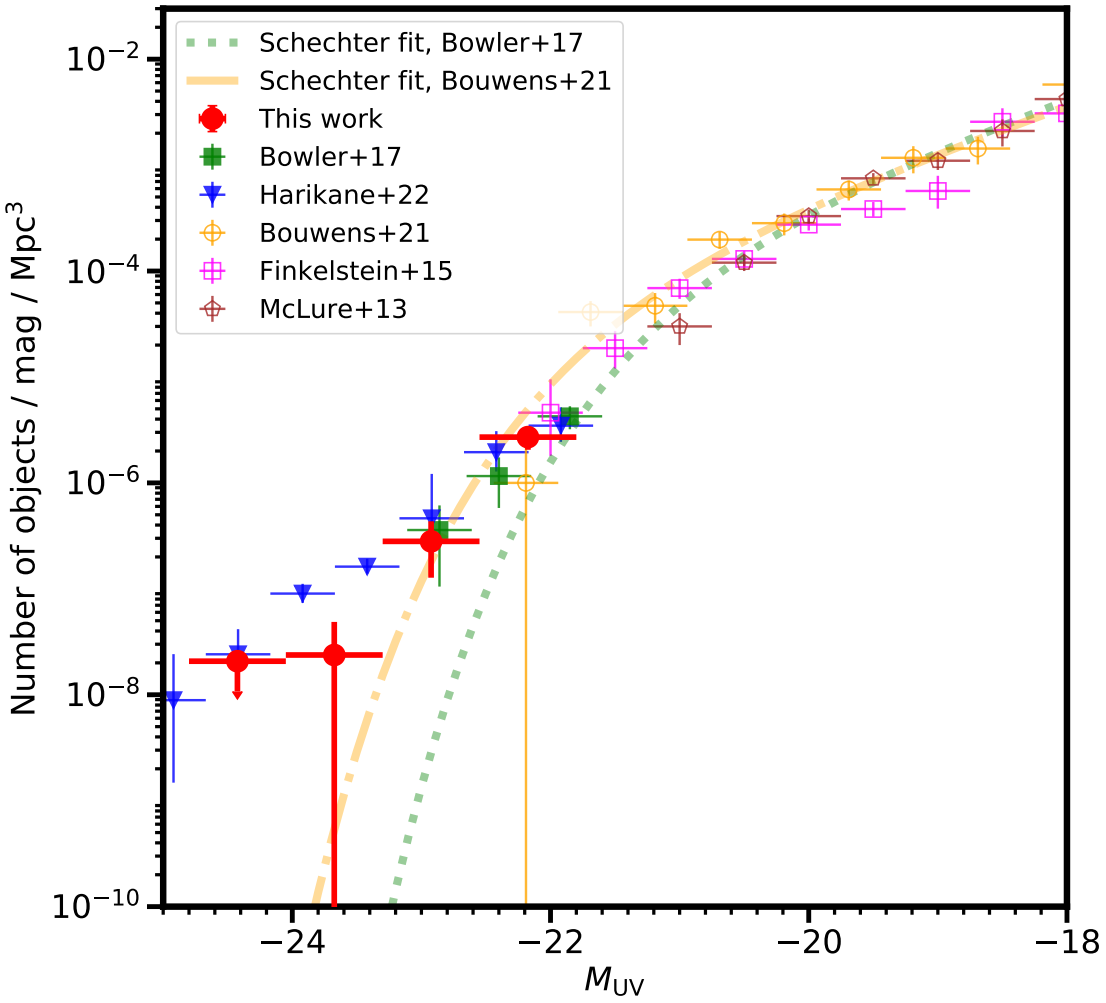

Figure 2.5: The rest-frame UV luminosity function at $z \simeq 7$ derived from 8.2 deg^2 of VIDEO data. The red filled circles show measurements of the number density from this work. We compute an upper limit on the number density of galaxies at $M_{\rm UV} = -24.425$ as described in Section 2.5. Other measurements from Harikane et al. (2022b), Bowler et al. (2017), McLure et al. (2013), Finkelstein et al. (2015) and Bouwens et al. (2021) are shown. The green dotted line and dot-dashed orange line show the best fitting Schechter functions from Bowler et al. (2017) and Bouwens et al. (2021) respectively.

limited to a smaller survey area of 1.65 deg^2. Harikane et al. (2022b) use 20.2 deg^2 of survey data comparable to the depths of optical bands in this work, allowing them to provide the first constraints on the $z \simeq 7$ UV LF beyond $M_{\rm UV} \lesssim -23$.

Our faintest point at $M_{\rm UV} \simeq -22.2$ is in agreement with those found by Finkelstein et al. (2015), Bowler et al. (2017), Bouwens et al. (2021) and Harikane et al. (2022b). Galaxies at $M_{\rm UV} \simeq -22$ represent the brightest that can be found by the widest-area *Hubble* surveys, and close to the faintest that can be found from

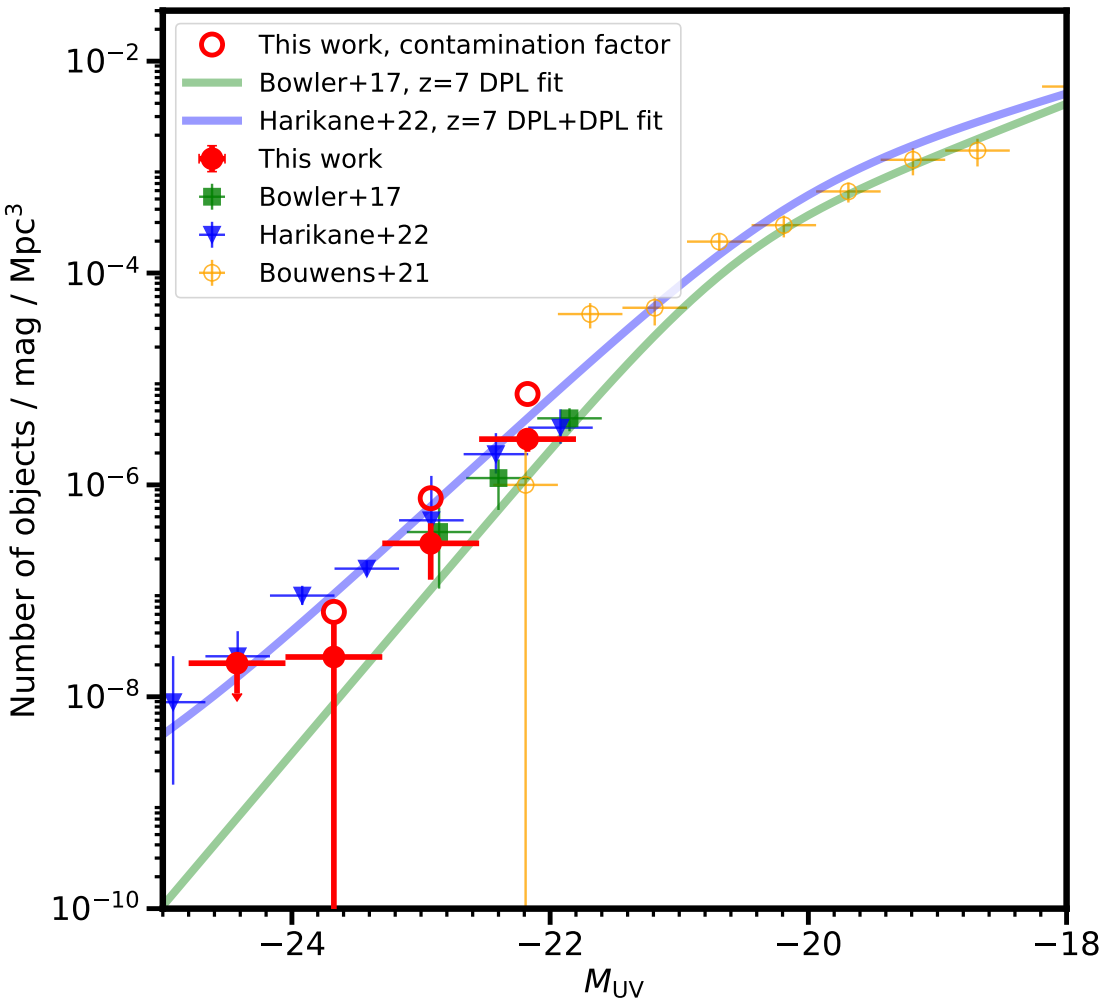

Figure 2.6: The rest-frame UV LF at $z \simeq 7$, as in Fig. 2.5. Here, we show the DPL fit derived by Bowler et al. (2017), and the DPL+DPL fit derived by Harikane et al. (2022b), shown as the green and blue lines respectively. The red open circles show our LF points incorporating a contamination factor of 50 per cent, as derived by SED fitting of objects from Harikane et al. (2022b) that overlapped with our catalogues.

VIDEO. The brightest candidate in the current widest area space-based survey (Bouwens et al., 2021) has an absolute UV magnitude $M_{\rm UV} \simeq -22.1$. Low number counts at this magnitude result in large error bars for their brightest bright bin, shown in yellow in Fig. 2.5. Our point at $M_{\rm UV} \simeq -22.9$ is in agreement with Bowler et al. (2017) and Harikane et al. (2022b), although errors between these three studies span over an order of magnitude. The Bowler et al. (2017) point lies roughly in the middle of our point and that of Harikane et al. (2022b). Our brightest point in the bin at $M_{\rm UV} \simeq -23.7$ is in tension with Harikane et al. (2022b)

at the 2σ level, being four times lower than their determination at $M_{\rm UV} \simeq -23.9$. In Fig. 2.2 we showed that the high-redshift solution of SED fitting for the two likely BDs in their sample (see Fig. 2.4 and Section 2.4.1) puts them at very bright absolute UV magnitudes of $M_{\rm UV} \sim -24$, explaining this tension. We note that our brightest bin contains only one galaxy, VIDEO_z7_28. This source could be a BD, as it is particularly luminous and at a similar redshift to the Harikane et al. (2022b) likely BDs (Fig. 2.2). If VIDEO_z7_28 is indeed shown to be a BD with later follow-up, this would change this point into a 1σ upper limit of 2.07×10^{-8} objects / mag / Mpc^3, leaving our conclusions unchanged. Finally, we compute an upper limit for the UV LF in a bin at $M_{\rm UV} \simeq -24.4$ with width $\Delta M = 0.75$, shown in Fig. 2.5. The LF point derived by Harikane et al. (2022b) at $M_{\rm UV} = -24.42$ lies on our upper limit, within the errors.

In summary, our determination of the UV LF agrees well with previous studies at $M_{\rm UV} \sim -22$. At brighter magnitudes, however, we find a deficit of sources in comparison to Harikane et al. (2022b). An analysis of the two brightest objects in their study suggests they are likely to be BDs. We therefore attribute this difference to contamination and emphasise the importance of NIR photometry in the selection of $z \simeq 7$ LBGs.

Schechter vs double power law fitting

In Fig. 2.5 we show the best-fitting Schechter function fits as derived by Bouwens et al. (2021) and Bowler et al. (2017). Our results appear to agree with the bright-end of the Bouwens et al. (2021) Schechter fit, although this is due to large errors on our brightest bin. The Schechter function fit derived by Bowler et al. (2017) uses results from McLure et al. (2013). Similarly to Bowler et al. (2017) and Harikane et al. (2022b), we find that the Schechter function does not fully reproduce the number density of bright galaxies, which our results show continues beyond $M_{\rm UV} \simeq -23$.

In Fig. 2.6 we show the DPL derived by Bowler et al. (2017) and the DPL+DPL (galaxy and AGN component) derived by Harikane et al. (2022b). These functions

provide a qualitative better fit to the UV LF measurements from our study. Furthermore, the reduced χ^2 value we compute for the DPL of Bowler et al. (2017) is $\chi^2_{\rm red} = 2.3$ which is preferred to their Schechter fit ($\chi^2_{\rm red} = 4.7$), as well as the Schechter fit of Bouwens et al. (2021) ($\chi^2_{\rm red} = 4.3$), providing further evidence for a DPL as the form of the rest-UV LF at $z \simeq 7$ continuing out to $M_{\rm UV} \simeq -24$. The DPL+DPL of Harikane et al. (2022b) is in excess of our results, with $\chi^2_{\rm red} = 6.2$. Our faintest two bins are in agreement with both Bowler et al. (2017) and Harikane et al. (2022b). In particular, the faintest bin is in closer agreement with Harikane et al. (2022b) and the middle bin lies closer to the Bowler et al. (2017) DPL. The differences are more pronounced at brighter magnitudes, where our results are in tension with the Harikane et al. (2022b) fit at the 2σ level. The Bowler et al. (2017) DPL is a factor of 5 lower at $M_{\rm UV} \simeq -22.9$, and a factor of 10 lower at $M_{\rm UV} \simeq -23.7$ than Harikane et al. (2022b). Our upper limit at $M_{\rm UV} \simeq -24.4$ lies just above the Harikane et al. (2022b) DPL+DPL. Assuming that AGN do not contribute to the bright end of rest-frame UV LF at $z \simeq 7$ (see Section 2.6.2) such that the number density continues to decline rapidly at brighter magnitudes, we expect that a measurement of the LF at this magnitude would lie closer to the DPL of Bowler et al. (2017), which is 20 times lower than predicted by Harikane et al. (2022b).

As shown in Section 2.4.1 and Fig. 2.4, the brightest objects from Harikane et al. (2022b) that lie in XMM-LSS are best fit by brown dwarf templates when $YJHK_s$ photometry is included. This suggests contamination in their brightest bins. The impact of this contamination on the LF is discussed further in 2.6.1. By utilising VIDEO photometry we have thus provided a robust measurement of the rest-frame UV LF at $z \simeq 7$ out to $M_{\rm UV} \simeq -24$.

2.5.4 Comparison to $z \simeq 8$ results

In this section we compare our results to various measurements of the rest-frame UV LF at $z \simeq 8$ to ascertain whether we find any evidence for evolution in the LF from $z \simeq 7 - 8$. Such a comparison is important for linking the rapid evolution seen in the bright end between $z = 5 - 7$ with ground-based studies (Bowler et al.,

2015) and the slow evolution seen with recent *JWST* results at $z \gtrsim 8$ (e.g. Donnan et al., 2023a). In Fig. 2.7 we plot results from other ground-based studies (Bowler et al., 2020; Donnan et al., 2023a) who both use deep optical and near-infrared imaging from VIDEO, UDS and UltraVISTA, in a similar manner to this work, to identify robust $z \simeq 8$ galaxy candidates. We also plot space-based results from Bouwens et al. (2021) of the faint-end of the $z \simeq 8$ LF. As expected, our results at $z \simeq 7$ are in excess of these results at $z \simeq 8$. We show the DPLs measured at $z \simeq 7$ and $z \simeq 8$ by Bowler et al. (2017) and Donnan et al. (2023a) respectively. Little evolution is expected in the bright-end between these epochs (Bowler et al., 2020; Harikane et al., 2023a), and this is reflected in the small differences between the DPLs and the slight excess of our results to those at $z \simeq 8$.

In Fig. 2.8 we show recent results from *Hubble* pure-parallel studies. Leethochawalit et al. (2023b) measure the $z \simeq 8$ LF in 0.41 deg^2 of the Search for the Brightest of Reionizing Galaxies and Quasars in *Hubble* Parallel Imaging Data (SuperBoRG), and Rojas-Ruiz et al. (2020) use similar data to derive comparable results. Both studies are in tension with this work. The DPL derived by Leethochawalit et al. (2023b) is a factor of 2.5-8 higher than our results, with the excess more pronounced at brighter magnitudes. At $M_{\rm UV} \simeq -24.4$, their DPL lies on the upper limit derived in this work. Similarly, the brightest LF point measured by Rojas-Ruiz et al. (2020) is 20 times higher than our measurement at $M_{\rm UV} \simeq -23.7$.

2.6 Discussion

Our results agree with other ground-based deep optical+NIR studies at $z \simeq 7-8$, but work using deep optical-only ground-based imaging and pure-parallel *Hubble* imaging derive an excess compared to our findings by up to an order of magnitude. In this section we discuss the potential contributions of quasars and brown dwarf contaminants, and implications of our results on the evolution of the bright-end of the rest-frame UV LF. We also consider how upcoming space-based wide-area missions can aid in building a clearer picture of bright LBG abundances at high redshift.

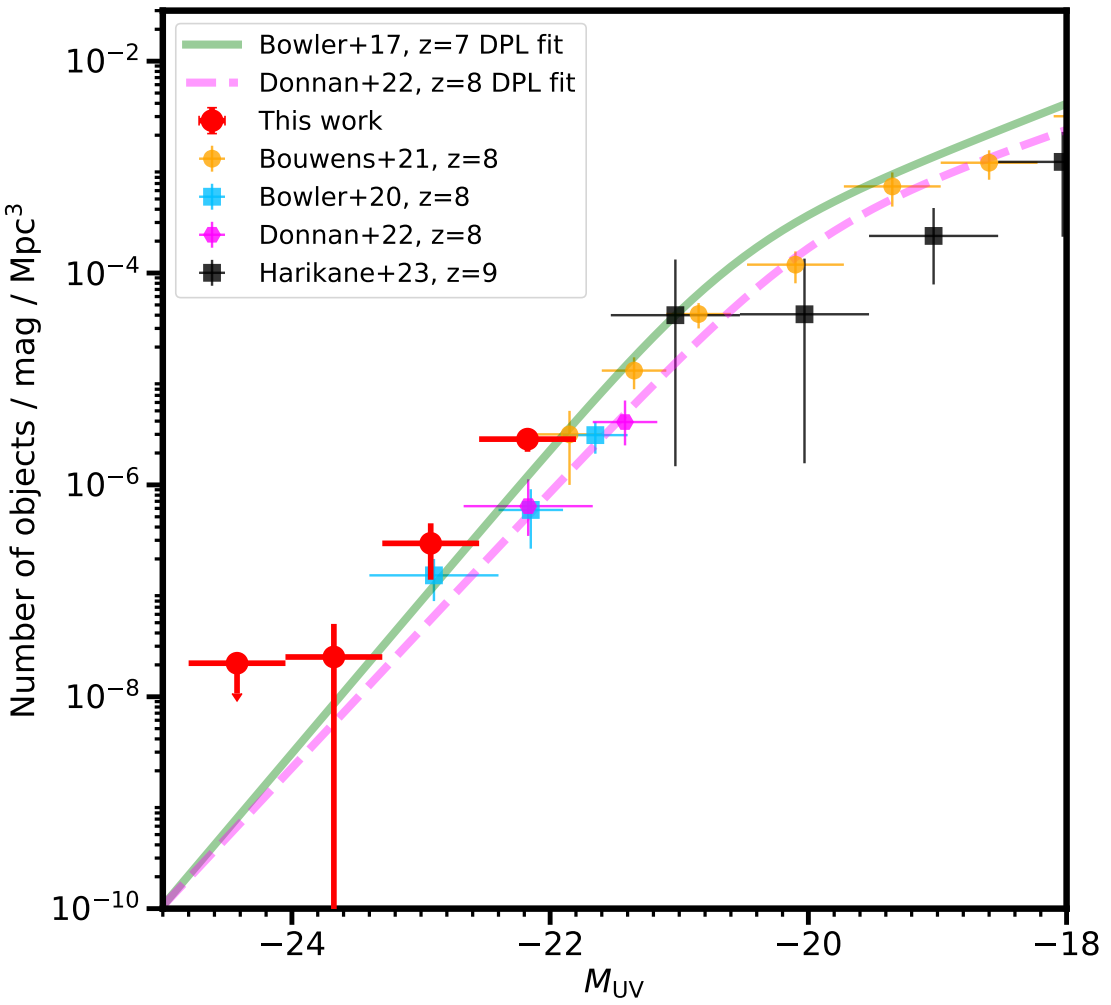

Figure 2.7: A comparison of our $z \simeq 7$ rest-UV LF results (red circles) and the $z \simeq 7$ DPL derived by Bowler et al. (2017) with various $z \simeq 8$ results. The blue squares show the $z \simeq 8$ rest-UV LF results from Bowler et al. (2020). The magenta hexagons show $z \simeq 8$ rest-UV LF results from Donnan et al. (2023a). Both of these studies use deep ground-based optical and NIR imaging. The magenta dashed line is the DPL fit derived by Donnan et al. (2023a). The yellow points are $z \simeq 8$ rest-UV LF results from Bouwens et al. (2021), derived from *Hubble* data.

2.6.1 Contamination in the bright end of the LF

In Section 2.5.3 and Fig. 2.6 we showed that our results are in agreement with the steeper DPL found by Bowler et al. (2017) and are in tension with the flatter decline found by Harikane et al. (2022b). Without the $YJHK_s$ bands, most $z \sim 7$ candidates found in HSC imaging appear as single band detections, or at most have a detection in the Z- and y-bands. Thus only a spectral break can be detected, leaving such samples more vulnerable to contamination. Moreover, by including

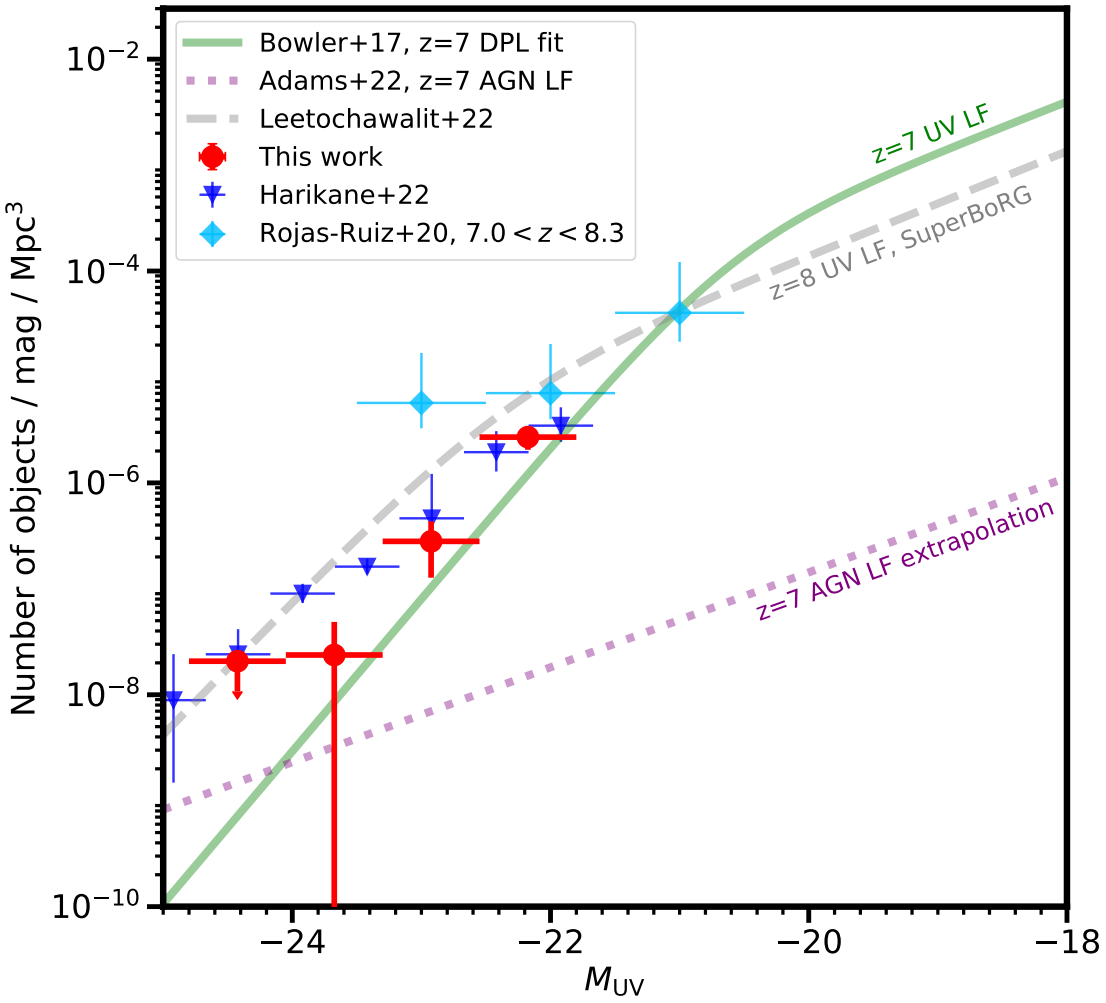

Figure 2.8: A comparison of our $z \simeq 7$ rest-UV LF results (red circles) and the $z \simeq 7$ DPL derived by Bowler et al. (2017). We include the $z \simeq 7$ rest-UV LF points found by Harikane et al. (2022b) as dark blue triangles. Here we compare to $z \simeq 8$ rest-UV LF results derived from *Hubble* pure-parallel programs, shown as light blue diamonds (Rojas-Ruiz et al., 2020) and the grey dashed DPL fit derived by Leethochawalit et al. (2023b). We also plot the $z \simeq 7$ extrapolation of the AGN LF found at $z = 3 - 5$ by Adams et al. (2023b) as the purple dotted line.

the HSC narrowbands our objects in XMM-LSS further gain the advantage of the NB921 and Y filters that overlap with the Z and y filters respectively, allowing for better determination of the nature of the break of an object. We find this to be powerful in detecting the slope of brown dwarf SEDs.

As discussed in Section 2.4.1, when the $YJHK_s$ data is included in the SED fitting analysis, we found that 4 out of 8 objects from the GOLDRUSH catalogue that overlaps with our data have poor $z \simeq 7$ SED fits. The fainter two of these

objects have best-fitting SEDs at $z < 6.5$, while the brighter two have best-fitting brown dwarf templates, as shown in Fig. 2.4. This gives us a fiducial contamination rate of 50 per cent. We apply this contamination factor to our derived LF points, shown as open red circles in Fig. 2.6, to assess the impact of contamination on our robust sample. For our faintest and middle bins, these contaminated points lie slightly above and on the fit derived by Harikane et al. (2022b), respectively. Our upper limit also suggests that their DPL+DPL is overestimated at $M_{\rm UV} \simeq -24.4$. This implies that not using $YJHK_s$ results in an overestimation of the bright end of the rest-UV LF at $z \simeq 7$. Note that our brightest contaminated LF point still lies slightly below the Harikane et al. (2022b) value at $M_{\rm UV} = -23.92$. This suggests that the fiducial contamination rate of 50 per cent could be higher at brighter magnitudes, with brighter bins preferentially affected by brown dwarfs or low-redshift galaxies when only optical data is included. This is in tension with the contamination rate estimated by Harikane et al. (2022b), who claim this is negligible based on results from their spectroscopic catalogue. They are also unable to use SED fitting to remove $z \sim 2$ interlopers at $z > 6$ due to lack of bands redwards of the Lyman break. This contamination likely causes the unphysical crossing of the UV LFs as derived in their study at $z \simeq 6$ and $z \simeq 7$ between $-25 \lesssim M_{\rm UV} \lesssim -23$ (see fig. 8 in Harikane et al., 2022b).

2.6.2 AGN contribution

In Section 2.5.3 we showed that the results of pure-parallel *Hubble* studies (Rojas-Ruiz et al., 2020; Leethochawalit et al., 2023b) at $z \simeq 8$ are significantly in excess of our results at $z \simeq 7$. Leethochawalit et al. (2023b) attribute this excess to a contribution by AGN. The motivation for this comes from Harikane et al., 2022b who suggest that the faint-end of the AGN LF dominates at $M_{\rm UV} \leq -24$ at $z = 4-7$. Adams et al. (2023b) measure the AGN LF in the same fields as this study at $z = 3-5$, as well as in the COSMOS field, and find that the AGN LF evolves more rapidly towards higher redshift. Matsuoka et al. (2018) find that this evolution continues to $z \simeq 6$: their AGN LF crosses the $z \simeq 7$ DPL of Bowler et al. (2017) at

$M_{\rm UV} \simeq -23.6$. Thus, if this strong decline in number density of faint UV-selected AGN continues to $z \simeq 7$ (AGN are rare at this epoch, and LRDs are generally fainter than $M_{\rm UV} \sim -23$, Mortlock et al., 2011; Bañados et al., 2018; Wang et al., 2021; Matthee et al., 2024), it is unlikely AGN contribute to the $z \simeq 7$ galaxy LF at the brighter magnitudes probed by this work and the pure-parallel studies from *Hubble*. Furthermore, In Fig. 2.8 we show the extrapolation of the AGN LF to $z = 7$ as estimated by Adams et al. (2023b). We extrapolate the $z = 4.8$ AGN LF to our mean redshift assuming a conservative value of $k = -0.82$ (where $k = \log_{10}(\Phi_{z_1}/\Phi_{z_2})/(z_1 - z_2)$ for mean redshifts z_1 and z_2 of two LFs used for comparison), providing a likely upper limit on the number density of faint $z \simeq 7$ AGN. Their extrapolation is $\simeq 10$ times lower than the double power law for SFGs computed by Bowler et al. (2017) at $M_{\rm UV} = -23$. Adams et al. (2023b) conclude that the AGN number density at $z \simeq 7$ is insufficient to contribute to the galaxy LF as found by Bowler et al. (2017). Instead, our results are consistent with little evolution in the bright-end between $z \simeq 7 - 8$, as determined by studies also using deep ground-based optical and NIR imaging (Bowler et al., 2020; Donnan et al., 2023a). Contamination in the Leethochawalit et al. (2023b) sample could be responsible for the excess of objects found in their work: for two thirds of their sample, only a single filter (F350LP) is available bluewards of the break. This is the same filter used in Rojas-Ruiz et al. (2020) to assert non-detections bluewards of the break, likely leading to imperfect removal of low-redshift galaxies and brown dwarfs. The true overlap between the galaxy and AGN LFs at $z \simeq 7$ therefore likely occurs somewhat brighter, at $M_{\rm UV} < -24$. We note that this discussion pertains to unobscured AGN - highly obscured AGN at $z \simeq 7$ have been discovered in the COSMOS field (Endsley et al., 2023).

2.6.3 Astrophysical interpretation

Robust measurements of the bright end of the rest-UV LF at $z \simeq 7$ are vital for understanding the evolution of the most star-forming and arguably massive galaxies between this epoch and the present day. The growth of massive galaxies

must somehow be suppressed to account for the change in shape of the UV LF over cosmic time, with a DPL observed at high-redshift to the Schechter form seen at low-redshift. One mechanism that may govern the shape of the bright end of the LF is quenching by AGN, where feedback is driven by energetic release from their accretion disk (e.g. Davé et al., 2019; Lovell et al., 2023), removing gas reservoirs from galaxies and limiting star formation. The AGN number density increases rapidly from $z = 6$ to $z = 5$, thus we know that AGN activity becomes more common (e.g. Matsuoka et al., 2018; Niida et al., 2020; Adams et al., 2023b). However, our results suggest that the contribution from AGN at $z \simeq 7$ to the rest-frame UV LF is minimal. This indicates that quenching of star formation by AGN is unlikely to impact bright galaxies at $z \simeq 7$.

Alternatively, the build-up of dust may lead to significant obscuration of UV light from galaxies, modifying the intrinsic rest-frame UV LF and causing a steeper decline in the observed bright end of rest-frame UV LF. Star formation enriches the ISM with dust, thus preferentially impacting the most massive galaxies. For example, Vijayan et al. (2021) use a simple model linking dust attenuation with ISM metal content and find that dust attenuation becomes important for galaxies with $M_{\rm UV} \lesssim -21$ at $z \simeq 7$. Our results suggest dust obscuration does not significantly impact the bright end of the rest-frame UV LF at this epoch. Dust attenuation values are low on average (see Table 2.5) with no dependence on $M_{\rm UV}$. These results suggest that a lack of dust attenuation at this epoch could explain the observed DPL shape and the almost constant number density of bright $z \simeq 7$ and $z \simeq 8$ sources (e.g. as shown in Ferrara et al., 2023). However, we note that the selection of rest-frame UV-bright galaxies can be blind to dust-obscured star formation, and recent studies are beginning to reveal the importance of this process (e.g. Bowler et al., 2022; Inami et al., 2022; Algera et al., 2023) and constrain dust properties at $z \gtrsim 6.5$ (e.g Inami et al., 2022; Sommovigo et al., 2022).

2.6.4 Outlook for upcoming surveys

At $z \simeq 7$ there is a need to bridge the gap between ground-based and space-based studies around the knee of the UV LF. A mismatch can be seen in Fig. 2.5 between the brightest bins of Bouwens et al. (2021) and the faintest bins of Bowler et al. (2017) and this work. At the knee, the former suffers from low number counts, and the latter suffers from a lack of depth. *Euclid* will be able to address this effectively: it will provide 50 deg^2 of YJH imaging down to 5σ depths of $m_{\rm AB} \simeq 26.4$ in its deep fields (van Mierlo et al., 2022), comparable to the depths of UltraVISTA (covering 1.5 deg^2). It will also be instrumental in providing much more accurate measurements of the ultra-bright end of the $z \simeq 7$ LF. It will provide 15,000 deg^2 of YJH imaging down to $m_{\rm AB} \simeq 24.5$ (Euclid Collaboration et al., 2022a), slightly deeper than VIDEO. Simply providing thousands more sources will vastly improve number statistics. Additionally, with much greater spatial resolution that comes with space-based observatories, blending will be less of an issue, and will allow a more accurate deconfusion of the *Spitzer*/IRAC data. The morphology of objects may even be used to distinguish between high-redshift galaxies (extended) and brown dwarfs or AGN (point-like). Since AGN are very rare at $z \simeq 7$, brown dwarf contaminants that appear as point sources could be efficiently removed from LBG samples via a size or morphology cut. Proper motion could also be used by comparing the astrometry of sources between *Euclid* and VISTA. We may also be able to finally probe bright enough to see contributions by the $z \simeq 7$ AGN LF, settling the debate about where the overlap between the AGN LF faint end and galaxy LF bright end begins.

Although *JWST* is finding many 'bright' candidates at ultra-high redshifts (e.g. Naidu et al., 2022), it may struggle to probe the very bright end ($M_{\rm UV} < -23$) of the UV LF during the Epoch of Reionisation since the area it can survey is more limited than ground-based observations. In Fig. 2.7 we plot the results of Harikane et al. (2023a) who measure the $z \simeq 9$ UV LF in ~ 90 square arcminutes of NIRCam imaging. The smaller area compared to this work means they are unable probe brighter than $M_{\rm UV} \simeq -22$. Wider area studies such as COSMOS-Web

(Casey et al., 2023) will be able to cover up to 0.5 deg^2, but this is still significantly smaller than what can be achieved from ground-based observatories and with *Euclid* and *Roman*. It is clear that within the next decade, the combination of *JWST* with wide-area space observatories will provide a revolution in the measurement of the $z > 6$ LF over a broad magnitude range.

2.7 Conclusions

We have conducted a wide-area search for $z \simeq 7$ Lyman break galaxies using deep near-infrared photometry from the VIDEO survey combined with deep optical data and *Spitzer*/IRAC photometry over an area of 8.2 deg^2. Candidates were selected in a $Y + J$ stack reaching 5σ depths of $m_{\rm AB} = 25.3$ in XMM-LSS and 8σ depths of $m_{\rm AB} = 24.8$ in ECDF-S, with non-detections required in bands bluewards of the Lyman break. We show that the inclusion of NIR data from VISTA and *Spitzer* enables a robust removal of low-redshift galaxies and Galactic brown dwarf contaminants.

We found 28 galaxy candidates with a mean redshift $\bar{z} = 6.74$ and UV absolute magnitudes in the range $-23.5 \leq M_{\rm UV} \leq -21.6$. We recovered two spectroscopically confirmed sources from the REBELS Survey (Bouwens et al., 2022a). The BAGPIPES SED fitting code was used to confirm the photometric redshifts and derive galaxy properties. We derived stellar masses of $9.1 \leq \log_{10}(M/M_{\odot}) \leq 10.9$ for objects with unconfused *Spitzer*/IRAC photometry, suggesting that these galaxies are some of the most massive at this epoch.

We measure the UV luminosity function at $z \simeq 7$ using our candidates and compare to the current widest area searches: Harikane et al. (2022b) who use optical-only data in an area of 20.2 deg^2, and Bowler et al. (2017) who use optical and near-infrared data in an area of 1.65 deg^2. Our results agree with the DPL fit of Bowler et al. (2017) to brighter magnitudes, however they lie significantly below the results of Harikane et al. (2022b). Through SED fitting of the Harikane et al. (2022b) candidates, utilizing the VIDEO $YJHK_s$ photometry and *Spitzer*/IRAC, we find that the brightest galaxy candidates identified by Harikane et al. (2022b) are likely to be brown dwarfs. Our results suggest that using optical data alone

to select $z \simeq 7$ galaxies leads to an overestimate by a factor of 2 at $M_{\rm UV} \simeq -23$ and by a factor of 10 at $M_{\rm UV} < -24$ due to contamination.

Extrapolating findings from Adams et al. (2023b) predicts a negligible contribution of unobscured AGN at the magnitudes we probe. This is in tension with the conclusions of recent pure-parallel *Hubble* results at $z = 8$ (Rojas-Ruiz et al., 2020; Leethochawalit et al., 2023b), which we find to be in excess of our $z = 7$ LF by a factor of > 10. Our results provide a robust measure of the bright end of the $z \simeq 7$ UV LF, which does not evolve significantly from $z \simeq 8$. This suggests a lack of dust attenuation and/or mass quenching between these epochs. Upcoming wide-area space missions such as *Euclid* and *Roman* will provide much larger samples extracted from thousands of deg^2 of NIR imaging to depths comparable to VIDEO, allowing for determinations of the UV LF beyond $M_{\rm UV} < -24$ at $z > 6$, whilst also providing superior resolution to ground-based imaging, permitting the removal point-like brown dwarf contaminants.

I have cultivated a culture of fear.

—F. R. Donnan

3

Discovery of bright $z \simeq 7$ Lyman-break galaxies in UltraVISTA and *Euclid* COSMOS

Contents

3.1 Introduction

A central goal of astrophysics is to unveil the formation and evolution of the first galaxies in the Universe (Stark, 2016; Adamo et al., 2024). In particular, at high-redshift ($z > 5$), observations of rare, luminous galaxies at the bright end ($L > L^*$) of the rest-frame UV LF provide key insight into astrophysical effects such as feedback and dust build-up (e.g. Bowler et al., 2015; Finkelstein and Bagley, 2022; Nikopoulos and Dayal, 2024; Algera et al., 2025). As discussed in Section 1.6, degree-scale ground-based imaging has been central to discovering and characterising these rare, luminous LBGs. Near-infrared surveys such the Ultra Deep Survey (UDS) field of the UKIRT Infrared Deep Sky Survey (UKIDSS, Lawrence et al., 2007) and UltraVISTA (McCracken et al., 2012) enabled the means to discover rare $L > L^*$ LBG candidates at $z > 5$ (McLure et al., 2009; Bowler et al., 2012). Subsequent ground-based studies have confirmed a double-power law LF with little evolution in the bright end at $z \simeq 6 - 10$ (Bowler et al., 2014; Ono et al., 2018; Stefanon et al., 2019; Bowler et al., 2020; Harikane et al., 2022b; Kauffmann et al., 2022; Donnan et al., 2023a, and results from Chapter 2). *Hubble* has placed strong complementary constraints on the faint end ($L < L^*$, McLure et al., 2013; Finkelstein et al., 2015; Bouwens et al., 2021). However, both ground-based telescopes and *Hubble* can only probe out to $\lambda \simeq 2\mu$m, placing a barrier at $z \simeq 10$. The unparalleled NIR capabilities of *JWST* has substantially advanced the redshift frontier, revealing an abundance of luminous blue galaxies and a markedly slow evolution of the rest-UV LF over the extremely high redshift range of $z \simeq 10 - 14$ (e.g. Donnan et al., 2023a; McLeod et al., 2024; Adams et al., 2024; Chemerynska et al., 2024; Whitler et al., 2025; Harikane et al.,

2025). This has invoked scenarios such as increased star formation efficiency or Pop III stars (Harikane et al., 2023a), ejection of dust by radiation-driven outflows (Ferrara et al., 2023), and even tension with ΛCDM (Labbé et al., 2023b). The SFHs of some luminous $z \simeq 7$ sources can require significant star formation at $z > 9$ (e.g. Whitler et al., 2023). This, combined with the slow evolution of the LF, means it is natural to return to the most massive, luminous sources at $z \simeq 7$ in order to understand their connection to bright *JWST* galaxies at $z > 10$.

The study of $z \simeq 7$ sources hinges on the ability to robustly detect them and remove interloper sources. A major issue facing ground-based studies at $z \simeq 7$ has been contamination by cool Galactic M-, L-, and T-type brown dwarfs (BDs, e.g. Stanway et al., 2008; Bowler et al., 2012; Wilkins et al., 2014). These sources have high number densities at the typical apparent magnitudes of $L > L^*$ LBGs, often matching or even exceeding the number of LBG candidates in most degree-scale extragalactic surveys (Ryan et al., 2011). The same molecular species responsible for making the Earth's atmosphere opaque at certain wavelengths in the NIR are also present in BD atmospheres, causing deep molecular absorption complexes at wavelengths impossible to probe from the ground. This means that in certain cases the NIR photometry of a BD can be confused with a flat rest-UV LBG continuum. Furthermore, while luminous $z \simeq 7$ LBGs are generally marginally resolved (Bowler et al., 2017), atmospheric seeing often prevents distinguishing BDs from LBGs based on their morphology.

As discussed in Section 1.6, the launch of *Euclid* signals the first time astronomers have had access to degree-scale, *space-based* NIR imaging. *Euclid* is a European Space Agency medium class mission (Euclid Collaboration et al., 2024a). Launched in July 2023 and equipped with a 1.2m primary mirror, its mission is to measure the nature of dark matter and dark energy via weak lensing and clustering. However, a major component of the mission is the legacy science possible with the telescope. *Euclid*'s Visible Camera (VIS, Euclid Collaboration et al., 2024b) instrument features a high resolution (0.16″) optical filter, I_E, equivalent to the ground-based riz filters. The Near-Infrared Spectrometer and Photometer (NISP, Euclid Collaboration et al.,

2024c) features three near-infrared filters, Y_E, J_E and H_E, which can critically probe NIR wavelengths inaccessible from the ground (see Fig. 3.1). The field of view of *Euclid* is $\sim 0.55\text{deg}^2$, and the main survey will eventually map out 14000 deg^2 of the extragalactic sky. The Early Release Observations (Cuillandre et al., 2024) have led to the identification of the first *Euclid*-selected $z > 6$ LBG candidates (Atek et al., 2024; Weaver et al., 2024), with the very deep I_E filter allowing for the removal of M-dwarfs and low-redshift galaxy interlopers by requiring a strong break in $I_E - Y_E$. However, due to the availability of only four relatively wide photometric filters, and the fact that the NISP images had a pixel scale of $0.3''$/pix (with resolution $0.36'' - 0.45''$) meant there were likely still high-levels of contamination by L- and T-type dwarfs.

Euclid will dedicate approximately 12% of its observing time to imaging the *Euclid* Deep Fields (EDFs), covering 53 deg^2 to depths of ~ 26 mag. The resulting imaging will represent a ~ 30 fold increase in area compared to previous NIR surveys reaching this depth (UltraVISTA, McCracken et al., 2012). The significantly wider area will lead to the discovery of thousands of $z \simeq 7$ galaxies brighter than $m_{\text{AB}} = 26$ (Bowler et al., 2017), allowing for definitive measurements of the bright end of the rest-frame UV LF. Until the *Euclid* Deep Survey is complete, early imaging from the *Euclid* Auxiliary Fields (EAFs), used for calibration, serves as an ideal testbed for selecting high-redshift galaxies with *Euclid*. In the COSMOS field, by combining NISP with complementary NIR photometry from VISTA, it may be possible to break the degeneracy between the colours of L- and T-type dwarfs and genuine high-redshift LBGs. The construction of pure $z \simeq 7$ samples is critical because there is still some tension between ground-based studies, which suggest a shallower decline in the bright-end akin to a DPL (Bowler et al., 2014; Bowler et al., 2017; Harikane et al., 2022b, and results from Chapter 2), and the widest-area *Hubble*-based study of Bouwens et al. (2021) who find a marked drop in the LF between $M_{\text{UV}} \simeq -21.5$ and $M_{\text{UV}} \simeq -22$, suggesting an exponential decline. The final data release (DR6) of the UltraVISTA survey provides the necessary depth to connect ground-based observations with space-based observations at the knee of

the LF, and its combination with *Euclid* imaging provides the means to construct clean samples of UltraVISTA-selected galaxies. Furthermore, with *Euclid*'s higher resolution we can resolve luminous ground-selected sources for the first time without the need for dedicated follow-up imaging from *Hubble* (Bowler et al., 2017; Stefanon et al., 2017). This could allow the removal of brown dwarfs as point sources and will unveil the morphologies of thousands of galaxies at $z > 6$.

This chapter is structured as follows: in Section 3.2, we describe the ground-based and space-based imaging used in this work, as well as the image preparation and photometric catalogue construction. Section 3.3 outlines the selection of our LBG candidates using SED fitting. For the SED fitting we conduct two separate selections with/without the additional *Euclid* photometry. We present each of our UltraVISTA-only and UltraVISTA+*Euclid* samples in Section 3.4, and we compute the $z = 7$ rest-UV LF in Section 3.5, comparing our results to results from *JWST* at $z > 7$. Then in Section 3.6 we discuss the improved SED constraints with *Euclid*, investigate *Euclid*'s ability to remove BDs as point sources, and highlight the unique capabilities of several overlapping filters to identify extreme Lyman-α emitters. Finally we conclude and summarise in Section 3.7.

3.2 Data and image processing

In this section we present the ground- and space-based data used in this work, and the steps taken to prepare the images for creating catalogues and conducting a high-redshift galaxy selection.

3.2.1 Ground-based imaging and *Spitzer*

We make use of extensive multi-wavelength imaging in the COSMOS field (Scoville et al., 2007). The UltraVISTA survey (McCracken et al., 2012) is an ultra-deep near-infrared survey covering 1.72 deg^2 at $\lambda \simeq 1 - 2.5\mu$m, vital for characterising the rest-UV continuum of high-redshift LBGs. Data Release 6, the final data release, provides uniform depths across all of the $YJHK_s$ bands, bringing in the 'deep' stripes up to the same depth as the 'ultradeep' stripes. The footprint of

the UltraVISTA survey is shown in Fig. 3.1. Deep optical data are available on the UltraVISTA footprint from the Subaru Strategic Program (HSC-SSP) Hyper Suprime-Cam DR3 (Aihara et al., 2022) in the $GRIZy$ bands at $\lambda \simeq 0.4 - 1\mu$m. This deep optical imaging is critical for ensuring non-detections bluewards of the Lyman break, where flux bluewards of 1216Å (rest-frame) is absorbed by neutral hydrogen in the intergalactic medium. There are also two narrowband filters, NB0816 and NB0921, powerful for reducing errors on photometric redshifts. The HSC and VISTA filter response curves are shown in Fig. 3.1. Additionally, infrared data from *Spitzer*/IRAC is available as part of the Cosmic Dawn Survey (CDS, Euclid Collaboration et al., 2022b) in the 3.6μm and 4.5μm filters. These lie beyond the Balmer break of $z \simeq 7$ galaxies, providing a measurement of their rest-frame optical flux. The depths of the imaging (measured in Section 3.2.5) in the above filters are presented in Table 3.1.

3.2.2 *Euclid*

We make use of performance verification (PV) imaging, taken for calibration of the instrument, in the COSMOS field over three months. The imaging used in this work is the result of 184 calibrated frames taken in COSMOS, which are the individual exposures in a single observation. Each observation comprises of 6 exposures for VIS (4 long exposures separated on the sky by the dither pattern and 2 short exposures on two of the dithers) and 4 exposures for NISP. The calibration involves computing the astrometric solution using *Gaia* DR3 (Gaia Collaboration et al., 2023), flat fielding, and photometric calibration. These calibrated frames are then coadded, background-subtracted, and split into mosaics with common astrometry and pixel scale ($17' \times 17'$ for the EDFs and EAFs with $0.1''\text{pix}^{-1}$). After just a few months of operations, the *Euclid* imaging in COSMOS reaches deeper limiting magnitudes than the UltraVISTA survey, which was conducted over nearly 15 years. The *Euclid* imaging covers 0.65 deg^2 of the UltraVISTA footprint, as shown in Fig. 3.1. The NISP Y_E, J_E, H_E bands are $0.2 - 0.6$ mag deeper than their VISTA counterparts, both when using the same $1.8''$ diameter aperture on the PSF-homogenised *Euclid*

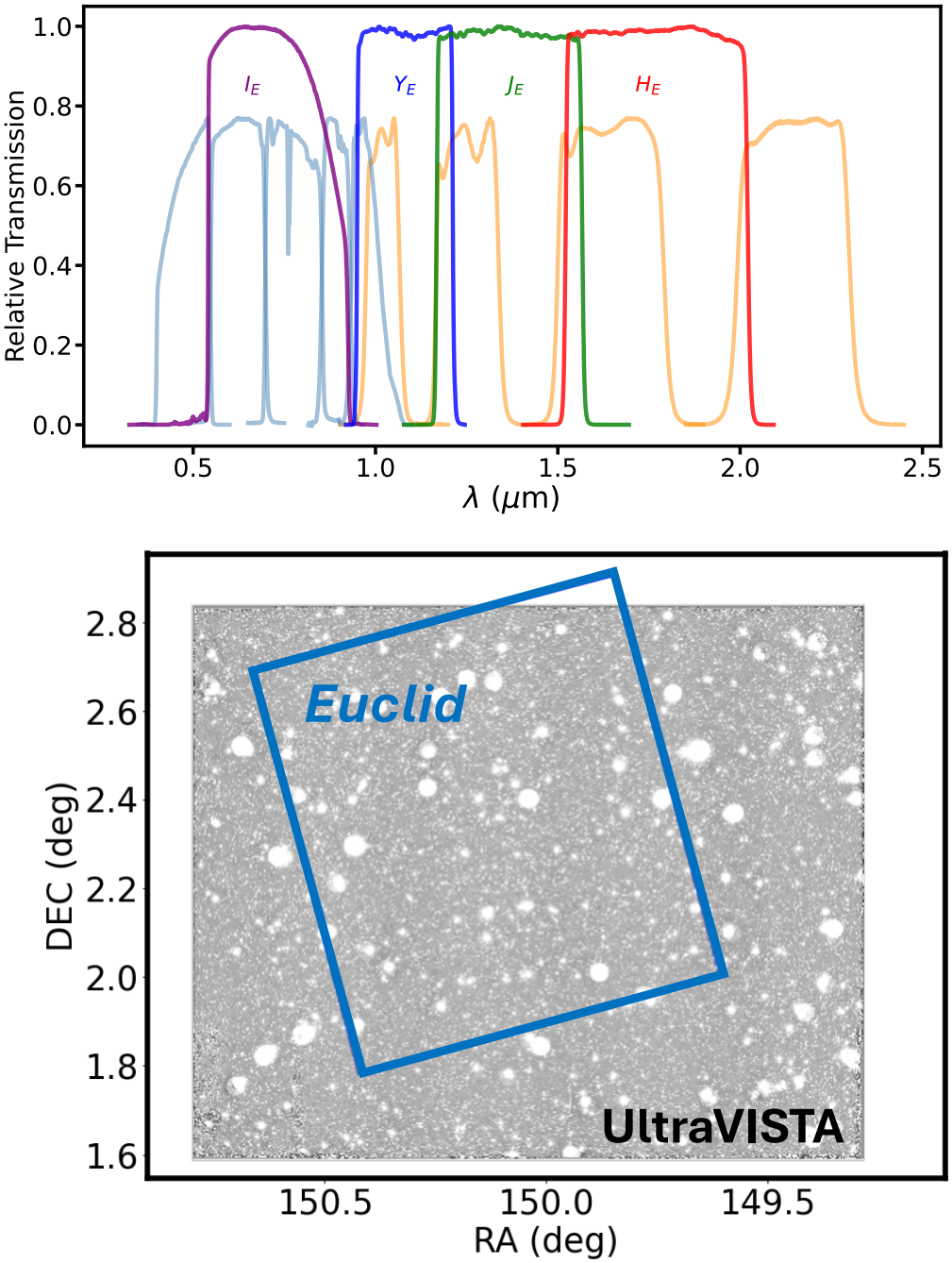

Figure 3.1: Top: normalised filter response curves for bands used in this work. The light blue bands are the HSC $GRIZy$ filters, and the yellow bands are the VISTA $YJHK_s$ filters. The *Euclid* filters are superimposed and labelled. Note that the *Euclid* NIR filters cover the gaps between the VISTA filters. These wavelengths are inaccessible from the ground due to the atmospheric absorption. **Bottom:** the COSMOS UltraVISTA (McCracken et al., 2012) footprint with the *Euclid* COSMOS PV footprint overlaid. Optical imaging from HSC-SSP DR3 (Aihara et al., 2022) covers the full UltraVISTA area.

images (see Sections 3.2.4 and 3.2.5) and in smaller 1.2″diameter apertures on the original higher-resolution *Euclid* images. Additionally, the high-resolution I_E filter from the VIS instrument, which covers the same wavelengths as HSC–R, I, Z, is $0.3 - 1.0$ mag deeper than these filters. We show the *Euclid* filter response curves in Fig. 3.1. The depths of the *Euclid* imaging are presented in Table 3.1.

3.2.3 Image preparation

We follow a similar procedure as in Chapter 2. The UltraVISTA data is matched to the *Gaia* EDR3 reference catalogue (Gaia Collaboration et al., 2021). We use SCAMP (Bertin, 2006) and SWARP (Bertin et al., 2002) to shift all other auxiliary data into the same frame as the UltraVISTA imaging. The *Euclid* 'MER' (merged) mosaics imaging over the UltraVISTA field consists of 23 of the $17' \times 17'$ tiles. SWARP was also used to resample the *Euclid* images to match the pixel scale of UltraVISTA, $0.15''\text{pix}^{-1}$, and to produce one large mosaic for each *Euclid* image matching the plate scale of UltraVISTA.

3.2.4 PSF homogenisation

In the ground-based seeing-dominated imaging, sources tend to be close to unresolved (PSF FWHM $\simeq 0.8$ arcsec). The differences in PSF between VISTA and *Euclid* and the possibility of sources being both resolved and unresolved depending on the instrument means that the fraction of flux falling within a fixed-size aperture depends strongly on the filter. We therefore homogenise all of the space-based imaging to match the VISTA Y-band PSF, chosen since it is the main detection band for $z \simeq 7$ LBGs and because it has the largest PSF of VISTA. Whilst this homogenisation may result in less sensitive *Euclid* images, we note that we are first selecting sources in the shallower VISTA imaging (see Section 3.3.1), meaning the homogenised *Euclid* images are still more sensitive than VISTA. We use PSFEX (Bertin, 2011) to construct an empirical PSF model. Stars are selected from the magnitude-FWHM diagram, with FWHMs determined by SEXTRACTOR (Bertin and Arnouts, 1996). We use PYPHER (Boucaud et al., 2016) to find the convolution

kernel between the *Euclid* PSFs and the VISTA Y-band PSF. The space-based images are convolved with this kernel, leading to PSF-homogenised images that are pixel-matched to UltraVISTA. We rerun PSFEx (Bertin, 2011) on the homogenised images using the same stars selected in the original *Euclid* images. The new PSF model is used to determine the enclosed flux within a 1.8″ diameter circular aperture, assuming a point source.

Prior to PSF homogenisation, the FWHMs of the Euclid PSFs are 0.20″ in I_E, 0.49″ in Y_E, 0.51″ in J_E and 0.53″ in H_E, as measured with PSFEx. These values are in agreement with PSF FWHMs measured by the *Euclid* pipeline. After homogenisation of the *Euclid* images, all PSF FWHMs match that of VISTA Y, 0.85″. We note that all *Euclid* postage stamp cutouts presented in this work are from the original images, prior to PSF homogenisation. We then check the PSF-homogenised *Euclid* photometry to ensure it is consistent with UltraVISTA. This is done by taking the stars selected in Section 3.2.4 and imposing the cut $|Y - J| < 0.05 \wedge |J - H| < 0.05$ to obtain stars with flat colours across the VISTA YJH bands. We then check the colour of each *Euclid* filter and its nearest VISTA counterpart. This check is shown in Fig. 3.2. Just as with the VISTA photometry, a minimum error of 5 per cent is placed on the *Euclid* photometry. There are no large colour differences between *Euclid* and VISTA filters for stars with flat NIR colours, indicating that there are no significant zeropoint or flux calibration issues in the *Euclid* COSMOS imaging.

3.2.5 Depths

We computed 5σ depths across the images by placing 1.8″ diameter circular apertures on empty regions of the image (determined using the SExtractor segmentation map). For the *Spitzer*/IRAC images we use a 2.8″ diameter circular aperture to account for the broader PSF. Local depth maps are determined by taking the closest 300 apertures to each point and measuring the median absolute deviation of the aperture fluxes. The depths reported in Table 3.1 are the mode of the

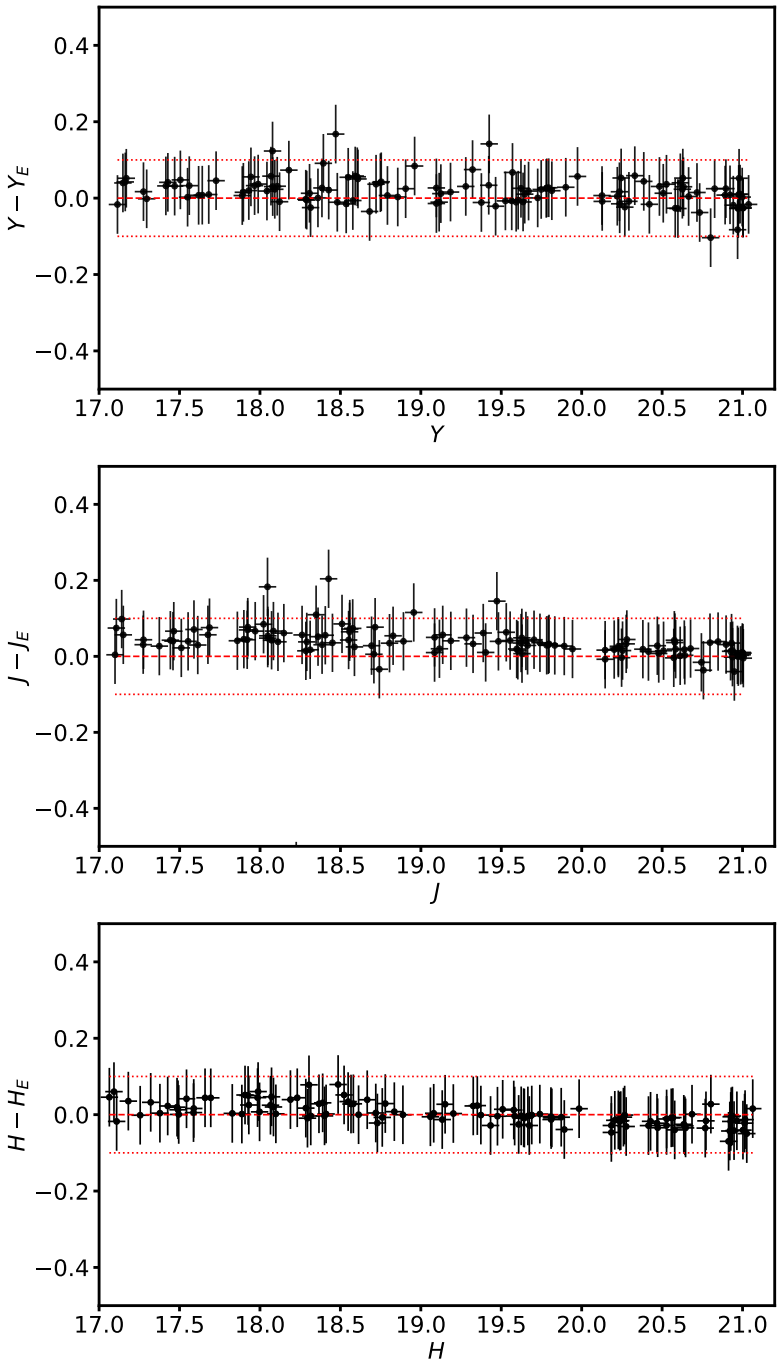

Figure 3.2: The difference in magnitude between VISTA Y and *Euclid* Y_E (top panel), VISTA J and *Euclid* J_E (middle panel), and VISTA H and *Euclid* H_E (bottom panel) and for bright stars with flat colours in VISTA, selected as $|Y - J| < 0.05 \wedge |J - H| < 0.05$. The red dashed line indicates no colour difference, and the red dotted lines indicate a difference of 0.1 mag. A minimum error of 5 per cent is imposed on the photometry.

Table 3.1: The 5σ limiting magnitudes for each band used in this work in the COSMOS field. The local depths were measured by placing 1.8 arcsec diameter circular apertures on empty regions of the images. The depth quoted here is the mode of these local depths. Depths for *Euclid* were measured on images pixel-matched and PSF-homogenised to the VISTA Y-band. IRAC depths were measured in 2.8 arcsec diameter circular apertures on the original resolution image to account for the poorer resolution.

Filter	Depth	Instrument
G	27.8	HSC
R	27.4	HSC
I	27.2	HSC
NB0816	26.2	HSC
Z	26.7	HSC
NB0921	26.0	HSC
y	26.0	HSC
Y	26.2	VISTA
J	26.0	VISTA
H	25.7	VISTA
K	25.3	VISTA
I_E	27.7	*Euclid*
Y_E	26.4	*Euclid*
J_E	26.4	*Euclid*
H_E	26.3	*Euclid*
3.6	25.2	*Spitzer*/IRAC
4.5	25.2	*Spitzer*/IRAC

local depths. The depths of the PSF homogenised *Euclid* images match the depths of the original image.

3.2.6 Catalogues

We run SExtractor in dual image mode on a VISTA $Y + J$ stacked image, using the same parameters as in Chapter 2. Photometry was performed in a 1.8 arcsec diameter circular aperture, enclosing 70-80 per cent of the total flux. This balances between high signal-to-noise whilst preventing the need for a large aperture correction. We use 2.8 arcsec diameter circular apertures for *Spitzer*/IRAC to account for its broader PSF. The raw aperture flux measurements must be corrected to account for light falling outside of the aperture in order to obtain a measure of the total flux. As discussed in Section 3.2.4, we use PSFEx to determine a PSF model with stars selected from the FWHM vs MAG_AUTO diagram. This empirical model

is used to measure the flux enclosed in a 1.8 arcsec diameter aperture, providing the PSF correction. A minimum error of 5 per cent is placed on photometry in all bands, except for *Spitzer*/IRAC where a minimum error of 20 per cent is imposed to account for contamination by neighbouring sources due to the broader PSF. When creating the catalogues, we also mask regions of low signal-to-noise and bright stars in the UltraVISTA images. This is accounted for a final area of 1.72 deg^2.

3.3 Candidate selection

In this section we outline the methods used to select the $z \simeq 7$ candidates. We conduct two different selections:

1. **The UltraVISTA-only selection**: we run the SED fitting steps with the HSC+VISTA+*Spitzer*/IRAC photometry, *without Euclid*.

2. **The UltraVISTA+*Euclid* selection**: we add in the *Euclid* photometry for the SED fitting and visual selection steps.

We stress that the sample is still UltraVISTA-selected, since sources are first selected based on their VISTA photometry (see Section 3.3.1). By keeping the selection based on ground-based imaging, we avoid the introduction of artefacts from *Euclid*, such as persistence (see Weaver et al., 2024). Additionally, selecting from the shallower VISTA imaging usually ensures a detection in the deeper *Euclid* imaging. The *Euclid* photometry is therefore *providing additional information* for the SED fitting of an UltraVISTA-selected sample. In both selections, ancillary HSC and *Spitzer* data were also used as required.

In the following sections, we outline the steps for the UltraVISTA-only sample. Then at the end, in Section 3.3.5, we present the UltraVISTA+*Euclid* SED fitting, highlighting the differences in the selection steps from the UltraVISTA-only sample. The selection steps and number of sources removed at each stage for both selections are summarised in Table 3.2.

3.3.1 Initial selection

Objects are first selected by requiring that they are sufficiently bright in the detection filters. We impose a 5σ detection threshold in $Y + J$, which removes roughly half of the sources in the catalogue (see Table 3.2). We then require non-detections ($< 2\sigma$ significance) in the HSC-G, R and I bands. No condition is imposed on HSC-Z, since the Lyman-break can enter this filter towards the lower end of the redshift range $z \in [6.5, 7.5]$. These non-detection conditions reduce the sample to 4849 objects. We again stress that this first selection is for a base UltraVISTA sample, without using *Euclid* data.

3.3.2 SED fitting

We use all ground-based filters available to conduct an SED fitting analysis in order to identify LBG candidates at $z \simeq 7$. SED fitting is, in general, more complete than a colour-colour selection (Adams et al., 2020), although can introduce a more complex selection function. We use the LePhare SED fitting code (Arnouts et al., 1999; Ilbert et al., 2006), which minimises χ^2 to find the best-fitting photometric redshifts and SEDs. Following Chapter 2, we use Bruzual and Charlot (2003) stellar population models with metallicities of $Z = [0.2, 0.4, 1.0]Z_{\odot}$. The star formation histories used are constant, instantaneous bursts, and exponentially declining with time-scales ranging from $\tau = 0.05 - 10$ Gyr. Uniform priors are placed on the following parameters. The redshift was allowed to vary between $z = 0 - 9$. Stellar population ages are allowed to vary between 10 Myr and 13.8 Gyr, limited by the age of the Universe at a given redshift, we use the Calzetti et al. (2000) attenuation law, allowing $A_V = 0.0 - 4.0$ mag, a Chabrier (2003) initial mass function is assumed, and IGM absorption is applied according to Madau (1995). We initially only use HSC+VISTA to determine photometric redshifts, excluding *Spitzer*/IRAC due to the large errors on photometry and high rates of confusion. It is used later in Section 3.3.4, in cases where there is no confusion, to rule out low-redshift interlopers.

Lyman-α emission can provide additional flux to the broad-band photometry, acting to increase the photometric redshifts of objects by up to $\Delta z \sim 0.5$ (Bowler

Table 3.2: Number of sources remaining in our catalogues after each selection step, beginning from the initial VISTA $Y + J$-selected catalogue. The first column shows the selection step. The second column shows the number of objects remaining. For the SED fitting steps (and the visual selection), we conduct two different selections: the **UltraVISTA-only** selection, where *Euclid* photometry *is not* included, and the **UltraVISTA+*Euclid*** selection, where *Euclid* photometry *is* included. In both selections, ancillary HSC and *Spitzer* data is also used as required. For the UltraVISTA+*Euclid* selection, we restrict the catalogue to the 0.65 deg^2 *Euclid* footprint. The high-redshift ($z > 6$) cut is defined as the best-fitting SED solution having its photometric redshift $z > 6$, $\chi^2 < 11.3$ (UltraVISTA-only) or 17.5 (UltraVISTA+*Euclid*), and $\Delta\chi^2 > 4$ between the low- and high-redshift solutions.

Selection step	Objects remaining	
Initial catalogue	1051995	
5σ $Y + J$ VISTA cut	706607	
$< 2\sigma$ in HSC-G	32165	
$< 2\sigma$ in HSC-R	13212	
$< 2\sigma$ in HSC-I	4849	
SED fitting step	UltraVISTA-only	UltraVISTA+*Euclid*
Overlap with *Euclid*	N/A	1850
Initial $z > 6$ cut	1872	403
Visual selection	751	341
Low-z galaxies: $\chi^2_{\rm low-z} < \chi^2_{\rm high-z}$	720	334
Brown dwarfs: $\chi^2_{\rm BD} < \chi^2_{\rm high-z}$	658	316
$6.5 \leq z_{\rm phot} \leq 7.5$, with Ly$\alpha$	291	141

et al., 2014). To account for this, we also add Lyman-α emission lines to the Bruzual and Charlot (2003) templates with equivalent widths $0 \leq \mathrm{EW}_0 \leq 240$ Å by measuring the continuum level between $\lambda = 1250 - 1300$ Å.

Based on the best-fit templates, candidates are first required to have their photometric redshift $z > 6$. The fits then had to be sufficiently good. Given the 5 degrees of freedom in the SED fitting, a 2σ significance threshold corresponds to $\chi^2 < 11.3$. Additionally, we require that the high-redshift solution is preferred to the low-redshift solution with 2σ significance, corresponding to $\Delta\chi^2 > 4$ between the two solutions.

3.3.3 Visual inspection

We carry out a visual selection (similar to Chapter 2) of the remaining objects to remove artefacts. These artfacts are typically diffraction spikes and cross-talk in the UltraVISTA images. The latter of these artefacts is caused during the readout from

the Vista InfraRed CAMera (VIRCAM) instrument, producing ghost images at regular pixel intervals from bright stars. We use a catalogue of bright stars selected from the UltraVISTA J-band using SExtractor to flag sources that lie a multiple of 128 pixels from a bright star. The crosstalk artefacts usually appear more diffuse and extended compared to real sources, and the visual presence in either HSC-Z or *Spitzer*/IRAC, which do not suffer from cross-talk, is a clear signpost for a real object. We also create an optical stack from HSC-G, R and I to check for low-level flux indicative of a low-redshift galaxy. We also smooth the optical stack with a Gaussian filter with $\sigma = 2$ pixels, which helps in searching for low-level flux. Single-band detections are also removed since they do not present robust candidates.

3.3.4 Removing interlopers

There are two primary classes of low-redshift interloper objects that act to contaminate $z \simeq 7$ LBG samples - dusty low-redshift galaxies and brown dwarfs.

Dusty galaxies at $z \sim 1-2$ can have Balmer breaks that can be confused as Lyman breaks. However, these galaxies do tend to have redder continuum slopes than $z \simeq 7$ sources, and are additionally usually very bright in *Spitzer*/IRAC (see e.g. Rodighiero et al., 2010). If the SED fitting prefers a low-redshift solution to the $z > 6$ solution when the *Spitzer*/IRAC imaging is included and unconfused, the object is removed.

Brown dwarfs of spectral type M, L and T have SEDs featuring very little blue optical flux and heavy molecular absorption complexes (see e.g. Burgasser et al., 2024; Luhman et al., 2024, for recent *JWST* spectroscopic observations). These sources present a pressing challenge for ground-based searches since the peaks of the BD SEDs usually coincide with the VISTA $YJHK_s$ filters, mimicking a flat NIR colour that can be confused with a blue $z \simeq 7$ rest-UV continuum. This occurs because the molecular species responsible for the absorption complexes (e.g. CH_4, H_2O) are the same species responsible for making Earth's atmosphere opaque at certain wavelength ranges in the NIR (e.g. Bailey et al., 2007). We use BD templates taken from the SpeX prism library (Burgasser, 2014) for the SED fitting.

We exclude the HSC-G and HSC-R bands from this fitting since the templates do not contain any information at these wavelengths. We remove sources with $\chi^2_{\rm BD} < \chi^2_{\rm high-z}$, i.e. the brown dwarf fit is preferred to the high-redshift solution.

3.3.5 Redoing the SED fitting with *Euclid*

We then rerun the SED fitting by combining *Euclid* with VISTA on the remaining objects after the initial photometric selection (Section 3.3.1). When the 4849 objects from this step are constrained to within the 0.65 deg^2 *Euclid* footprint, there are 1850 remaining. The additional four filters changes the χ^2 cut we impose for the initial high-redshift selection in Section 3.3.2, increasing this to $\chi^2 < 17.5$. This initial high-redshift cut with *Euclid* photometry removes many more objects than the same step without *Euclid* photometry. This is because VISTA artefacts have non-detections in *Euclid*, leading to poor SED fits. Following on from this, the *Euclid* imaging is also extremely powerful for the visual check – existence of a source in both *Euclid* and VISTA immediately confirms it as real, and not an artefact. Such a technique may also be used in reverse for future studies that use VISTA+*Euclid* imaging – selections based on *Euclid* can use VISTA to rule out common artefacts such as ghosts and persistence (seen e.g. in Weaver et al., 2024). The results of the selection steps after incorporating *Euclid* photometry for the SED fitting and visual selection are also shown in Table 3.2.

3.3.6 Expected number of brown dwarfs

Using the model from Bowler et al. (2015) (provided by Rebecca Bowler) of a single exponential disc with a scale height of 300 pc, we expect that there will be $\simeq$ 800 BDs in the full UltraVISTA field. For the UltraVISTA-only selection, the BD removal step removes 62 objects, which is fewer than expected. However, prior to the initial high-redshift cut, of the 4849 objects there are 1372 objects with a best-fitting brown dwarf SED. The increased number is likely caused by upscattering of brown dwarfs into the selection, some faint galaxies being misidentified as brown dwarfs, and crosstalk artefacts which had not yet been removed in a visual selection.

Now restricting to the *Euclid* footprint for the UltraVISTA+*Euclid* selection, we expect $\simeq 250$ BDs. The BD removal step cuts only 18 objects. However, the remaining brown dwarfs are removed prior to the initial $z > 6$ cut, where 205 objects have a best-fitting brown dwarf SED. This indicates that brown dwarfs are well-characterised with the *Euclid* photometry, meaning they do not pass the initial $z > 6$ cut due to poorer high-redshift SED solutions.

This is much closer to the expected number. The *Euclid* photometry better probes the deep molecular absorption features than VISTA alone (see Section 3.6.1), and *Euclid* non-detections immediately rule out VISTA crosstalk artefacts, explaining the elevated number of objects with best-fit brown dwarf SEDs in the UltraVISTA-only selection (relative to the prediction).

In Chapter 2, a large fraction (80 per cent) of sources were identified as possible BDs, since sources sampled the magnitude range $24.1 \leq J \leq 25.2$, where the number density of BDs peaks (Ryan et al., 2011). Chapter 2 used the VISTA Deep Extragalactic Observations survey (VIDEO, Jarvis et al., 2013), covering 8.2 deg^2 in the ECDF-S and XMM-LSS fields and reaching 5σ depths in Y of 25.2. UltraVISTA is a magnitude deeper than VIDEO, and the sample in this chapter probes down to $J \simeq 26$ where the BD number density declines. We note that the number of sources best-fit as BDs that make it through the initial high redshift cut (62 for UltraVISTA only, 18 for UltraVISTA+*Euclid*) is smaller than the final sample of LBGs (see Table 3.2), showing that BD contamination is not as severe as in Chapter 2, but still a significant issue.

3.4 Candidate galaxies

The final UltraVISTA-only sample consists of 291 candidates selected from 1.72 deg^2 of UltraVISTA imaging. We show the SED fitting of an example galaxy, ID 381772, in Fig. 3.3. We measure the absolute rest-UV magnitude, $M_{\rm UV}$, by placing a top-hat filter on the best-fit SED at 1500Å, with width 100Å. The sample spans a range of over two magnitudes, $-22.5 \leq M_{\rm UV} \leq -20.2$. Their distribution in $M_{\rm UV}$ and photometric redshift $z_{\rm phot}$ is shown in Figure 3.4. Our sample overlaps in $M_{\rm UV}$ with

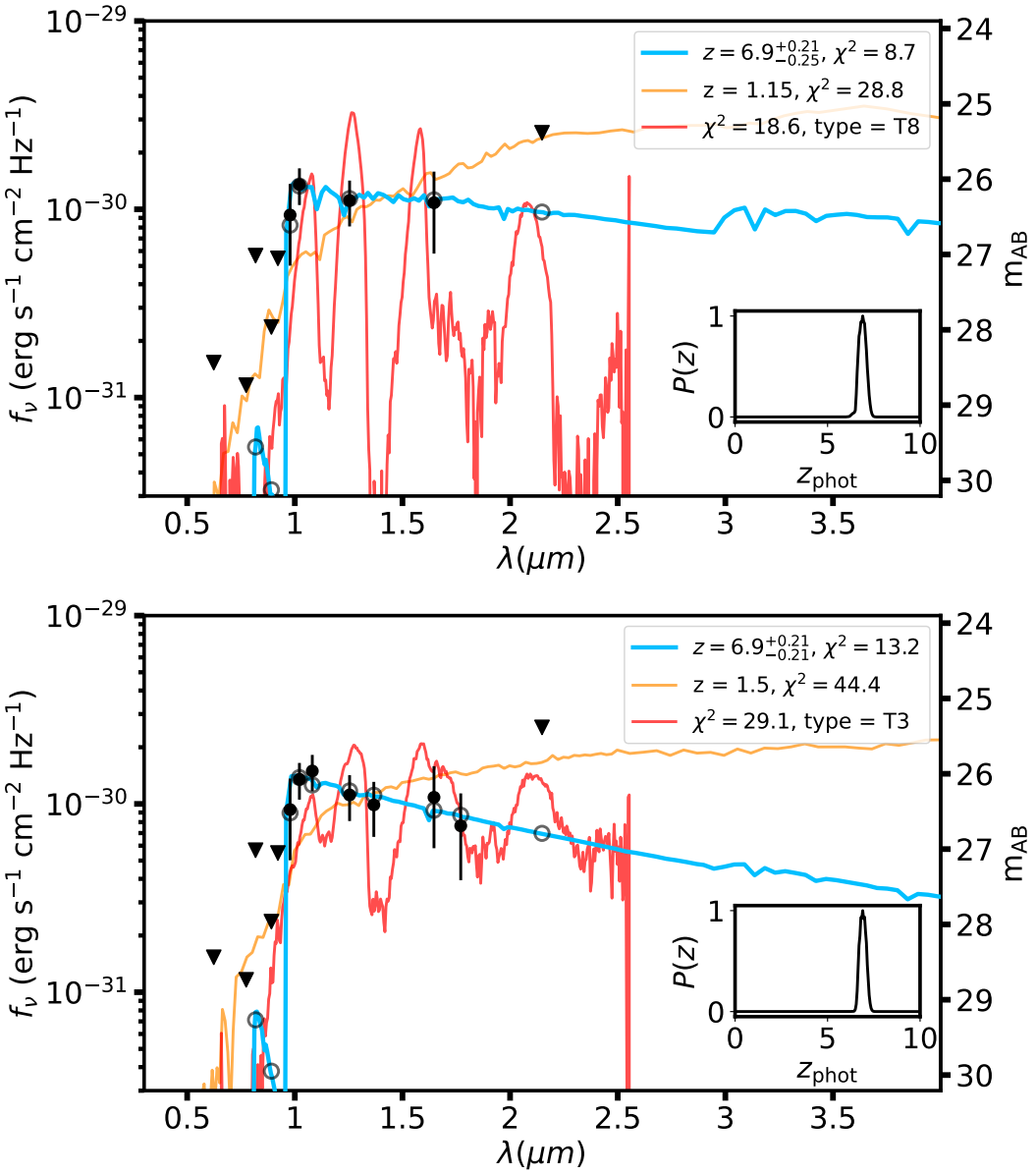

Figure 3.3: SED fitting of a candidate LBG, ID 381772, at $z = 6.90$. **Top:** The SED fitting without *Euclid* data, as part of the UltraVISTA-only selection. **Bottom:** The SED fitting including *Euclid* data, as part of the UltraVISTA+*Euclid* selection. The black points show the photometry. The blue curve shows the best high-redshift solution, and the grey open circles are its expected model photometry. The orange curve shows the best dusty low-redshift solution, and the red curve shows the best BD solution. The legend in the top right shows the redshift and χ^2 of the galaxy solutions, and the χ^2 and spectral type of the BD solution. The inset panel shows the redshift probability distribution for this source. The inclusion of *Euclid* data excludes the BD template.

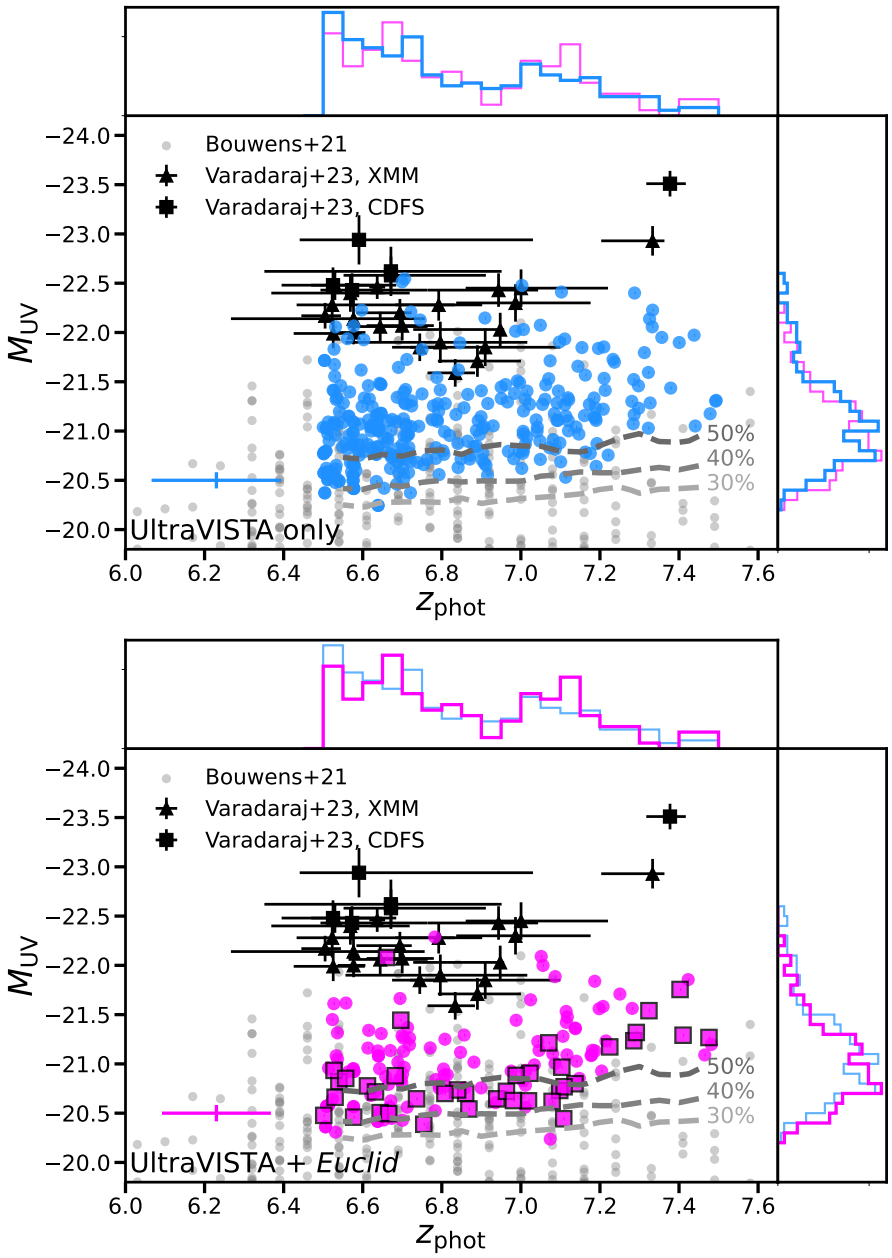

Figure 3.4: The $z \simeq 7$ LBG sample from this work plotted in photometric redshift $z_{\rm phot}$ and absolute rest-UV magnitude $M_{\rm UV}$ space. **Top:** the UltraVISTA-only sample (blue), where *Euclid* photometry has *not* been included during the SED fitting. **Bottom:** the UltraVISTA+*Euclid* sample (magenta), where *Euclid* photometry *has* been included during the SED fitting. The magenta squares with a black outline indicate galaxies which are not recovered in the UltraVISTA-only sample, and are thus unique to the UltraVISTA+*Euclid* sample. In both panels, we also show the candidates from Chapter 2 in the XMM-LSS and ECDF-S fields, and the *Hubble*-selected candidates from Bouwens et al. (2021). The dashed gray lines show the 30%, 40% and 50% completeness limits, as derived from the injection-recovery simulation (see Section 3.5.1). We also show the marginalised distributions in $z_{\rm phot}$ and $M_{\rm UV}$ as normalised histograms, and also overplot the opposing sample distribution as the thinner, fainter line for comparison. The mean errors are shown on the bottom left.

the sample presented in Chapter 2, where we used 8.2 deg^2 of shallower ($m_{\rm AB} \sim 25$) imaging to select ultra-luminous $z \simeq 7$ candidates. Of course, by nature of the smaller area of UltraVISTA, our sample does not probe as bright as we could in the wider XMM-LSS and ECDF-S fields, but we are able to find a much fainter sample since UltraVISTA is one magnitude deeper than the VIDEO survey. Comparing to the previous search for $z \simeq 7$ LBGs in UltraVISTA by Bowler et al. (2014) on DR2 imaging, we find an additional 257 galaxies by means of the increase in depth by a magnitude, combined with an effective doubling in survey area since the 'deep' stripes have been brought up to the same depth as the 'ultradeep' stripes. UltraVISTA DR6 is also deep enough to reach magnitudes comparable to the bright end of the rest-UV LF presented in Bouwens et al. (2021) (see Fig. 3.4), the widest-area *Hubble* search for LBGs at $z \simeq 7$, bridging the gap between space-based and ground-based observations of the rest-UV LF at this redshift for the first time.

When we include *Euclid* imaging over the 0.65 deg^2 which overlaps with UltraVISTA, for the UltraVISTA+*Euclid* selection, our sample consists of 141 galaxies. Of these, 103 are also found in the UltraVISTA-only sample. The remaining 38 galaxies are unique to the UltraVISTA+*Euclid* sample. In Fig. 3.3, we also show the SED fitting of ID 381772 when the *Euclid* photometry is included. We show the distribution of the UltraVISTA+*Euclid* sample in Fig. 3.4, including the 38 galaxies that are not selected in the UltraVISTA-only sample. These 38 galaxies have $M_{\rm UV}$ largely corresponding to the 40-50% completeness range, showing that the deeper *Euclid* photometry recovers fainter galaxies in the sample. Additionally, of these 38 galaxies, 7 lie at $z > 7.2$ with brighter magnitudes, $M_{\rm UV} < -21$, where VISTA photometry is more susceptible to contamination by brown dwarfs and cross-talk artefacts. These 38 galaxies represent all cases where galaxies are found exclusively in the UltraVISTA+*Euclid* sample. However, there is also the converse scenario to consider, when galaxies that appear in the UltraVISTA-only sample are absent from the UltraVISTA+*Euclid* sample. These sources were initially identified as high-redshift candidates based on UltraVISTA NIR data alone, but the addition

of *Euclid* photometry either prefers a low-redshift interloper SED or reveals them to be an artefact such as crosstalk. There are 53 such sources.

We present the SED fitting and postage stamp images of the brightest 30 galaxies in the UltraVISTA+*Euclid* sample in Appendix D. A visual inspection of the full UltraVISTA+*Euclid* sample gives a clumpy/irregular fraction of 0.177. This is consistent with the *JWST* study of Kartaltepe et al. (2023), who find an irregular fraction of 0.2 in their $z > 6$ bin.

3.5 The rest-frame UV LF with UltraVISTA and *Euclid*

In this section we present the calculation of the rest-UV LF at $z \simeq 7$ using *both* the UltraVISTA-only and UltraVISTA+*Euclid* samples. We then fit a DPL and Schechter function using the UltraVISTA+*Euclid* sample, before comparing our results to *JWST* determinations of the rest-UV LF at $z > 7$.

3.5.1 Completeness

Incompleteness of the final galaxy sample must be accounted for before computing the LF. Genuine high-redshift galaxies can become blended with other objects, and near the limiting magnitude of the detection images, photometric scattering can cause objects to drop in/out of the selection. We therefore run injection-recovery simulations to derive corrections for these effects in bins of $M_{\rm UV}$ and $z_{\rm phot}$. We first populate a redshift–absolute-magnitude grid with steps of $\Delta z = 0.05$ and $\Delta M = 0.1$, assuming the DPL luminosity function derived in Harikane et al. (2025). The absolute magnitude grid extends down to $M_{\rm UV} = -19$, well below the limiting magnitude of UltraVISTA DR6, to account for the photometric up-scattering of faint sources. The grid consists of 10^6 sources. We then generate mock Y and J photometry. We draw rest-UV slopes $\beta_{\rm UV}$ (where $f_\lambda \propto \lambda^\beta$) from a Gaussian distribution centred on $\beta_{\rm UV} = -2$ with standard deviation $\sigma = 0.2$ (Bowler et al., 2014). We inject empirical PSF models (see Section 3.2.4) into the imaging, assuming sources are generally unresolved in ground-based imaging (see Bowler et al., 2014).

Table 3.3: The rest-UV LF values at $z = 7$. The first column shows the central absolute UV magnitude $M_{\rm UV}$ of the bin. We then show the number of galaxies $n_{\rm gal}$ and the LF value and error for two cases: firstly for the UltraVISTA-only sample, and secondly for the UltraVISTA+*Euclid* sample when *Euclid* photometry is included in the SED fitting. The brightest two bins centred at $M_{\rm UV} = -22.6$ and -22.2 have a width of $\Delta M_{\rm UV} = 0.4$, and the remaining bins have width $\Delta M_{\rm UV} = 0.2$.

	UltraVISTA-only		UltraVISTA+*Euclid*	
$M_{\rm UV}$ (mag)	$n_{\rm gal}$	ϕ (mag^{-1} Mpc^{-3})	$n_{\rm gal}$	ϕ (mag^{-1} Mpc^{-3})
-22.6	5	$1.31 \pm 0.44 \times 10^{-6}$	0	–
-22.2	12	$3.33 \pm 0.75 \times 10^{-6}$	3	$2.13 \pm 0.93 \times 10^{-6}$
-21.9	13	$7.34 \pm 1.56 \times 10^{-6}$	4	$6.03 \pm 2.21 \times 10^{-6}$
-21.7	11	$6.28 \pm 1.41 \times 10^{-6}$	6	$9.16 \pm 2.83 \times 10^{-6}$
-21.5	26	$1.57 \pm 0.25 \times 10^{-5}$	10	$1.59 \pm 0.40 \times 10^{-5}$
-21.3	43	$2.74 \pm 0.36 \times 10^{-5}$	19	$3.23 \pm 0.64 \times 10^{-5}$
-21.1	58	$4.13 \pm 0.50 \times 10^{-5}$	24	$4.24 \pm 0.78 \times 10^{-5}$
-20.9	47	$3.83 \pm 0.47 \times 10^{-5}$	28	$6.06 \pm 1.05 \times 10^{-5}$

We inject 10^3 sources at a time into the $Y + J$ image so as to not artificially boost the number density. We then run SExtractor in the same manner as in Section 3.2.6 and select sources using the same cuts. We show the 30, 40 and 50 per cent completeness limits in Fig. 3.4. The faintest sources in our sample correspond roughly to the 40 per cent contour, below which the completeness drops rapidly.

3.5.2 The rest-frame UV LF

We use the final sample of LBGs to determine the rest-UV LF at $z \simeq 7$ using the $1/V_{\rm max}$ method (Schmidt, 1968), just as in Chapter 2. $V_{\rm max}$ is the maximum volume a galaxy in our sample can occupy and still be included in our selection. The galaxy SEDs were redshifted in steps of $\Delta z = 0.01$ until they fell out of the 5σ detection threshold in $Y + J$, giving us its maximum redshift $z_{\rm max}$ at which it would still be detected in our selection. $V_{\rm max}$ is then the comoving volume between $z = 6.5$ and $z = z_{\rm max}$. The value of $z_{\rm max}$ cannot exceed $z = 7.5$, the maximum considered redshift. The LF in a given bin of absolute magnitude, $\Phi(M)$, in the redshift range $6.5 < z < 7.5$, is calculated using Equation 2.1 with Poissonian errors given by Equation 2.2. We also account for the effect of cosmic variance. Since

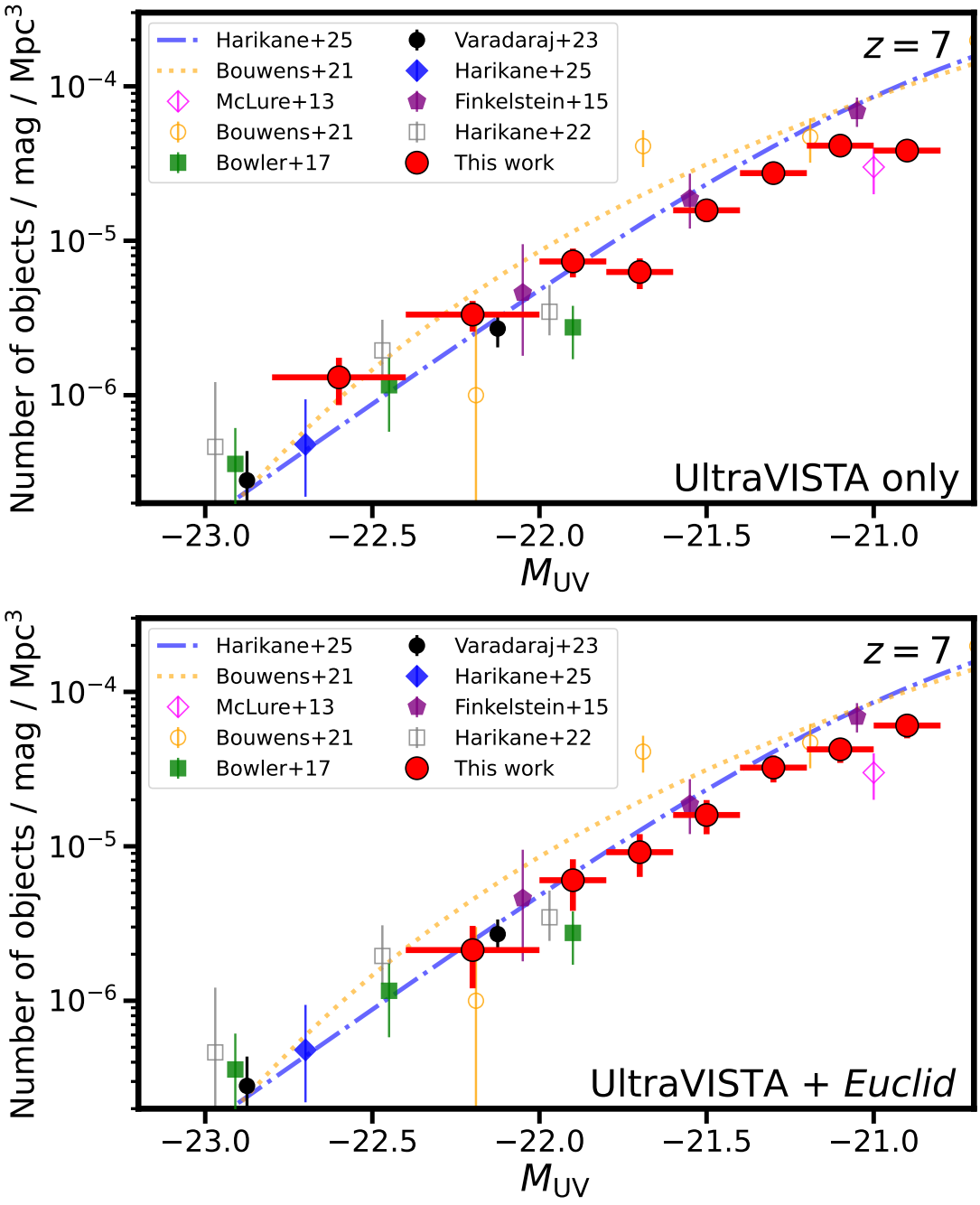

Figure 3.5: The UltraVISTA rest-frame UV LF at $z \simeq 7$. The red points show the results from the UltraVISTA samples presented in this work. **Top**: the LF points based on LBG samples where the *Euclid* photometry *isn't* included in the SED fitting. **Bottom**: the LF points calculated when *Euclid* photometry *is* included in the SED fitting. We use the same binning in both cases, and the LF values are presented in Table 3.3. We show results from McLure et al. (2013), Finkelstein et al. (2015), Bowler et al. (2017), Bouwens et al. (2021), Harikane et al. (2022b), and Harikane et al. (2025) and also the results from Chapter 2 (indicated by Varadaraj+23). Also shown are the best-fit Schechter and double-power law fits found by Bouwens et al. (2021) and Harikane et al. (2025) respectively.

galaxy surveys sample the wider large-scale structure of the Universe, over/under-densities such as filaments and voids can bias measurements of the LF. We use the Trenti and Stiavelli (2008) calculator to estimate the uncertainty due to this effect. We find that cosmic variance contributes no more than 12 per cent to the total error budget in our brightest bin, with Poissonian errors dominating. We add these cosmic variance contributions in quadrature to the errors calculated with Equation 2.2. When computing the LF, we truncate to only include galaxies with $M_{\rm UV} < -20.7$, corresponding to the 50 per cent completeness limit for the upper end of our redshift bin (see Fig. 3.4), to ensure a robust and complete sample is used for the LF determination. We choose $M_{\rm UV}$ bins such that they span the magnitude range of the sample down to the 50 per cent completeness limit. The brightest bins centred at $M_{\rm UV} = -22.6$ and -22.2 have widths $\Delta M_{\rm UV} = 0.4$ to ensure that at least five galaxies lie within them for the UltraVISTA-only sample. The remaining bins centred at $M_{\rm UV} = -21.9$ down to $M_{\rm UV} = -20.3$ have widths of $\Delta M_{\rm UV} = 0.2$. This provides a finer binning than used for *Hubble* results of Finkelstein et al. (2015) and Bouwens et al. (2021), whilst keeping at least ten galaxies in each bin, benefiting both the fitting and the comparison with other studies. We use the same binning scheme for the UltraVISTA+*Euclid* sample to provide a direct comparison between the two samples. The rest-UV LFs from the two selections (UltraVISTA-only and UltraVISTA+*Euclid*) are presented in Fig. 3.5, and the LF values are presented in Table 3.3.

3.5.3 Improved LF measurement with *Euclid*

Comparing the two panels in Fig. 3.5, it is immediately clear that the UltraVISTA-only LF points show significant scatter, whereas when *Euclid* is included in the SED fitting, the points follow a smooth decline towards the bright end. This is due to the additional *Euclid* photometry providing a better characterisation of LBGs and low-redshift interlopers, and including *Euclid* also allows for a more straightfoward removal of VISTA crosstalk artefacts. Additionally, the *Euclid* photometry better probes the deep molecular absorption features seen in brown dwarf SEDs, which

are largely inaccessible with only ground-based NIR filters. It is therefore also the case that the brown dwarf removal step, namely removing objects with $\chi^2_{\rm BD} < \chi^2_{\rm gal}$, performs better with *Euclid* photometry since the degeneracy between a brown dwarf SED and a flat rest-UV continuum is broken. Using only VISTA photometry, genuine high-redshift LBGs may removed, causing an underestimate of the LF. Additionally, the faintest UltraVISTA-only bin at $M_{\rm UV} = -20.9$ decreases compared to the bin at $M_{\rm UV} = -21.1$ (although are consistent within the errors). When objects are selected in VISTA $Y + J$, the faintest sources may *only* have their detection in one or two of these filters, since the VISTA H and K_s filters drop in depth significantly (see Table 3.1). On the other hand, *Euclid* provides uniform depth across all its NIR filters, leading to detections of the rest-UV continuum across $\lambda_{\rm obs} \simeq 1 - 2.5\mu$m for the faintest sources, leading to their robust characterisation as high-redshift LBGs. We further discuss the improved SED fitting constraints *Euclid* provides in Section 3.6.1.

3.5.4 Double-power law and Schechter function fitting

Numerous studies have now shown that a DPL provides a better fit to the rest-UV LF at $z = 7$ compared to a Schechter function, due to the excess of galaxies seen at $L > L^*$ (Bowler et al., 2014; Bowler et al., 2017; Harikane et al., 2022b; Harikane et al., 2025, and results from Chapter 2). This double-power law has the functional form

$$\phi(M) = \frac{\phi^*}{10^{0.4(\alpha+1)(M-M^*)} + 10^{0.4(\beta+1)(M-M^*)}} \tag{3.1}$$

where ϕ^* is the normalisation, M^* is the characteristic magnitude, α is the faint-end slope and β is the bright-end slope. We fit a DPL to our UltraVISTA+*Euclid* points, those from Chapter 2, and we use faint-end results from Finkelstein et al. (2015). The results of our fitting are presented in Table 3.4, and we show the best-fit DPL on Fig. 3.6. We find a bright-end slope of $\beta = -4.59^{+0.32}_{-0.37}$, consistent with Bowler et al. (2017) and Harikane et al. (2025). Our faint-end slope of $\alpha = -2.11^{+0.21}_{-0.17}$ is also consistent with Bowler et al. (2017) and Harikane et al. (2025), as well as the

Schechter function determinations of Finkelstein et al. (2015) and Bouwens et al. (2021). The key constraining power afforded by deep ground-based imaging is on the knee of the LF by joining up with space-based observations to provide reliable sampling around $-22 \leq M_{\rm UV} \leq -21$. We find that the characteristic magnitude $M^* = -21.13^{+0.27}_{-0.25}$ is in agreement with Finkelstein et al. (2015) and Bowler et al. (2017) and Harikane et al. (2025) (although note that the value of M^* derived from a Schechter fit by Finkelstein et al., 2015 is different to that for a DPL fit by the remaining studies). Our value of $\phi^* = 0.91^{+0.66}_{-0.38} \times 10^{-4}$ mag^{-1} Mpc^{-3} is also consistent with the aforementioned studies, but with smaller errors. This work represents the first time ground-based imaging has been able to probe fainter than the knee of the LF at $z \geq 6$. Overall, our results are in agreement with Harikane et al. (2025), who use a sample of spectroscopically confirmed galaxies, eliminating any contamination. This further suggests that we have effectively mitigated the encroachment of low-redshift interlopers into our $z \simeq 7$ UltraVISTA+*Euclid* sample. Our best-fit DPL is also consistent with that of Bowler et al. (2017), with slight shifts in the knee of the LF to higher M^* and lower ϕ^*, but all within the errors. This implies that the constraining power of ground-based imaging on the form of the DPL, prior to having significant overlap with space-based studies, was already quite strong. However, our results show that the gentle DPL decline continues down to the knee of the LF, providing a definitive measurement of the bright-end slope. This suggests that there are no significant systematics causing major differences between, e.g., Bowler et al. (2017) and Finkelstein et al. (2015). Otherwise, our faintest points—based on similar but deeper data used in Bowler et al. (2017) with similar selection steps—would likely show inconsistencies with Finkelstein et al. (2015). Instead, the strongest factor impacting both ground- and space-based determinations of the $z = 7$ rest-UV LF is contamination by low-redshift interlopers and brown dwarfs, reflected by relative excesses seen in Harikane et al. (2022b) (as we have discussed in Chapter 2) and Bouwens et al. (2021).

We also fit a Schechter function, which is given by

$$\phi(M) = 0.4\ln(10)\phi^* 10^{0.4(M-M^*)(\alpha+1)} \exp\left(10^{-0.4(M-M^*)}\right) \tag{3.2}$$

Table 3.4: The best-fit parameters for the DPL (top row) and Schechter (bottom row) fit to our LF points, those from Chapter 2 and faint-end results from Finkelstein et al. (2015).

ϕ^* mag^{-1} Mpc^{-3}	M^* mag	α	β	Form
$0.91^{+0.66}_{-0.38} \times 10^{-4}$	$-21.13^{+0.27}_{-0.25}$	$-2.11^{+0.21}_{-0.17}$	$-4.59^{+0.32}_{-0.37}$	DPL
$1.61^{+0.75}_{-0.57} \times 10^{-4}$	$-20.98^{+0.19}_{-0.20}$	$-1.99^{+0.16}_{-0.15}$	–	Sch.

where we now have an exponential cutoff in the bright end. We show the best-fitting Schechter function on Fig. 3.6 and present the best-fitting parameters in Table 3.4. Our gradual decline in the range $-22 < M_{\rm UV} < -20.7$ is consistent with a Schechter function which has a slightly lower ϕ^* and M^* than that found by Bouwens et al. (2021), although is consistent within the errors. In fact, the DPL and Schechter function are indistinguishable at $M_{\rm UV} \gtrsim -22.5$ However, at $M_{\rm UV} \lesssim -22.5$, the Schechter function diverges from the best-fit DPL, and the latter clearly provides a better fit for the brightest LF points of Bowler et al. (2017), and Harikane et al. (2025), and results from Chapter 2.

3.5.5 Comparison with other studies

In Fig. 3.5 we compare our LF points to other studies. Our results are consistent with the bright-end studies of Bowler et al. (2017), Harikane et al. (2022b), and Harikane et al. (2025) and Chapter 2, confirming a gradual decline in the LF at $M_{\rm UV} < -22$. The constraining power of UltraVISTA DR6 is best seen at $M_{\rm UV} > -22$. For this, we focus on the UltraVISTA+*Euclid* results. Our LF points are remarkably consistent with the *Hubble* results of Finkelstein et al. (2015), indicating that our determination of the LF is consistent with theirs, and any differences in methodology do not cause significant systematic offsets. For example, brown dwarf contaminants were removed by Finkelstein et al. (2015) using a combination of the SExtractor FWHM and their colours, whereas we use SED fitting. As we will show in Section 3.6.2, it is not possible to remove faint brown dwarfs as being unresolved in the *Euclid* imaging at the magnitudes probed in this work. Additionally, Finkelstein et al. (2015) calculate the effective volume for a galaxy using their injection-recovery simulations, whereas

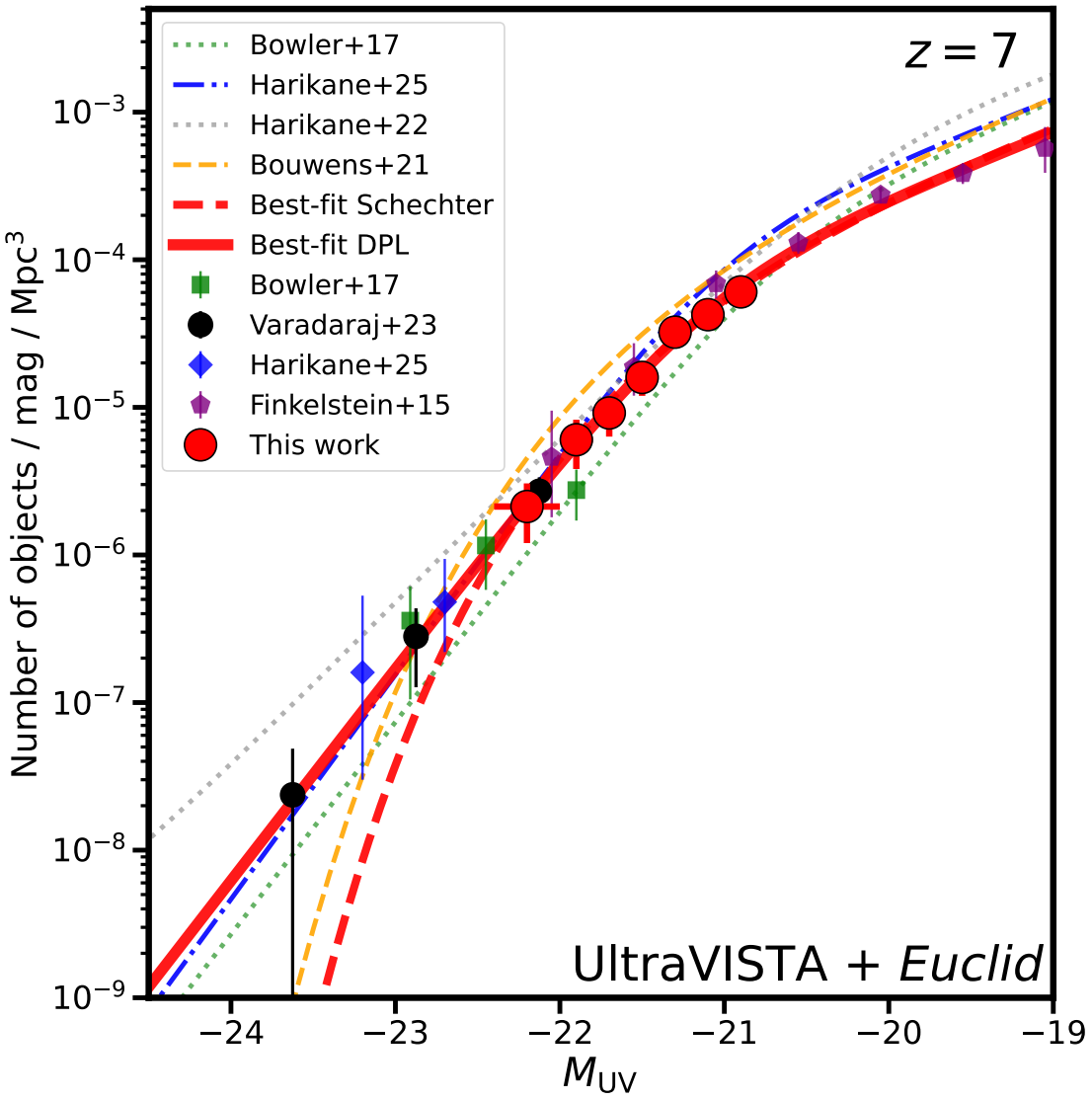

Figure 3.6: The best-fit double-power law (DPL) for the rest-frame UV LF at $z = 7$, shown by the red line. For the fitting we use results from this work (red points, the UltraVISTA+*Euclid* sample), bright-end results from Chapter 2 (black points), and faint-end results from Finkelstein et al. (2015) (purple pentagons). Bright-end LF results from Bowler et al. (2017) and Harikane et al. (2025) are also shown. For comparison, we plot the best-fit DPLs from Bowler et al. (2017), Harikane et al. (2022b), and Harikane et al. (2025).

we directly redshift the SED of each galaxy iteratively to determine its maximum redshift, and then its maximum occupied volume. In their simulations, they also allow the galaxy size to vary. Finkelstein et al. (2015) note that had they fixed their galaxy sizes to $r_e = 1$ kpc, they would have derived similar effective volumes, mirroring results from Grazian et al. (2012). Finkelstein et al. (2015) also determine their LF points using a non-parametric stepwise maximum likelihood calculation, although this approach produces equivalent results to the $1/V_{\rm max}$ method for bins with high enough number counts. The consistency with Finkelstein et al. (2015), despite slight differing strategies for removing low-redshift interlopers, suggests that both of our approaches are successful at mitigating significant contamination.

Our four brightest UltraVISTA+*Euclid* bins are in some tension with the brightest bins of Bouwens et al. (2021), who see a drop of 1.6 dex between the two bins from $M_{\rm UV} = -21.7$ to $M_{\rm UV} = -22.2$. Since we are able to use narrower binning than the $\Delta M = 0.5$ mag bins used by Bouwens et al. (2021) in this range, we can probe the finer evolution in number density across this magnitude range. We observe a gentle decline in the number density across our four brightest bins, dropping by only ~ 0.9 dex, which is more consistent with the behaviour of the underlying DPL distribution of Harikane et al. (2025) compared to the Schechter function found by Bouwens et al. (2021). Whilst the discovery of numerous $M_{\rm UV} < -22.5$ galaxies at $z \simeq 7$ has convincingly ruled out the Schechter function form for the LF (Bowler et al., 2014; Harikane et al., 2022b, and results from Chapter 2), our results show this gradual decline also occurs from the knee of the LF. As discussed by Finkelstein et al. (2015) and Bowler et al. (2017), the discrepancy with Bouwens et al. (2021) may be due to a lack of deep Y-band imaging in the majority of the CANDELS fields, critical for determining the strength of a break to rule out brown dwarfs and low-redshift galaxy interlopers.

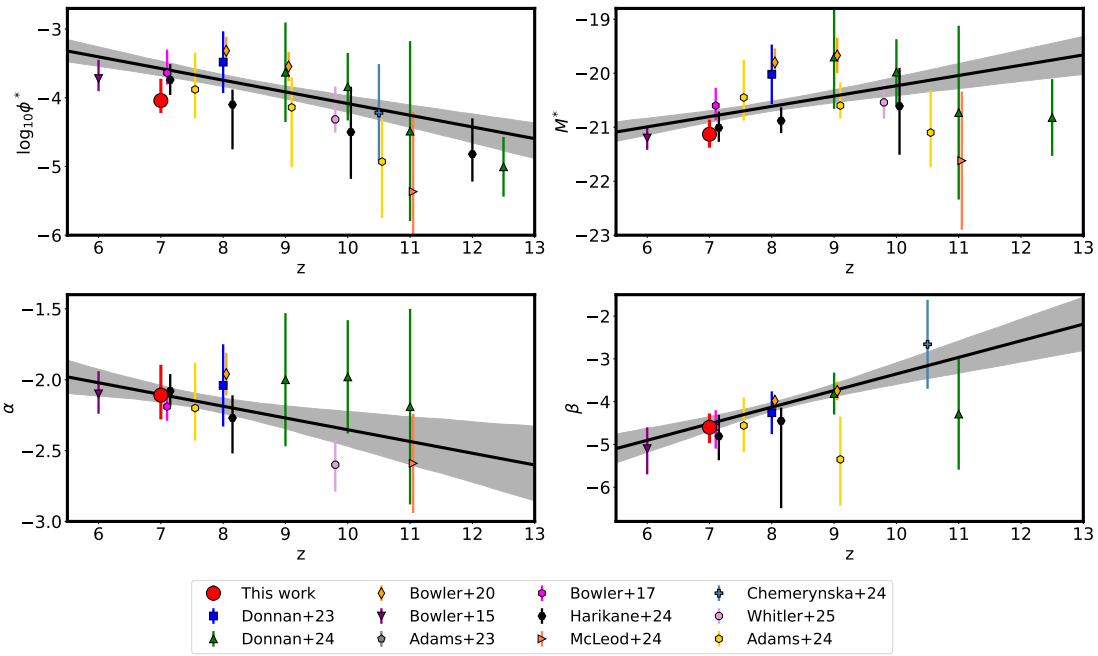

Figure 3.7: The evolution of the DPL parameters with redshift, namely the normalisation ϕ^*, the characteristic magnitude M^*, the faint-end slope α, and the bright-end slope β. The red points show the parameters derived from DPL fitting in this work. We show a compilation of results at $z = 6 - 12.5$ from Bowler et al. (2015), Bowler et al. (2017), Bowler et al. (2020), Adams et al. (2023b), Adams et al. (2024), Donnan et al. (2023a), Donnan et al. (2024), Chemerynska et al. (2024), McLeod et al. (2024), Harikane et al. (2025), and Whitler et al. (2025) with some slight offsets in redshift for clarity. We do not show points from these studies which were fixed during the DPL fitting, and we have excluded studies which use a Schechter fit (Finkelstein et al., 2015; Bouwens et al., 2021; Pérez-González et al., 2023). For the bright-end slope β, we only show studies which have at least two LF points brighter than their M^*, i.e. they have some constraints on the bright-end slope. The black line indicates the best-fit straight-line to the $z \geq 6$ data.

3.5.6 Comparison with *JWST*: a gradual evolution in the bright-end slope?

JWST has revolutionized our understanding of the $z > 7$ Universe by discovering luminous sources at early cosmic time (e.g. Naidu et al., 2022; Finkelstein et al., 2022; Castellano et al., 2022). However, ground-based imaging is still highly important for probing the bright-end of the rest-UV LF at $z > 6$. Currently, *JWST* lacks the volume to probe the bright end. Additionally, at $z = 6 - 7$, without deep ancillary optical imaging from *Hubble*, *JWST* does not have enough dropout filters bluewards of the expected position of the Lyman break at $\lambda_{\rm obs} \sim 1\mu$m. We also note that most of the luminous sources discovered by *JWST* are fainter than the

brightest ground-based candidates presented in this work and in Chapter 2. Our $z \simeq 7$ LBGs may be linked to these early sources. It is likely that $M_{\rm UV} < -22$ sources abundant in ground-based imaging occupy similar haloes to that of the brightest *JWST* sources such as JADES-GS-z14-0 and JADES-GS-z14-1 (Carniani et al., 2024), GHZ2 (Castellano et al., 2024) and GNz-11 (Bunker et al., 2023). It is thus natural to compare our rest-UV LF results to $z > 7$ *JWST* results to understand the evolution of luminous LBGs in the first Gyr of cosmic time.

In Fig. 3.7 we show the evolution of the LF parameters across $z = 6 - 13$ from a range of ground-based, *Hubble* and *JWST* studies. We only show results from DPL fitting, and for the bright-end slope β we only show results which have at least two LF points at $M_{\rm UV} < M^*$, such that they sufficiently probe the bright end. Note that *JWST* bright-end determinations have large error bars at $z > 9$ due to the limited volume available. We fit straight lines to these studies at $z \geq 6$ to probe the linear evolution, and find that, relative to $z = 6$, these can be expressed as:

$$\begin{aligned} \log_{10}(\phi^*) &= (-3.40 \pm 0.15) + (-0.17 \pm 0.05)(\mathrm{z} - 6) \\ M^* &= (-20.99 \pm 0.15) + (0.19 \pm 0.07)(z - 6) \\ \alpha &= (-2.02 \pm 0.09) + (-0.08 \pm 0.05)(z - 6) \\ \beta &= (-4.90 \pm 0.29) + (0.39 \pm 0.13)(z - 6) \end{aligned} \tag{3.3}$$

for the DPL LF parameters. Overall, our results are consistent with an evolution in the LF driven by a shallower bright-end slope β at higher redshifts, a mild evolution in the position of the knee, ϕ^* and M^*, and weak evolution in the faint-end slope α. These results differ slightly from those of Bowler et al. (2020), who found that the evolution of the LF was dominated by β and M^*, with ϕ^* remaining relatively constant over $z = 7 - 10$. Donnan et al. (2024) use *JWST* multi-field imaging to show that ϕ^* has a stronger evolution than M^*, although they are required to fix their M^* at some redshifts. However, their evolution in ϕ^* is consistent with the luminous sources found at $z > 7$, with a gentle evolution in M^* allowing for the existence of these sources.

We note that a major caveat is that the LF parameters are degenerate during the fitting, limiting discussion regarding the evolution of ϕ^* and M^*. However,

ground-based studies are able to probe sufficiently bright to determine the bright-end slope and allow for a meaningful discussion of the bright-end evolution. When fitting the evolution of the bright-end slope β, we again note that we only used *JWST* studies which had at least two LF bins brightwards of their M^*, i.e. such that they sufficiently probe the bright-end of the LF. Comparing to the number of studies in the plot above for M^*, most *JWST* studies do not have the dynamic range to provide reliable measurements of the bright-end of the rest-UV LF at $z > 8$, because large areas are needed to find the rarest sources. This is reflected in much smaller errors on β from ground-based studies (Bowler et al., 2015; Bowler et al., 2017; Bowler et al., 2020; Donnan et al., 2023a, and results of this chapter). A lack of bright-end measurements also results in weaker constraints on the knee of the LF. This can be seen in the large amounts of scatter in the values of M^* found by *JWST* studies. In fact, the increasing trend we see towards higher redshift is driven by the small errors (relative to the *JWST* studies) on M^* found by the ground-based study of Bowler et al. (2020). It is therefore not entirely clear whether M^* increases at higher redshift (as suggested by ground-based studies) or remains fairly constant with redshift (as suggested by *JWST* studies, but with large error).

The DPL form of the rest-UV LF at $z \simeq 7$ is more akin to the functional form of the halo-mass function than a Schechter function, indicating that quenching of star formation and/or dust obscuration has not begun to dominate luminous LBGs at this epoch (Bowler et al., 2014). However, numerous studies have also shown that $z \simeq 7$ LBGs can host significant dust reservoirs and exhibit signs of significant dust obscuration (e.g. Bowler et al., 2024; Algera et al., 2025). The discrepancy arises due to unobscured star formation being probed by optical+NIR studies such as this work, and obscured star formation requiring sub-millimetre observations to measure the dust emission. Interestingly, we observe a gradual steepening in the bright-end slope β from $z = 9$ down to $z = 6$ based on ground-based studies. The results of Chemerynska et al. (2024) and Donnan et al. (2024) are consistent with this gradual evolution in β, but with larger errors. Note that Chemerynska et al. (2024) use a large redshift bin of $9 < z < 12$, a useful strategy for boosting number counts over

a redshift range corresponding to only ~ 180 Myr. The bright-end slope is sensitive to dust obscuration (e.g. Cai et al., 2014) and quenching of star formation (Peng et al., 2010), so a gradual steepening at these epochs suggests a steady and gradual physical mechanism driving the evolution. Donnan et al. (2025) find tentative evidence that at fixed stellar mass, dust attenuation increases with decreasing redshift, in line with our steepening of β. Some simulations show a change in the bright-end slope β due to dust obscuration (e.g. Cai et al., 2014; Vijayan et al., 2021; Mauerhofer and Dayal, 2023). However, a challenge they face is the volume required to provide statistical samples of luminous galaxies. We stress that *Euclid* studies are necessary to complement *JWST* for constraining the bright-end of the rest-UV LF at $z \simeq 8-10$, which will reduce the ~ 2 mag scatter in M^* at these redshifts. *Euclid* studies will do this by identifying thousands of $M_{\rm UV} < -22$ sources in 53 deg^2 of imaging in the *Euclid* Deep Fields (EDFs) to depths comparable to UltraVISTA.

3.6 Outlook with *Euclid*

In this section we explore the additional information provided by *Euclid* for our sample of $z \simeq 7$ LBGs, in terms of photometry and morphology.

3.6.1 SED fitting with *Euclid*

In Section 3.5 we showed that adding *Euclid* photometry to SED fitting of our UltraVISTA-selected sample eliminates scatter in the LF points due to contamination and loss of genuine high-redshift galaxies, and in Section 3.4 we showed that *Euclid* recovers faint galaxies that are removed in the UltraVISTA-only selection. In this section we explore in further detail the additional information provided by the *Euclid* photometry with some example SED fits.

Returning to Fig. 3.3, where we show the SED fitting of a candidate LBG, ID 381772, we still find remarkably flat photometry after combining VISTA with *Euclid*. In this case, the *Euclid* J_E band in particular helps to strongly rule out the brown dwarf solution, which overlaps with a deep moleuclar absorption feature. The photometry clearly exhibits a flat rest-UV continuum, which aligns well with

the expectations for the LBG solution and disfavors the brown dwarf scenario where the molecular absorption features would dominate. The *Euclid* photometry is therefore powerful for identifying flat rest-UV continuum slopes, and the deep I_E imaging strongly rules out low-redshift galaxy and M-type dwarf solutions, which do not exhibit as strong a break as LBGs. Although beyond the scope of this work, combined VISTA+*Euclid* photometry is powerful for rest-UV slope measurements. In this case, the addition of *Euclid* suggests a bluer rest-UV slope than for the SED found with UltraVISTA NIR data alone. Note that the VISTA filters have shallower depths at longer wavelengths (see Fig. 3.1). The *Euclid* NISP filters have uniform depths, so the deep H_E imaging can allow for the discovery of very blue galaxies which would be undetected in VISTA H and K_s.

A major contaminant in ground-based studies at $z \simeq 7$ are Galactic brown dwarfs of spectral type M, L and T. Their number density peaks at the typical apparent magnitude of $z \geq 7$ galaxies in ground-based surveys (Ryan et al., 2011). In the *Euclid*-only search for high-redshift LBGs by Weaver et al. (2024), M-dwarfs could be removed by requiring a strong break between I_E and Y_E. However, they found that L- and T-type dwarfs show similar $I_E - Y_E$ vs $J_E - H_E$ colours to LBGs, and are difficult to remove with SED fitting. In Fig. 3.8 and Fig. 3.8 we show the SED fitting and postage stamp cutouts of two candidate T-type brown dwarfs - one bright with $m_{\rm AB} \simeq 25$, and one faint with $m_{\rm AB} \simeq 26$. We first note that the brighter brown dwarf has a clear point source morphology, which would allow for its removal from a LBG sample as being a point source. However, the visual morphology of the fainter source is more ambiguous, with noise spikes beginning to contribute to the shape of the object, giving it a 'fuzzier' morphology. We discuss the prospect of removing BDs as based on size further in Section 3.6.2. Now looking to the SEDs, we first note that the wavelength coverage of the *Euclid* NISP filters and their closest VISTA counterpart are not quite the same (see Fig. 3.1). This allows *Euclid* to probe the deep molecular absorption features inaccessible with VISTA. This is clearly seen in both SEDs, with the *Euclid* photometry showing a defecit relative to the VISTA filters. The SED fitting for the brighter source also

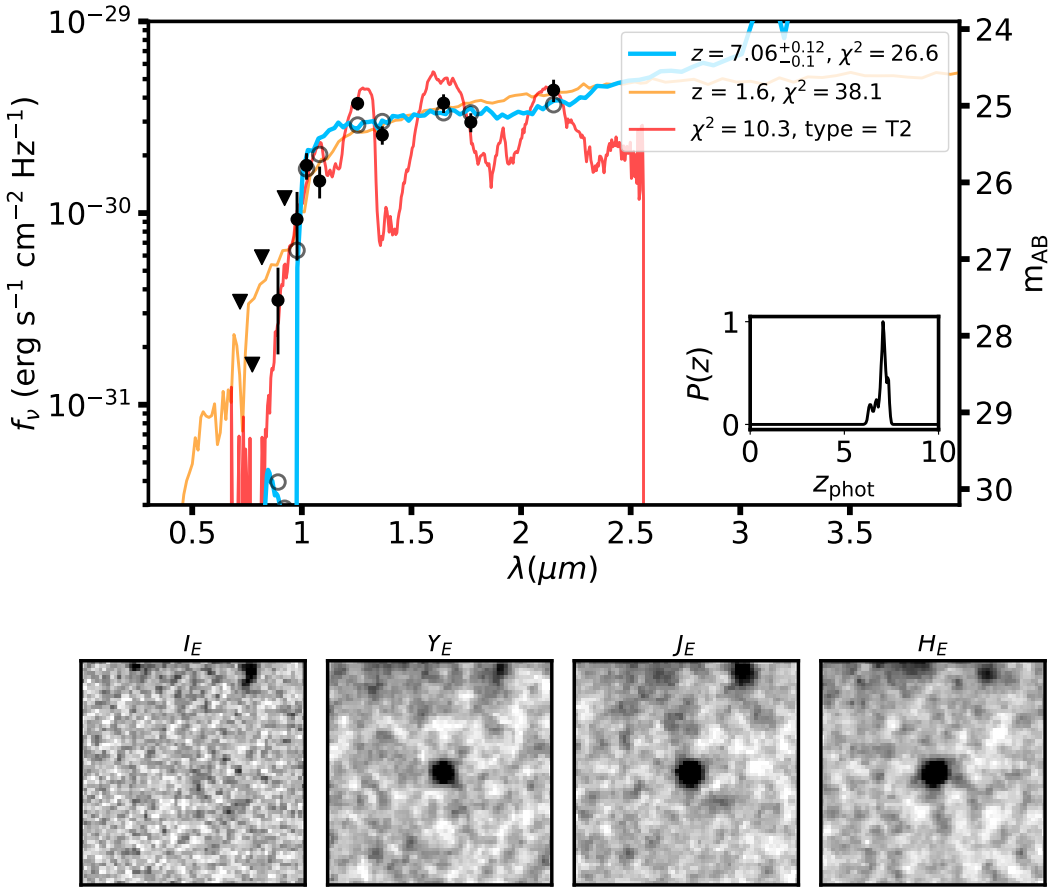

Figure 3.8: SED fitting (see caption of Fig. 3.3 for a description of the plots) and *Euclid* postage stamp cutouts of a bright ($m_{AB} \simeq 25$) candidate T-type brown dwarf. Note the clear molecular absorption features seen by the VISTA+*Euclid* NIR photometry at $\lambda > 1$ μm. Also note the PSF-like morphology for this bright source, but a more irregular morphology for the faint source driven by noise. The *Euclid* postage stamp cutouts are $10 \times 10''$, and are scaled to saturate at $\pm 3\sigma$ above/below the noise level.

benefits from the pre-existing HSC optical photometry being able to detect the more gentle blue slope relative to a Lyman break. Prior to *Euclid*, this gentle blue slope, combined with deviations from flat NIR photometry, was the main discriminant used to remove brown dwarfs in ground-based data. However, for the fainter brown dwarf, the blue slope is not visible. As a result, it is more challenging to extend LBG searches down to the signal-to-noise limit without *Euclid*. This was a challenge encountered in Chapter 2 in the ECDF-S field due to a lack of deep optical imaging, where we selected objects in $Y + J$ at a brighter 8σ significance to account for

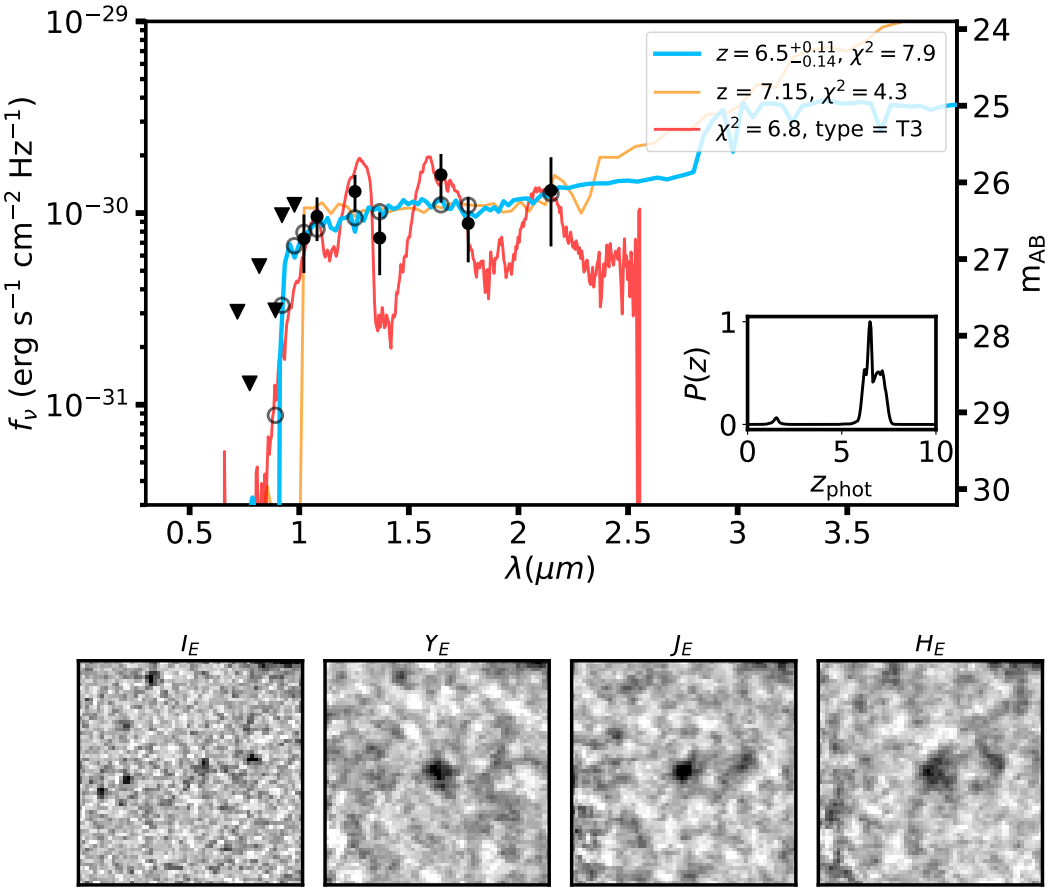

Figure 3.8: SED fitting (see caption of Fig. 3.3 for a description of the plots) and *Euclid* postage stamp cutouts of a faint ($m_{\rm AB} \simeq 26$) T-type brown dwarf. Note the clear molecular absorption features seen by the VISTA+*Euclid* NIR photometry at $\lambda > 1$ μm. Note the more irregular morphology for the faint source driven by noise, compared to the bright brown dwarf candidate in Fig. 3.8. The *Euclid* postage stamp cutouts are $10 \times 10''$, and are scaled to saturate at $\pm 3\sigma$ above/below the noise level.

this, resulting in only six luminous galaxy candidates. VISTA imaging is available in the EAFs and in the *Euclid* Deep Field Fornax as part of VIDEO imaging in ECDF-S. This overlap will be powerful for providing additional photometry on $z \geq 7$ sources found in ground-based imaging (e.g. Stefanon et al., 2019; Bowler et al., 2020; Donnan et al., 2023a), as well as identifying new ones.

3.6.2 Can brown dwarfs be removed as point sources with *Euclid*?

It may be expected that space-based imaging with *Euclid* will allow for the removal of brown dwarfs from LBG samples as unresolved sources. The first results from the Early Release Observations (EROs) were based on data that had a $0.3''\text{pix}^{-1}$ pixel scale, which is larger than ground-based surveys such as VIDEO ($0.2''\text{pix}^{-1}$, Jarvis et al., 2013). This allowed for the identification of I_E dropout sources as $z > 6$ LBG candidates, but objects were generally undersampled (Atek et al., 2024; Weaver et al., 2024). Weaver et al. (2024) injected PSF, clumpy, and disc models into the imaging and find that galaxies and PSFs are indistinguishable at this pixel scale, so no attempt was made to separate sources based on morphology.

We use SExtractor FWHMs to conduct a first-order analysis of LBG and BD sizes in VISTA and *Euclid* performance verification imaging. We first investigate the sizes of PSFs in the *Euclid* imaging. We take point sources from the *JWST* COSMOS-Web survey (Casey et al., 2023), selected from the F444W FWHM-magnitude diagram using a catalogue produced with SExtractor. The COSMOS-Web imaging was reduced by Nathan Adams. We then crossmatch these point sources with *Euclid*. F444W is thus used to provide the 'ground-truth', since the objects are unambiguously PSFs. Since F444W is much deeper than J_E (5σ depth of 26.9 following the methodology in Section 3.2.5), we are able to select these 'ground-truth' PSFs far below the limiting magnitude of the *Euclid* imaging. Whilst F115W and F150W would have provided higher-resolution imaging for this, we find they have depths of 26.1 and 26.2 respectively, slightly shallower than the *Euclid* NISP imaging (26.4). In Fig. 3.9, the gray region show the SExtractor FWHM in *Euclid* J_E imaging of these *JWST* PSFs as a function of their J_E magnitude. This region is determined as the interquartile range around the median in magnitude bins of width 0.5 mag. For very bright ($J_E \lesssim 24$) sources, PSFs in *Euclid* are consistent with the FWHM measured in Section 3.2.4, as expected. However, as we approach fainter magnitudes, the mean and standard deviation both begin to increase, before turning over near the limiting magnitude of the J_E imaging. This

behaviour is expected as noise begins to boost the FWHM measurements of faint sources. Additionally, the turnover is caused by biases in the selection of faint PSFs in the *Euclid* imaging - only those with an associated large positive noise will be detected. Bowler et al. (2014) conduct a similar investigation by injecting PSFs into UltraVISTA and UDS imaging, and find similar behaviour. In Fig. 3.9 we also show the FWHM-J_E magnitude distribution of LBGs and BDs identified through SED fitting with combined HSC+VISTA+*Euclid* photometry for the UltraVISTA+*Euclid* sample. The FWHMs of the BDs are consistent with the shaded region. Additionally, none of the BDs identified with SED fitting exceed a FWHM of 1 arcsec. Whilst a significant fraction of the LBG sample has FWHMs above 1 arcsec, the majority are consistent with the scatter in sizes measured for point sources. We also show the size-luminosity relations determined by Bowler et al. (2017) from *Hubble* imaging of a ground-based sample, and Shibuya et al. (2015) & Yang et al. (2022) based on *Hubble* samples. The size-luminosity relation can be written as

$$R_e = R_0 \left(\frac{L}{L_0} \right)^{\gamma} \tag{3.4}$$

where L_0 is the characteristic luminosity corresponding to an absolute magnitude $M = -21$, R_0 is the size at L_0 and γ is the slope of the relation. We convert their relations for the effective radius in terms of R_e in kpc to a FWHM by assuming the galaxies have a Sérsic profile with index $n = 1$, corresponding to an exponential disk. Results from *JWST* show that galaxies at $z \simeq 7$ are well-fit by such profiles (e.g. Kartaltepe et al., 2023; Ormerod et al., 2024; Westcott et al., 2024). We then convolve the literature size-luminosity relations with the *Euclid* PSF in order to simulate what would be seen with *Euclid* in terms of FWHM. For this, we follow Oesch et al. (2010a) and add the measured PSF size in quadrature. Yang et al. (2022) base their results on lensed galaxies to place constraints on the ultra-faint end of this relation. Yang et al. (2022) only have one source at $M_{\rm UV} < -22$ at $z = 6 - 7$. Shibuya et al. (2015) is based on a brighter sample, but only have two sources with $M_{\rm UV} < -22$ at $z \simeq 7$ (see their fig. 9). We are thus extrapolating these size-luminosity relations far beyond their $M_{\rm UV}$ basis. Recent results from

JWST tend to use large redshift bins to increase high-redshift sample sizes (Yang et al., 2022; Morishita et al., 2024; Ono et al., 2024; Sun et al., 2024). These studies also tend to only have a handful, if any, of sources with $M_{\rm UV} < -22$. We show the rest-optical size-luminosity relation derived by Sun et al. (2024) on Fig. 3.9. All of the relations are consistent with the LBG sample at $24.5 \lesssim J_E \lesssim 27$. At $J_E < 24$, extrapolations of existing size-luminosity relations appear to bifurcate. Yang et al. (2022) find steep relations with $\gamma \simeq 0.46 - 0.50$. These studies correct for incompleteness in R_e and $M_{\rm UV}$, but are based on faint samples. On the other hand, Shibuya et al. (2015) and Yang et al. (2022) find shallower relations with $\gamma \simeq 0.27 - 0.29$. We note that Shibuya et al. (2015) do not correct for incompleteness, and Yang et al. (2022) is a rest-optical relation. The latter point is important since the rest-UV morphologies of luminous LBGs tend to be clumpy (e.g. Bowler et al., 2022), whereas rest-optical studies show disc-like morphologies at these redshifts (e.g. Kartaltepe et al., 2023). The relation determined by Bowler et al. (2017) is the only relation which samples galaxies at $M_{\rm UV} < -22$ (with *Hubble* follow-up of ground-selected LBGs), once again highlighting the necessity for ground-selected samples prior to *Euclid*. Their relation is more akin to the steeper space-based studies, with $\gamma = 0.50$. This provides the most positive case for removing BDs as PSFs as point sources, since it suggests that galaxies will grow rapidly in size at $M_{\rm UV} < -22$. In both cases ($\gamma \sim 0.3$ or $\gamma \sim 0.5$), the expected size of point sources deviates from the size-luminosity relations at $J_E \lesssim 24.5$. This suggests that within the *Euclid* Deep Fields at these magnitudes, where VISTA imaging is not available to remove BDs with SED fitting, it will be possible to remove BDs as unresolved sources in bright samples (noting expected 5σ depths in the *Euclid* Deep Fields of ~ 26). We also note that proper motion could also be used to remove BDs, with multi-epoch *Euclid* (since the EDFs will be revisited over the course of the mission) imaging and by comparing with future LSST imaging (Ivezić et al., 2019).

The key VISTA fields (COSMOS for UltraVISTA, XMM-LSS and ECDF-S for VIDEO) will cover ~ 10 deg^2 and overlap with both the *Euclid* Deep/Auxiliary Fields, which will reach 5σ NISP depths of ~ 26. This offers the unique opportunity

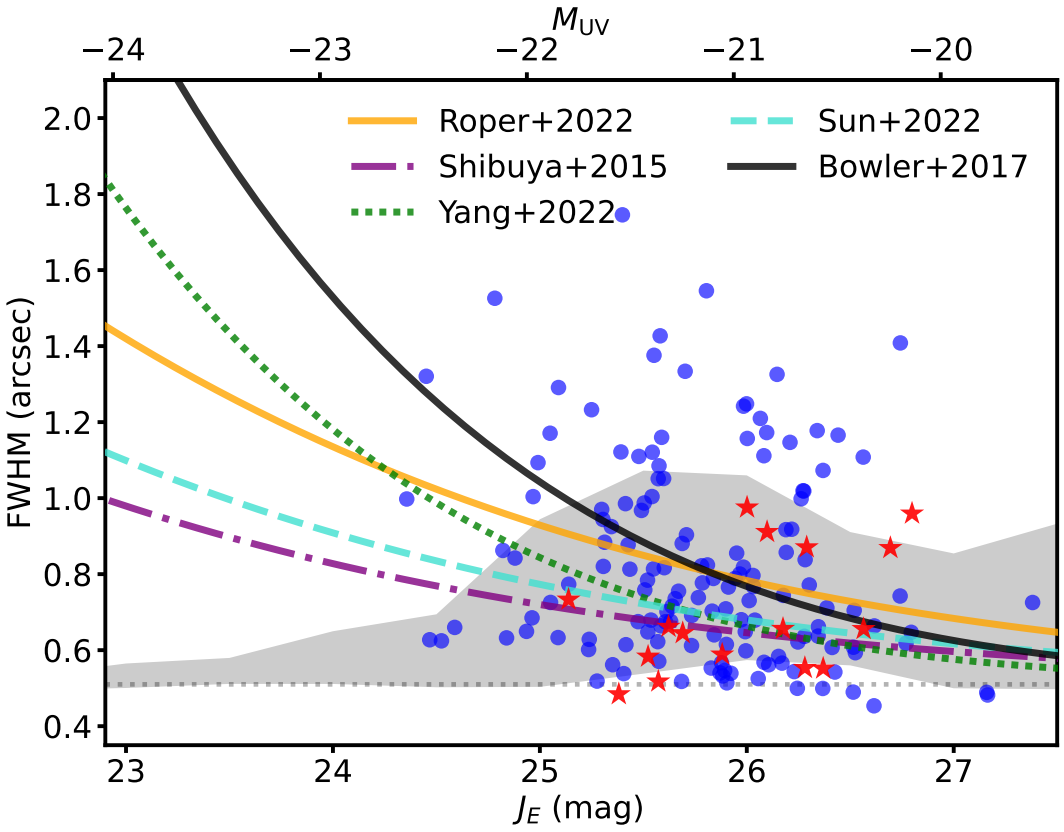

Figure 3.9: The *Euclid* J_E FWHMs for sources identified as LBGs (blue dots) and BDs (red stars) using SED fitting on HSC+VISTA+*Euclid* photometry. Also shown are size-luminosity relations from *Hubble* (Shibuya et al., 2015; Yang et al., 2022), *JWST* (Sun et al., 2024), *Hubble* imaging of a bright ground-selected sample (Bowler et al., 2017), and the prediction from the FLARES simulation (Roper et al., 2022). The dotted gray line is the *Euclid* PSF FWHM. The gray shaded region shows the FWHMs of PSFs selected from *JWST F444W* imaging when they are observed in *Euclid* J_E.

to identify LBGs and BDs with powerful SED fitting and determine a size-luminosity relation for the most luminous $z \simeq 7$ LBGs. Additionally, at $z \simeq 6$ the rest-UV continuum will enter I_E, which has a significantly smaller PSF FWHM than NISP. *Euclid* will thus provide the some of first resolved measurements of ultra-luminous sources in the middle of and towards the end of reionisation.

3.6.3 Lessons learned for the *Euclid* Deep Fields

Our results have shown that the combination of ground-based NIR photometry with *Euclid* photometry is powerful for removing L- and T-type brown dwarfs via SED

fitting, which *Euclid* alone is unable to do due to its broad filter response curves (see Fig. 3.1 and Weaver et al., 2024). We then go on to show that in the range $25 < J < 27$, brown dwarfs cannot be cleanly removed from an LBG sample as point sources because noise spikes contribute to the morphology of faint point sources, and the size-luminosity relation of LBGs corresponds to a small FWHM. This is critical for the *Euclid* Deep Fields because they will eventually reach 5σ depths of ~ 26, allowing for the discovery of many sources in this magnitude range. At $J \lesssim 24.5$, this will be much easier since BDs will have a clear PSF morphology and LBGs are expected to be much larger (Bowler et al., 2017). At these magnitudes, one may expect to also find quasars which will have a PSF morphology. It may be possible to distinguish these from brown dwarfs based on the strength of the $I_E - Y_E$ break at $z > 6$ (Euclid Collaboration et al., 2019). These bright magnitudes ($J \lesssim 24.5$) are the strength of the EDFs, where there will be enough area to discover many of these rare, ultra-luminous LBGs. However, the EDFs will not have ancillary NIR data to help remove BDs via SED fitting — although LSST will provide imaging in the optical *ugrizy* filters allowing for the brown-dwarf blue-end slope to be detected (see Fig. 3.8). This means relatively faint samples at $J > 25$ may still suffer from contamination by BDs. This magnitude range is, however, the strength of the key VISTA fields, namely XMM-LSS, ECDF-S and COSMOS, where VISTA surveys such as VIDEO (Jarvis et al., 2013) and UltraVISTA (McCracken et al., 2012) have/will have overlap with *Euclid* imaging. We suggest that $z \gtrsim 7$ LBG searches in the EDFs should focus on bright selections at $J < 25$ to mitigate contamination, and supplement this with selections in the VISTA fields where SED fitting can be used to construct clean samples. Not only is SED fitting powerful in these fields, but since *Euclid* imaging has been taken over a decade after the beginning of VIDEO and UltraVISTA, it will be possible to remove many BDs by their proper motion.

3.6.4 Lyman$-\alpha$ emitters with pseudo-narrowbands

Euclid not only provides strong colour information on L- and T-type dwarfs when combined with VISTA, but can also reveal the nature of LBGs with strong emission

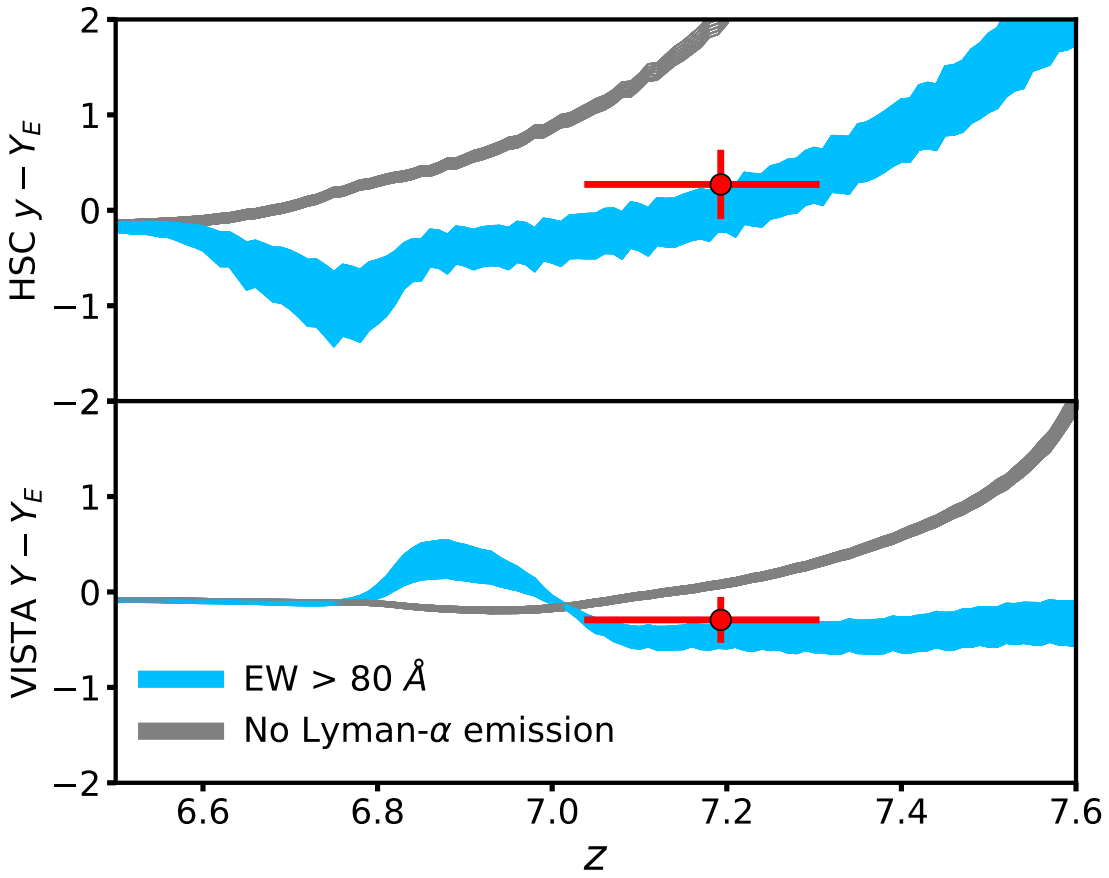

Figure 3.10: The expected HSC $y - Y_E$ (top) and VISTA $Y - Y_E$ (bottom) colours of LBGs (gray) and strong ($EW_0 > 80$Å) LAEs (blue) as a function of redshift, generated using mock BAGPIPES galaxies. The red point shows the position of our LAE candidate (see Fig. 3.11) in this colour-redshift space.

lines. The identification of emission lines with photometry has been done before using *Spitzer*/IRAC colours to identify strong [OIII]+Hβ emitters (e.g. Smit et al., 2015; Roberts-Borsani et al., 2016) some of which are found to be LAEs through spectroscopic follow-up (e.g. Oesch et al., 2015, although strong nebular emission does not necessarily imply Lyα emission). Ground-based studies have used narrowbands to identify LAEs in narrow redshift ranges (e.g. Endsley et al., 2021b; Umeda et al., 2025), and *JWST* has used medium- and narrow-bands to search for flux excess relative to the broadband photometry (e.g. JELS, Duncan et al., 2024; Pirie et al., 2024). The overlap of the HSC-y, VISTA-Y and *Euclid* Y_E filters around $\lambda = 1$ μm (see Fig. 3.1) provides a unique opportunity to identify strong Lyman-α emitters, since the filters will behave differently as the line is redshifted

through the filters relative to a normal Lyman-break. We use BAGPIPES to generate the synthetic galaxy photometry with $A_V \in [0, 0.6]$, allowing ages up to the age of the Universe at a given redshift and subsolar metallicity $Z = 0.2Z_\odot$. Since BAGPIPES does not model Lyα emission, we add the line with equivalent widths $\mathrm{EW}_0 \in [80, 240]$Å. This is done in the same manner as in Section 3.3.2, by measuring the continuum level between $\lambda_{\mathrm{rest}} = 1250 - 1300$Å. In Fig. 3.10, we show the HSC $y - Y_E$ and VISTA $Y - Y_E$ colours of LBGs and LAEs with rest-frame equivalent width $\mathrm{EW}_0 > 80$Å. A strong colour difference can be seen between the LBGs and LAEs at $z > 7$. In our LBG sample, one object at $z = 7.19$ (ID 591643) lies within the LAE colour region. The SED fitting for this galaxy, along with postage stamp cutouts, is shown in Fig. 3.11. A clear excess in flux is seen in VISTA-Y relative to HSC-y and Y_E, boosted by a potential strong Lyα emission line. The morphology in VISTA-Y also differs from Y_E with an additional clump to the north-east. Physical offsets between the rest-UV continuum and Lyα emission are often seen in LAEs targeted by MUSE (e.g. Claeyssens et al., 2022), thought to be caused by star-forming substructures, merging galaxies or scattering effects inside the circumgalactic medium. This source also overlaps with *JWST* COSMOS-Web, and these stamps are also shown in Fig. 3.11. We use BAGPIPES to conduct SED fitting using the additional *JWST* photometry to determine the physical properties of this galaxy. We fix the redshift to that found by LePhare, $z = 7.19$. We use a delayed-τ SFH and allow the time since star formation began to vary between 10 Myr and the age of the Universe at this redshift, and allow the characteristic timescale τ to vary between 50 Myr and 10 Gyr. We fix metallicity to $Z = 0.2\ Z_\odot$. We find that this galaxy has a mass of $\log_{10}(M/M_\odot) = 9.81^{+0.13}_{-0.20}$ and a star formation rate of $\sim 26\ M_\odot\ \mathrm{yr}^{-1}$. This source was previously identified in the COSMOS2015 catalogue as a $z = 1.48$ galaxy with ID COSMOS2015 626610 (Laigle et al., 2016). However, the deep I_E imaging and unique colours in filters around 1μm rule out this low-redshift solution. This galaxy is an ideal candidate for follow-up observations with *JWST* and ALMA, since similar sources have shown signs of primordial ISM conditions, Lyα halos and complex gas exchange mechanisms between components,

hinting at merging activity (e.g. Himiko and CR7, Ouchi et al., 2013; Sobral et al., 2015; Marconcini et al., 2024). Looking forward, the three filters used to identify this source will also be available in the XMM-LSS field as part of the EAFs and *Euclid* Wide Survey, providing additional opportunities to identify strong LAEs embedded in the Epoch of Reionisation. In the *Euclid* Wide Survey, overlap with the LSST y filter can also be used to identify such sources. Finally, LAEs at lower redshifts can be identified in the *Euclid* Deep Fields by comparing HSC-R, I and Z to the *Euclid* I_E filter, although this will be more difficult due to overlap between only two filters at a time and the large width of I_E.

3.7 Conclusions

We have conducted a search for $z \simeq 7$ LBGs in the final data release (DR6) of the UltraVISTA survey, covering 1.72 deg^2. We combine this NIR imaging with deep optical imaging from HSC and infrared imaging from *Spitzer*/IRAC to conduct a full SED fitting analysis using LePhare. We conduct two different selections: one where *Euclid* photometry is included for the SED fitting (the UltraVISTA+*Euclid* sample), and one without the use of *Euclid* (the UltraVISTA-only sample). The UltraVISTA-only sample consists of 291 candidate galaxies at $6.5 \leq z_{\rm phot} \leq 7.5$ with $-22.5 \leq M_{\rm UV} \leq -20.2$. With the improved depth of UltraVISTA DR6, this sample reaches faint enough magnitudes to overlap significantly with the *Hubble*-selected samples of Finkelstein et al. (2015) and Bouwens et al. (2021). The UltraVISTA+*Euclid* sample consists of 141 galaxies, with 38 *not* identified in the UltraVISTA-only sample. *Euclid* acts to recover very faint galaxies which lack robust SED constraints in VISTA photometry alone. With *Euclid*'s higher resolution, by visual inspection we identify a clumpy/irregular fraction of 0.177, in line with *JWST* morphology studies (Kartaltepe et al., 2023).

We find that *Euclid* comprehensively addresses contamination by brown dwarfs and artefacts, as well as the unintended removal of genuine galaxy candidates, seen as scatter in the rest-UV LF points computed from the UltraVISTA-only sample. Correspondingly, the rest-UV LF based on the UltraVISTA+*Euclid* sample

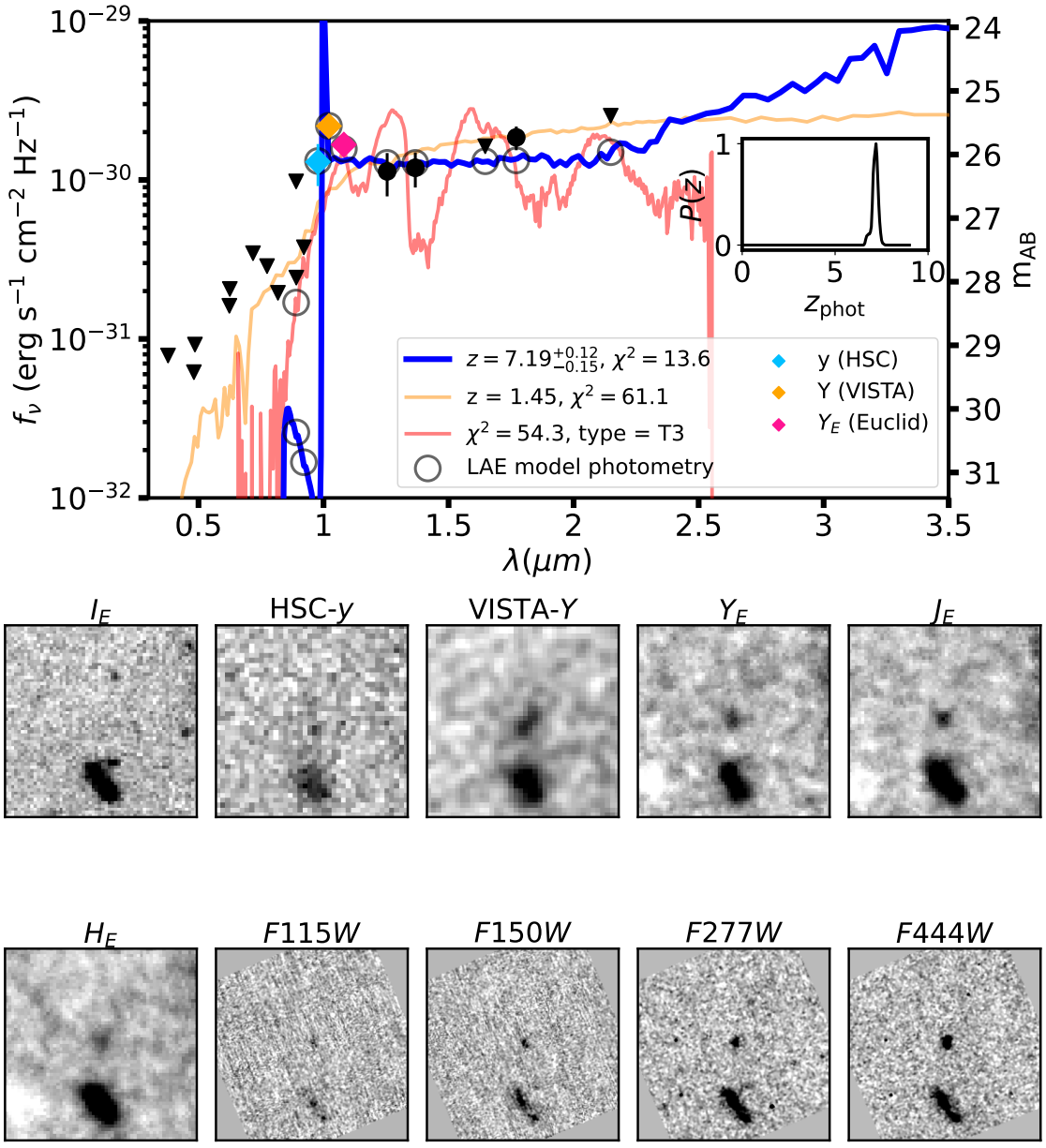

Figure 3.11: SED fitting (top) and postage stamp cutouts (bottom) of our LAE candidate, ID 591643. The SED fitting plot is similar to Fig. 3.3, but here we colour the HSC y, VISTA Y and *Euclid* Y_E filters differently to highlight them. The stamps are $10 \times 10''$and saturate at the $\pm 3\sigma$ level above/below the noise.

shows a smooth decline in number density towards brighter magnitudes, in excellent agreement with Finkelstein et al. (2015) as well as previous bright-end studies (Bowler et al., 2017; Harikane et al., 2025, Chapter 2). Our DPL fitting reveals that this ground-selected sample probes fainter than the LF knee for the first time at $z > 6$. We compare our rest-UV LF at $z \simeq 7$ to *JWST* results at $z > 7$. We find some evidence for a gentle evolution in the bright-end slope, although this is limited by a lack of robust measurements of the bright end at $z > 9$, which will require robust samples from current and upcoming degree-scale *JWST* programmes as well as the *Euclid* Deep Fields.

We then explore in further detail the additional information provided by *Euclid* for this UltraVISTA-selected sample. We then show that whilst combined VISTA+*Euclid* photometry is powerful for removing faint brown dwarfs via SED fitting, at the magnitudes probed in this work brown dwarfs cannot be separated morphologically from LBG samples as point sources. This is because faint point sources have their FWHMs boosted by positive noise spikes. At $J \lesssim 24.5$, since the size-luminosity relation of galaxies rapidly increases, we forecast that it will be straightforward to remove brown dwarfs based on their morphology. This is particularly crucial for the *Euclid* Deep Fields where ancillary NIR data is lacking.

Finally, we also present an extreme Lyman-α emitter candidate at $z = 7.2$ identified via its strong colours in HSC $y - Y_E$ and VISTA $Y - Y_E$, differing significantly from the expected colours of a normal LBG. The differences in morphology between VISTA Y and Y_E may indicate a Lyα-emitting clump physically offset from the rest-UV continuum. These three slightly different y filters will be available in XMM-LSS, providing further opportunity for the identification of extreme sources during the Epoch of Reionisation. Such sources are prime candidates for follow-up with *JWST*.

Woof!

—My dog Buttons, when I read this chapter to her

4

The sizes of bright Lyman-break galaxies at $z \simeq 3-5$ with the *JWST* PRIMER survey

Contents

4.1 Introduction

The diversity of galaxy shapes and size have fascinated astronomers for decades. Early visual classification of structure within galaxies established the Hubble tuning fork, a classification system still used to this day (Hubble, 1926). In the distant Universe, where galaxies are still evolving into the structures we see locally, their sizes are a highly useful probe into the fundamental physics of their growth (e.g. see Conselice, 2014).

Luminous, massive ($\log_{10}(M_\star/M_\odot) > 9$) galaxies at high-redshift ($z \gtrsim 3$) are excellent laboratories for galaxy physics. These galaxies populate the most massive dark matter haloes (Wechsler and Tinker, 2018) and must be more evolved than their low-mass counterparts to accumulate such large stellar mass. This means they have had time to undergo major mergers, and there may have been enough time for star-forming clumps to coalesce and form bulges and disks (e.g. Dekel et al., 2009b; Rujopakarn et al., 2023). Massive galaxies are amongst the first to undergo a quenching of their star formation (e.g. Cowie et al., 1996; Peng et al., 2010; McLeod et al., 2021). Studying the resolved properties of these galaxies can thus enable us to learn about the earliest structural formation and feedback processes. The search for these rare massive galaxies was revolutionised by the advent of degree-scale ground-based imaging (e.g. Miyazaki et al., 2002; Lawrence et al., 2007; McCracken et al., 2012; Jarvis et al., 2013), necessary due to the low surface densities of high-redshift LBGs. Since then, various number statistics of these rare high-redshift galaxies have been well-constrained at $z \simeq 3-10$, such as the rest-UV LF (e.g. Bowler et al., 2014; Ono et al., 2018; Stefanon et al., 2019; Bowler et al., 2020; Bouwens et al., 2021; Harikane et al., 2022b; Adams et al., 2023b; Donnan et al., 2023a, and results from Chapters 2 and 3) and the two-point correlation function (clustering, e.g. Adelberger et al., 2005; Bian et al., 2013; Durkalec et al., 2015; Hatfield et al., 2018; Harikane et al., 2022b). However,

since ground-based images are often seeing-dominated (e.g. Bowler et al., 2017), resolved properties have hitherto been difficult to measure.

Space-based telescopes such as *Hubble* do not suffer from atmospheric seeing, providing a clear view of galaxy morphology (e.g. Ferguson et al., 2004; Trujillo et al., 2006; Mosleh et al., 2011; Law et al., 2012; Grazian et al., 2012; van der Wel et al., 2014; Shibuya et al., 2015; Whitney et al., 2019), but rest-frame optical-wavelength shapes were only observable out to $z \simeq 3$. This limited the comparison of high-redshift morphologies with local optical observations, as well as the comparison between young and old stellar populations (as probed by the rest-UV and rest-optical respectively) in high-redshift galaxies. *JWST*'s infrared coverage and unparalleled resolution has opened the window to rest-UV *and* rest-optical for the first time at $z \gtrsim 3$ (e.g. Ferreira et al., 2023; Kartaltepe et al., 2023; Leethochawalit et al., 2023a; Ormerod et al., 2024) revealing early mass assembly and a significant fraction of disk galaxies by $z \simeq 6$.

As discussed in Section 1.3.2, models describe galaxy disk formation by creating rotationally supported exponential disks from baryons. These disks have mass and angular momentum that are some fixed fraction of the host dark matter (DM) halo. The disk scale radius is proportional to a dimensionless 'spin parameter' λ, which is related to the angular momentum, mass and energy of the system (Fall and Efstathiou, 1980; Mo et al., 1998; Bullock et al., 2001). These models can be tested with various size scaling relations. First, if the size of galaxies are determined from their host halo angular momentum, then we expect the size distribution of galaxies to follow a log-normal distribution (de Jong and Lacey, 2000). Second, the disk model of Fall and Efstathiou (1980) predicts that the disk size of a galaxy scales with redshift as $r \propto (1+z)^{-1}$ in the case of a fixed circular velocity of the host DM halo, and as $r \propto (1+z)^{-1.5}$ in the case of fixed virial mass. Prior to *JWST*, various studies have supported each relation, as well as for values in-between (e.g. Hathi et al., 2008; Oesch et al., 2010a; Mosleh et al., 2011). Furthermore, Curtis-Lake et al. (2016) argue that if one considers the *typical* (modal) sizes of galaxies then no strong evolution is seen, with the effect driven by incompleteness in *Hubble* samples at

$z \gtrsim 3$. Third, the size-mass relation (and the related size-luminosity relation) gives insight into quenching mechanisms. In the local Universe, quiescent galaxies follow a steeper size-mass relation than star-forming galaxies (SFGs, van der Wel et al., 2014). The onset of quenching may thus be seen in an evolution of the high-redshift size-mass relation. Additionally, within the framework of these disk formation models, van der Wel et al. (2014) find no evolution in the size-mass relation of SFGs, suggesting that their sizes are still controlled by their host DM halos. Note however that large scatter and uncertainty exists in these measurements (e.g. Huang et al., 2013; Curtis-Lake et al., 2016; Shibuya et al., 2015; Whitney et al., 2019).

JWST has opened a new dimension to the study of size scaling relations via their wavelength dependence. Since rest-optical and rest-UV observations probe stellar populations of different ages, we may expect differences based on how and where stars form in high-redshift galaxies. Simulations of LBGs at a broad range of wavelengths have made enticing predictions for the *JWST* era of astronomy. García-Argumánez et al. (2023) simulate observations from the Cosmic Evolution Early Release Science (CEERS) Survey (Finkelstein et al., 2017) with Illustris-1 (Vogelsberger et al., 2014) and find that progenitors of local galaxies with $M > 10^{11} M_{\odot}$ form $\sim 25\%$ of their $z \sim 1$ stellar masses by $z \simeq 2.7$, suggesting significant mass build-up at high redshift. Shen et al. (2024b) use the THESAN simulation (Kannan et al., 2022) to show that massive ($M_{\star} > 10^{9} M_{\odot}$) galaxies become increasingly compact as one moves from $z = 6$ out to $z = 10$. Additionally, their sizes roughly agree with analytical predictions from disk formation models, governed by the spin parameter λ (Fall and Efstathiou, 1980; Mo et al., 1998; Bullock et al., 2001).

In the First Light And Reionization Epoch Simulations (FLARES, Lovell et al., 2021), Roper et al. (2022) find intrinsically negative size-luminosity relations. At $z = 5 - 10$, the inclusion of dust attenuation predicts observed size-luminosity relations with increasingly positive slopes at shorter wavelengths, building on similar predictions by Marshall et al. (2022). Costantin et al. (2023) also simulate CEERS observations with Illustris TNG50 (Pillepich et al., 2019) at $z = 3 - 6$ and predict a size-redshift evolution in the rest-optical consistent with fixed circular velocity

of DM haloes, as well as negative observed size-mass relations with wavelength at $z = 5-6$. Both Roper et al. (2022) and Costantin et al. (2023) explain their findings by requiring that massive galaxies undergo episodes of centrally concentrated star formation, leading to small sizes at high mass and high dust attenuation in the cores of massive galaxies. Studying massive galaxies with *JWST* allows us to test these predictions.

Having established the versatility of galaxy size measurements for understanding galaxy evolution, we now discuss how sizes are measured. Galaxy sizes can be complex to define depending on the morphology, so comparing like-for-like with other observations and simulations can often be complicated by the choice of definition. The Sérsic (1963) brightness profile is a common functional form fit to galaxies following $r^{1/n}$ for a given 'Sérsic index' n. This profile assigns galaxies an effective radius R_e which contains half the total light. Various values of n are effective at fitting both late- and early-type massive galaxies in the local Universe (e.g. Lange et al., 2015). Additionally, *JWST* has continued to find that galaxies at high-redshift which appear disky are well-fit by a Sérsic profile with $n \simeq 1$ (Adams et al., 2023a; Kartaltepe et al., 2023; Ormerod et al., 2024). Alternatively, non-parametric measurements using some form of a circularised half-light radius are a popular choice in simulations at high redshift (Roper et al., 2022; Katz et al., 2023). Such definitions make no assumptions on the shape of the galaxy, allowing a measurement to be made for disturbed and clumpy morphologies which are commonly seen at high redshift (Shibuya et al., 2016; Huertas-Company et al., 2024; Kartaltepe et al., 2023; Jacobs et al., 2023). It is thus vital that studies on galaxy size consider various definitions to test differences between parametric and non-parametric fitting, allow for a diverse range of galaxy morphologies, and provide like-for-like comparison with simulations and between redshifts.

In this work we measure the sizes of massive, rest-UV bright galaxies at $z = 3-5$ selected from ground-based imaging. We use NIRCam imaging from Public Release IMaging for Extragalactic Research (PRIMER, Dunlop et al., 2021) that overlaps with the ground-based imaging from Visible and Infrared Survey Telescope for

Astronomy (VISTA) Deep Extragalactic Observations (VIDEO, Jarvis et al., 2013), UltraVISTA (McCracken et al., 2012) and the Hyper-Suprime Cam Subaru Strategic Program (HSC-SSP, Aihara et al., 2022) to measure sizes across a broad wavelength range, $0.9 - 4.4\mu$m. We use Sérsic and non-parametric size fitting to measure the redshift evolution of sizes, as well as the size-mass and size-luminosity relations. We also test the wavelength dependence of the size-mass and size-luminosity relations, comparing with predictions from simulations.

The layout of this Chapter is as follows: in Section 4.2 we outline the ground-selected catalogues and *JWST* imaging used in this work. Section 4.3 describes the creation of postage stamp images and the size fitting of the sample. Our results are presented in Section 4.4, where we discuss the size-redshift evolution, the size-mass relations and the size-luminosity relations. In Section 4.5 we discuss our results in the context of disk formation models. We also explore difficulties in measuring sizes and the size-redshift evolution. We then examine the comparison of our results to simulations, after which we discuss the implications of our results and simulation comparison for the scenario of compact central star formation at high-redshift. We finally conclude in Section 4.6.

4.2 Data and sample

In this section we outline the deep degree-scale ground-based imaging and derived catalogues, as well as the *JWST* imaging used in this work. Although the area covered by PRIMER is much smaller than ground-based surveys, the improvement in resolution allows us to measure resolved properties in what was previously a seeing-limited sample. We do not conduct a new selection with the *JWST* data to make use of this fact - a seeing-dominated sample is less biased by the sizes, with galaxies being purely selected by being bright in the rest-frame UV, providing a better representation of typical galaxy sizes and avoiding selection effects.

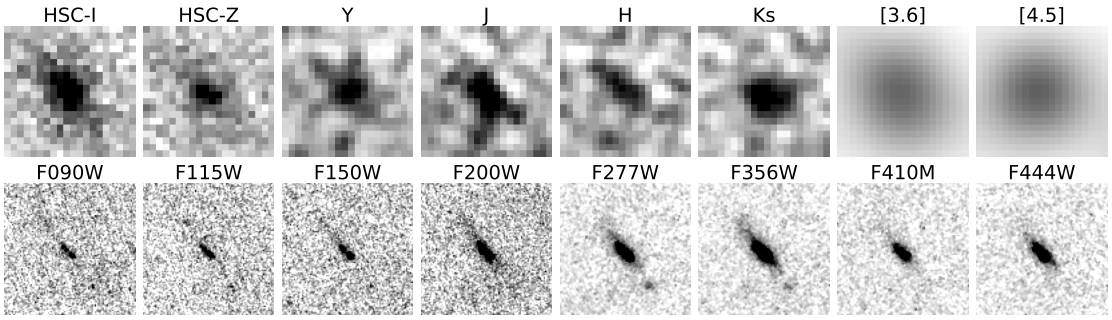

Figure 4.1: Stamps of an example galaxy at $z = 4.58$. **Top:** the ground-based imaging from HSC and VISTA used to select this object, as well as *Spitzer*/IRAC imaging of this galaxy at 3.6μm and 4.5μm. **Bottom:** the *JWST* NIRCam imaging of the same object. The stamps are ordered in increasing wavelength. The resolution is $\sim$ five times better with NIRCam for the seeing-dominated $IZYJHK_s$ bands, and the large FWHM of the *Spitzer* point spread function (PSF) in the [3.6] and [4.5] bands means no morphological information could previously be interpreted. With *JWST*, we can qualitatively see a disk-like morphology in the reddest bands, and a decrease in size to shorter wavelengths. Note that the stamps above/below one another do not necessarily correspond to the same wavelength. The stamps are 4×4 arcsec. North is up and east is to the left. All stamps are scaled with a lower limit at 2σ below the noise level (white). The galaxy (black) saturates at 5σ above the noise level in the top row, 4σ in the short-wavelength NIRCam bands and 10σ in the long-wavelength NIRCam bands.

4.2.1 Ground-based catalogues

We make use of rest-UV selected catalogues in the 1.5 deg^2 COSMOS field and 4.3 deg^2 *XMM*-Large Scale Structure (XMM-LSS) field created by Adams et al. (2023b). The full details of the selection can be found within their section 2, however we summarise it here. Ground-based near-infrared imaging from the UltraVISTA survey (McCracken et al., 2012) in COSMOS and VIDEO (Jarvis et al., 2013) in XMM-LSS is combined with deep optical data from the Canada-France-Hawaii-Telescope Legacy Survey (CFHTLS, Cuillandre et al., 2012) and the Hyper Suprime-Cam Subaru Strategic Program Data Release 2 (HSC-SSP DR2, Aihara et al., 2019) to create multi-wavelength photometric catalogues spanning $0.3-2.4\mu$m. The XMM-LSS field contains the Ultra-Deep Survey (UDS, Lawrence et al., 2007). We update the photometry with the most up-to-date survey data, including HSC-SSP Data Release 3 (Aihara et al., 2022) and UltraVISTA Data Release 5. We show an example galaxy at $z = 4.58$ in these filters in Fig. 4.1. Fluxes are measured in 2 arcsec diameter circular apertures. The LePhare spectral energy

distribution (SED) fitting code (Arnouts et al., 1999; Ilbert et al., 2006) is used to calculate photometric redshifts and classify objects into galaxies, active galactic nuclei (AGN) and Milky Way stars. Objects are split into redshift bins at $z \simeq 3$, 4 and 5 ($2.75 < z < 3.5$, $3.5 < z < 4.5$ and $4.5 < z < 5.5$ respectively). They are then required to be detected at a 5σ threshold in the deepest band containing the rest-frame ultraviolet continuum emission. These are HSC-R, HSC-I and HSC-Z for each redshift bin in the regions containing the *JWST* imaging, outlined in Section 4.2.3. The 5σ depths of the R, I and Z bands are 27.1, 26.9 and 26.5 in COSMOS and 26.4, 26.3 and 25.7 in UDS based on a 2 arcsec diameter circular aperture. For the $z \simeq 5$ sample, a $< 3\sigma$ limit is imposed on the CFHT-u band to ensure a strong Lyman break and to remove further low-redshift interlopers. A cut of $\chi^2 < 100$ is applied to the best-fitting SED solution to remove artefacts and contaminants. *Spitzer*/IRAC data are not used due to blending issues introduced by the large point spread function (PSF). The catalogues are then cross-matched with a spectroscopic sample to test the reliability of the photometric redshifts. The outlier rate (the fraction of photometric redshifts which differ from the spectroscopic redshift by more than $0.15 \times (1 + z)$) is no more than 4.5% in any of the redshift bins. The recovery rate of objects in the spectroscopic sample is also greater than 80% for the redshifts of interest. The COSMOS and XMM-LSS catalogues contain 175,508, 47,978 and 14,875 objects in the $z = 3, 4, 5$ bins respectively.

4.2.2 Photometry and SED fitting

Some objects, particularly at $z \simeq 3$, have effective radii significantly larger than the 2 arcsec diameter aperture used to measure their photometry, resulting in underestimates of the total flux. We use SExtractor (Bertin and Arnouts, 1996) to measure FLUX_AUTO (which uses a flexible elliptical aperture to estimate total flux) in each ground-based filter. We then apply a correction to the aperture fluxes in each band based on the ratio of FLUX_AUTO to the aperture flux in K_s (Adams et al., 2023a). We find that the ratio is similar in the other bands. We then use this corrected ground-based photometry to estimate properties of the sample using

a SED fitting analysis with Bayesian Analysis of Galaxies for Physical Inference and Parameter EStimation (BAGPIPES, Carnall et al., 2018). We use a fiducial constant star formation history (CSFH). Although this choice may not capture complex star formation histories and episodes, it has been found that a CSFH finds similar stellar masses to non-parametric SFHs for very high-redshift galaxies (Whitler et al., 2023). We set the redshift to be the photometric redshift found by Adams et al. (2023b) with LePhare, allowing it to vary by ± 0.1. We adopt a uniform prior on the ionization parameter, $-4 \leq \log U \leq -2$. The metallicity is allowed to vary in the range $0.2 \leq Z/Z_{\odot} \leq 1$, and we assume $Z_{\odot} = 0.02$. Dust reddening was prescribed by the Calzetti et al. (2000) dust law, with attenuation in the range $0.0 \leq A_V \leq 4.0$. The time since star formation switched on varies between the start of the Universe and the redshift being considered. Fig. 4.2 shows the mass and photometric redshift distribution of the sample. For our analysis we take objects with stellar masses $\log_{10}(M_{\star}/M_{\odot}) > 9$ to focus on the massive objects whilst balancing against incompleteness towards lower mass, particularly at higher redshift. By comparing to the stellar mass distribution in a wider area around the PRIMER imaging, we estimate that the $z = 5$ bin is 85% complete. Additionally, the $\log_{10}(M_{\star}/M_{\odot}) > 9$ is the same cut used by Costantin et al. (2023), allowing for a direct comparison to their simulation results. This leaves 1429, 366 and 236 objects in the $z = 3, 4, 5$ bins. We then estimate the *rest-frame* magnitudes of objects in each NIRCam band by convolving the SED found from the ground-based photometry with the NIRCam filter transmission curves. Ideally, we would have used the directly measured NIRCam fluxes to estimate rest-frame magnitudes. However, to ensure consistency with the rest-frame $M_{\rm UV}$ estimation by Adams et al. (2023b), we instead convolve the best-fit SEDs from the ground-based photometry with the NIRCam filter transmission curves. We find that the resulting fluxes are in close agreement with the observed NIRCam photometry, with minimal impact on our results.

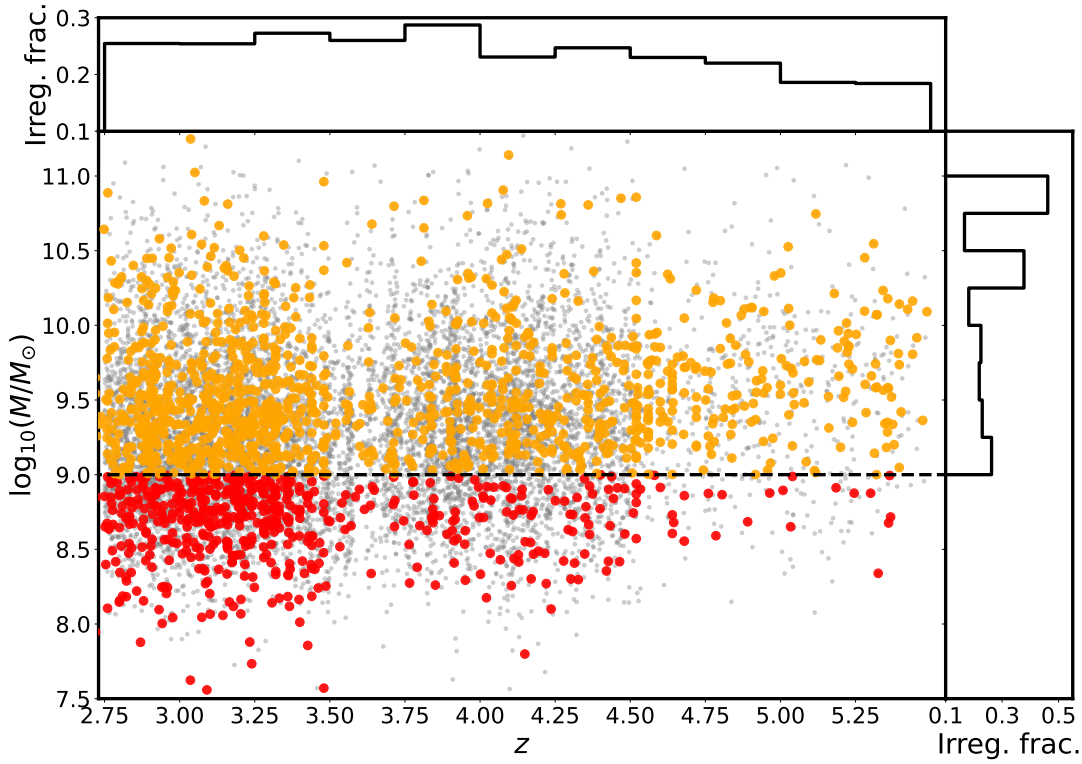

Figure 4.2: The stellar masses (measured using a CSFH with BAGPIPES) of the COSMOS and XMM-LSS catalogues from Adams et al. (2023b) that overlap with the PRIMER imaging, in terms of their photometric redshift. We apply a stellar mass cut at $\log_{10}(M_\star/M_\odot) > 9$. The gray points are stellar masses for objects in a wider region around the PRIMER imaging. The histograms show the fraction of galaxies removed because the PyAutoGalaxy Sérsic fit does not converge, in bins of redshift and mass. These poor fits are used as a proxy of irregular morphology (see Section 4.4.2), and hence this fraction is a proxy for the irregular fraction. Note the different axis scales for each histogram.

4.2.3 *JWST* PRIMER imaging

Public Release IMaging for Extragalactic Research (PRIMER) is a *JWST* Cycle-1 program (GO PID: 1837, PI: J. Dunlop) focusing on two key *Hubble* CANDELS (Grogin et al., 2011; Koekemoer et al., 2011) fields, COSMOS and UDS. The PRIMER imaging used in this chapter was reduced by the PRIMER team [1]. This chapter focuses on the overlap between the COSMOS and XMM-LSS catalogues produced by Adams et al. (2023b) and the 340 arcmin^2 CANDELS-COSMOS and CANDELS-UDS fields imaged by *JWST*, respectively. These fields contain 1572, 1056 and

[1] https://primer-jwst.github.io/team.html

275 objects from the ground-based catalogues in the $z = 3, 4, 5$ bins. Imaging is taken in ten NIRCam+MIRI bands. We make use of the eight deep NIRCam filters, namely F090W, F115W, F150W and F200W from the short-wavelength detector and F270W, F356W, F410M and F444W from the long-wavelength detector, allowing us to probe the rest-frame UV and optical emission of $z \simeq 3-5$ galaxies. We show an example galaxy at $z = 4.58$ in these filters in Fig. 4.1, and show a comparison to the ground-based filters outlined in Section 4.2.1. In this work we primarily make use of F115W, F200W, F356W and F444W. The rest-frame wavelengths covered by these filters at $z = 3-5$ are $\lambda \simeq 0.2-0.3\mu$m, $0.3-0.5\mu$m, $0.6-0.9\mu$m and $0.7-1.1\mu$m respectively. We use version 0.5 of the PRIMER reduction, which contains observations between Dec. 2022 and Jan. 2023. The NIRCam data is reduced using the "jwst_1039.pmap" calibration reference file, and the *JWST* Pipeline version 1.9.4 (Bushouse et al., 2023). Custom steps are taken to remove excess 1/f striping, mask residual snowball artifacts and remove wisp artifacts in F150W and F200W. The astrometry is aligned to *Gaia* Data Release 3 (Gaia Collaboration et al., 2023). The pixel scale of the imaging is 0.03 arcsec per pixel. The 5σ depths of the images used in this work are 27.4 in F115W, 27.9 in F200W, 28.5 in F356W and 28.5 in F444W, measured in 0.3 arcsec diameter circular apertures and using an aperture correction to obtain a total magnitude assuming a point source.

4.3 Methods

In this section we describe how the NIRCam imaging is used for the morphological analysis. The longest wavelength NIRCam filters (F356W, F410M and F444W) provide us with a new view into the rest-frame optical emission of $z \simeq 3-5$ galaxies previously only covered by *Spitzer*/IRAC, opening up a new resolved rest-optical view of high-redshift LBGs.

4.3.1 NIRCam stamps and PSFs

In order to make use of the superior resolution of *JWST* compared to ground-based imaging, we crossmatch the ground-based COSMOS and UDS catalogue

with the PRIMER imaging to extract 20 × 20 arcsec postage stamps of the objects. This corresponds to 667 × 667 pixels. We then use PHOTUTILS (Bradley, 2023) to perform a 2D background subtraction with a box size of 50 pixels, masking objects and bad pixels at a 2σ threshold. We convolve the per-pixel noise maps (corresponding to the "ERR" extension and used for the size fitting) with a Gaussian filter (with standard deviation of two pixels) to remove erroneous very low values, which otherwise lead to artificially high signal-to-noise in individual pixels, causing the morphological fits to fail.

The *JWST* PSF is required for measuring the sizes of galaxies in the sample. A popular tool for modelling the *JWST* PSF is WebbPSF (Perrin et al., 2014). However, it has been found that empirical PSFs constructed from NIRCam imaging often have broader FWHMs than constructed by WebbPSF (e.g. Ding et al., 2022; Ono et al., 2023; Tacchella et al., 2023), likely because PSFs generated by WebbPSF are not drizzled. Additionally, Zhuang and Shen (2024) find strong variation in the NIRCam PSF over the field of view, with variations increasing at shorter wavelengths. They recommend using PSFEx (Bertin, 2011) to construct a grid of empirical PSFs across the image. We use a global PSF model due to the limited number of stars in the field, identified from the FWHM-magnitude diagram with FWHMs taken from SEXTRACTOR. Zhuang and Shen (2024) find that a global PSF still leads to good results, with an average $\lesssim 0.02$ mag systematic offset and $\lesssim 0.05$ mag random scatter when later attempting AGN-host decomposition (see Section 4.3.2). The PSF FWHMs as measured by PSFEx are 0.07, 0.09, 0.16 and 0.17 arcsec in F115W, F200W, F356W and F444W respectively (the filters used in this work). These are shown for F200W and F356W on Fig. 4.8.

4.3.2 Size fitting

In order to compare directly with other studies and with simulations, we use both a parametric and non-parametric method to measure the sizes of galaxies in our sample.

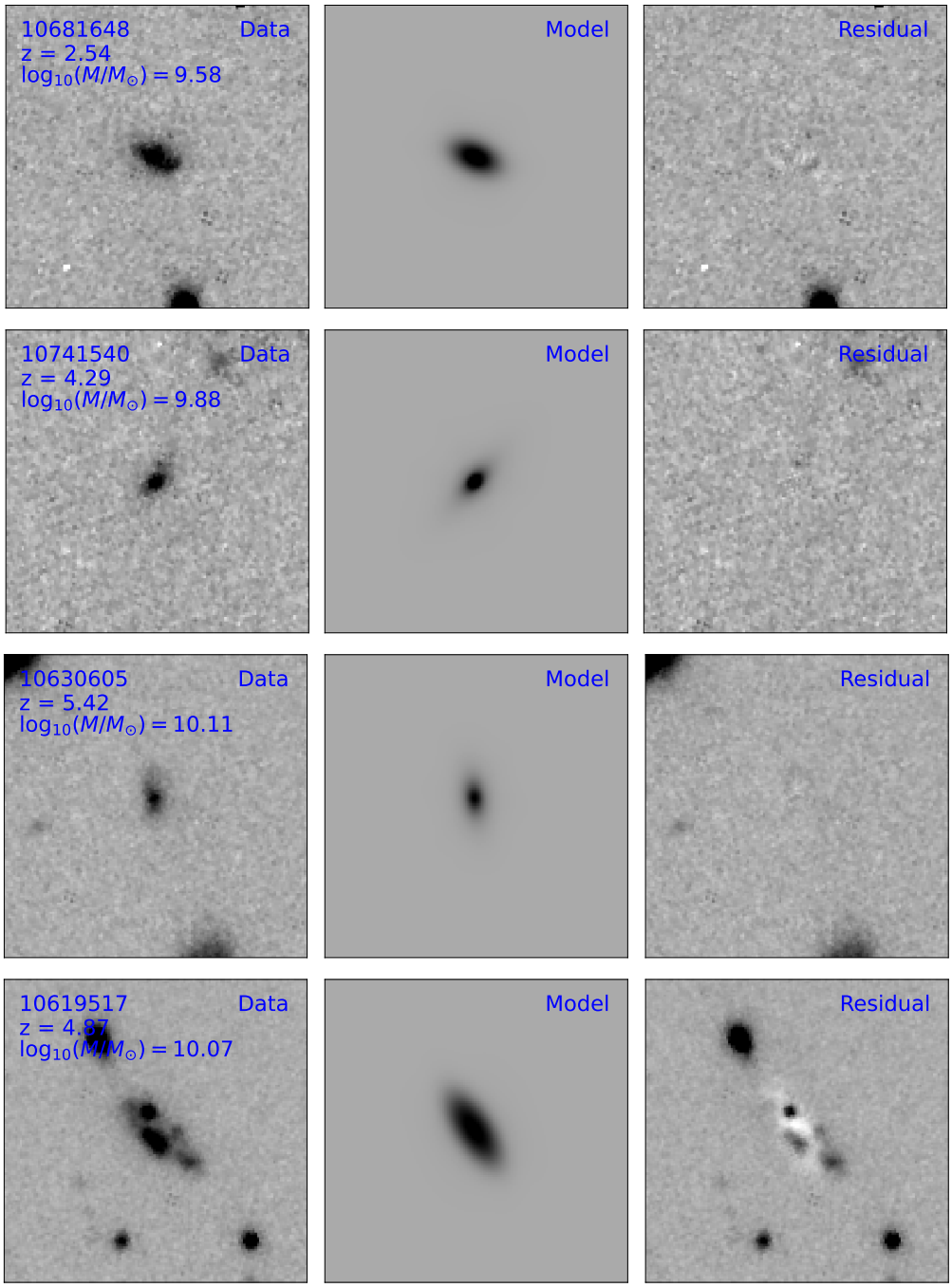

Figure 4.3: Four examples of Sérsic fitting to different galaxies in the sample. In each plot we show the data, model and the residual (data minus model). The ID, photometric redshift and stellar mass of the object are labelled on the data stamp of each galaxy. The top row and bottom left plots show examples from the $z = 3, 4, 5$ bins respectively. The bottom right plot shows an example of a clumpy galaxy where the Sérsic fitting does not perform well, leading to large residuals. The stamps are 4×4 arcsec. North is up and east is to the left. The scaling is set to a lower limit of -0.1 MJy/sr and saturates at 0.3 MJy/sr, which highlights the residuals in the case of poor fits.

Parametric sizes

We make use of PyAutoGalaxy[2] (version 2022.07.11.1, Nightingale et al., 2023) to measure the sizes of galaxies in the NIRCam filters. This takes in the image, noise map and PSF and uses fully automated Bayesian model fitting of galaxy two-dimensional surface brightness profiles to return the best-fit parameters, allowing us to extract the Bayesian Information Criterion (BIC) and assess model fits. We first mask the postage stamp of each object to a circular region of radius 0.7 arcsec, expanding to 1.8 arcsec for the largest objects at $z \simeq 3$. We find that these sizes are sufficient for including the entire object whilst balancing against the number of pixels that are fitted for. These choices also do not affect the results as the best-fit sizes are much smaller than these circular regions. We use a simple Sérsic profile to measure the effective radius R_e. We employ a Gaussian prior on the Sérsic index n, centred at $n = 1$ with a standard deviation of $\sigma_n = 2$ and truncated at an upper limit at $n = 4$ (Kartaltepe et al., 2023). We place a uniform prior on the centre of the object, allowing it to vary within the central 0.2 arcsec to account for any differences in the centroid between the ground-based and *JWST* imaging. The effective radius is allowed to vary between $0-3$ arcsec, and we allow the ellipticity to vary freely. We make use of the 'linear light profiles' available in PyAutoGalaxy where the intensity of the profile is solved for implicitly with linear algebra, reducing the dimensionality of the fitting and removing degeneracies that can occur between intensity and other profile parameters. However, we note that degeneracies can still occur between Sérsic index and size. We input the empirical PSF described in Section 4.3.1 to convolve with the model. We discard bad fits by inspection of residuals in F115W and F444W to check the most extreme wavelengths probed in this work. These bad fits almost always arise in the case of clumpy or irregular morphologies, leading to very large residuals. This leaves 1203, 278 and 187 objects in the $z = 3, 4, 5$ bins. This means we remove 16%, 24% and 21% of the objects that remain from the mass cut in each redshift bin respectively. We show four examples of the Sérsic fitting in Fig. 4.3, including one case of a poor fit to a clumpy galaxy.

[2]https://github.com/Jammy2211/pyautogalaxy

Since the sample selected in Adams et al. (2023b) included both AGN and SFGs, we need to account for objects that may contain accretion-dominated emission and contaminate the total flux, leading to overestimates of stellar mass and inaccurate size measurements. We run a second round of fitting with a PSF+Sérsic profile to account for this, using the initial round of fitting to further inform the priors. We place a Gaussian prior on the centre of the PSF and Sérsic components with a standard deviation of 0.05 arcsec, centred on the position found by the Sérsic-only fitting. Similarly, we employ a Gaussian prior on the ellipticity and Sérsic index, with standard deviations of 0.2 and 0.5 respectively, centred on the values found in the previous round of fitting. These are generally wide enough to account for large differences in the best-fit parameters. We no longer use linear light profiles for the fitting, instead allowing the intensity of both profiles to vary freely so that the contribution from each component can be measured. We apply this fitting in F115W and F444W in order to check for a PSF contribution in both the rest-frame UV *and* the rest-frame optical, motivated by recent discoveries of highly reddened AGN found by *JWST* (e.g. Kocevski et al., 2023; Matthee et al., 2024; Labbe et al., 2025; Juodžbalis et al., 2023; Scholtz et al., 2023). We compute the BIC for both rounds of fitting for each object in order to compare the models. We find that when the PSF+Sérsic fit is preferred according to the BIC, it is preferred in *both* NIRCam filters, revealing no hidden, highly reddened AGN candidates in this UV-selected sample. Objects with a preferred PSF+Sérsic fit (2% at $z = 5$, 6% at $z = 4$, 1% at $z = 3$) are discarded from the sample. We find that the fraction of sources with a PSF component increases towards brighter $M_{\rm UV}$. They are interesting in their own right as Type I AGN candidates, but in this work the sample size of such candidates is small.

We also fit a Sérsic model to the PSFs from the filters used in this work to test the smallest size measurable by PyAutoGalaxy. The Sérsic indexes are typically ~ 0.2. The modal effective radius is 0.15 arcsec and they range from 0.013 arcsec to 0.021 arcsec, comparable to the pixel scale of the imaging (0.03 arcsec). These sizes are significantly smaller than the PSF FWHM (see

Section 4.3.1). At $z = 3, 4, 5$ the maximum size of 0.021 arcsec corresponds to $\log_{10}(R_e/\mathrm{kpc}) = -0.79, -0.84, -0.88$ respectively (see Fig. 4.8).

Non-parametric sizes

We measure a non-parametric size following the pixel-based method of Roper et al. (2022) to compare like-for-like size-luminosity relations. This method is better suited to deal with clumpy and irregular morphologies. We select pixels in the image at a 5σ threshold and then place a circular aperture with a diameter of 2 arcsec on each object, which is large enough to capture the entire object. We then order the pixels in this aperture from most to least luminous. We take the number of pixels containing half the luminosity, and use the pixel area A to compute the radius using $R = \sqrt{A/\pi}$. Roper et al. (2022) use an aperture size enclosing 30 pkpc which is too large for our objects ($\sim 4-5$ arcsec diameter) as neighbouring objects occasionally enter the aperture. The number of pixels containing half the luminosity is generally much smaller than the total number of pixels in the aperture, so our choice of aperture radius does not impact the non-parametric size measurements. The size measured is also broadened by the PSF. To allow for comparison with simulations, we need to account for this effect. We first scale the PSFs constructed in Section 4.3.1 to match the luminosity of the object in each filter. We then measure the size of the PSF in the same manner as before, and then deconvolve assuming the PSF is a Gaussian (by subtracting the PSF size from the initial size in quadrature). In the next section we present a brief comparison of the Sérsic and non-parametric sizes.

Comparison between Sérsic and non-parametric sizes

In Fig. 4.4 we show the ratio of Sérsic size to non-parametric size as a function of both stellar mass and redshift for objects with a good Sérsic fit, as measured in F356W. We bin the data such that there is an equal number of galaxies in each bin. The errors are the standard error on the mean. The mean ratios in the bins show little evolution across mass and redshift, remaining at a value just above one. As discussed in Section 4.4.5, this is expected as in some cases the Sérsic fitting

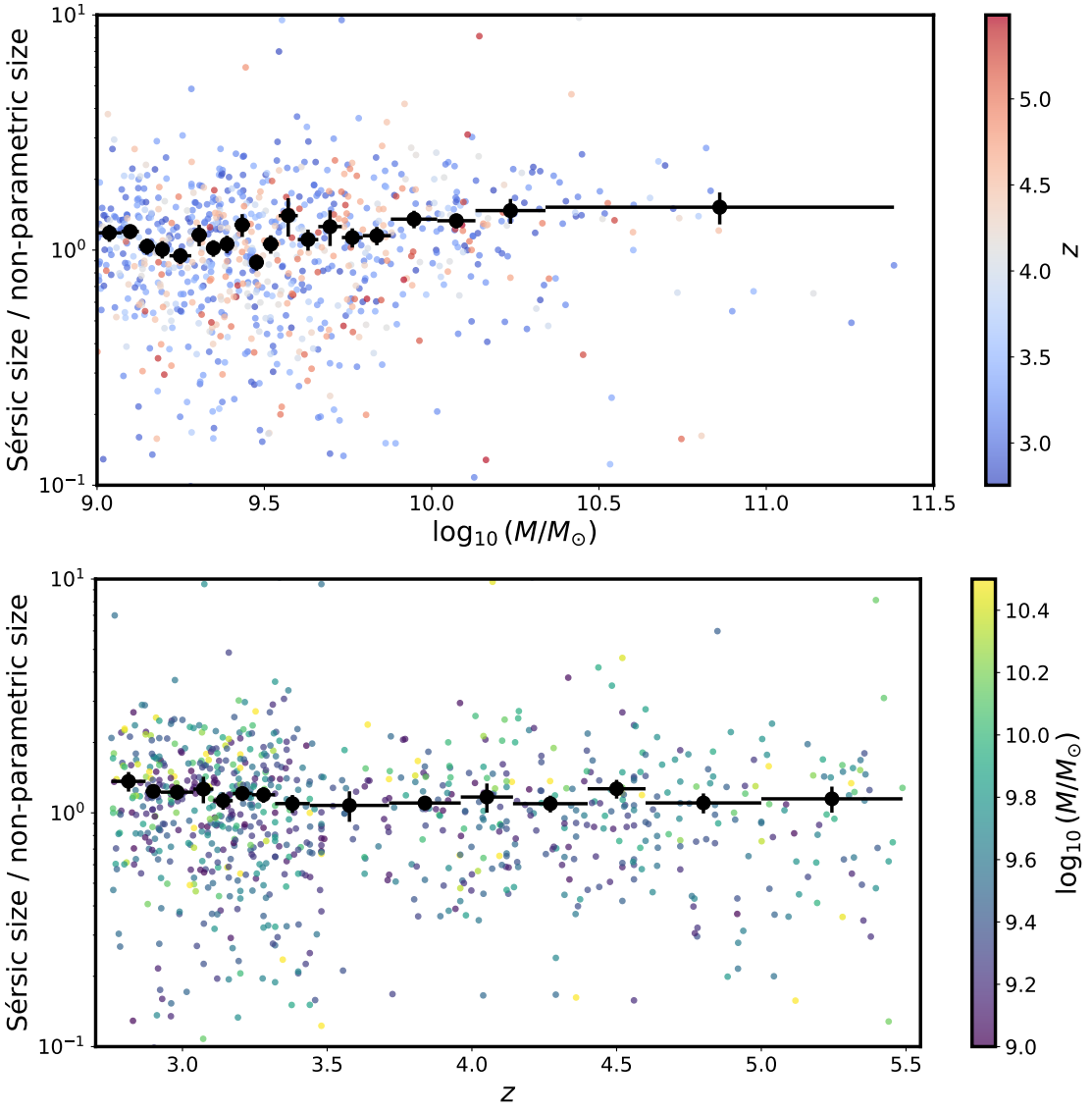

Figure 4.4: Top: the ratio of Sérsic size to non-parametric size in F356W as a function of stellar mass for galaxies with a good Sérsic fit. Individual galaxies are coloured by their photometric redshift. **Bottom:** now the ratio is plotted as a function of photometric redshift, with galaxies coloured by their stellar mass. In both panels, the black points show the results of binning the size ratio.

Table 4.1: The mean, median and modal (log-normal peak) Sérsic sizes of galaxies in this work in redshift bins at $z = 3, 4, 5$.

	Mean (kpc)	Median (kpc)	Log-normal peak (kpc)
$z = 3$	1.56 ± 0.07	1.10 ± 0.03	0.86 ± 0.03
$z = 4$	1.40 ± 0.04	1.03 ± 0.04	0.88 ± 0.07
$z = 5$	1.16 ± 0.05	0.98 ± 0.05	0.79 ± 0.08

may tend to find larger sizes. The amount of scatter appears to be consistent with simulations (e.g. Costantin et al., 2023; LaChance et al., 2025).

4.4 Results

In this section we present the results of the size fitting and the dependence of size on redshift, stellar mass and luminosity. The sizes reported in the log-normal distributions and the size-redshift relations are measured in F356W to compare directly with the predictions of Costantin et al. (2023), probing $0.6 - 0.9$ μm in the rest frame. Similarly, the Sérsic size-mass relations are reported in F200W (probing rest-frame $0.3 - 0.5$ μm) and F356W to compare directly with Costantin et al. (2023). For the size-luminosity relations (with both size measurement methods) we use F115W and F444W, which probe $0.2 - 0.3$ μm and $0.7 - 1.1$ μm respectively, to maximise the difference in wavelength to provide a clearer comparison to the predictions of Roper et al. (2022).

4.4.1 Log-normal distribution fitting

In the top panel of Fig. 4.5 we show histograms of Sérsic sizes in each redshift bin. We also show the log-normal fit to each distribution. We use SciPy (Virtanen et al., 2020) to fit a log-normal function to the size distributions in each redshift bin. Errors on the peak of the fit are estimated with bootstrapping. We find that the size distributions are well-described by the log-normal function, with reduced χ^2 values of $\chi^2_{\rm red} = 1.16, 1.11, 1.08$ in the $z = 3, 4, 5$ bins respectively. Using the peak as a measure of typical (modal) galaxy size in each bin, we find sizes of $\bar{R}_e = 0.79 \pm 0.08$ kpc at $z \simeq 5$, $\bar{R}_e = 0.88 \pm 0.07$ kpc at $z \simeq 4$ and $\bar{R}_e = 0.86 \pm 0.03$ kpc at $z \simeq 3$. These values are consistent with no evolution in the typical size of

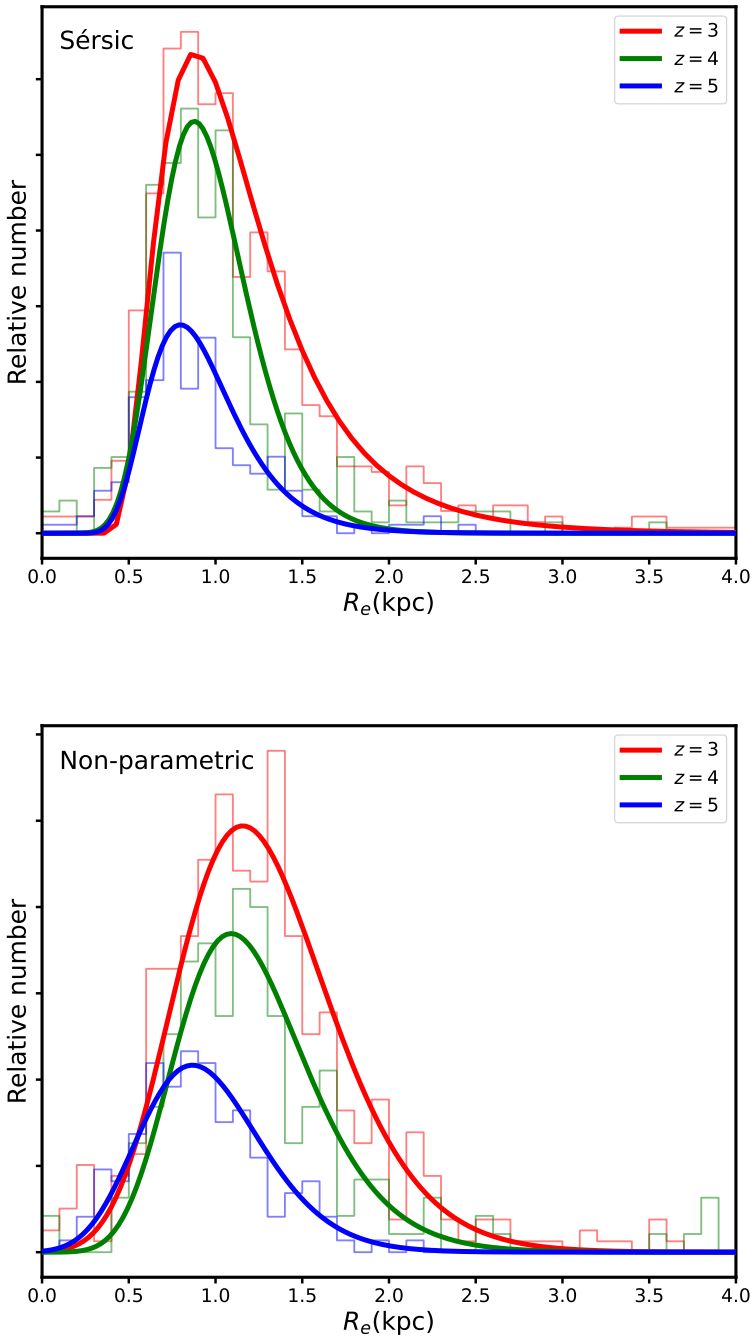

Figure 4.5: The size distribution of galaxies in each of our redshift bins measured in F356W. **Top:** Sérsic size fitting. **Bottom:** non-parametric size fitting. We show the distributions as histograms, and then plot the log-normal fit to the distributions. The $z = 4$ and 5 distributions are scaled by a factor of two and three respectively to emphasise the relative positions of the peaks. This peak is taken as the size of a typical galaxy in each redshift bin.

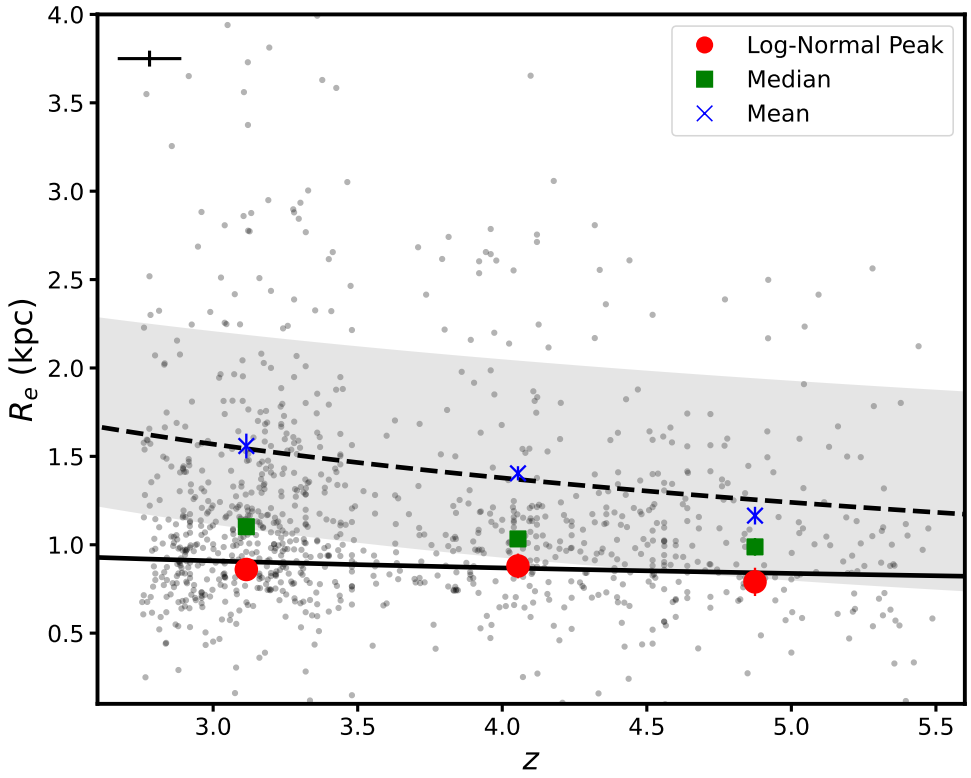

Figure 4.6: The size-redshift distribution of our galaxies as measured in F356W. **Top:** Individual galaxy size and photometric redshift measurements are shown by the grey circles. The typical error is shown in the top left. At the mean redshift of each redshift bin ($\bar{z} = 2.96, 4.04, 4.91$) we plot different measures of the typical size and their errors. Circles represent the fit of the log-normal fit to the Sérsic size distribution, squares represent medians and crosses represent means (values are reported in Table 4.1). The black dashed line represents the best-fit redshift evolution to all the data without binning, $R_e = 3.51(1+z)^{-0.60\pm0.22}$ kpc, and the shaded region shows the error. The solid black line shows the best-fit line if we fix the power α in this relation to $\alpha = -0.20$, following the evolution found by Curtis-Lake et al. (2016) at $z = 4 - 8$.

galaxies over $z = 3 - 5$. This weak evolution extends the findings of Curtis-Lake et al. (2016) at $z = 4 - 8$ to lower redshifts (although we note the different size definition of circularised half-light radii in that work). Shibuya et al. (2015) also find compact Sérsic sizes ($R_e < 1$kpc) at $z > 3$ using the peak of the log-normal distribution. They find this for a bright ($L_{\rm UV} = 0.3 - 1L^*_{z=3}$) *Hubble*-selected sample, where $L^*_{z=3}$ is the characteristic luminosity of LBGs at $z = 3$, corresponding to $M_{\rm UV} = -21$ (Steidel et al., 1999).

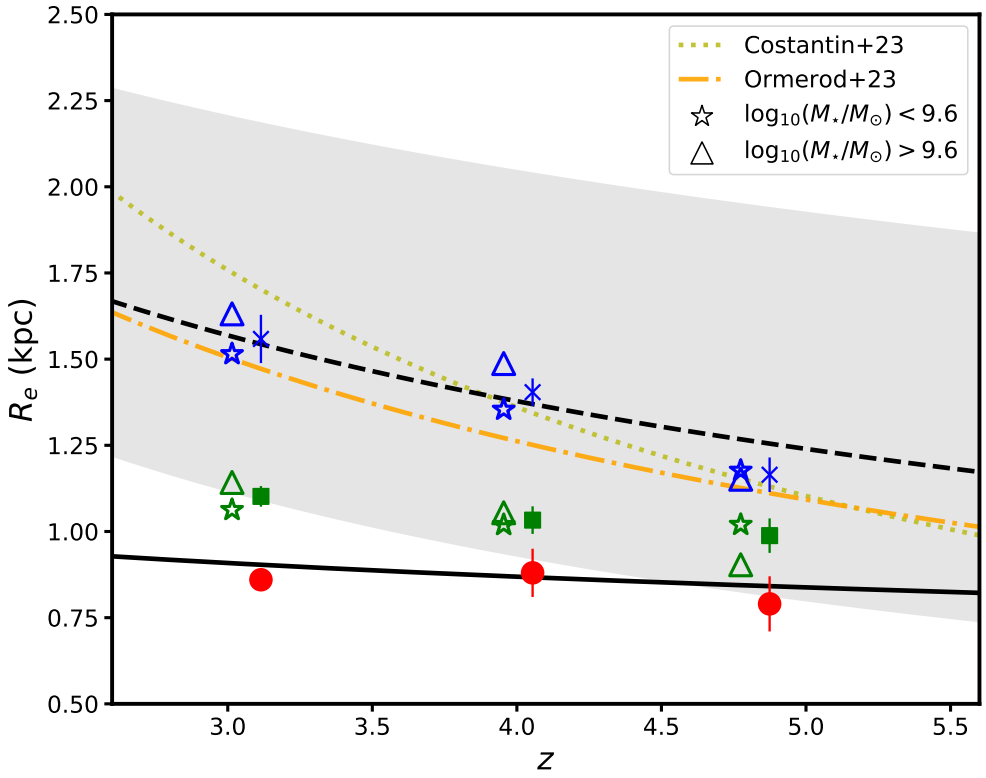

Figure 4.7: The size-redshift distribution of our galaxies as measured in F356W, as in Fig. 4.6, but with individual measurements removed. Here we compare our best-fit evolution, median and log-normal peak measurements as in the left panel to results from Ormerod et al. (2024) and predictions from Costantin et al. (2023). We also plot the median and mean values when the sample is split into two mass bins at $\log_{10}(M_\star/M_\odot) = 9.6$. Note the narrower R_e axis compared to Fig. 4.6 for clarity.

There appears to be some evolution in the tail of the distribution via emergence of objects with $R_e \gtrsim 2$ kpc between $z \simeq 3-4$. To test whether this is a genuine build-up in the tail or due to the limited volume probed and the evolving rest-UV luminosity function over $z = 3-5$ (Adams et al., 2023b), we scale the $z = 3$ distribution by the total number of galaxies at $z = 4$ and 5 and calculate the expected number of large galaxies by integrating under the curve at $R_e > 2$ kpc. If the intrinsic distributions are the same across redshift and only changes due to the limited volume, then the expected numbers from the scaled distribution should match the observed distributions. At $z = 4$ and $z = 5$ we expect 5^{+12}_{-4} and 6^{+21}_{-5} galaxies with $R_e > 2$ kpc respectively by integrating the tail of the curve. The

scaled $z = 3$ distribution predicts 133^{+17}_{-16} and 77^{+10}_{-9} galaxies with $R_e > 2$ kpc at $z = 4$ and $z = 5$. This points to a genuine build-up in the tail of the distribution in the high-mass end, suggesting a transition between $z = 3$ and $z = 4$, where much larger, extended structures begin to develop within galaxies.

A source of bias in measuring this tail of large galaxies comes from cosmological surface brightness dimming. This makes low-surface brightness regions of galaxies more difficult to detect at higher redshift. To test this, a sub-sample of the $z = 3$ sources (including $R_e > 2$ kpc galaxies) were redshifted out to $z = 5$. The scatter in the redshifted sizes is 20%, consistent with the error on the size measure. There is no dependence on the initial size at $z = 3$, i.e. the scatter is not larger for galaxies with extended morphologies. We conclude that cosmological dimming does not significantly bias our results.

4.4.2 Irregular galaxies

We note that the Sérsic fitting employed here fails on disturbed/irregular and clumpy galaxies, and such fits are discarded. Huertas-Company et al. (2024) conduct a morphological analysis of $\log_{10}(M_\star/M_\odot) > 9$ galaxies in CEERS at $z = 0 - 6$. They find that the disturbed fraction of galaxies in F150W at $z \simeq 3 - 6$ remains high at $\sim 70\%$ for $\log_{10}(M_\star/M_\odot) \sim 9 - 10.5$. Although we measure sizes in F356W where we find a lower fraction of disturbance, we may still underestimate a tail of large objects due to the failure of the Sérsic fitting for irregular morphologies. We therefore also carry out the log-normal fitting on our non-parametric sizes, shown in the bottom panel of Fig. 4.5. The distributions are still well-fit by the log-normal distribution, with reduced χ^2 values of $\chi^2_{\rm red} = 1.11, 1.13, 1.07$ in the $z = 3, 4, 5$ bins respectively. There appears to be a mild evolution in the typical size when clumpy/irregular galaxies are included, with $\bar{R}_e = 0.86 \pm 0.11$ kpc at $z \simeq 5$, $\bar{R}_e = 1.09 \pm 0.07$ kpc at $z \simeq 4$ and $\bar{R}_e = 1.15 \pm 0.03$ kpc at $z \simeq 3$. The distributions are also broader than their Sérsic counterparts due to the contribution by large ($R_e > 1$ kpc) clumpy/irregular systems.

We can use the fraction of bad Sérsic fits as a proxy for the irregular fraction. Here, irregular includes disturbed and clumpy morphologies. In Fig. 4.2 we show the irregular fraction binned in both redshift and stellar mass. The irregular fractions drops from 0.25 at $z = 5$ to 0.20 at $z = 3$. This agrees with visual classification results from Ferreira et al. (2023), who find that galaxies with $\log_{10}(M_\star/M_\odot) > 9$ at $z > 3$ are not dominated by irregular structures. Our results are also in agreement with Kartaltepe et al. (2023), who find that the irregular fraction increases from 0.2 at $z = 5$ to 0.3 at $z = 3$. Our results differ from the visual classification by Jacobs et al. (2023), who find a very high peculiar fraction of ~ 0.9 at $z \approx 4.9$, dropping to nearly zero at $z \approx 2.5$ for $\log_{10}(M_\star/M_\odot) > 9.5$, although the number of galaxies in their high-mass bins is small. They see a constant peculiar fraction of ~ 0.6 over $z = 3-5$ in their lower-mass bin, $\log_{10}(M_\star/M_\odot) < 9.5$. This higher value compared to our fraction may be caused by the inclusion of low-mass galaxies ($\log_{10}(M_\star/M_\odot) < 9$) where we apply a cut. In terms of stellar mass, our irregular fraction decreases slightly between $10^9 M_\odot$ and $10^{10} M_\odot$. This trend broadly agrees with Jacobs et al. (2023), who find that the fraction of peculiars is higher at $\log_{10}(M_\star/M_\odot) < 9.5$. However, our irregular fraction spikes up to larger values at $M > 10^{10.5} M_\odot$. In the high-mass regime, a visual inspection reveals that the irregular galaxies in our sample appear to be merging systems, such as the bottom-right galaxy in Fig. 4.3.

4.4.3 Size-redshift evolution

In Fig. 4.6 and Fig. 4.7 we show the size evolution of our sample with redshift. Fig. 4.6 shows the individual measurements for each LBG, as well as various measures of the average size (mean, median and log-normal peak) in each redshift bin. These values are reported in Table 4.1. The mean and median values in each bin are significantly larger than the log-normal peaks (based on Sérsic sizes), due to being skewed by large objects. The black dashed line shows the best fit derived from fitting to the full sample (all galaxies with $\log_{10}(M_\star/M_\odot) > 9$) using a power law parameterisation $R_e = R(1+z)^\alpha$. Our best fit finds $R_e = 3.51(1+z)^{-0.60\pm0.22}$ kpc. This evolution in R_e suggests larger sizes at lower redshift, differing from

the roughly constant sizes with redshift implied by the log-normal peaks in Fig. 4.6, which trace the typical galaxy size. However, due to large scatter in the sizes there is large uncertainty in the power-law fitting.

In Fig. 4.7 we compare our results to other studies using *JWST*. Our power-law fit and mean sizes in each redshift bin are remarkably consistent with the power-law fitting of Ormerod et al. (2024), who measure the size evolution of galaxies across $z = 0 - 8$. Their relation is based on the mean size of galaxies with redshift. We note that they use a slightly smaller area than this study (64 arcmin^2). Their power-law index is in agreement with ours with $\alpha = 0.71 \pm 0.19$. Our results also agree with the evolution determined by Ward et al. (2024), who find a size evolution with power-law index of $\alpha = 0.63 \pm 0.07$ using 97 arcmin^2 of *JWST* imaging. We note that their determination differs slightly - they find the evolution at a fixed stellar mass of $5 \times 10^{10} M_{\odot}$.

The build-up in the tail of the log-normal distribution (see Section 4.4.1) is complemented by a size-redshift relation that finds larger sizes at lower redshift. Together, they suggest an emergence of large ($R_e > 2$) galaxies at $z = 3$. We can complement this result with a measure of the evolution of *typical* galaxy sizes by focusing on our log-normal peaks. Our use of log-normal distribution fitting is based on the results of Curtis-Lake et al. (2016), which is physically motivated (see Section 4.5.1) and better accounts for the typical size of galaxies by incorporating a tail for the largest objects. Additionally, using the log-normal peak of the distribution allows for a determination of the typical size of the galaxy in samples that are down to 50% complete. Curtis-Lake et al. (2016) mention that selection effects need to be accounted for carefully with certain flux cuts to ensure the typical sizes of galaxies can be recovered. They find that selection effects in previous works (e.g. Shibuya et al., 2015) preferentially biases towards smaller sizes due to their choice in selection methodology. Shibuya et al. (2015) require a signal-to-noise of 15 in a 0.35 arcsec diameter aperture, tending to select smaller galaxies. We do not expect to be preferentially skewed to smaller galaxies because the 5σ depths of the PRIMER imaging is $\sim 0.3 - 3$ mag deeper than the ground-based filters used to

select the sample. Additionally, the ground-based selection is seeing-dominated and therefore less affected by size. Curtis-Lake et al. (2016) find a redshift evolution $R_e \propto (1+z)^{-0.20}$ kpc at $z = 4-8$ when fitting to their log-normal peaks, a much weaker evolution than Shibuya et al. (2015) and Costantin et al. (2023). If we fix the exponent $\alpha = -0.20$, also shown in Fig. 4.6 and fit for the power law coefficient to our log-normal peaks, we find a relation that agrees with our typical galaxy sizes, extending the results of Curtis-Lake et al. (2016) to $z = 3$.

Comparison with other studies

The illustrisTNG simulation (Pillepich et al., 2018) is used by Costantin et al. (2023) to measure the sizes of $\log_{10}(M_\star/M_\odot) > 9$ galaxies with artificial noise added to match the depth of the Cosmic Evolution Early Release Science survey (CEERS, Finkelstein et al., 2017). Our mean sizes are 15% smaller than the predictions of Costantin et al. (2023) at $z = 3$. They conclude that their upturn in the size evolution is attributed to more massive galaxies becoming larger at $z \simeq 3$, and our best-fit derived from the full sample recovers a similar trend, but not as steep (although agreeing within the errors). Similarly, Ormerod et al. (2024) do not observe a redshift evolution as steep in their *Hubble* + *JWST* sample. The CEERS fields have an area of ~ 100 arcmin^2, a factor of ~ 3.8 less than PRIMER. Although scaling the log-normal distributions (see Section 4.4.1) suggests a genuine build-up of large galaxies, we caution that conclusions regarding the growth of high-mass galaxies require a similar analysis on larger volumes.

Costantin et al. (2023) measure median values in three mass bins centred at $\log_{10}(M_\star/M_\odot) = 9.1, 9.4$ and 10.0. In Figure 4.7 we show our mean and median sizes when split into two mass bins at $\log_{10}(M_\star/M_\odot) = 9.6$. We use two bins because there are too few objects in the low- and high-mass bins when using the same binning as Costantin et al. (2023). Additionally, this value approximately splits the sample in half. We find that at $z = 5$, both the mean and median sizes in the low-mass bin are larger than in the high-mass bin. At $z = 3-4$ the mean and median sizes are larger in the high-mass bin. A similar trend is seen in Costantin

Table 4.2: The best-fit values for the size-mass relation given by $\log_{10}R_e = a \times \log_{10}(M_\star/M_\odot) + b$ and the intrinsic scatter $\sigma_{\log R_e}$ in each redshift bin and for each filter used.

F200W	**a**	**b**	$\sigma_{\log R_e}$ (dex)
$z = 3$	0.11 ± 0.05	-0.96 ± 0.32	0.28 ± 0.01
$z = 4$	0.06 ± 0.05	-0.48 ± 0.48	0.30 ± 0.01
$z = 5$	-0.11 ± 0.06	1.04 ± 0.56	0.24 ± 0.01
F356W	**a**	**b**	$\sigma_{\log R_e}$ (dex)
$z = 3$	0.05 ± 0.03	-0.46 ± 0.29	0.25 ± 0.01
$z = 4$	0.03 ± 0.04	-0.26 ± 0.38	0.23 ± 0.01
$z = 5$	0.03 ± 0.05	-0.32 ± 0.44	0.21 ± 0.01

et al. (2023), and this reflects the flat/negative size-mass relations (see Section 4.4.4). Costantin et al. (2023) also see a broadening in their median sizes towards lower redshift and a convergence to similar values at higher redshift when binning in mass (see their fig. 8). Although we see this to some extent, the broadening of sizes between the bins by $z = 3$ is not as pronounced - they differ by no more than 0.15 kpc at any redshift (compared to > 0.5 kpc in Costantin et al. (2023)). This suggests a weak mass dependence of the size-redshift evolution in our sample.

To summarise, we find that whilst the *typical* size of galaxies does not evolve significantly over $z = 3 - 5$ (as measured by the log-normal peaks of Sérsic sizes in each redshift bin), there is evidence for an emergence of large ($R_e > 2$ kpc) galaxies when we fit for the entire sample (i.e. all galaxies with $\log_{10}(M_\star/M_\odot) > 9$).

4.4.4 Size-mass relations

In Fig. 4.8 we present the Sérsic size-mass relations in each redshift bin for both F200W and F356W in order to compare directly with the predictions of Costantin et al. (2023). They use the illustrisTNG simulation (Pillepich et al., 2018) to measure the Sérsic sizes of $\log_{10}(M_\star/M_\odot) > 9$ synthetic galaxies matching those found in the Cosmic Evolution Early Release Science survey (CEERS, Finkelstein et al., 2017). We fit straight lines of the form $\log_{10}R_e = a \times \log_{10}(M_\star/M_\odot) + b$. The independent variables in our size-mass and size-luminosity relations themselves possess errors, complicating the task of fitting a straight line. Bartlett and Desmond (2023) find that common approaches to dealing with both x and y errors can ignore

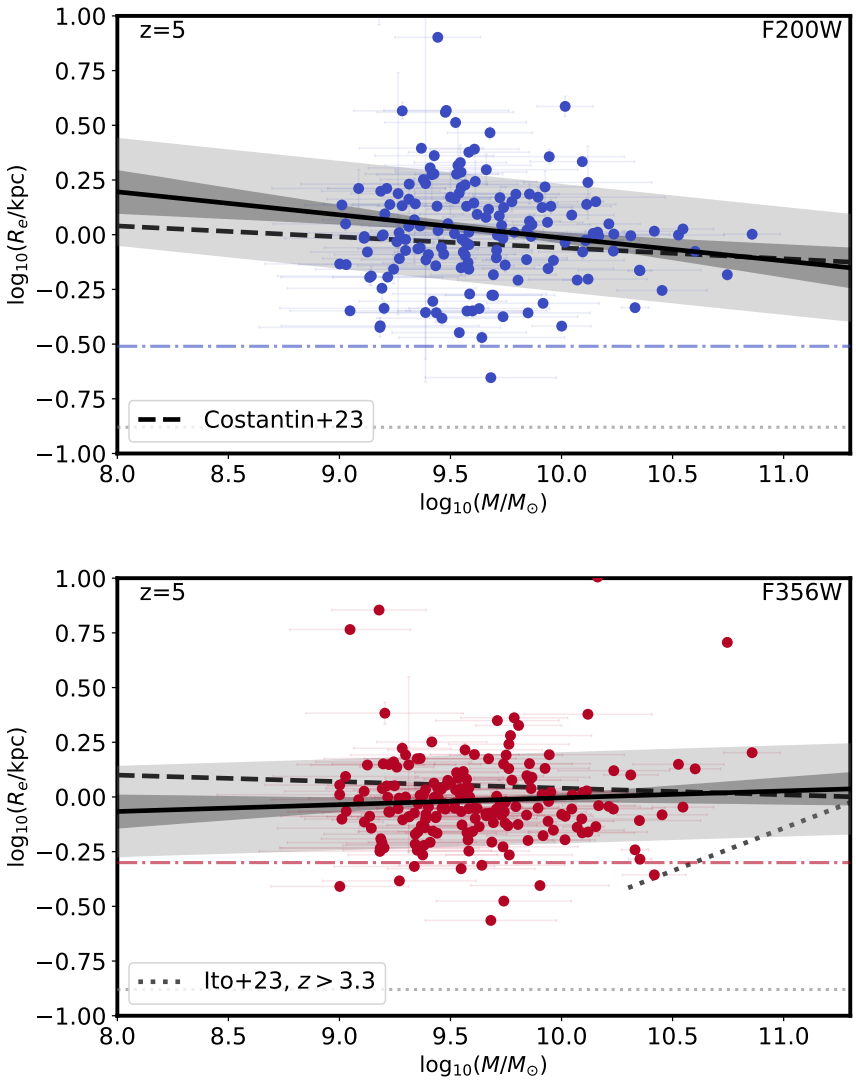

Figure 4.8: The Sérsic size-mass relations of our sample. Each set of two plots shows a redshift bin (labelled in the top-left of each panel), beginning with $z = 5$. The first of the two plots shows size measurements made in F200W, and the second shows F356W. The points and errors show individual measurements, and the black solid line shows the best-fit line. The light-gray shaded region represents the intrinsic scatter, and the dark-gray shaded region represents the statistical error. The dashed black line shows predictions for the size-mass relations in each filter and redshift bin from Costantin et al. (2023). The horizontal dash-dotted line represents the PSF FWHM of each filter, converted to an equivalent radius at each redshift. The horizontal dotted gray line at the bottom of each panel represents the size inferred for a point source by PyAutoGalaxy (see Section 4.3.2). On the F356W results we also show the rest-optical size-mass relations at $z = 3-5$ for massive quiescent galaxies found by Ito et al. (2024).

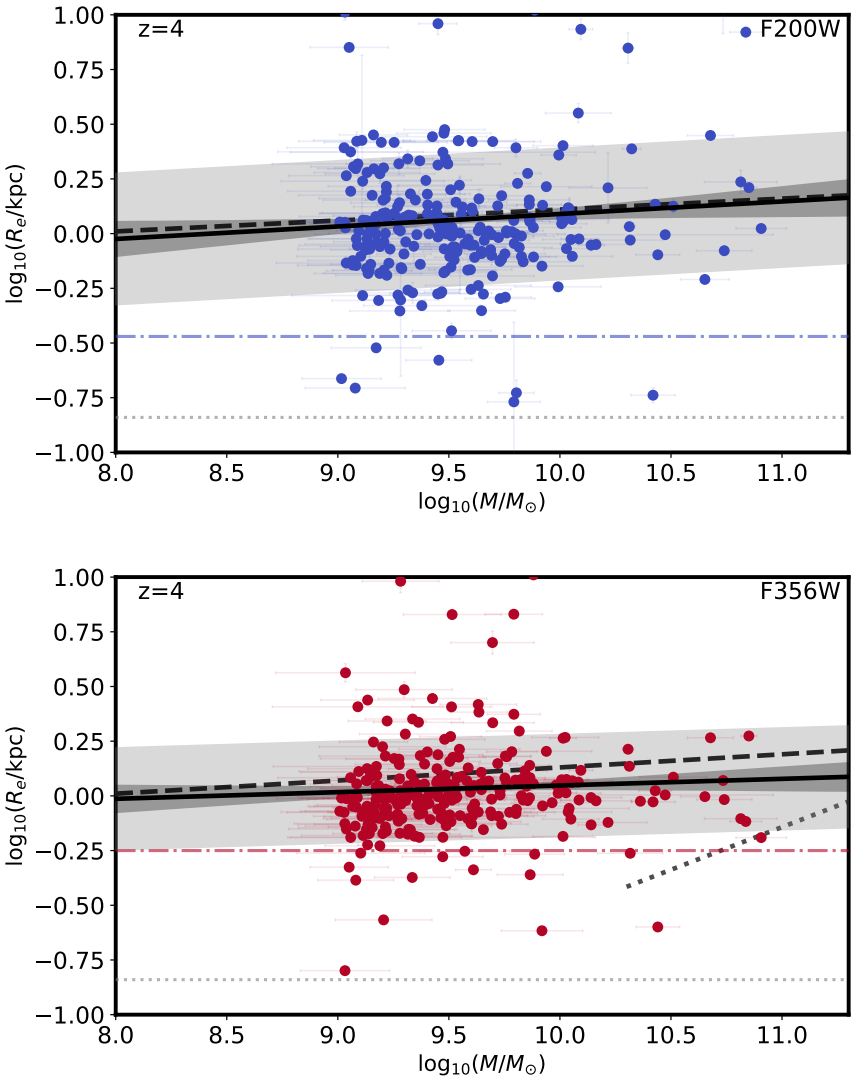

Figure 4.8: Continued, $z = 4$.

the underlying distribution of the true independent variable values, leading to biased results (see references therein). They find that using a single Gaussian prior (with mean and variance to be determined as part of the inference) on 'latent variables' describing the true values of the independent variables performs best, and they dub this 'Marginalised Normal Regression'. It is key that this works in the presence of intrinsic scatter, an additional property we want to measure. We therefore use their *Regression and Optimisation with X and Y errors* (ROXY) package[3] to fit the size relations. We measure the intrinsic scatter and compare it to the statistical error

[3]https://github.com/DeaglanBartlett/roxy

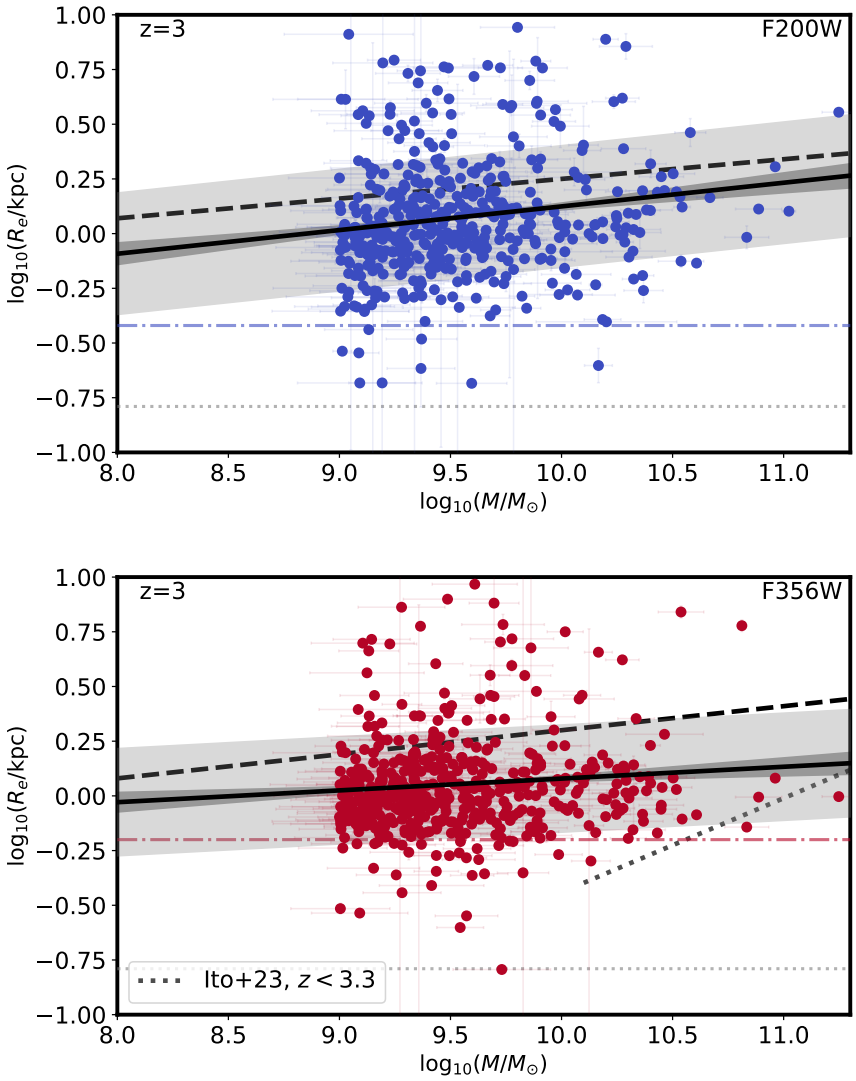

Figure 4.8: Continued, $z = 3$.

of the fitting. We present the best-fit values in Table 4.2. In order to assess the robustness of measuring very small sizes, we compare the PSF sizes (see Section 4.3.1 and Fig. 4.8) to the sizes of our sample. The PSF FWHMs correspond to sizes of 0.38 kpc (0.63 kpc) at $z = 3$ in F200W (F356W), 0.34 kpc (0.56 kpc) at $z = 4$ in F200W (F356W) band, and 0.31 kpc (0.50 kpc) at $z = 5$ in F200W (F356W). In these bands, 95% of the sample is larger than the PSF FWHM, meaning the majority of sources are resolved. We verified that removing the unresolved sources from the sample does not significantly change the size-mass relation. We note that any observational biases towards larger sizes in this work due to the PSF minimum

size are also present in Costantin et al. (2023), still allowing for a direct comparison. IllustrisTNG indeed predicts sizes smaller than the PSF FWHM (see their fig. 7), which are not measurable in the mock observations.

Interestingly, at $z = 5$ we see some evidence for a negative size-mass relation in F200W, consistent with the prediction of negative slopes by Costantin et al. (2023). A negative slope is allowed in F356W within errors. At $z = 4$, the slopes in F200W and F356W are both positive and consistent with one another. We also find that the slopes are consistent with Costantin et al. (2023). At $z = 3$, the slope in F356W appears to be flatter than that in F200W. We test whether the fit is being skewed by the relatively compact objects at $\log_{10}(M_\star/M_\odot) \gtrsim 10.5$ in F356W by re-fitting without them, and find that the results do not change significantly. The relation in F200W is consistent with Costantin et al. (2023), and the F356W relation appears flatter but is consistent within 2σ. Our slopes are flatter than those found by Ward et al. (2024), who measure the rest-5000Å sizes of star-forming galaxies in 97arcmin^2 of CEERS imaging. They find a gradient of $a = 0.25$ in a redshift bin of $z = 3.0 - 5.5$, and a gradient of $a = 0.15$ in a redshift bin of $z = 2.0 - 3.0$. We note some differences between our methodologies - our redshift bins span almost the whole range of their highest redshift bin, and their $z = 2.0 - 3.0$ bin will contain objects at lower redshifts than we can select for, complicating the comparison. Broadly speaking, Ward et al. (2024) find a flattening of the size-mass relation at lower redshifts, and we see hints of this from $z = 5$ to $z = 4$. Similarly, Pandya et al. (2024) find some evidence for a flattening size-mass relation over $z = 3 - 8$.

Intrinsic scatter

One notable result is that the intrinsic scatter of objects about the best-fit relation increases with decreasing redshift, and is lower in F356W than in F200W by 0.03-0.07 dex. The values are reported in Table 4.2. By plotting both the intrinsic scatter and statistical error in Fig. 4.8, we can see that the intrinsic scatter dominates over measurement errors in the fitting. Morishita et al. (2023) measure the size-mass relation in star-forming galaxies at $5 < z < 14$ and find a redshift-corrected intrinsic

scatter of $\sigma_{\log R_e} = 0.30 \pm 0.01$ dex, consistent with our findings at $z = 3-4$ in F200W but higher than our findings in F356W (see Table 4.2). Our intrinsic scatters increase by 0.04 dex from $z = 5$ to $z = 3$ in both F200W and F356W. The values in F200W are larger than low-redshift ($z < 1$) results for both star-forming and quiescent galaxies, being more consistent with our results in F356W ($\sigma_{\log R_e} \simeq 0.20$ dex, Kawinwanichakij et al., 2021). Whilst our values in F356W broadly agree with Ward et al. (2024), the increase we find is in disagreement with their constant intrinsic scatter (~ 0.2 dex) out to $z = 5.5$. This is likely due to the fact that their highest redshift bin nearly encapsulates all three of our redshift bins.

Comparison with quiescent galaxies

The infrared coverage provided by *JWST* has allowed for the selection of massive quiescent galaxies at $z > 3$, implying extremely early quenching episodes at $z \gtrsim 5$ (e.g. Carnall et al., 2023a; Carnall et al., 2023b; Long et al., 2024; Ito et al., 2024; Ji et al., 2024). We can thus compare our results for star-forming LBGs to the quiescent population in the rest-optical at $z = 3-5$. In Fig. 4.8 we show the findings of Ito et al. (2024) to compare to our F356W results. Although our number counts are low at $\log_{10}(M_\star/M_\odot) > 10.5$, extrapolating our results would suggest that quiescent galaxies tend to be more compact than star-forming galaxies, as seen at lower redshifts (van der Wel et al., 2014). Additionally, Ji et al. (2024) also find compact sizes for massive ($\log_{10}(M_\star/M_\odot) > 10$) quiescent galaxies at $z = 1.6-5$.

Ito et al. (2024) note that AGN may result in apparent compact sizes for some objects, but do not remove any objects since none have X-ray detections. They also find that quiescent galaxies are more compact with increasing wavelength, which could be caused by inside-out quenching that produces compact morphologies for evolved stellar populations. Although wider areas are needed to better constrain the positions of the most massive objects in the size-mass plane, perhaps this explains the flatter relation we find using F356W compared to F200W at $z = 3$ where massive galaxies are still undergoing intense star formation, but have begun to quench in their centres. Ormerod et al. (2024) find a similar trend for both

star-forming and passive galaxies at $z < 3$, also interpreting this as evolved stars occupying the central regions of galaxies with star formation occuring at larger radii. Similarly, at $z = 3-4$ Allen et al. (in prep.) find a flattening of the size-mass relation at longer wavelengths. Correspondingly, at $z = 1-2.5$ Suess et al. (2019a) find that most star-forming and quiescent galaxies have negative colour gradients (i.e. redder in their centres and bluer at larger radii). They also find that the colour gradient evolves rapidly over this redshift range (Suess et al., 2019b), broadly fitting into the picture of inside-out growth and quenching.

Overall, we find good agreement of our results with predictions from simulations. Although the slope of the relations appear to transition from positive to negative at $z = 4-5$, a lack of dynamic range in mass limits this conclusion. However, we do find a decrease in the intrinsic scatter with increasing redshift. Better dynamic range in massive objects is required to better constrain and confirm the negative slopes at $z = 5$, the flattening of the F356W slope, and the evolution of the gradients. We note that in order to compare directly with Costantin et al. (2023) we use the same filters across the full redshift range, meaning there is a shift in the rest-frame wavelengths probed ($\lambda \simeq 0.3-0.5\mu$m, $0.6-0.9\mu$m for F200W and F356W respectively). A good alternate probe of the evolution would be with consistent rest-frame wavelengths (Allen et al., in prep.).

4.4.5 Size-luminosity relations

In Fig. 4.9 we present the results of our size-luminosity fitting in the F115W and F444W filters to the functional form $\log_{10}R_e = a \times M_{\text{rest frame}} + b$, where $M_{\text{rest frame}}$ is the rest-frame absolute magnitude in each filter. We choose these filters to maximise the difference in wavelength between the relations, providing a better test of the wavelength dependence predicted by Roper et al. (2022). These filters probe $0.2-0.3\mu$m and $0.7-1.1\mu$m in the rest frame, respectively. The top panel shows the results for the Sérsic fitting, and the bottom panel shows the non-parametric results. The best-fit values are presented in Table 4.3. As in Section 4.4.4, we briefly compare our non-parametric sizes with the PSF sizes. At $z = 3-4$, 97% of the sizes are larger

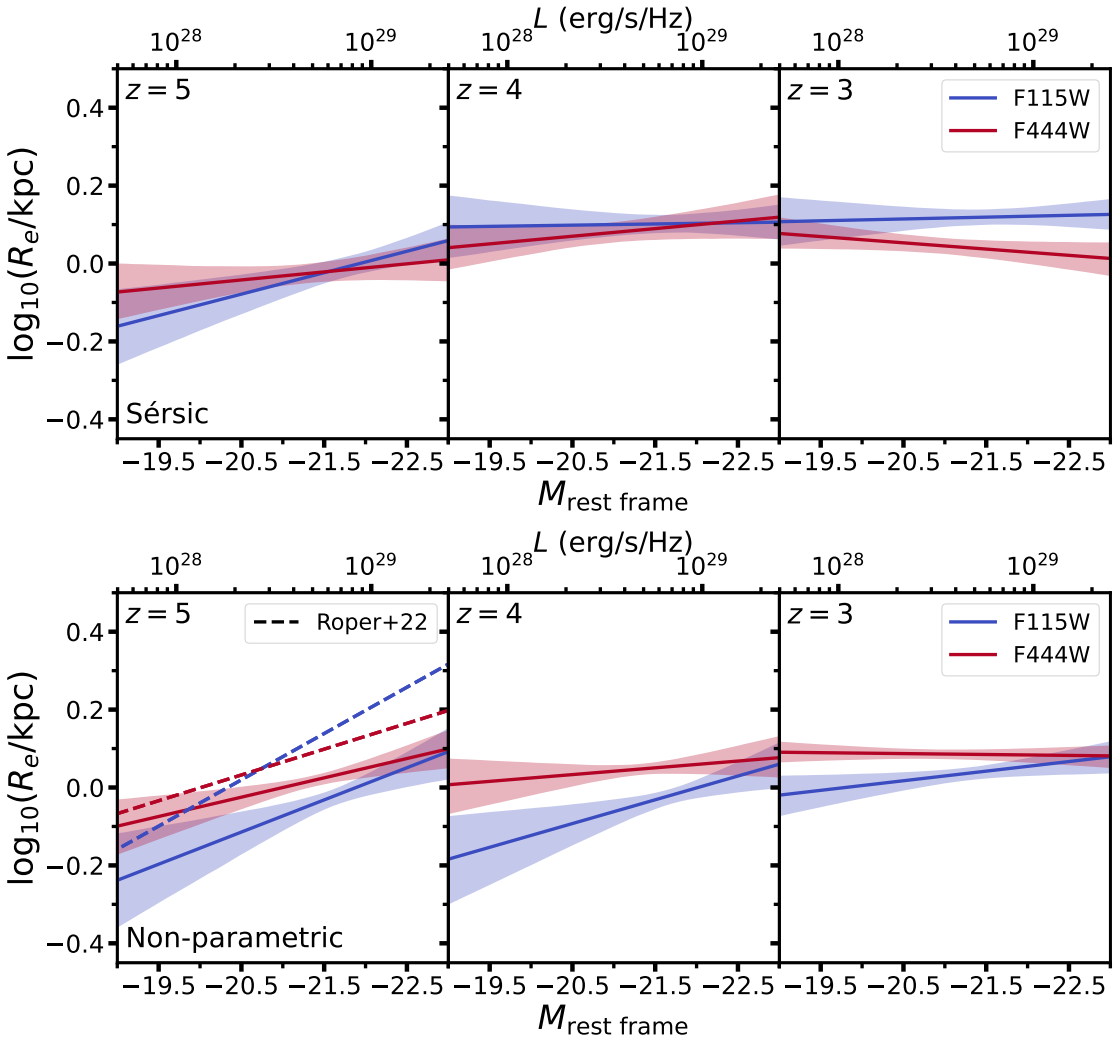

Figure 4.9: The size-luminosity relations in each redshift bin (labelled in the top-left of each panel) in F115W and F444W. **Top:** results from our Sérsic fitting. The rest-frame absolute magnitudes calculated for each of F115W and F444W (see Section 4.2.2) are shown on the x-axis, with the equivalent luminosity on the top axis. We also plot the 1σ error contours. **Bottom:** results from our non-parametric size fitting. The plots are the same as the top panel, but we also show predictions from the FLARES model of Roper et al. (2022) at $z = 5$ with the dashed lines.

Table 4.3: The best-fit values for the size-luminosity relation givens by $\log_{10}R_e = a \times M_{\text{rest frame}} + b$ in each redshift bin and for each filter used. The top table shows the results from Sérsic size fitting, and the bottom table shows results from the non-parametric sizes.

Sérsic

F115W	a	b
$z = 3$	-0.00 ± 0.02	0.02 ± 0.50
$z = 4$	-0.00 ± 0.03	0.03 ± 0.63
$z = 5$	-0.06 ± 0.03	-1.23 ± 0.72
F444W	a	b
$z = 3$	0.02 ± 0.02	0.40 ± 0.38
$z = 4$	-0.02 ± 0.03	-0.33 ± 0.55
$z = 5$	-0.02 ± 0.03	-0.46 ± 0.62

Non-parametric

F115W	a	b
$z = 3$	-0.02 ± 0.02	-0.49 ± 0.47
$z = 4$	-0.06 ± 0.04	-1.35 ± 0.93
$z = 5$	-0.08 ± 0.05	-1.80 ± 1.00
F444W	a	b
$z = 3$	0.00 ± 0.01	0.15 ± 0.26
$z = 4$	-0.02 ± 0.03	-0.35 ± 0.65
$z = 5$	-0.05 ± 0.03	-1.05 ± 0.62

than the PSF FWHMs in F115W and F444W. At $z = 5$, nearly 93% of the sizes are larger. The majority of the sample is therefore resolved. We verified that removing sources consistent with the PSF FWHM from the sample does not significantly change the size-luminosity relations. First looking at the Sérsic results, at $z = 4 - 5$ we find that the relations are consistent with one another. It also appears that for a given magnitude, galaxies become larger between $z = 4 - 5$. At $z = 3$ the F444W relation becomes negative and the sizes are more compact than in F115W.

The results from non-parametric size fitting described in Section 4.3.2 are slightly different. The non-parametric size-luminosity relations generally show a flattening of the relation with decreasing redshift, and the sizes in F115W are more compact than in F444W for any given luminosity. We do not find significant differences between the gradients in these bands at a given redshift.

Comparing our two size-fitting methods, we find that at $z = 4 - 5$ the non-parametric sizes have slightly steeper relations than the Sérsic sizes. This is likely

due to the inclusivity of the non-parametric method to massive, clumpy/irregular galaxies. Whilst the Sérsic fitting may fit to an individual clump or fail altogether (see Fig. 4.3), the non-parametric method better accounts for this, meaning we do not have to discard any fits. Indeed, if we remove clumpy galaxies the non-parametric size-luminosity relations flatten slightly, but the results are not changed significantly.

Massive galaxies can thus contribute to the population with larger sizes. By $z = 3$ the relations for both methods are relatively flat. The offsets between the bands differs across the two methods. In the Sérsic fitting, the offset between the red and blue bands disappears by $z = 4$. For the non-parametric relations a significant offset remains between the two bands at $z = 3-4$. Since the non-parametric method is agnostic to where the light in the galaxy lies, it may perform better on disturbed profiles in F115W where the Sérsic fitting converges, but may not be the most appropriate size measure. A visual inspection of the galaxies in each NIRCam filter reveals that objects which appear disk-like at long wavelengths can often have slightly irregular morphologies at short wavelengths. For example, in Fig. 4.1 the object appears to be disk-like in the long-wavelength filters, whereas in the short-wavelength filters it appears to be comprised of two components. In these cases we find that the Sérsic fitting ignores the clumps and still fits a disk, similar to the bottom right panel in Fig. 4.3 but to a less extreme extent. This may slightly overestimate these sizes, leading to the agreement in the Sérsic relations across wavelength. We thus conclude that galaxies tend to be more compact in their rest-UV light compared to their rest-optical light. There also appears to be a flattening of the relations towards lower redshift across both measurement methods. In Appendix 4.3.2 we compare the Sérsic and non-parametric sizes for galaxies that have a good Sérsic fit.

Comparison with the literature

We can also compare our results from both size-fitting methods to the literature. Assuming $R \propto L^{-\beta}$, Huang et al. (2013) find power laws of $\beta = 0.22^{+0.058}_{-0.056}$ and $0.25^{+0.15}_{-0.14}$ at $z = 4$ and $z = 5$ respectively for LBGs using Sérsic fitting. Converting our

relations from magnitude to luminosity, the non-parametric relations in F115W have power laws with exponent $\beta = 0.15 \pm 0.10$ and 0.20 ± 0.08 at $z = 4$ and $z = 5$ respectively. The Sérsic relations in F115W have exponents $\beta = 0.00 \pm 0.08$ and 0.15 ± 0.08 at $z = 4$ and $z = 5$ respectively. Our Sérsic results are thus slightly shallower in slope than Huang et al. (2013) (although the errors are large), and our non-parametric results are consistent within the errors. The non-parametric results are also consistent with Shibuya et al. (2015) and Curtis-Lake et al. (2016) who both find values spanning $\beta \simeq 0.1 - 0.27$ over $z = 3 - 5$. We also note that these results are consistent with size-luminosity relations of bright galaxies at $z > 5$ found by, e.g., Holwerda et al. (2015) and Shibuya et al. (2015). However, results from lensed galaxies at $z > 5$ (thus probing intrinsically fainter galaxies) tend to show much steeper slopes around $\beta \sim 0.5$ (e.g. Grazian et al., 2012; Kawamata et al., 2018; Bouwens et al., 2022b; Yang et al., 2022). Yang et al. (2022) find that different lensing models all produce the same steeper relation, and Bouwens et al. (2021) still find steep slopes after accounting for surface-brightness selection effects. Kawamata et al. (2018) recover this steeper relation in a simple analytic model where smaller galaxies have lower specific angular momenta.

Our results are complementary to those of Suess et al. (2022). For a sample of 1179 galaxies at $z = 1 - 2.5$ with $\log_{10}(M_\star/M_\odot) \geq 9$ selected from CEERS, they compare the observed 1.5μm ($\lambda_{\rm rest} \sim 0.55\mu$m) and 4.4μm ($\lambda_{\rm rest} \sim 1.6\mu$m) sizes using the F150W and F444W NIRCam filters, respectively. This work is similar to their results in that the rest-frame wavelengths vary over the redshift range due to the fixed choice of filters ($\lambda \simeq 0.2 - 0.3\mu$m, $0.7 - 1.1\mu$m in F115W and F444W), thus the focus is on the relative differences between the relations. They find that the observed 4.4μm sizes are more compact than at 1.5μm, and that the size difference is more pronounced at higher stellar mass. This is in agreement with our Sérsic size-luminosity relation at $z = 3$ - sizes in F444W are more compact than in F115W, and this size difference increases towards brighter magnitudes.

Comparison with Roper et al. (2022)

We also compare our results to predictions from Roper et al. (2022), who use the FLARES simulation (Lovell et al., 2021) to predict the size-luminosity relation of massive galaxies at $z = 5-10$ as a function of wavelength. The non-parametric size measurement we use follows their method, and hence they can be directly compared (although see the discussion in Section 4.5.3). Note that we can only compare our results against their $z = 5$ predictions. The closest matching synthetic filter to F115W in the rest-frame is their MUV-band, and the closest to F444W is their R-band. Our gradients are consistent with Roper et al. (2022), with the relation in F115W being steeper than in F444W. However, there is a significant offset between our relations and their predictions. Their relations also cross, leading to objects appearing larger in F115W at the bright end (see Fig. 4.9). This behaviour is not seen in our non-parametric results, but is seen in the Sérsic results. We note that the Sérsic results use a sub-sample of all galaxies in the PRIMER imaging, as poor fits are discarded. We test the impact of this by rerunning the non-parametric size-luminosity relations on this sub-sample. The relations flatten slightly but it does not change the results significantly.

4.5 Discussion

Our results point to an emergence of large ($R_e > 2$ kpc) galaxies by $z = 3$, whilst simultaneously pointing to little evolution in the *typical* size of galaxies over $z = 3-5$. Our Sérsic size-mass relations show hints of a negative slope at $z = 5$, intrinsic scatter that increases towards lower redshift and is larger in bluer bands, and some consistency with the predictions by Costantin et al. (2023). Our size-luminosity relations exhibit a flattening towards lower redshift in both the Sérsic and non-parametric sizes. The slopes of our non-parametric relations at $z = 5$ are consistent with the predictions by Roper et al. (2022) from FLARES, with an offset in the intercept. In this section, we discuss and interpret these

results in the context of disk formation models and explore the implications of the agreement of our results with simulation works.

4.5.1 Formation of disks at high-redshift

The use of log-normal fitting to the size distribution of galaxies is motivated by the disk formation model of Fall and Efstathiou (1980). In this theoretical framework the size of a galaxy is governed by its angular momentum, given to the system by tidal torques with neighbouring objects. Peebles (1969) express the total angular momentum in terms of a dimensionless spin parameter $\lambda = JE^{1/2}M^{-5/2}G^{-1}$ where J is the angular momentum of the system, E is the total energy, M is the total mass (all dominated by the DM halo before collapse) and G is the gravitational constant. In the picture of hierarchical structure formation, the distribution of spin parameters follows a log-normal distribution. Assuming the disk is relaxed, we then expect $R_e \propto \lambda R_{\rm vir}$ where $R_{\rm vir}$ is the virial radius of the DM halo (Bullock et al., 2001; Curtis-Lake et al., 2016). As described in Section 4.4.3 and shown in Fig. 4.5, our size distributions are well-described by a log-normal distribution, consistent with these theoretical models out to $z = 5$. Previous studies with *Hubble* (Shibuya et al., 2015; Curtis-Lake et al., 2016) also found strong agreement with a log-normal distribution out to $z \simeq 6$ (beyond which sample sizes are small), but this was limited to rest-UV emission at $z \gtrsim 3$. These results are thus complementary to *Hubble* results, revealing consistency between rest-UV and rest-optical size distributions at these redshifts.

The disk model of Fall and Efstathiou (1980) and Mo et al. (1998) also predicts that the size of a galaxy scales with redshift as $r \propto (1+z)^{-1}$ in the case of the host halo having a fixed circular velocity, and as $r \propto (1+z)^{-1.5}$ for a fixed halo mass. However, as discussed by Curtis-Lake et al. (2016), rest-UV selected samples do not necessarily also select for DM halos with constant mass or circular velocity. Therefore fitting this relation only reveals whether the rest-optical light of the UV-selected sample in this work best traces one of these scenarios, if certain assumptions hold. For example, the disk mass and angular momentum are assumed to be fixed fractions $m_{\rm d}$ and $j_{\rm d}$ of the total mass M and total angular momentum

J, which are dominated by the dark matter halo. Mo et al. (1998) assume $m_{\rm d}$ is the same for all disks, and they also largely assume $m_{\rm d} = j_{\rm d}$. Curtis-Lake et al. (2016) discuss results from Danovich et al. (2015), where high-redshift massive galaxies accrete angular momentum via cold gas streams, resulting in a high value of $j_{\rm d}$ and breaking the assumption that the disk is relaxed. This would drive up the value of the spin parameter λ for our most massive sources, and this may partially explain the build-up of objects at $R_e > 2$ kpc at $z = 3$ relative to $z = 4-5$. Prior to this build-up, within the THESAN simulation at $z \gtrsim 6$, Shen et al. (2024a) find that the sizes of massive galaxies agree better with model predictions where $j_{\rm d}/m_{\rm d}$ is small, keeping sizes compact at earlier times. However, this does not explain the shallower redshift evolution we find compared to the predictions. Our value of $R_e = 3.51(1+z)^{-0.60\pm0.22}$ is in tension with the fixed circular velocity scenario at the 2σ level. Legrand et al. (2019) find that for the least massive haloes ($\log_{10}(M_h/M_\odot) \lesssim 12.5$), the stellar-mass to halo-mass ratio decreases towards higher redshift. Since we cut at a constant mass over all redshifts, by $z = 3$ we may be sampling lower-mass haloes compared to $z = 5$. Thus in our sample for a given low-mass halo, at $z = 3$ the halo is more likely to be occupied by a more massive galaxy than at $z = 5$. We therefore may be selecting lower-mass haloes towards lower redshift, which could explain the shallower evolution that we find.

We can gain further insight into disk formation via the evolution of the intrinsic scatter in the size-mass relations. In disk formation models, the intrinsic scatter is related to the distribution of spin parameters (Bullock et al., 2001). The larger scatter we see at lower redshift may thus reflect that galaxies have had more time to undergo processes that drive them away from the standard disk evolution-based relation, such as mergers. This is also higher in the rest-frame UV than the rest-frame optical, suggesting that by $z = 5$ the rest-optical stellar populations are well established, but rest-UV emission exhibits a greater diversity in size perhaps caused by gas accretion driving star formation. This fits well with the build-up of large ($R_e > 2$ kpc) galaxies seen in the tail of the log-normal distributions by $z = 3$ - mechanisms forming much larger galaxies begin to dominate between $z = 3-4$,

driving up the intrinsic scatter. We note that the Universe increases in age by $\sim 40\%$ between $z = 3 - 4$, a time step of ~ 600 Myr.

Our findings of the fraction of irregular galaxies are consistent with an emerging picture of rest-optical morphology via visual classification with *JWST* (see Section 4.4.3, Kartaltepe et al., 2023; Ferreira et al., 2023; Jacobs et al., 2023). Whilst our Sérsic fitting fails on these objects, the evolution of the irregular fraction provides insight into processes that drive galaxies away from relaxed disks. A large increase in the irregular fraction towards higher mass (see Fig. 4.2) could reflect a high fraction of merging systems. Mergers may be one cause of driving galaxies away from the size-mass relation at $z = 3$, breaking the relaxed disk assumption in the formalism of Mo et al. (1998) and causing the increase in intrinsic scatter. Essentially, whilst disky galaxies are well-established by $z = 5$ as shown by the well-fit log-normal distributions, by $z = 3$ they begin to undergo processes such as mergers which disturb the disks (e.g. Ventou et al., 2017), and also push them to larger sizes as seen by the build-up in the tail of the $z = 3$ log-normal distribution.

4.5.2 Difficulties in size measurements

Many studies attempt to fit a $r \sim (1+z)^{\alpha}$ relation to the average or peak size to test different disk formation model scenarios, and agreement has been found with both $r \propto (1+z)^{-1}$ in the case of the galaxy sample following a fixed circular velocity of DM halos, and $r \propto (1+z)^{-1.5}$ for a fixed halo mass. (e.g Hathi et al., 2008; Oesch et al., 2010a; Mosleh et al., 2011). The most recent determinations with *JWST* are by Ormerod et al. (2024), who use 64 arcmin^2 to measure the size evolution of galaxies across $z = 0 - 8$, and Ward et al. (2024) who use 97 arcmin^2 to measure sizes from $z = 0.5 - 5.5$. Both studies find a weaker evolution in size than predicted by the disk formation models, $\alpha = -0.71 \pm 0.19$ and $\alpha = -0.63 \pm 0.07$. They agree with our value of $\alpha = -0.60 \pm 0.22$, which would appear to rule out the fixed virial mass scenario. However, as we have shown in Section 4.4.3 and discussed in the previous section, there are several competing effects governing the strength of this evolution. First, we do see evidence for a larger proportion of galaxies at $R_e > 2$

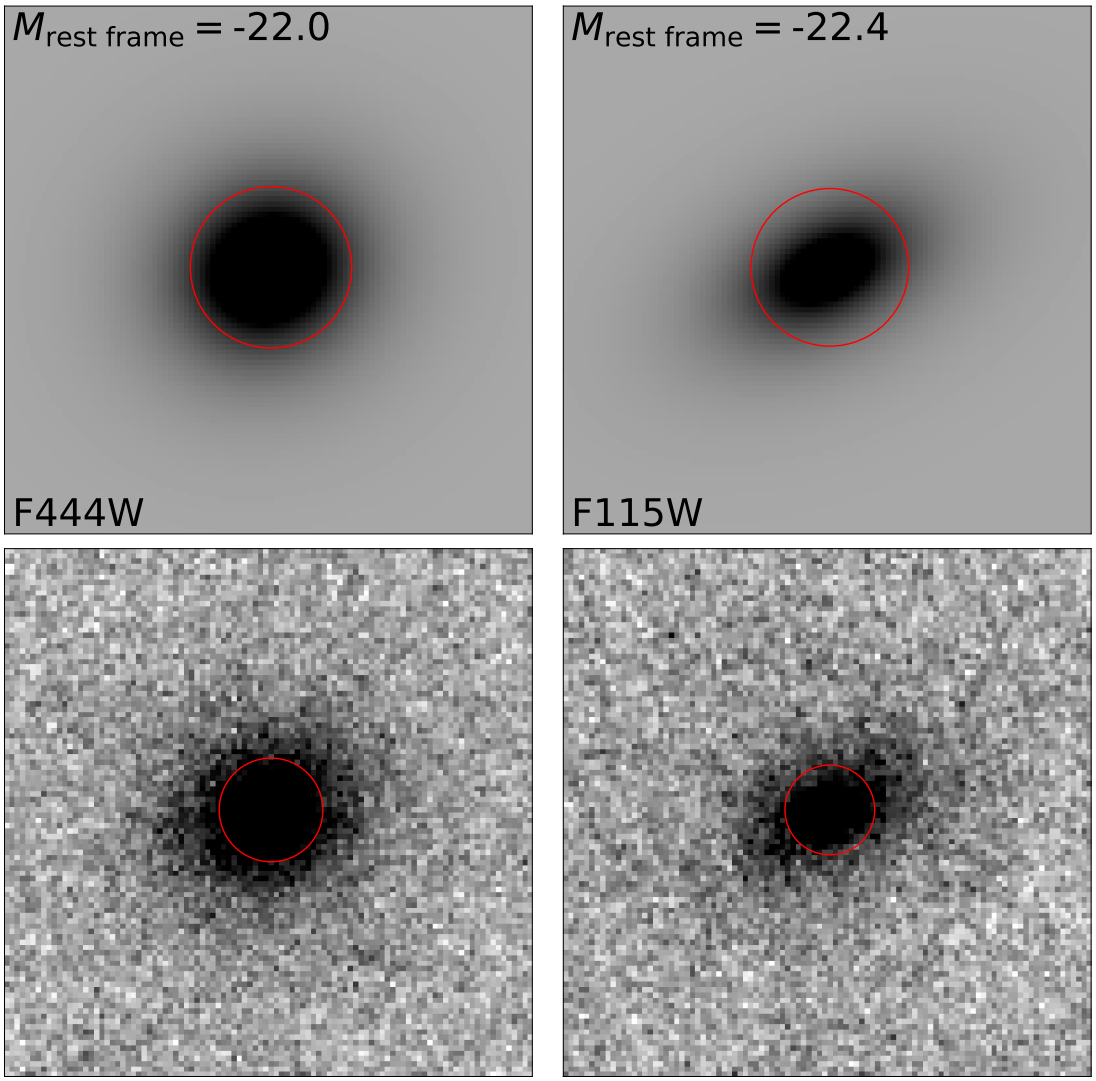

Figure 4.10: Results of non-parametric fitting on synthetic galaxies in FLARES (Vijayan et al., 2021). The top row shows the synthetic galaxy image, and a circular aperture corresponding to the size measured in this noiseless image. We also note the rest-frame absolute magnitude and the filter the object is injected to in the bottom row, where we re-measure the size and plot the corresponding aperture. The modal 5σ depth of the PRIMER imaging measured in a 0.3" diameter aperture is 27.4 in F115W and 28.5 in F444W.

kpc at $z = 3$ relative to $z = 4 - 5$. Second, from the mass-size and mass-luminosity relations, we generally expect the largest galaxies to be the brightest and most massive, which are the rarest (Adams et al., 2023b). Thus due to our limited area of 340 arcmin^2, coupled with an evolving luminosity function, it is difficult to draw conclusions on our value of the exponent (derived from fitting to the full sample) which is strongly affected by the largest galaxies. Third, the constant stellar mass cut with redshift may result in a non-constant cut in DM halo masses. Fourth, Ward et al. (2024) find ~ 1000 more galaxies than Ormerod et al. (2024) in a narrower redshift range (with fairly similar areas), suggesting large differences in the way these galaxies are selected in *Hubble* and *JWST* data. Arguably, our sample avoids issues surrounding the selection function with *JWST* by using ground-selected galaxies. For example, Curtis-Lake et al. (2016) discuss size-dependent incompleteness and under-estimation of the sizes of the largest *Hubble*-selected galaxies in Shibuya et al. (2015) caused by the use of high signal-to-noise required in small aperture sizes. Due to the ground-based imaging being seeing-dominated, the selection of our sample is largely agnostic to size and morphology. We thus can avoid these biases that may be introduced in a *JWST*-selected sample. Finally, large scatter in size leads to large uncertainty on our exponent of the size-redshift relation derived using the full sample. However, based on the build-up of large ($R_e > 2$ kpc) galaxies at $z = 3$, we may conclude that whilst the typical size of galaxies does not change, the same processes that increase the intrinsic scatter towards decreasing redshift also result in the establishment of a population with large sizes. Further constraining their evolution with redshift requires a wide-area study such as *Euclid*.

An additional complication in size measurements arises from the various definitions used in the literature (e.g. Sérsic, 1963; Petrosian, 1976; Kron, 1980) as well as multiple non-parametric measurement methods (e.g. Conselice et al., 2000; Oesch et al., 2010a; Roper et al., 2022). Comparing like-for-like with other studies and with simulations is thus rendered more difficult. This motivated our choice of using a parametric *and* non-parametric size fitting method in this work, allowing us to directly compare to current *JWST* studies and simulations. The Sérsic profile

choice is natural following from disk formation models. However, many fits must be discarded due to irregular morphology. The non-parametric method deals with this in a better manner, but arguably gives us less insight into disk formation at high-redshift. These two choices allow us to compare directly to predictions from Roper et al. (2022) and Costantin et al. (2023), who each use different size definitions to make predictions on wavelength dependence of size scaling relations.

4.5.3 Comparison with simulations

The two key simulation studies we compare to in this work are that of Costantin et al. (2023) and Roper et al. (2022). Costantin et al. (2023) use the illustrisTNG simulation (Pillepich et al., 2018) to measure the sizes of $\log_{10}(M_\star/M_\odot) > 9$ galaxies with noise added to match the depth of CEERS (Finkelstein et al., 2017). Roper et al. (2022) use the FLARES simulation (Lovell et al., 2021) to predict the size-luminosity relation of massive galaxies at $z = 5-10$ as a function of wavelength. We note that our measurements provide a like-for-like comparison with these two studies, avoiding possible systematics that arise from, for example, comparing half-mass and half-light radii (e.g. Wu et al., 2020). Our size-redshift evolution is slightly weaker than predicted by Costantin et al. (2023), and reasons for this have been discussed in Sections 4.5.1 and 4.5.2. Looking to the size-mass relations, our results are in good agreement with the predictions, including a possibly negative relation at $z = 5$. One reason for this is that the depths of CEERS are not too dissimilar to PRIMER. In a similar vein, our derived gradients of the size-luminosity match predictions from Roper et al. (2022), but our relations are offset to smaller sizes at the 2σ level. In this case, they do not simulate mock images at typical *JWST* depths. When using the non-parametric size-fitting method, the addition of noise dominates over the low-surface brightness outer regions of galaxies, reducing the total light measured for the galaxy. This leads to a smaller number of pixels used to calculate the effective half-light radius. We generate mock galaxies with Sérsic profiles using Synthesizer (Vijayan et al., 2021), which uses the same FLARES simulation as in Roper et al. (2022). In Fig. 4.10 we show the impact of this effect. We use the

same simple stellar population model as Roper et al. (2022) - v2.2.1 of the Binary Population and Spectral Synthesis (BPASS) stellar population synthesis models (Stanway and Eldridge, 2018) and assume a Chabrier (2003) initial mass function. We measure the non-parametric size of the mock galaxy, inject it into empty regions of our F115W and F444W imaging, and then re-measure the size. We overplot an aperture corresponding to the measured size. The sizes are clearly smaller after injection into our noisy images, and this may explain the bulk of the offset. In Fig. 4.11 we show how seven objects on the Roper et al. (2022) size-luminosity relations behave after they are each injected 20 times into different empty regions of our images. We generate mock galaxies at rest-frame absolute magnitudes of $M_{\rm F115W} = -21.8, -22.1, -22.4, -22.8$ and $M_{\rm F444W} = -21.5, -22, -22.5$. The 5σ depths of the PRIMER imaging measured in a 0.3 arcsec diameter aperture are 27.4 in F115W and 28.5 in F444W, corrected to a total magnitude assuming a point source. For brighter objects, the sizes are reduced onto our relations. Fainter objects fall below our relation, but noise in the images causes large scatter in the derived size since the depth of the imaging varies over the COSMOS and UDS fields. Additionally, there is a large difference in depth between F115W and F444W, so the impact noise has on measured size is stronger in F115W. This explains slightly larger offsets seen in F115W compared to F444W between the clean mock galaxy sizes and the sizes after injection into noisy images, and suggests an ideal depth of ~ 28 for such analyses, where our faintest sources are not washed out completely by the noise. This simple simulation has highlighted that direct comparisons between observational data, influenced by background noise, and clean simulated galaxies are difficult, limiting what can be learned about the physics governing size scaling relations. Comparisons to simulations where *JWST*-like noise, PSFs and pixel scales have been applied may enable more reliable comparisons to be undertaken.

4.5.4 Compact central star formation?

Considering our tentative agreement with the simulation works of Roper et al. (2022) (once instrumental noise is accounted for) and Costantin et al. (2023) (a

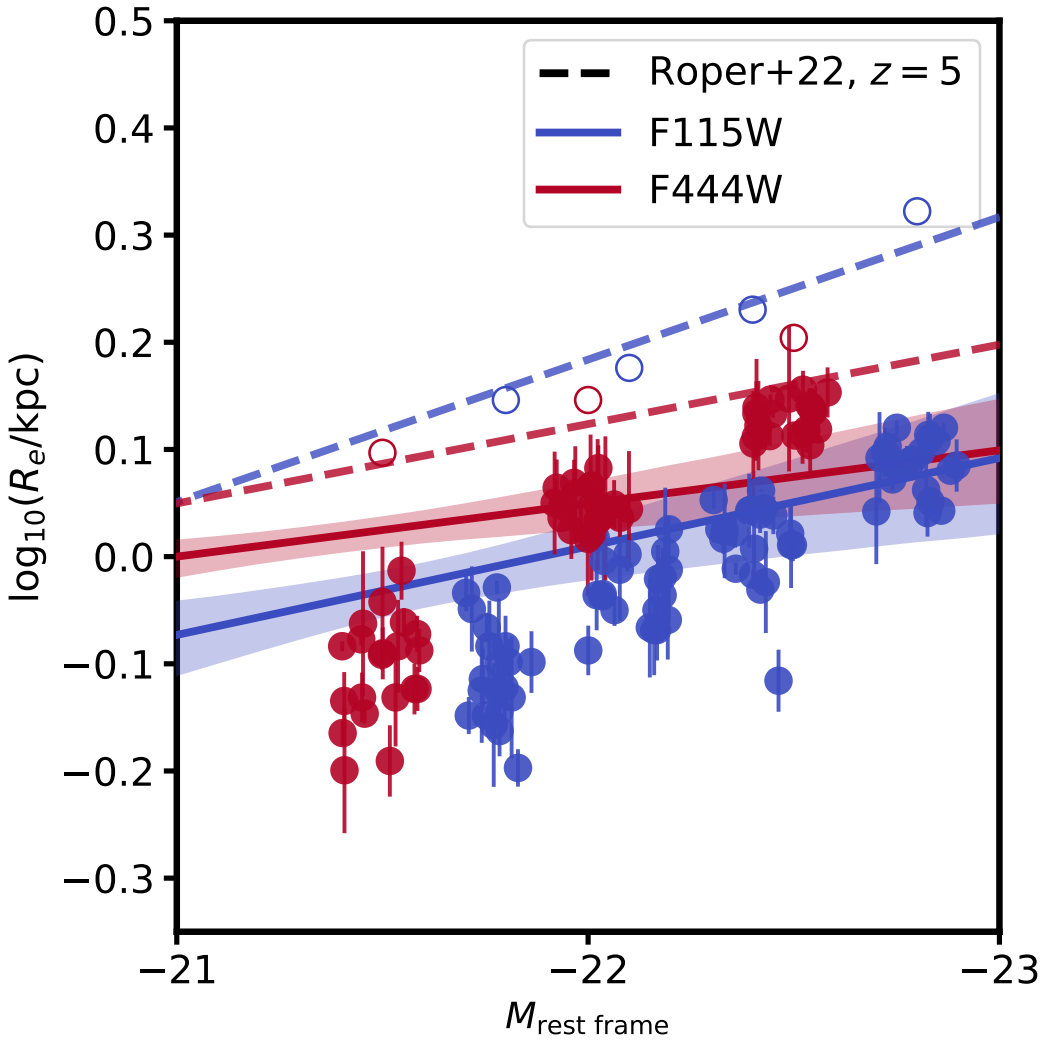

Figure 4.11: The size-luminosity relations at $z = 5$, as shown in Fig. 4.9 but with a comparison to simulated mock galaxy images. The open circles represent mock galaxies created as in Fig. 4.10, and the filled circles show their size after injection into an empty region of our imaging. We offset the injected sizes in magnitude within 0.2 mag for clarity. The colours of the circles match the filters used.

possible negative size-mass relation at $z = 5$), it is natural to ask: what physical mechanisms drive the evolution of these simulated galaxies? To explain the negative size-mass relations at $z = 5$ and steepening size-luminosity slopes with decreasing wavelength, both studies appeal to compact central star formation in the most massive galaxies. Specifically, Roper et al. (2022) and Roper et al. (2023) find that the most massive galaxies at $z \gtrsim 5$ develop dense cores leading to the negative slopes and to higher star formation. This enriches the cores of the galaxies, allows for metal-line cooling and inhibiting stellar/AGN feedback, driving further star formation, akin to the beginnings of inside-out galaxy formation and quenching (e.g. Pichon et al., 2011; Nelson et al., 2016; Baker et al., 2025; Shen et al., 2024a). It is difficult to ascertain from our limited sample at $z = 5$ whether there is a true negative relation. However, we note that the non-parametric size-luminosity relations show more compact sizes in the rest-UV compared to the rest optical. This is not seen in the Sérsic sizes, but as discussed in Section 4.4.5 the blue Sérsic sizes could be slightly over-estimated due to a larger profile being fit to more clumpy morphologies. Further studies constraining the size-luminosity relations at higher redshift and allowing for a wider dynamic range in mass and luminosity will provide stronger tests for these scenarios. We note that other physical mechanisms may affect the sizes seen in Roper et al. (2022). For example, the Hα emission line crosses into F444W at $z = 5$ (Davis et al., 2024) and approximately traces star formation. If not accounted for, this will act to decrease R_e. Additionally, the manner in which dust is modelled in these simulations is important. Roper et al. (2022) use a dust-to-metal ratio to calculate line-of-sight attenuation. They do not directly simulate dust production and destruction, instead using proxies from observed UV luminosity functions. Direct simulation of dust production/creation, such as with THESAN (Kannan et al., 2022), may be required if dust is the primary driver behind these size scaling relations. The agreement of slopes with Roper et al. (2022) is encouraging, but stronger differences between size-luminosity gradients with wavelength are predicted at $z > 5$ which remain to be tested with observations. Despite this, we have provided strong initial tests of predictions of the size-mass and

size-luminosity relations by using size measurements that enable direct comparisons, providing tentative evidence for centrally compact star formation at high-redshift.

4.6 Conclusions

We present size measurements of 1668 rest-frame UV selected galaxies with stellar masses $\log_{10}(M_\star/M_\odot) > 9$ using data from PRIMER. These sources were selected from the ground-based study of Adams et al. (2023b). The sample was selected from seeing-dominated data, and hence presents an unbiased sampling of the morphology and size distributions of luminous sources. Additionally, the wavelength coverage of *JWST* NIRCam allows us to measure rest-optical sizes at $z > 3$, previously not possible with *Hubble*. We measure Sérsic and non-parametric sizes to test models of disk formation, measure the size-mass and size-luminosity relations, and compare directly to predictions of these relations from simulations.

- Galaxy sizes in F356W follow a log-normal distribution in both Sérsic and non-parametric sizes, following predictions from Fall and Efstathiou (1980) and Bullock et al. (2001), implying disk formation as early as $z = 5$. Whilst this has been seen in rest-UV morphologies out to $z = 6$ with *Hubble*, we confirm this result for rest-optical morphologies at $z = 4-5$.

- We find evidence for the build-up of large ($R_e > 2$ kpc) galaxies in the tail of the log-normal distribution at $z = 3$, implying a transition from compact to extended sizes from $z \simeq 3-4$ for rarer objects. This is supported by a size-redshift evolution of $R_e = 3.51(1+z)^{-0.60\pm0.22}$ kpc derived from fitting to the full sample, consistent with other *JWST* findings (Ormerod et al., 2024; Ward et al., 2024).

- Simultaneously, following Curtis-Lake et al. (2016), if we fix the exponent of the evolution to -0.20, we find a size-redshift relation consistent with the peaks of our log-normal distributions. This suggests that the size of a *typical* galaxy does not evolve significantly over $z = 3-5$, remaining compact with $R_e \simeq 0.8-0.9$ kpc.

- We measure Sérsic size-mass relations in F200W and F356W and find agreement with predictions from Costantin et al. (2023) who use Illustris TNG50 to predict the size-mass relation in CEERS. We find the intrinsic scatter is larger in F356W than in F200W in each redshift bin, and the intrinsic scatter is larger at lower redshift. We speculate that this is because galaxies at $z = 3$ have had more time to undergo processes such as mergers and gas accretion that drive them away from the relation.

- The gradients of our non-parametric size-luminosity relations agree with predictions from the FLARES simulation of Roper et al. (2022), but with an offset that we believe is driven by larger sizes measured for the simulations when instrumental noise is unaccounted for.

- Simulations suggest the scaling relations are driven by compact central star formation at high-redshift, and our results provide tentative evidence for this mechanism. Further observations that improve the dynamic range of this sample are needed to place stronger constraints on interesting cases such as negative size-mass relations and more compact size-luminosity relations in the rest-UV compared to the rest-optical.

Additional results from PRIMER (Allen et al. in prep.) will produce a multi-wavelength view of galaxy sizes over a wide mass range, allowing us to understand size evolution in a diverse population. Furthermore, a similar analysis in a larger volume will allow for stronger constraints on the emergence of large ($R_e > 2$kpc) galaxies at $z \simeq 3 - 4$. Just as degree-scale ground-based imaging revolutionized constraints on high-redshift number statistics such as the bright-end of luminosity functions (e.g. Bowler et al., 2014; Stefanon et al., 2019; Harikane et al., 2022b), missions such as *Euclid*, which will achieve near-*Hubble* resolution over degree-scale fields (Euclid Collaboration et al., 2022a), will revolutionize our understanding of resolved properties of the very same galaxies.

Just get it done.

—R. A. A. Bowler, M. J. Jarvis

5 Conclusions

Contents

5.1 Summary and conclusions

In this thesis, I have presented results on the statistical properties of luminous star-forming galaxies in the first two billion years of cosmic time to better understand the physical processes governing the evolution of the earliest galaxies. This analysis is based on the latest data releases from large ground-based telescopes, such as Subaru and VISTA, as well as next-generation space telescopes, *Euclid* and *JWST*. I measured the rest-frame UV luminosity function at $z \simeq 7$ using degree-scale optical and NIR imaging, providing definitive observational constraints while mitigating contamination from low-redshift interlopers, primarily brown dwarfs, in $z \simeq 7$ LBG samples. Additionally, I measured the size-scaling

relations of luminous LBGs at $z \simeq 3-5$ with *JWST*, enabling direct comparisons with simulations to improve our understanding of star formation and dust accumulation in massive galaxies during this epoch.

In Chapter 2 I conducted a search for $z \simeq 7$ LBGs over 8.2 deg^2 of deep near-infrared photometry from the VIDEO survey (5σ depth of 25.2 in Y), combined with deep optical and *Spitzer*/IRAC photometry. Through a full photometric SED fitting analysis I found 28 galaxy candidates spanning $-23.5 \leq M_{\rm UV} \leq -21.6$ with stellar masses $9.1 \leq \log_{10}(M/M_{\odot}) \leq 10.9$ and little dust attenuation ($A_V < 0.5$), representing some of the most luminous and massive galaxies at this epoch. Measurements of the rest-UV LF were consistent with previous findings of a double-power law decline in the bright end, based on early ground-based NIR data from VISTA and UKIRT. I found that the brightest ($M_{\rm UV} \simeq -24$) candidate LBGs in red-optical-only studies were likely to be brown dwarf contaminants, based on the inclusion of $YJHK$ photometry in the SED fitting, leading to an overestimate in the bright end by a factor of 10 at $M_{\rm UV} < -24$ in these studies. By extrapolating measurements of the AGN LF from $z = 3-5$ to $z = 7$, I predicted a negligible contribution of AGN to the total rest-UV LF until $M_{\rm UV} < -24$. This was in tension with *Hubble* pure-parallel studies, which found excesses of $> 10\times$ in the LF at $z = 8$ relative to my findings at $M_{\rm UV} < -22$. These studies suggested the strong excess was caused by a significant AGN contribution. Instead, my results suggested an imperfect removal of brown dwarfs in these studies. My findings provided a robust measure of the bright end of the $z \simeq 7$ rest-UV LF, showing little evolution from $z \simeq 8$. This suggested a lack of dust attenuation and/or mass quenching between these epochs.

In Chapter 3, I extended the analysis outlined in Chapter 2 to the UltraVISTA survey, covering 1.72 deg^2 down to 5σ depths of 26.2 in Y, identifying 291 galaxy candidates with $-22.5 \leq M_{\rm UV} \leq -20.2$. I also performed a separate selection that combined *Euclid* photometry in the SED fitting. In the 0.65 deg^2 overlap between UltraVISTA and *Euclid*, I identified 141 galaxy candidates covering a similar magnitude range. These samples, combined with the candidates presented in

Chapter 2, provided a total dynamic range of $-23.5 \leq M_{\rm UV} \leq -20.2$, probing from the bright end down to magnitudes probed by *Hubble* studies. This work therefore provides the first ground-selected samples at $z \geq 6$ which overlapped significantly with space-based studies. I found that the *Euclid* photometry is powerful for removing brown dwarf contaminants since it probes the deep molecular absorption features in the brown dwarf SED which are inaccessible from ground-based imaging alone due to atmospheric absorption. Additionally, the *Euclid* photometry helps to recover more faint ($M_{\rm UV} \gtrsim -21$) galaxies. When measuring the rest-UV LF, this leads to less scatter in the LF points due to a reduction in both contamination and loss of genuine galaxies. Based on the UltraVISTA+*Euclid* sample, I find a gradual decline in the LF at $M_{\rm UV} < -20.8$ which matches the LF at $M_{\rm UV} < -21.6$ in Chapter 2. I then investigated the potential of using the superior resolution of *Euclid* over seeing-dominated ground-based imaging to remove brown dwarfs based on their morphology. I took point sources from the *JWST* COSMOS-Web survey and measured their FWHMs in the *Euclid* imaging. I find that at $J \gtrsim 24.5$, galaxy FWHMs are largely consistent with the sizes of point sources. This is because at these magnitudes, the size-luminosity relation indicates that these galaxies are compact. Additionally, the FWHMs of faint point sources are boosted by noise spikes. However, at $J \lesssim 24.5$, where the size-luminosity relation rapidly evolves, I forecast that in the *Euclid* Deep Fields it will be possible to separate point sources from extended, resolved LBGs. At the end of Chapter 3 I make use of the unique combination of the HSC y, VISTA Y and *Euclid* Y_E filters, all with slightly different wavelength responses, to identify a candidate high-equivalent width Lyman-α emitter at $z \simeq 7.2$ seen by an excess in VISTA Y relative to HSC y and *Euclid* Y_E. This demonstrates the synergistic power these three instruments will have in the *Euclid* Auxiliary Fields to find extreme emission line sources embedded in the Epoch of Reionization.

In Chapter 4, I moved to slightly lower redshift, $z \simeq 3-5$, to measure the size-scaling relations of luminous, massive $\log_{10}(M/M_{\odot}) > 9$ galaxies with the *JWST* PRIMER survey, covering 340 arcmin^2. The sample was selected from ground-based,

seeing-dominated data, presenting an unbiased sampling of the morphology and size distributions of luminous sources. *JWST* also allows for measurements of rest-optical sizes at $z > 3$, which was not possible with *Hubble*. Sizes were measured with two methods - a parametric Sérsic profile fit, and a non-parametric method which finds the effective radius for pixels containing half the total galaxy light. I found that the parametric and non-parametric sizes in redshift bins at $z = 3, 4, 5$ followed a log-normal distribution, following the predictions of a simple disc formation model outlined in Section 1.3.2. I also found evidence for a build-up of large ($R_e > 2$ kpc) galaxies in the tail of the $z = 3$ distribution. This was supported by the Sérsic size-redshift evolution derived from fitting to the full sample, $R_e(z) = (1 + z)^{-0.60 \pm 0.22}$ kpc. Simultaneously, I found little evolution in the *typical* (modal) galaxy size over this redshift range. I found that the intrinsic scatter of the size-mass relations in the redshift bins at $z = 3, 4, 5$ increases towards lower redshift, possibly probing the fact that by $z = 3$ galaxies have had more time to undergo dissipative processes such as mergers and gas accretion, in line with findings from the log-normal distributions and size-redshift evolution. Finally, I measured the non-parametric size-luminosity relations at $z = 3, 4, 5$ to provide a direct comparison with the FLARES simulation. I found consistent gradients with their predictions, but offset to smaller sizes. An injection-recovery analysis of mock FLARES galaxies into empty regions of the PRIMER imaging revealed that the smaller sizes were caused by the loss of low-surface brightness regions to noise in the imaging. Consistency with predictions from FLARES, up to the application of *JWST*-like PSFs, noise and pixel scales, provided evidence for centrally concentrated star formation in the most massive galaxies at high redshift, leading to dust attenuation in galaxy cores. With the non-parametric method, this results in larger sizes towards lower redshift.

5.2 Future work

In this section, I outline future research which would build on the results of this thesis, primarily focusing on *Euclid* data. As I have shown in this thesis, luminous, massive LBGs at high redshift ($z \gtrsim 3$) are ideal laboratories for understanding

the astrophysics of galaxies. In the era of *JWST*, they may be the progenitors of massive quiescent galaxies discovered at high-redshift, which have undergone very early quenching episodes (e.g. Carnall et al., 2023a). Additionally, theoretical studies suggest radiation-driven feedback expelling dust is required to explain large numbers of luminous blue galaxies at $z \gtrsim 10$ (e.g. Ferrara et al., 2024). Accurate measurements of the bright-end of the rest-UV LF probe the role of such feedback processes in the evolution of these galaxies. Despite providing the best constraints to-date on the bright end of the LF at $z \simeq 7$ in Chapter 1 and 2, wide-area ground-based data have been unable to peel back further layers shaping the LF, such as morphology evolution, due to its seeing-limited nature. I would combine imaging in the *Euclid* Auxiliary Fields (EAFs) with the deepest ground-based surveys to obtain a resolved view of luminous LBGs. This would establish a crucial link to extreme *JWST* populations, enabling a deeper understanding of the processes within, and evolution of, the very first galaxies in the Universe.

5.2.1 The impact of mergers on the rest-UV LF at $z = 4-10$

Euclid represents a paradigm shift, providing degree-scale space-based near-infrared imaging for the first time, with superior resolution compared to ground-based imaging. It will cover 53 deg^2 in the EDFs, more than 5$\times$ the area covered in Chapters 2 and 3, completely unveiling the nature of luminous LBGs. I will begin by conducting a selection for bright LBGs in the *Euclid* auxiliary fields (XMM-LSS, ECDF-S and COSMOS) at $z = 4-10$, covering 10 deg^2. This will build on my expertise in these fields and be highly complementary to selections performed by members of the *Euclid* Collaboration. With *Euclid*'s superior resolution, I will be able to distinguish bright brown dwarfs as point sources, and conduct SED fitting by combining photometry with VISTA (see Fig. 3.11). I would perform a complete injection-recovery analysis to accurately determine the completeness function, essential for reliable LF measurements, and simulate a range of physical properties (e.g. rest-UV slopes and morphology) for the injected LBGs in order to forward model the LF and probe its dependence on these physical parameters.

I would also make use of novel interloper mitigation techniques, such as using our knowledge of the rest-UV LF to place comoving volume priors on the redshift probability distribution (Donnan et al., 2024), and a clustering analysis to estimate the contamination rate by low-redshift galaxies (Hilmi et al., 2024). Finally, I would use this sample to measure the total rest-UV LF over $z = 4 - 10$. Leveraging the ability to detect merging systems, this analysis will go beyond current ground-based LF determinations by examining how the LF shape changes when considering individual components of merging/clumpy systems separately. If clumpiness arises from merging systems, then a shallower LF with individual components would suggest an earlier onset of mass quenching or dust obscuration than inferred from imaging which cannot resolve mergers. If galaxies at $z \simeq 7$ are intrinsically clumpy, the presence of bright compact clumps would imply high star formation rate surface densities, suggesting that these luminous galaxies are undergoing intense starbursts. Kinematic observations with ALMA would provide further insight into whether clumpy systems are merging or are all part of the same galaxy (e.g. Jones et al., 2021).

5.2.2 Size-scaling relations with *Euclid*

With a robust sample of luminous LBGs in hand, supplemented by samples from the *Euclid* Collaboration, I would investigate size-scaling relations. Galaxy sizes are thought to change with a redistribution of their angular momentum due to feedback processes (e.g. Wyithe and Loeb, 2011). Currently, the size-luminosity relation at $M_{\rm UV} \leq -22$ remains highly uncertain due to the relatively small areas covered by *JWST* (see Fig. 3.9). I aim to extend this relation to $M_{\rm UV} \simeq -24$. By using both Sérsic and non-parametric fitting, I would provide a comprehensive study across the diversity of morphologies commonly found at high-redshift. I would also enable direct comparisons with simulations - essential for understanding star formation histories, dust build-up, and dust geometry in massive LBGs — a key science aim I have explored in Chapter 4.

5.2.3 Disentangling the AGN and galaxy LFs

By disentangling the bright end of the rest-UV LF using a PSF+disk decomposition to separate point-source AGN light from the extended galaxy rest-UV emission, I would be able to measure the AGN fraction as a function of magnitude (noting that compact star formation will need to be distinguished from an AGN component). This PSF+disk decomposition was briefly used in Chapter 4 to remove AGN from the LBG sample, but was not explored further. With this analysis, I would be able to place significantly tighter constraints on the functional form of the galaxy LF and the faint-end slope of the AGN LF during epochs where AGN contribute substantially to the number density ($z \simeq 3-6$ at $M_{\rm UV} \simeq -23$, see Fig. 2.5). At these redshifts, it will be possible to use the high-resolution *Euclid* I_E filter for this analysis. Currently, both Schechter functions and double-power laws provide good fits to the galaxy LF at $z \simeq 3-5$ (Adams et al., 2023b), rendering it difficult to probe feedback processes in LBGs at these epochs. An additional effect which can alter the bright-end shape is gravitational lensing. Building on my previous experience with the DEVILS team (Davies et al., 2018), I would use a novel geometric approach of measuring the LF in fields near- and far-from foreground objects to de-lens the LF, and leverage lensing models developed for the bright end (Ferrami and Wyithe, 2023; Ferrami and Wyithe, 2024). Armed with well-constrained galaxy LFs over the first 2.5 Gyr, I would search for a steepening of the bright-end slope of the galaxy LF and a decline in the number density of LBGs with $M_{\rm UV} \lesssim -23$, thus pinpointing the onset of feedback processes in these massive systems. This will provide a benchmark for comparison to simulations (e.g. Lewis et al., 2023; Vijayan et al., 2024). Additionally, strong constraints on the bright end allows for a fitting of the full LF, aiding determinations of the faint end.

5.2.4 Spectroscopic follow-up of rare sources

Many unusual objects at $z \gtrsim 4$ will be identified in the LBG samples by virtue of the new parameter spaces unlocked by combining VISTA and *Euclid*. For example, the excellent colour information provided by VISTA, *Euclid*, and *Spitzer* will enable

the identification of extremely red objects and Little Red Dots (Matthee et al., 2024), probing the full parameter space of LBGs. The power of *Euclid* to identify red sources has already been demonstrated (Euclid Collaboration et al., 2025). Little Red Dots have a characteristic blue rest-UV slope and red rest-optical slope. As discussed in Chapter 3, *Euclid*'s uniform depths across its NISP filters will allow for the identification of galaxies with very blue rest-UV slopes. Those that are also bright in *Spitzer*/IRAC with a red $[3.6] - [4.5]$ colour would serve as candidate Little Red Dots. Additionally, as I showed in Chapter 3, powerful Lyα emitters can be identified using pseudo-narrowbands with overlapping ground-based and *Euclid* (and even *JWST*) filters (see Fig. 3.11), signposting ideal sites for mapping reionization (e.g. Lu et al., 2024). In Chapter 3 I presented a Lyman-α Emitter candidate, and the double-peaked morphology observed in VISTA-Y, but not in Y_E, suggests the presence of a strong Lyα-emitting clump spatially offset from the rest-UV emission. To investigate this source (and similar sources which would be identified in the sample), I would write follow-up proposals with *JWST* and ALMA, providing a strong case with robust SED fitting. *JWST* NIRSpec will determine whether such objects host an extended Lyα nebula and provide measurements of the conditions within the galaxy (such luminous sources are also prime for follow up even with MIRI to find rest-optical lines such as Hα at $z > 7$, Zavala et al., 2025). ALMA [CII] and dust continuum observations could provide key constraints on the gas-phase metallicity and enrichment of these galaxies. These observations will offer crucial insight into the assembly of luminous Lyman-break galaxies during the Epoch of Reionization.

5.3 Final remarks

The work presented in this thesis serves as a key link between degree-scale ground-based imaging and the emergence of degree-scale, space-based NIR imaging, marking a pivotal transition in the quality of survey data available to astronomers in the coming decade. By combining space- and ground-based imaging, my approach provides clean, uncontaminated samples of high-redshift galaxies while mitigating

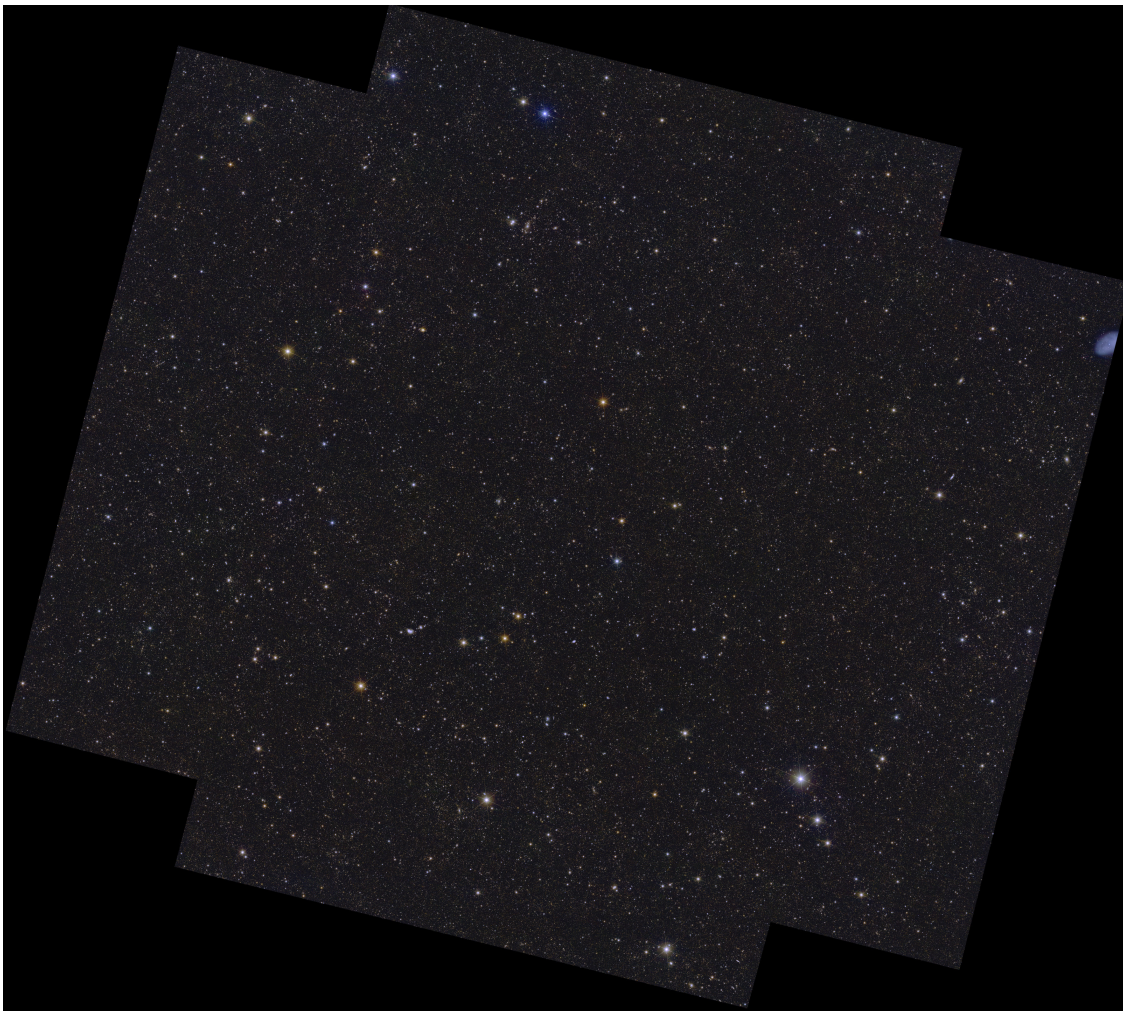

Figure 5.1: *Euclid* Deep Field Fornax. Image credit: ESA/Euclid/Euclid Consortium/NASA, image processing by J.-C. Cuillandre, E. Bertin, G. Anselmi

selection effects that may arise in purely space-based surveys. With the progression of the *Euclid* survey, as well as upcoming surveys from LSST and *Roman*, it will be crucial to combine multi-wavelength data across these observatories to maximise scientific return. While my work demonstrates this approach within a small area ($\lesssim 10$ deg^2) relative to these upcoming surveys, future extensions across the full 53 deg^2 of the *Euclid* Deep Fields (e.g., the *Euclid* Deep Field Fornax, shown in Fig. 5.1), and eventually across thousands of square degrees with the *Euclid* Wide Survey, will provide a comprehensive understanding of the evolution of the most luminous galaxies across cosmic time.

Appendices

A

Adding inclusive candidates to the LF from Chapter 2

Table A.1: The photometry of our $z \simeq 7$ inclusive candidates. The top section shows objects in XMM-LSS, and the bottom section shows objects in ECDF-S. Objects are ordered by their photometric redshift. The first column shows the object ID, and the next two columns show the coordinates of the candidate. The remaining bands show the photometry in the bands available in each field. We require $< 2\sigma$ detections bluewards of and including the i/I-bands, so we only present bands redwards of this. The photometry is measured in a 2.0 arcsec diameter circular aperture apart from the *Spitzer*/IRAC bands where 2.8 arcsec diameter apertures are used to account for the broader PSF. The photometry is corrected to a total flux assuming a point-source correction using a 10×10 grid of PSFs measured by PSFEx across each VIDEO tile.

ID	RA	DEC	Z	NB921	y	Y	J	H	Ks	[3.6]	[4.5]
170389	02:16:38.75	-04:28:50.98	> 26.7	> 26.4	> 25.8	$24.8^{+0.3}_{-0.2}$	$24.6^{+0.3}_{-0.2}$	$24.3^{+0.4}_{-0.3}$	> 24.0	> 24.5	$24.8^{+0.6}_{-0.4}$
1415071	02:25:49.21	-04:02:38.00	> 26.2	$25.7^{+0.6}_{-0.4}$	$24.8^{+0.5}_{-0.3}$	$24.8^{+0.3}_{-0.2}$	$24.6^{+0.3}_{-0.2}$	$24.8^{+0.7}_{-0.4}$	> 24.0	$23.7^{+0.2}_{-0.2}$	$24.1^{+0.5}_{-0.3}$
1017553	02:22:52.86	-05:04:37.97	> 26.4	> 26.0	> 24.6	$24.7^{+0.3}_{-0.2}$	$24.7^{+0.4}_{-0.3}$	$24.5^{+0.4}_{-0.3}$	> 23.9	$23.3^{+0.2}_{-0.1}$	$24.1^{+0.5}_{-0.4}$
914913	02:22:07.26	-05:24:02.32	> 26.3	> 25.5	> 24.9	$25.1^{+0.2}_{-0.2}$	$25.2^{+0.5}_{-0.3}$	$25.1^{+0.7}_{-0.4}$	$24.8^{+0.7}_{-0.4}$	$24.0^{+0.2}_{-0.2}$	$24.5^{+0.7}_{-0.4}$
1495402	03:35:25.99	-28:38:19.13	> 25.1	-	-	$23.9^{+0.1}_{-0.1}$	$22.9^{+0.1}_{-0.1}$	$22.6^{+0.1}_{-0.1}$	$22.4^{+0.1}_{-0.1}$	$22.5^{+0.2}_{-0.2}$	$23.0^{+0.2}_{-0.2}$
705214	03:30:30.53	-27:23:16.47	> 25.4	-	-	$24.6^{+0.1}_{-0.1}$	$24.6^{+0.3}_{-0.2}$	$24.8^{+0.6}_{-0.4}$	> 24.1	$24.1^{+0.2}_{-0.2}$	> 24.7
1090797	03:32:28.28	-27:48:02.25	> 25.5	-	-	$24.2^{+0.1}_{-0.1}$	$23.8^{+0.2}_{-0.1}$	$24.1^{+0.3}_{-0.2}$	$24.2^{+0.5}_{-0.3}$	$24.3^{+0.2}_{-0.2}$	$24.7^{+0.3}_{-0.2}$
834371	03:31:09.95	-28:43:55.05	> 25.0	-	-	$25.1^{+0.3}_{-0.2}$	$23.5^{+0.1}_{-0.1}$	$22.9^{+0.1}_{-0.1}$	$22.6^{+0.1}_{-0.1}$	$21.8^{+0.2}_{-0.2}$	$21.6^{+0.2}_{-0.2}$

Table A.2: Inclusive candidates in XMM-LSS (top) and ECDF-S (bottom). These are defined as having good brown dwarf fits, $\chi^2_{\rm BD} < 10$, yet have significantly better galaxy fits, $\chi^2_{\rm BD} - \chi^2 > 4$ when fitted without GR in XMM-LSS and $ugrGR$ in ECDF-S. The first column shows the object ID. The next four columns show properties of the high-z solution: photometric redshift, absolute magnitude in a tophat filter at 1500Å with width 100Å, extinction, and χ^2 value. The next two columns show the secondary photometric redshift and χ^2. The final two columns show the stellar type for fitting to MLT dwarfs, and $\chi^2_{\rm BD}$.

ID	z	$M_{\rm UV}$ / mag	A_V / mag	χ^2	$z_{\rm gal2}$	$\chi^2_{\rm gal2}$	Stellar Type	$\chi^2_{\rm BD}$
170389	$7.34^{+0.10}_{-0.14}$	-22.6 ± 0.2	0.0	5.3	9.0	26.5	T8	9.8
914913	$6.53^{+0.64}_{-0.10}$	-21.7 ± 0.3	0.0	4.3	1.2	14.4	T3	8.1
1017553	$6.93^{+0.26}_{-0.34}$	-22.2 ± 0.2	0.0	0.9	1.5	13.5	T3	6.2
1415071	$6.58^{+0.03}_{-0.10}$	-22.1 ± 0.1	0.2	1.6	1.4	18.4	T3	9.0
705214	$6.61^{+0.66}_{-0.18}$	-22.3 ± 0.3	0.2	3.8	1.45	11.5	T8	9.8
834371	$6.99^{+0.56}_{-0.07}$	-23.4 ± 0.2	0.0	1.8	1.7	12.2	L7	6.4
1090797	$7.33^{+0.07}_{-0.19}$	-23.3 ± 0.2	0.0	3.2	1.5	38.4	T8	6.8
1495402	$7.39^{+0.04}_{-0.46}$	-24.1 ± 0.2	0.0	1.6	1.6	25.8	L4	5.7

In this Appendix we present a more inclusive selection of candidates to those presented in Chapter 2, which includes sources that have a plausible brown dwarf fit but are still better represented by a high-redshift galaxy model. Bowler et al. (2015) state that removing objects with a good brown dwarf fit $\chi^2 < 10$, likely removes genuine high-redshift galaxies. We retain objects that have good brown dwarf fits and significantly better galaxy fits, $\chi^2_{\rm star} - \chi^2 > 4$. These candidates are not robust due to the well-fitted brown dwarf SEDs. However, they pass our other selection criteria. We find four inclusive candidates in XMM-LSS, and four in ECDF-S. Their photometry is shown in Table A.1. The results of SED fitting analysis with LePhare is shown in Table A.2. In ECDF-S the candidates are much brighter than our primary sample: 4 have absolute UV magnitudes $M_{\rm UV} < -23$, and 1 has $M_{\rm UV} < -24$. The SED fitting and stamps for the inclusive candidates are shown in Fig. B.4 and Fig. B.5. We add these objects to the primary sample and conduct a separate calculation of the rest-UV LF at $z \simeq 7$, as outlined in

Table A.3: The rest-UV luminosity function points at $z \simeq 7$, calculated by incorporating the inclusive candidates. The first two columns show the absolute UV magnitude of the bin and the width of the bin. The third column shows the number of galaxies in the bin. The fourth column shows the comoving number density of galaxies we calculate with Equations **??** and **??**. The final column shows the median completeness in each bin.

Bin / mag	Bin width / mag	$n_{\rm gal}$	ϕ / mag / Mpc^3	Completeness
-22.05	0.5	18	$2.57 \pm 0.97 \times 10^{-6}$	0.68
-22.55	0.5	10	$8.40 \pm 4.51 \times 10^{-7}$	0.74
-23.175	0.75	5	$2.02 \pm 1.19 \times 10^{-7}$	0.79
-23.925	0.75	1	$2.37 \pm 2.50 \times 10^{-8}$	0.82

Section 2.5. The result is shown in Fig. A.1. We also plot the DPL fits derived by Bowler et al., 2017 and Harikane et al., 2022b, and their LF points. We include Bouwens et al. (2021) LF points to represent the faint end. The bins are centred at -22.05, -22.55, -23.175 and -23.925, with bin widths of $\Delta M = 0.5$ for the two fainter bins and $\Delta M = 0.75$ for the two brighter bins. The bins contain 18, 10, 5 and 1 candidate galaxies respectively. The LF points are summarised in Table A.3. If we include the contamination factor of 50 per cent derived in Section 2.4.1, our three faintest bins lie slightly above the DPL+DPL derived by Harikane et al., 2022b. The brightest bin is consistent with both DPLs, although the Poisson errors are large. The value of the LF in our brightest bin is a factor of four lower than the Harikane et al. (2022b) bin at $M_{\rm UV} = -23.92$. The contamination factor pushes this bin onto their DPL. To summarise, the fiducial UV LF we present in Fig. 2.5 is our best estimate of the number density of genuine $z \simeq 7$ sources. However, even if we relax our selection criterion to allow sources which have a plausible brown dwarf fit into the sample, we still find the UV LF to be significantly lower than that found in optical-only surveys for our brightest bins.

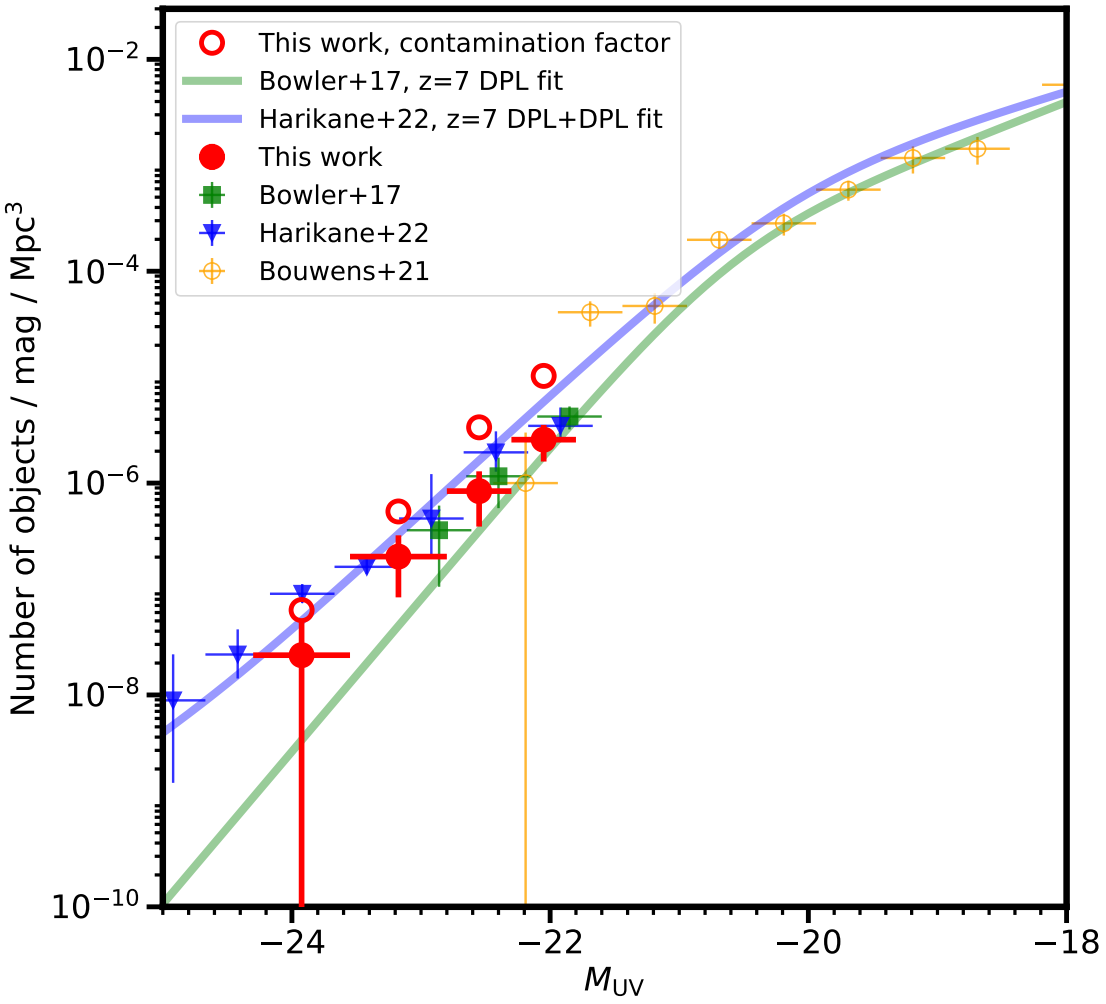

Figure A.1: The UV luminosity function at $z = 7$, computed including the inclusive sample. The red circles show measurements of the number density from this work. Other measurements from Harikane et al. (2022b), Bowler et al. (2017) and Bouwens et al. (2021) are shown. The solid lines show the best fitting double power laws from Harikane et al. (2022b) (blue) and Bowler et al. (2017) (green). The red open circles show our LF points incorporating a contamination factor of 50 per cent, as derived by SED fitting of objects from Harikane et al. (2022b) that overlapped with our catalogues.

B

Candidate postage stamps and SEDs from Chapter 2

In this Appendix we present postage stamps and SED fitting of all candidates in 2. Fig. B.1 shows the candidates in XMM-LSS, and B.2 shows the candidates in ECDF-S. Fig. B.3 shows objects in XMM-LSS which require a Lyman-α emission line to be included in the sample. Fig. B.4 and Fig. B.5 show the stamps and SEDs of the inclusive candidates presented in Appendix A.

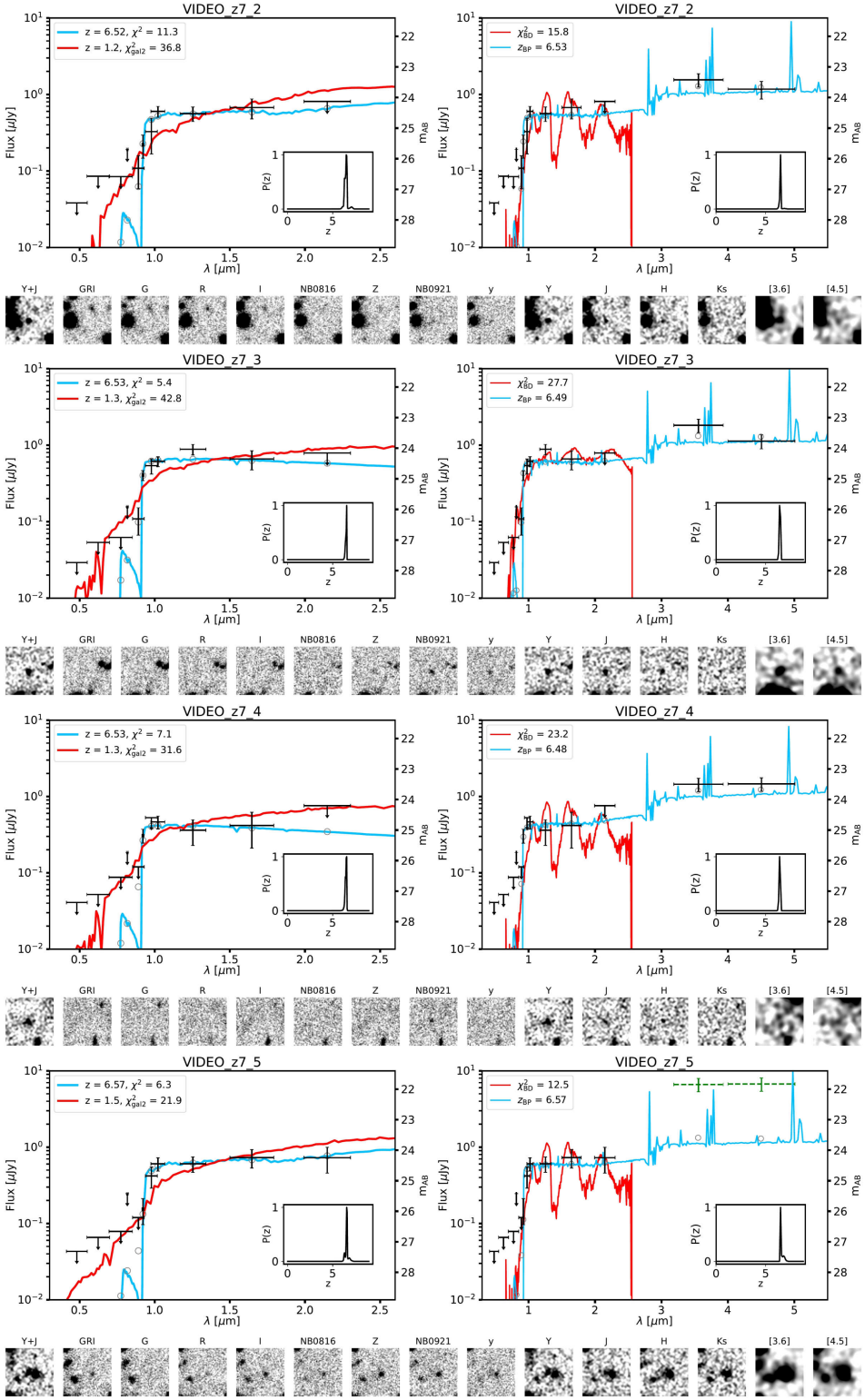

Figure B.1: Candidate galaxies in XMM. The plots and stamps are the same as Fig. 2.3. Confused IRAC photometry is shown in green with dashed wavelength error bars.

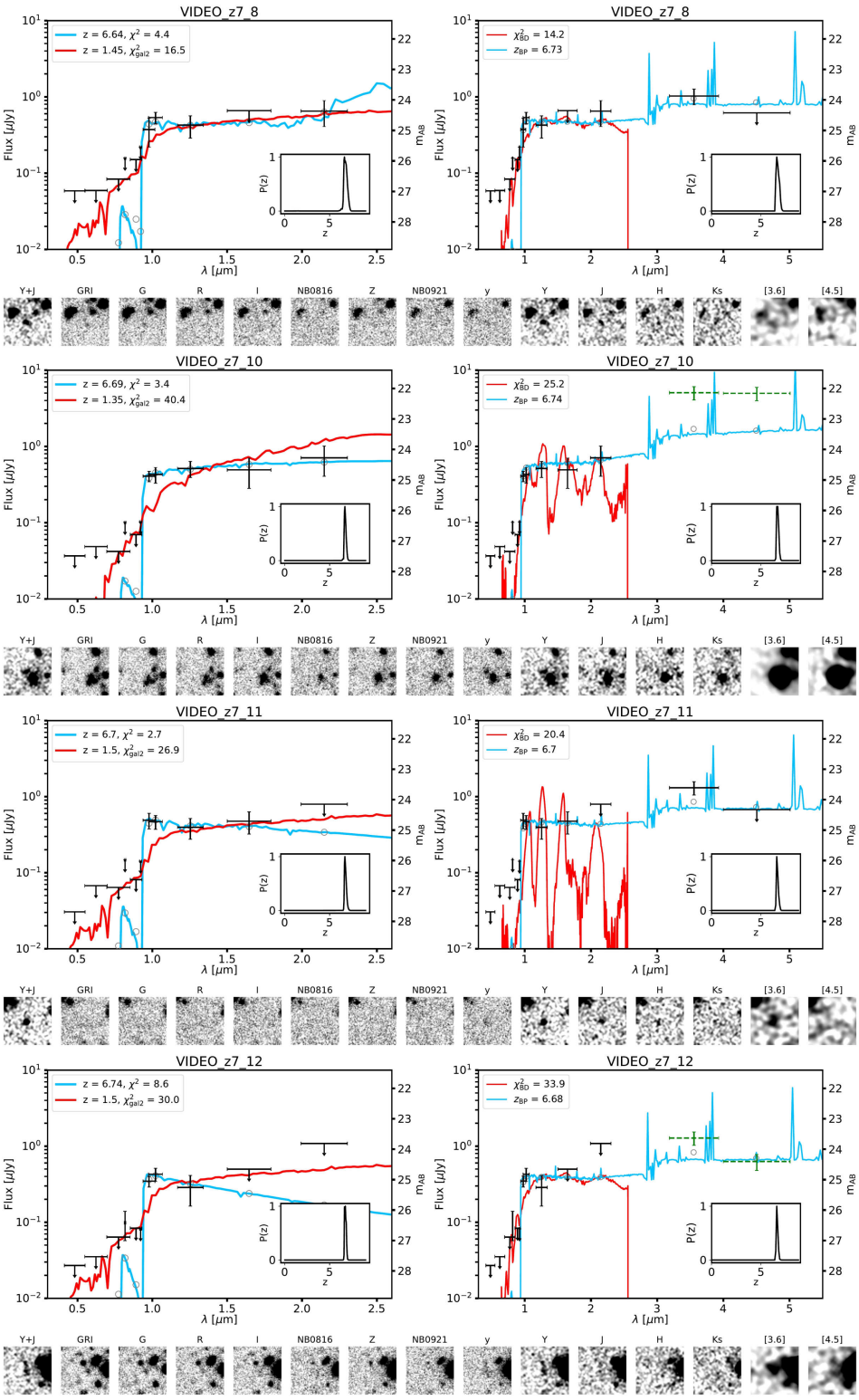

Figure B.1: Continued.

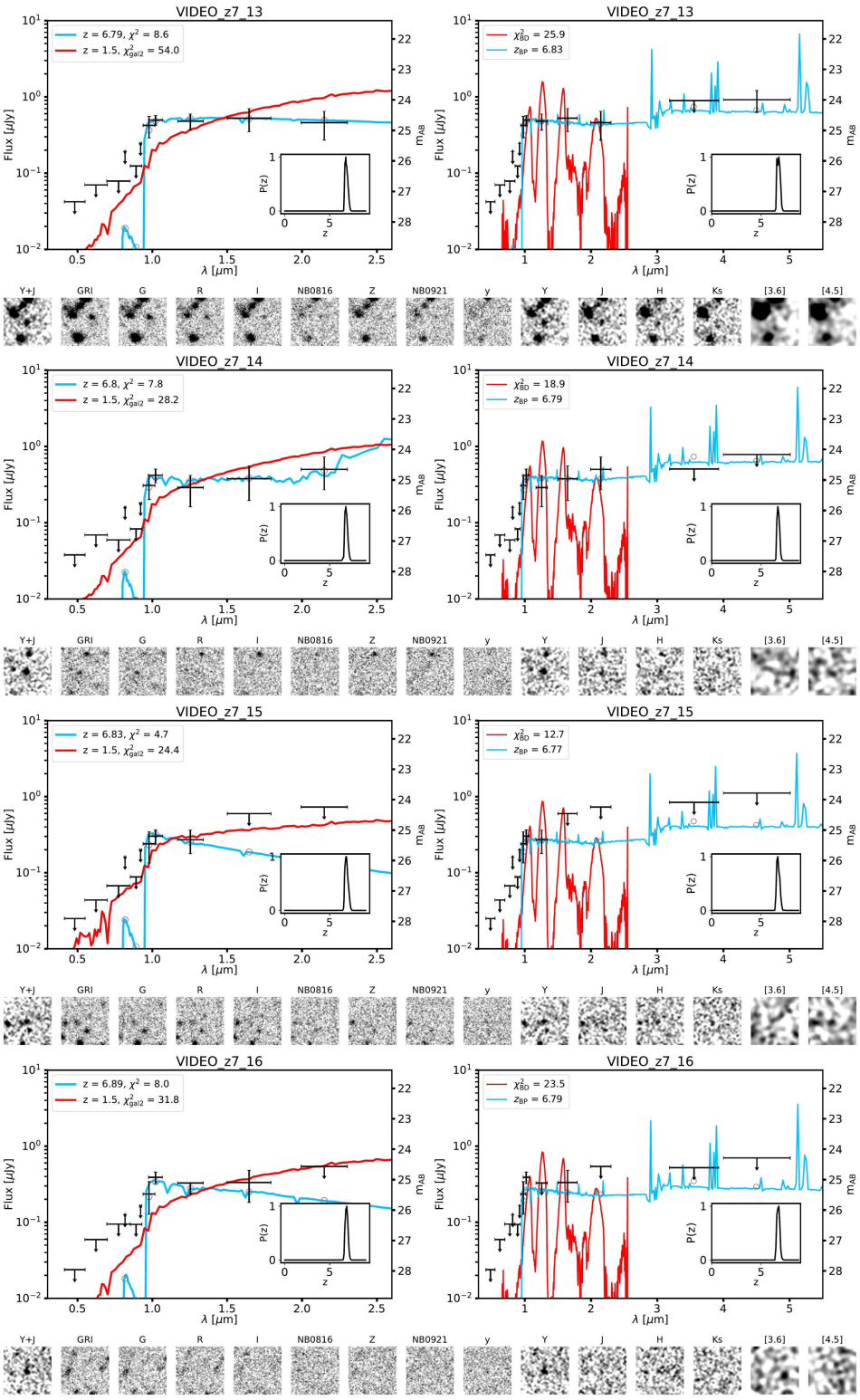

Figure B.1: Continued.

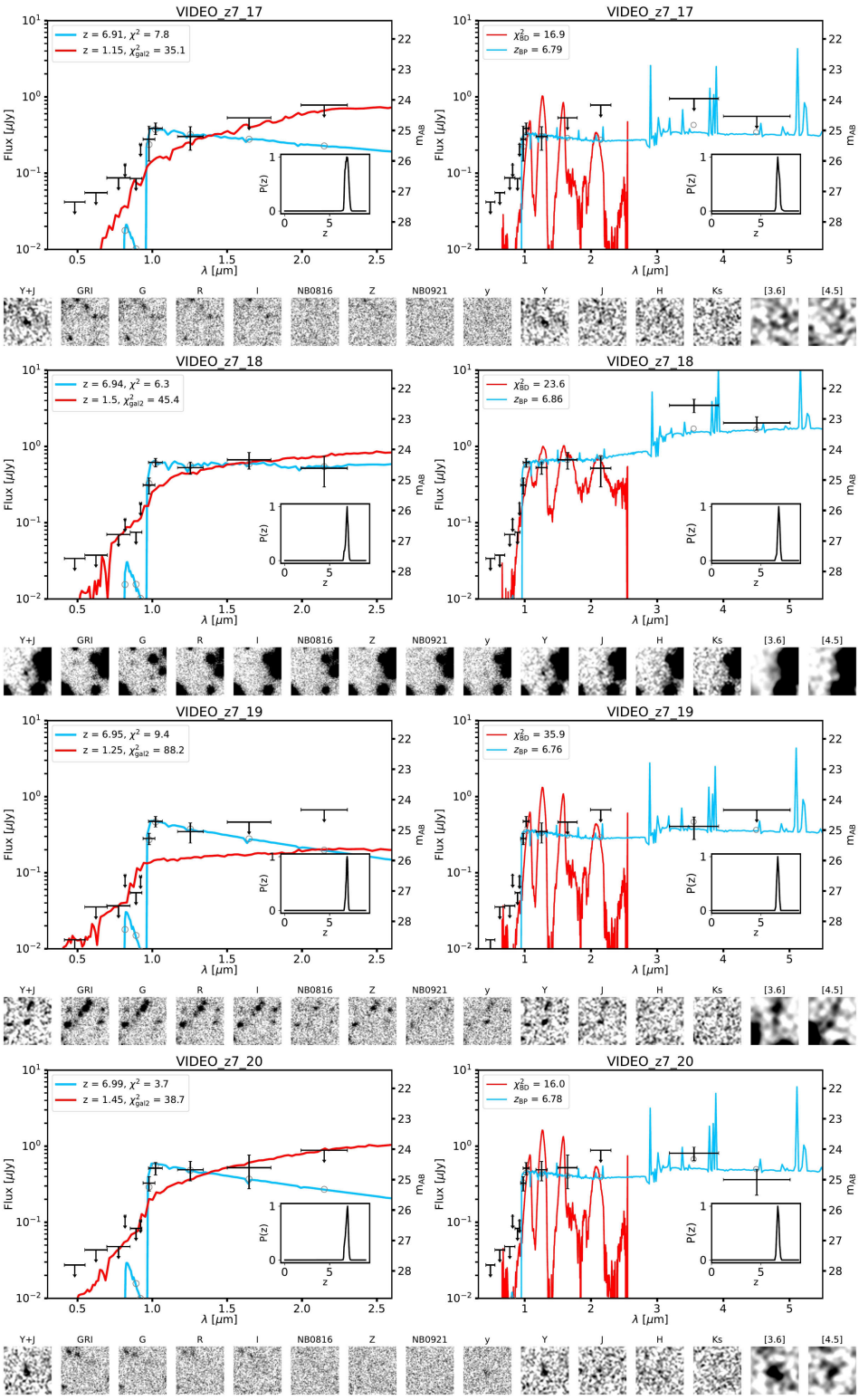

Figure B.1: Continued.

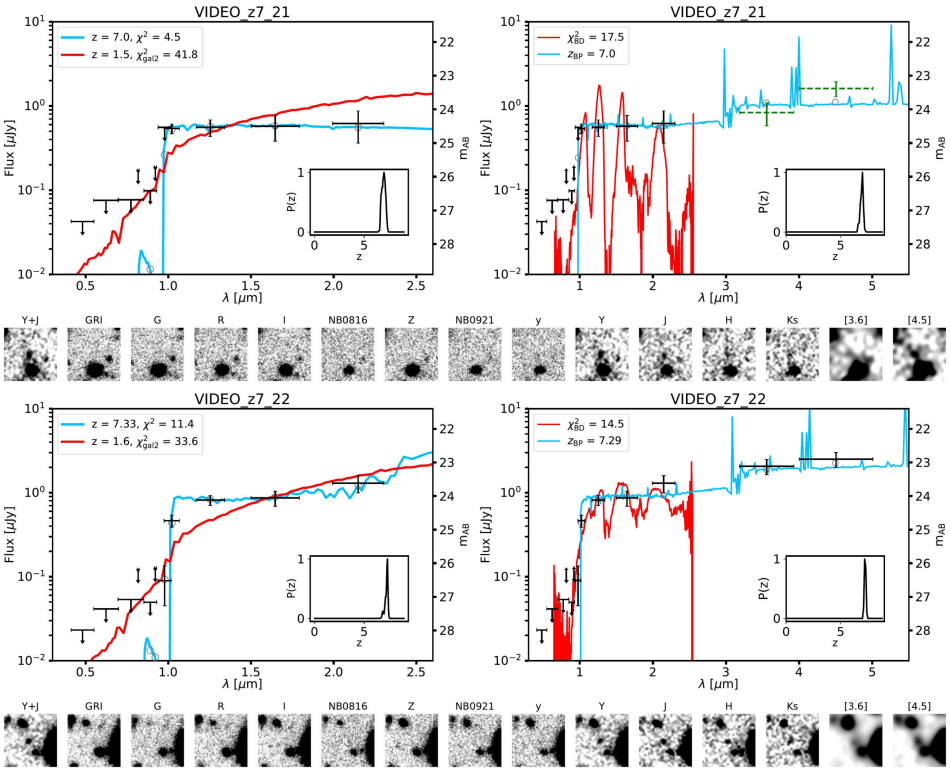

Figure B.1: Continued.

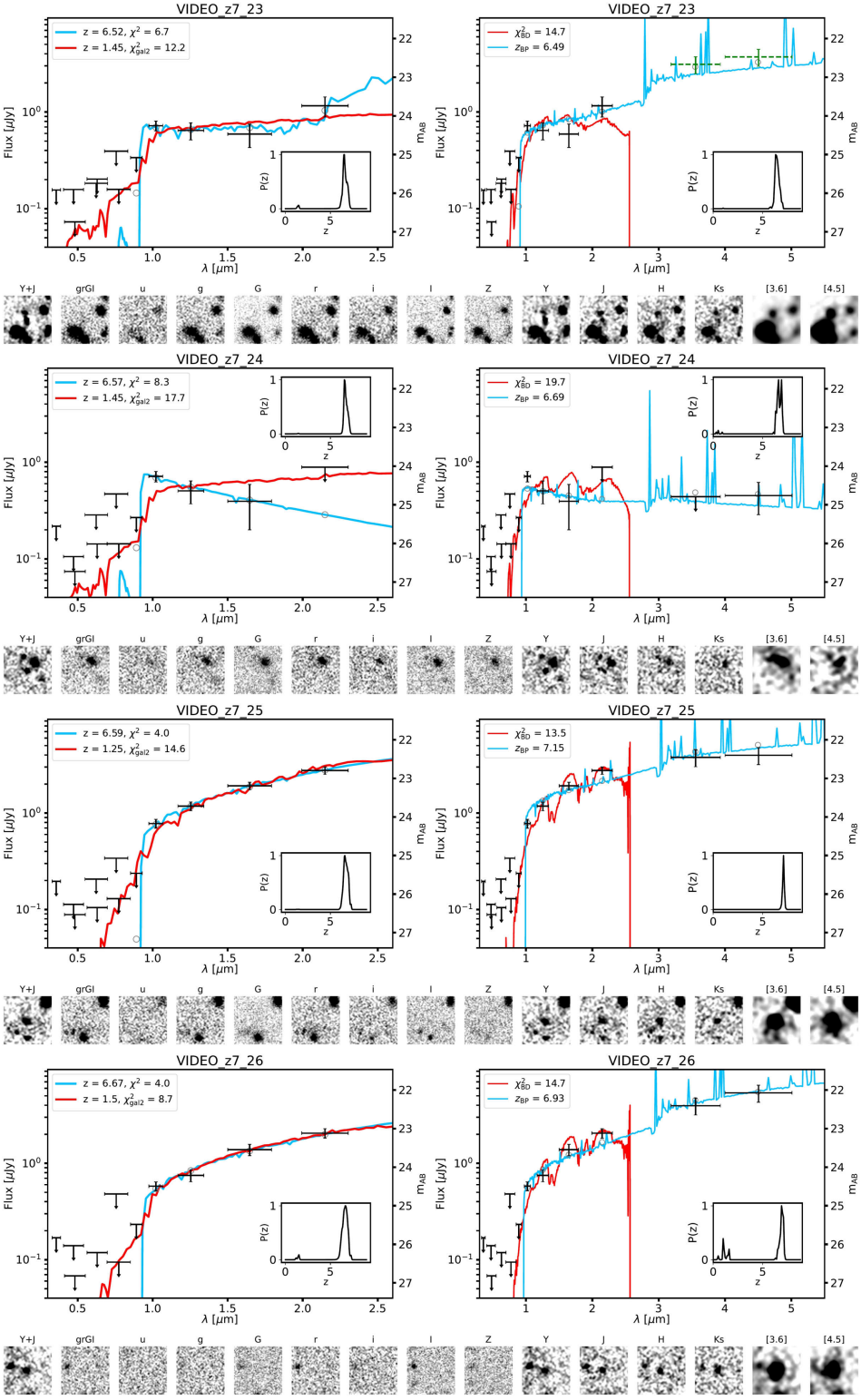

Figure B.2: Candidate galaxies in CDFS. The plots and stamps are the same as Fig. 2.3. Confused IRAC photometry is shown in green with dashed wavelength error bars.

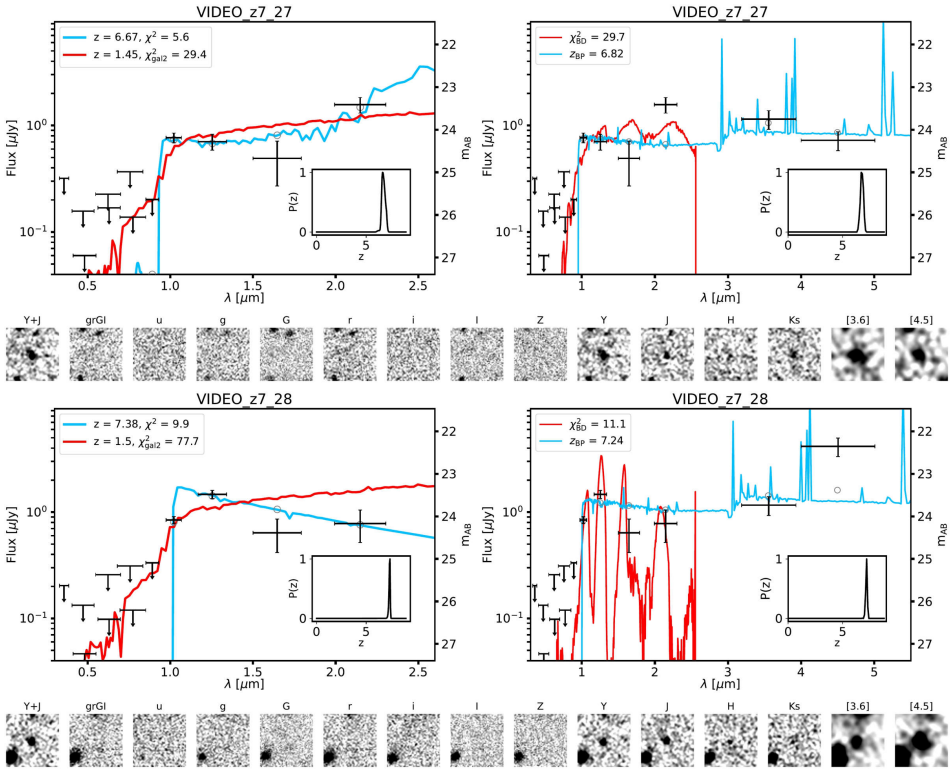

Figure B.2: Continued.

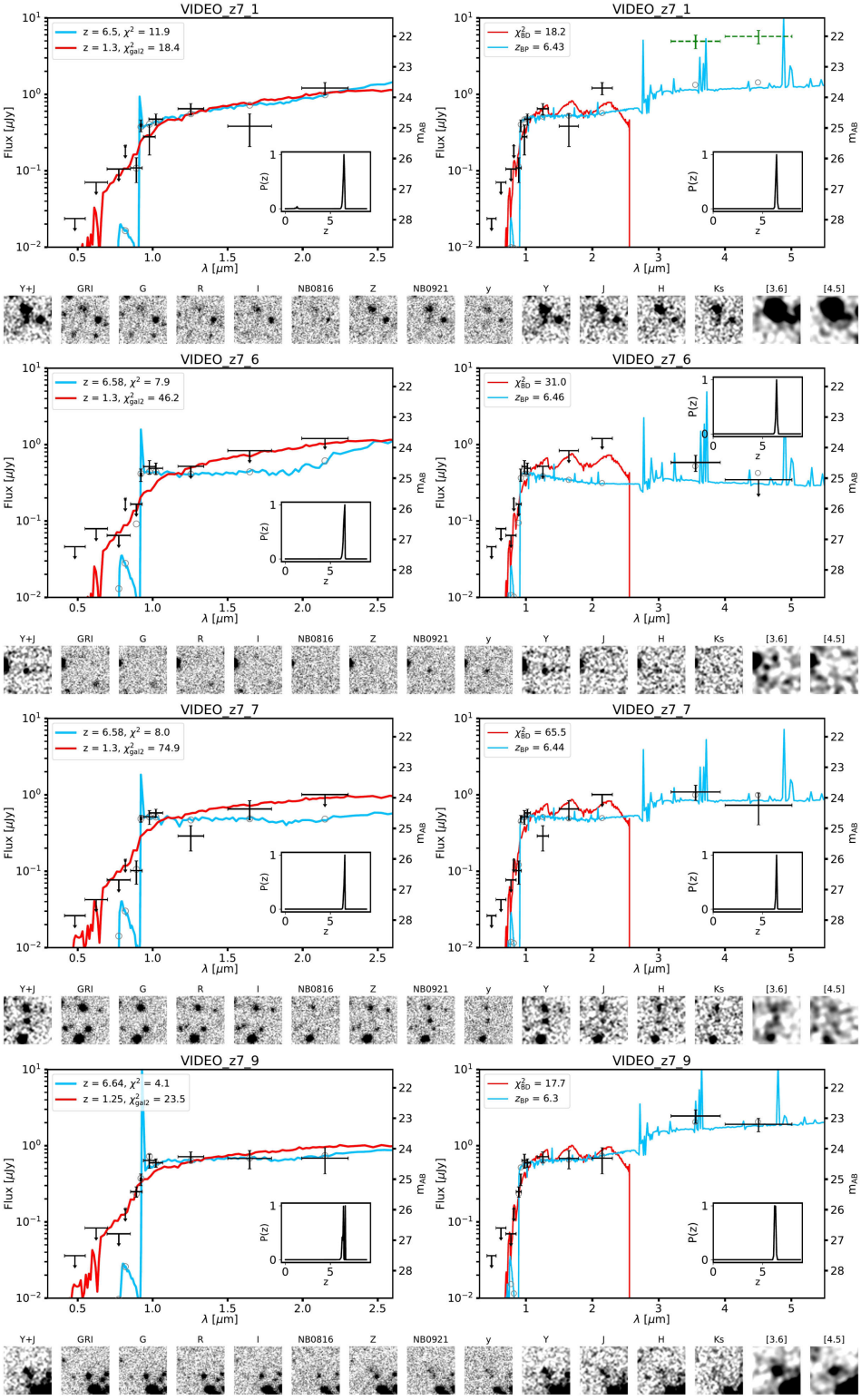

Figure B.3: Candidate galaxies in XMM that require a Lyman-α emission line to be included in our sample. The plots and stamps are the same as Fig. 2.3. Confused IRAC photometry is shown in green with dashed wavelength error bars.

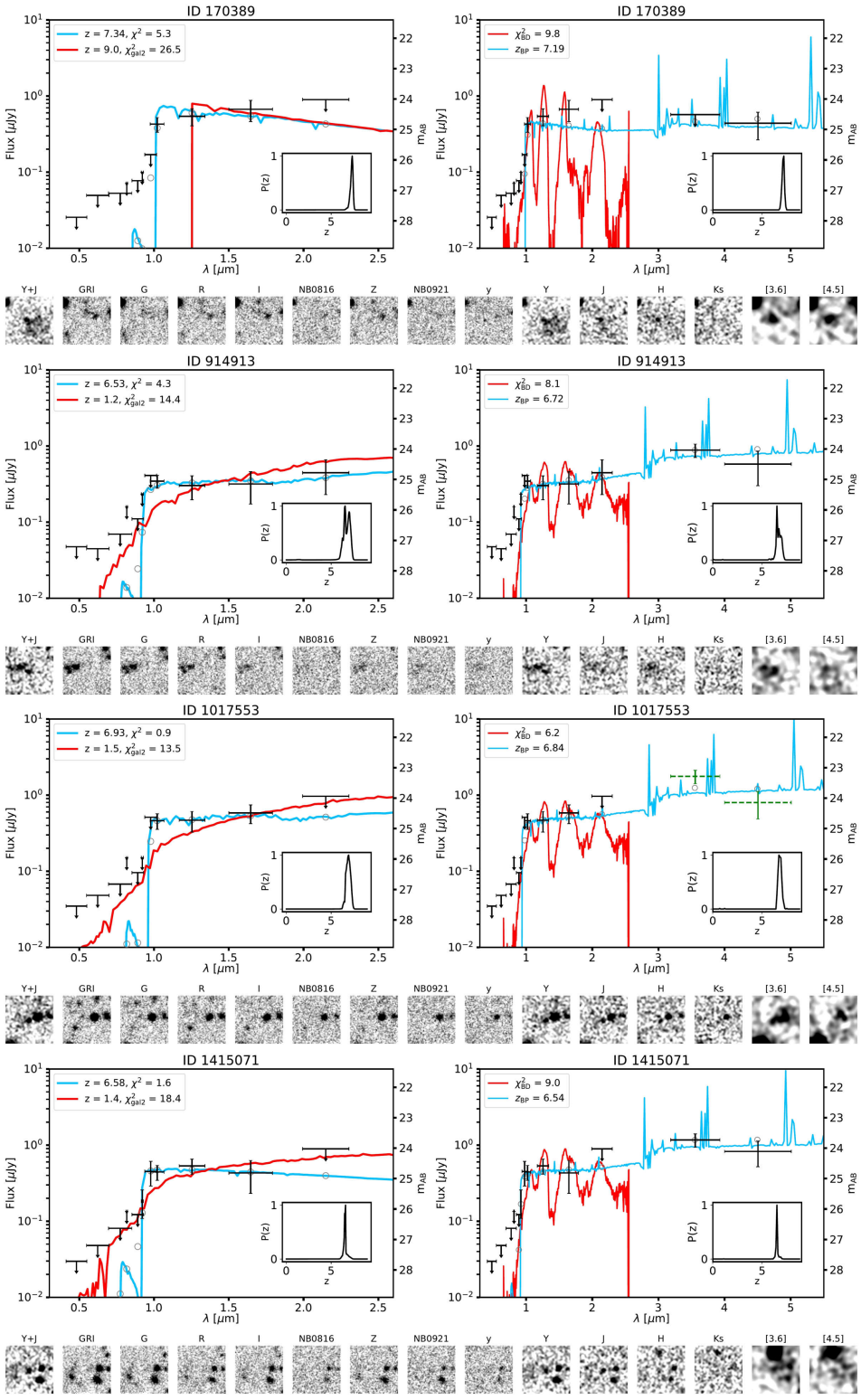

Figure B.4: Inclusive candidates in XMM-LSS. These are defined as having good brown dwarf fits, $\chi^2_{\rm star} < 10$, yet have significantly better galaxy fits, $\chi^2_{\rm star} - \chi^2 > 4$ when fitted without *GR*. The plots and stamps are the same as Fig. 2.3. Confused IRAC photometry is shown in green with dashed wavelength error bars.

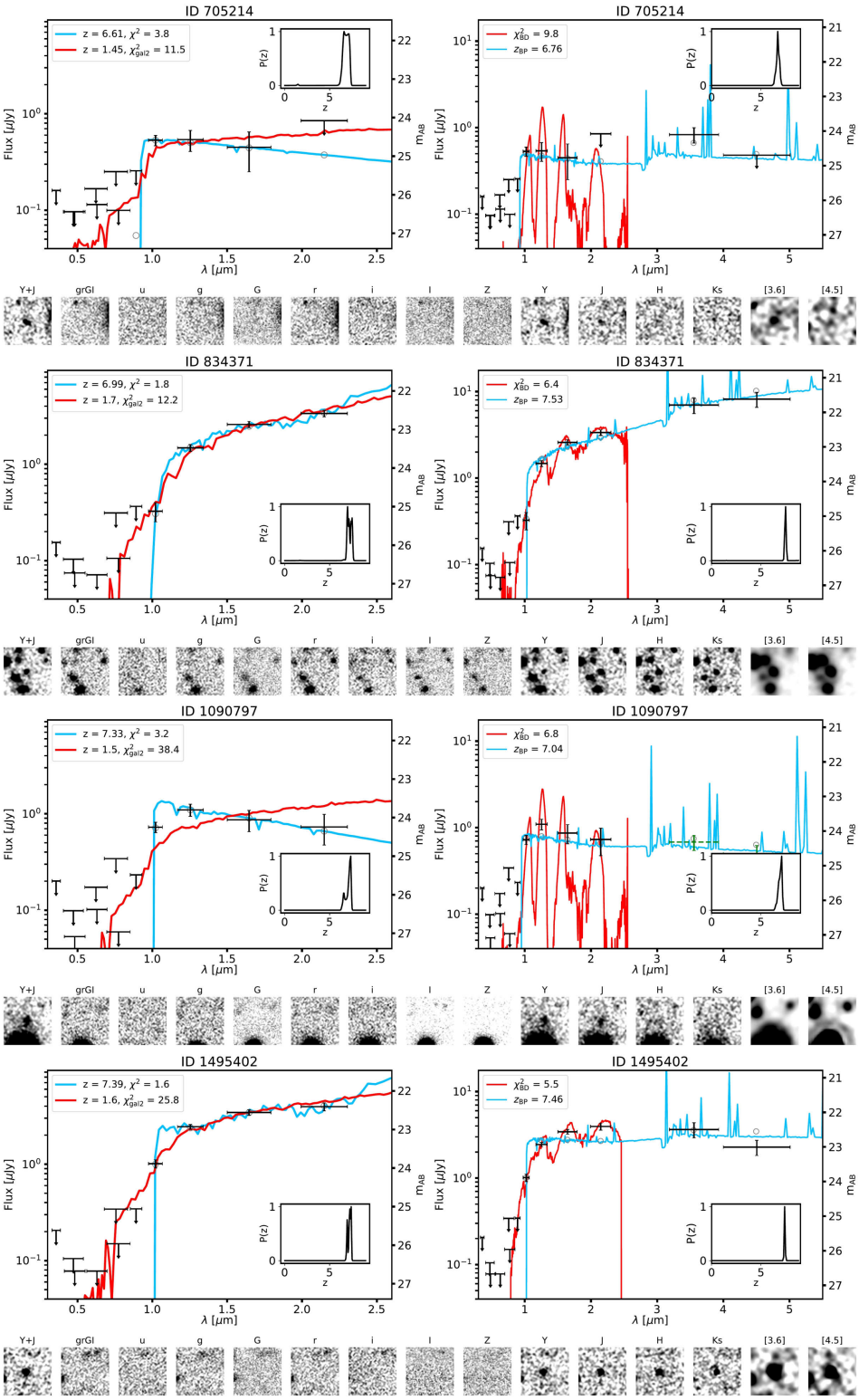

Figure B.5: Inclusive candidates in ECDF-S. These are defined as having good stellar fits, $\chi^2_{\rm star} < 10$, yet have significantly better galaxy fits, $\chi^2_{\rm star} - \chi^2 > 4$ when fitted without *ugrGR*. The plots and stamps are the same as Fig. 2.3. Confused IRAC photometry is shown in green with dashed wavelength error bars.

C

Unusual object in XMM-LSS

In this Appendix we present the SED and postage stamp images of ID 1610530, an unusual object noted in Section 2.3.3. If this object is at high redshift, the rest-frame UV is very bright ($M_{\rm UV} = -24.4$), but the *Spitzer*/IRAC photometry appears unusually faint, around 3.5-4 mag fainter than suggested by the model. When *Spitzer*/IRAC photometry is included in the SED fitting, the fit becomes very poor with $\chi^2 = 167.6$. A crosstalk artifact is perhaps ruled out by the 3.5σ detection in the [3.6] band. Additionally, the object is not detected in WIRDS-J. In Fig. C.1 we present a measurement of the WIRDS-J flux in a 2 arcsec diameter aperture at the position of the object. The measured flux is ~ 3 mag lower than measured in VIDEO-J.

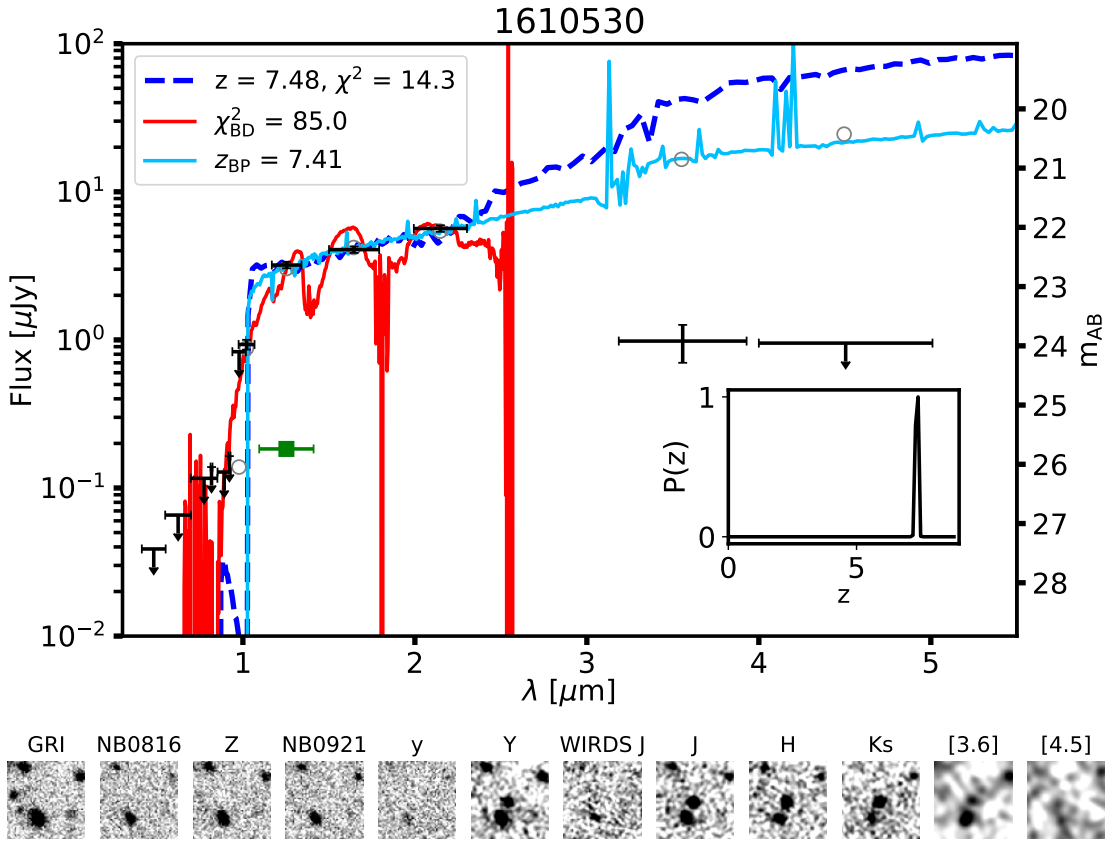

Figure C.1: SED fitting (top) and postage stamp images (bottom) of ID 1610530, the unusual object discussed in Section 2.3.3. In the top panel, the black points in both plots are the measured photometry, with non-detections replaced by 2σ upper limits. The blue dashed curve shows the best-fitting LePhare solution. The solid light blue curve shows the best-fit BAGPIPES solution, with its model photometry shown as the grey circles. The red curve shows the best-fitting BD solution. The legend shows the redshift and χ^2 of the best-fitting LePhare solution (without IRAC), $\chi^2_{\rm BD}$ (fit without G, R and IRAC) and the redshift of the BAGPIPES solution, $z_{\rm BP}$. The inset black curve is the redshift probability found by BAGPIPES. The bottom panel shows the 10 arcsec $\times$ 10 arcsec postage stamps of the object in the filters used. We also show the WIRDS J-band, where the object is not detected. The green square point in the top panel corresponds to the photometry measured in a 2 arcsec diameter circular aperture in WIRDS-J.

D

Candidate postage stamps and SEDs from Chapter 3

In Fig. D.1 we present the results of the SED fitting and postage stamp images for the 30 most luminous galaxies in the UltraVISTA+*Euclid* sample from Chapter 3, spanning $-22.3 < M_{\rm UV} < -21.3$.

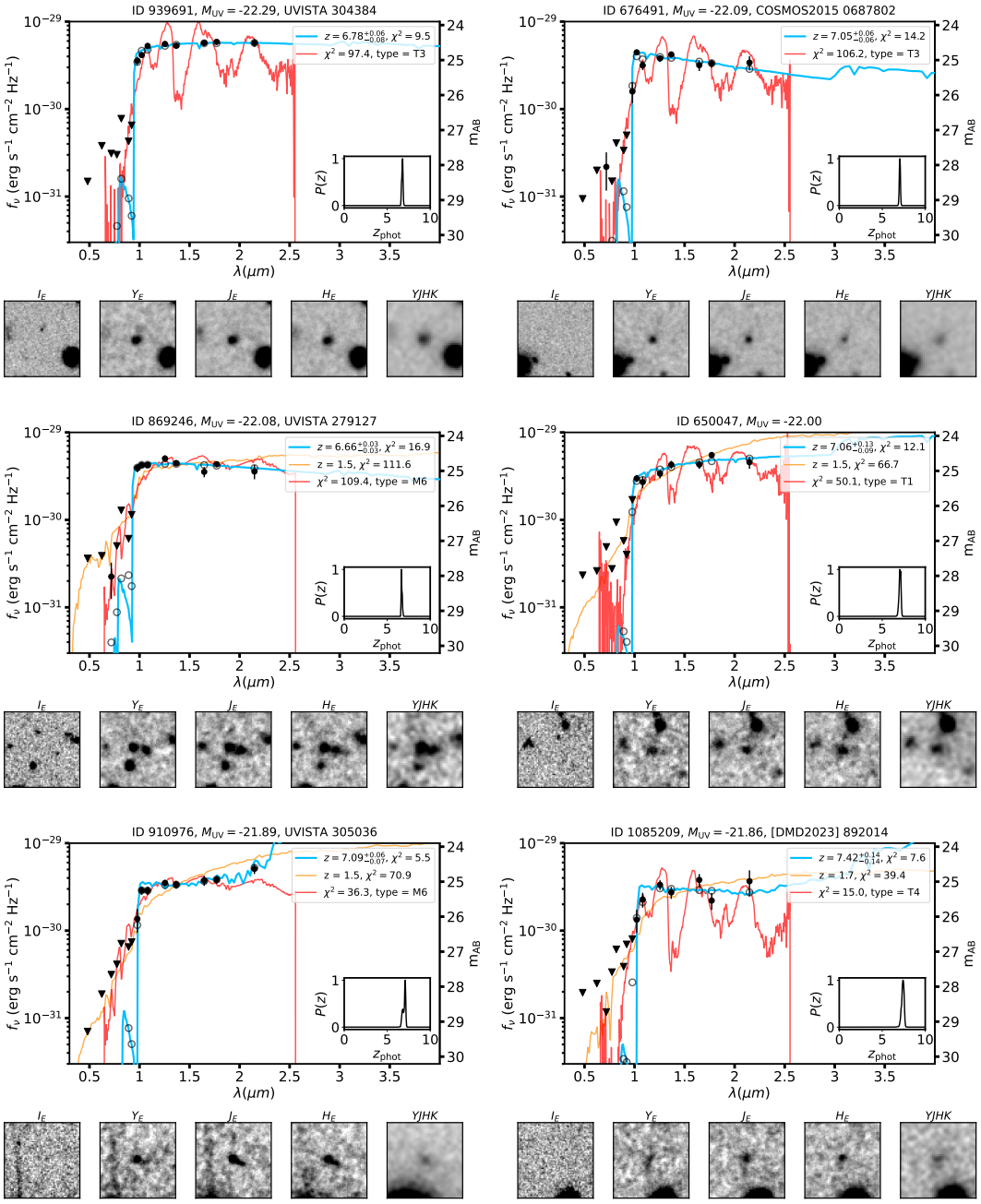

Figure D.1: SED fits (top) and postage stamp cutouts (bottom) of the thirty most luminous galaxies in the UltraVISTA+*Euclid* sample. See Fig. 3.3 for a description of the SED plots. The title of the SED indicates the object ID, absolute magnitude $M_{\rm UV}$, and the literature ID if it has been previously identified. The postage stamps, from lef to right, are from I_E, Y_E, J_E and a VISTA $YJHK$ stack. The stamps are $6 \times 6''$and are scaled to saturate at $\pm 3\sigma$ above/below the noise level. Objects with names beginning with UVISTA were identified in Bowler et al. (2014). Objects with names labelled as [ESC2021] and [ESC2021a] were first identified in Endsley et al. (2021b) and Endsley et al. (2021a), respectively. [DMD23] 892014 is from Donnan et al. (2023a). COSMOS2015 and COSMOS2020 objects were identified in Laigle et al. (2016) and Weaver et al. (2022), respectively. S-CANDELS objects are galaxies identified in *Hubble* imaging (Ashby et al., 2015), and LAE-17 was identified in Hu et al. (2017). The SSTSL source is also identified as REBELS-21 (Bouwens et al., 2022a).

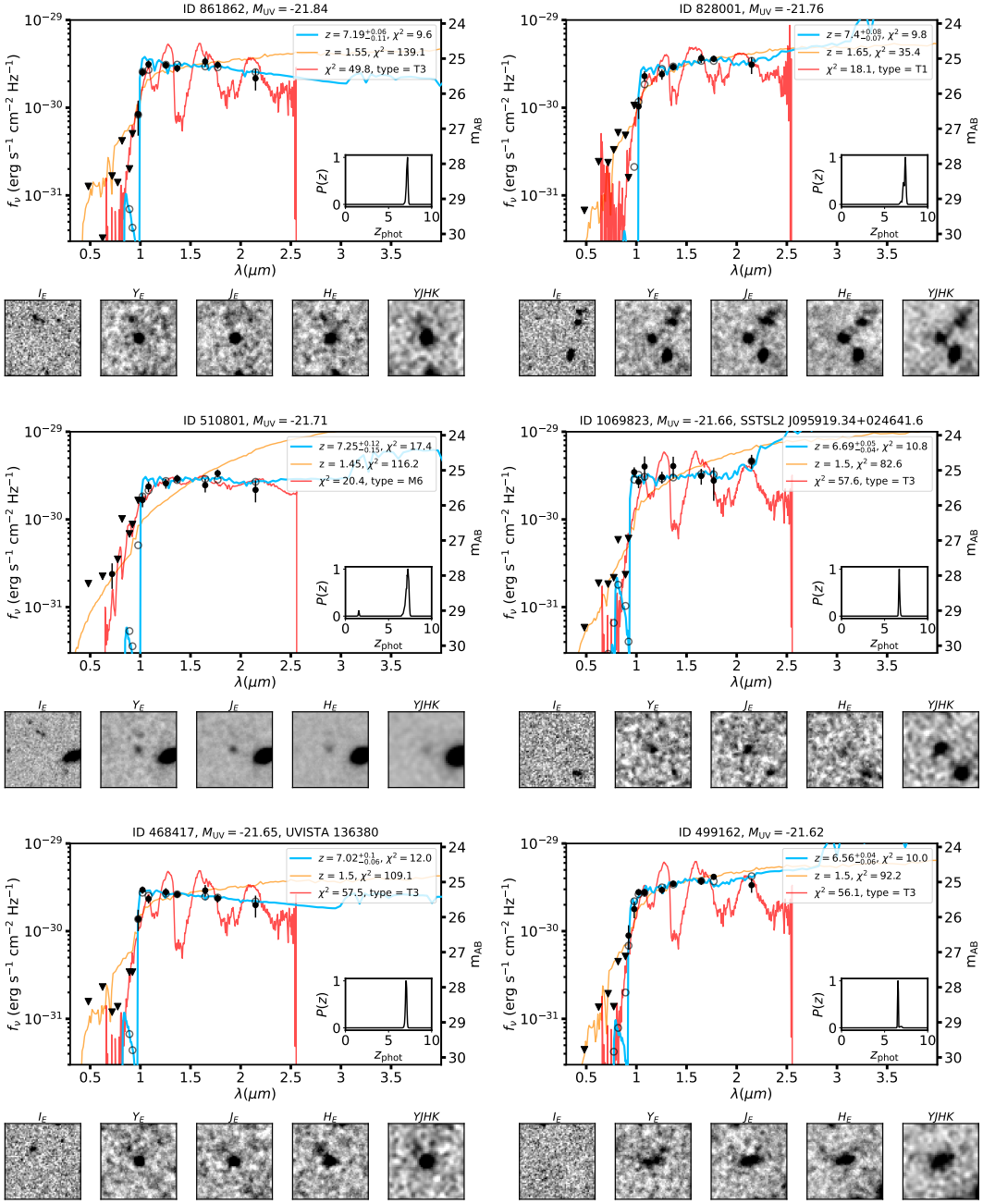

Figure D.1: Continued.

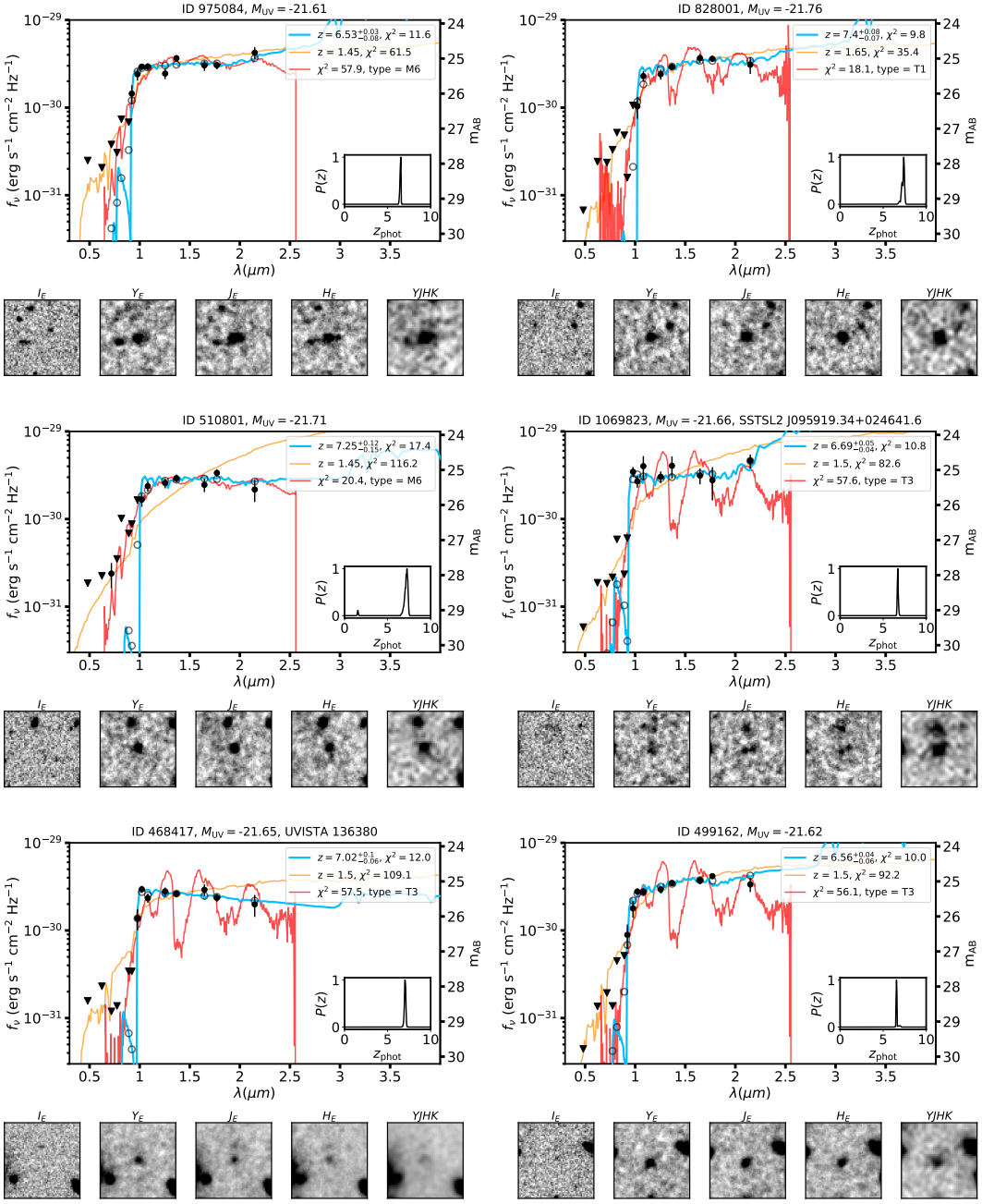

Figure D.1: Continued.

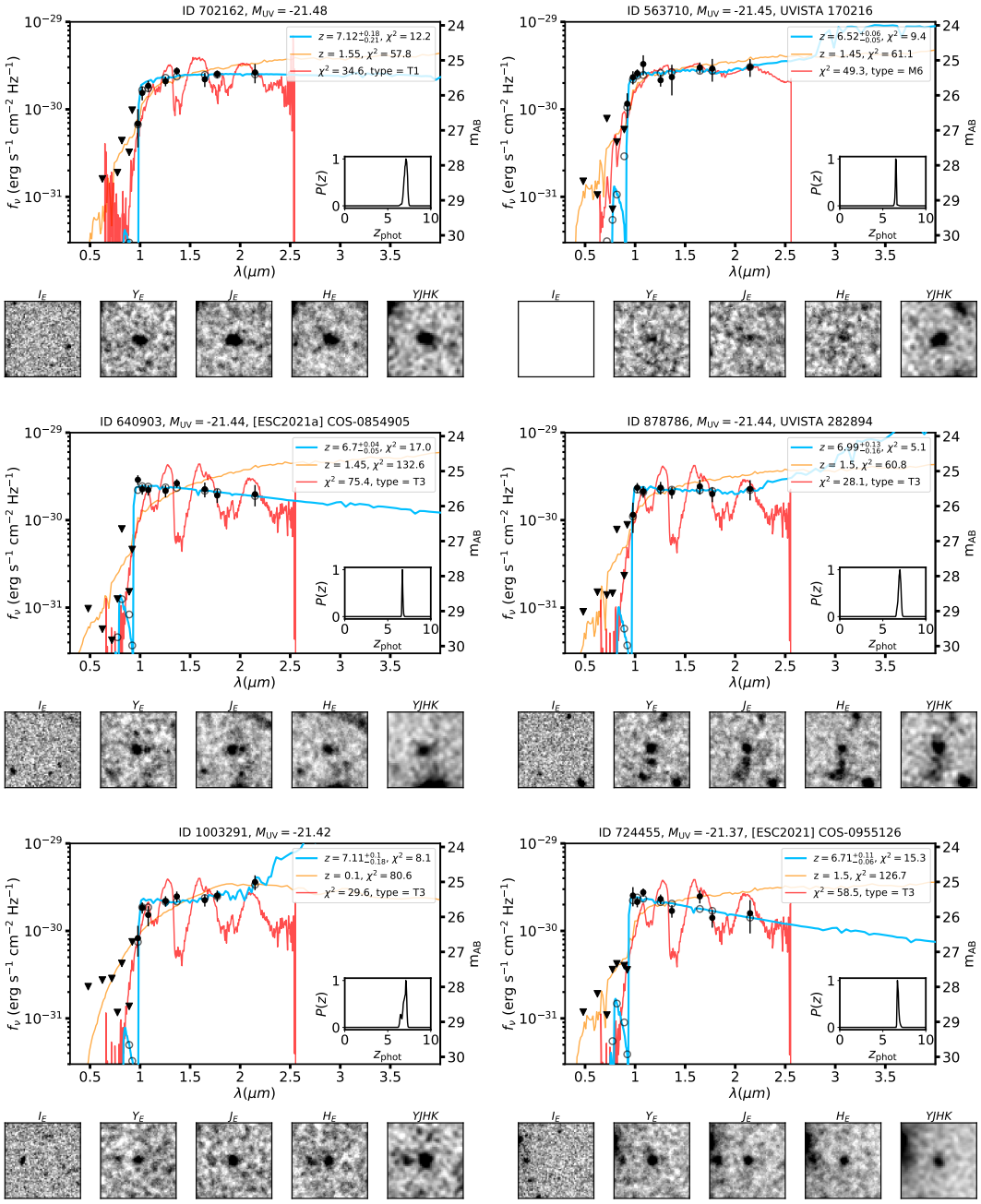

Figure D.1: Continued.

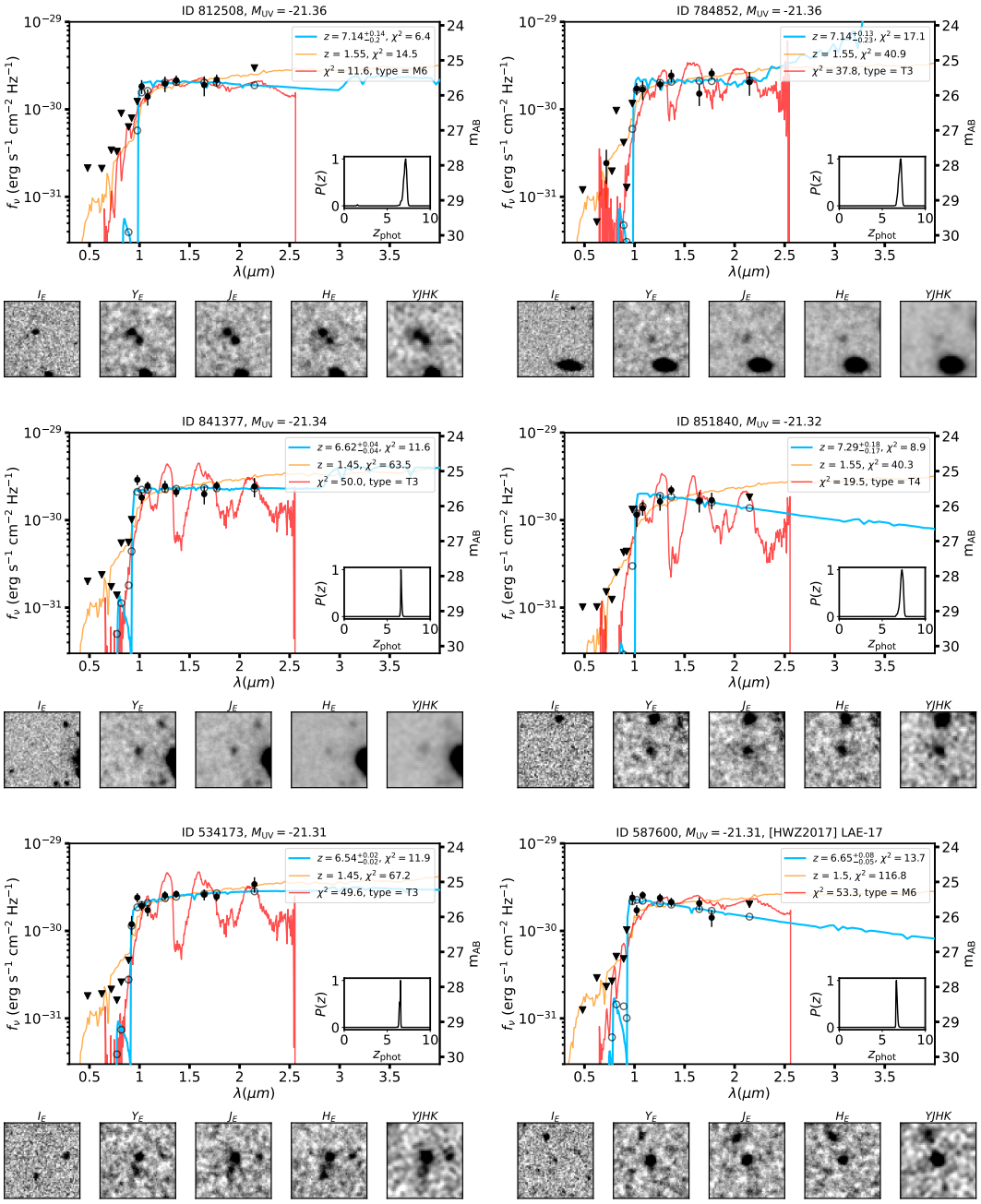

Figure D.1: Continued.

Homogenous green!
Homogenous green yummy!!
Homogenous green!!!

— R. G. Varadaraj

References

Abel, T., Bryan, G. L., and Norman, M. L. (2002). *Science* 295.5552, pp. 93–98.

Adamo, A. et al. (2024). *arXiv e-prints*, arXiv:2405.21054.

Adams, N. J. et al. (2020). MNRAS 494.2, pp. 1771–1783.

Adams, N. J. et al. (2023a). MNRAS 518.3, pp. 4755–4766.

Adams, N. J. et al. (2023b). MNRAS 523.1, pp. 327–346.

Adams, N. J. et al. (2024). ApJ 965.2, p. 169.

Adelberger, K. L. et al. (2005). ApJ 619.2, pp. 697–713.

Aihara, H. et al. (2019). *PASJ* 71.6, p. 114.

Aihara, H. et al. (2022). PASJ 74.2, pp. 247–272.

Algera, H. et al. (2025). *arXiv e-prints*, arXiv:2501.10508.

Algera, H. S. B. et al. (2023). MNRAS 518.4, pp. 6142–6157.

Arnouts, S. et al. (1999). MNRAS 310.2, pp. 540–556.

Arrabal Haro, P. et al. (2023). Nature 622.7984, pp. 707–711.

Ashby, M. L. N. et al. (2013). ApJ 769.1, p. 80.

Ashby, M. L. N. et al. (2015). ApJS 218.2, p. 33.

Atek, H. et al. (2024). *arXiv e-prints*, arXiv:2405.13504.

Atek, H. et al. (2023a). *JWST's GLIMPSE: gravitational lensing & NIRCam imaging to probe early galaxy formation and sources of reionization*. JWST Proposal. Cycle 2, ID. #3293.

Atek, H. et al. (2023b). MNRAS 519.1, pp. 1201–1220.

Bailey, J., Simpson, A., and Crisp, D. (2007). PASP 119.852, pp. 228–236.

Baker, W. M. et al. (2025). *Nature Astronomy* 9, pp. 141–154.

Bañados, E. et al. (2018). Nature 553.7689, pp. 473–476.

Bañados, E. et al. (2025). *Nature Astronomy* 9, pp. 293–301.

Barkana, R. and Loeb, A. (2001). Phys. Rep. 349.2, pp. 125–238.

Barkana, R. and Loeb, A. (2000). ApJ 531.2, pp. 613–623.

Bartlett, D. J. and Desmond, H. (2023). *The Open Journal of Astrophysics* 6, p. 42.

Becker, R. H. et al. (2001). AJ 122.6, pp. 2850–2857.

Beckwith, S. V. W. et al. (2006). *The Astronomical Journal* 132.5, pp. 1729–1755.

Behroozi, P. S., Wechsler, R. H., and Conroy, C. (2013). *ApJ* 770.1, p. 57.

Benson, A. J. et al. (2003). *ApJ* 599.1, pp. 38–49.

Bertin, E. (2006). In: *Astronomical Data Analysis Software and Systems XV*. Ed. by C. Gabriel et al. Vol. 351. Astronomical Society of the Pacific Conference Series, p. 112.

Bertin, E. (2011). In: *Astronomical Data Analysis Software and Systems XX*. Ed. by I. N. Evans et al. Vol. 442. Astronomical Society of the Pacific Conference Series, p. 435.

Bertin, E. and Arnouts, S. (1996). A&AS 117, pp. 393–404.

Bertin, E. et al. (2002). In: *Astronomical Data Analysis Software and Systems XI*. Ed. by D. A. Bohlender, D. Durand, and T. H. Handley. Vol. 281. Astronomical Society of the Pacific Conference Series, p. 228.

Bezanson, R. et al. (2024). ApJ 974.1, p. 92.

Bian, F. et al. (2013). ApJ 774.1, p. 28.

Bielby, R. et al. (2012). A&A 545, A23.

Blandford, R., Meier, D., and Readhead, A. (2019). ARA&A 57, pp. 467–509.

Boucaud, A. et al. (2016). A&A 596, A63.

Bouwens, R. J. et al. (2006). ApJ 653.1, pp. 53–85.

Bouwens, R. J. et al. (2011). ApJ 737.2, p. 90.

Bouwens, R. J. et al. (2021). *AJ* 162.2, p. 47.

Bouwens, R. J. et al. (2022a). ApJ 931.2, p. 160.

Bouwens, R. J. et al. (2022b). ApJ 927.1, p. 81.

Bower, R. G., Benson, A. J., and Crain, R. A. (2012). MNRAS 422.4, pp. 2816–2840.

Bower, R. G. et al. (2006). MNRAS 370.2, pp. 645–655.

Bowler, R. A. A. et al. (2018). MNRAS 481.2, pp. 1631–1644.

Bowler, R. A. A. et al. (2012). MNRAS 426.4, pp. 2772–2788.

Bowler, R. A. A. et al. (2014). MNRAS 440.3, pp. 2810–2842.

Bowler, R. A. A. et al. (2015). MNRAS 452.2, pp. 1817–1840.

Bowler, R. A. A. et al. (2017). MNRAS 466.3, pp. 3612–3635.

Bowler, R. A. A. et al. (2020). MNRAS 493.2, pp. 2059–2084.

Bowler, R. A. A. et al. (2022). MNRAS 510.4, pp. 5088–5101.

Bowler, R. A. A. et al. (2024). MNRAS 527.3, pp. 5808–5828.

Bradley, L. D. et al. (2012). *ApJ* 760.2, p. 108.

Bradley, L. (2023). *astropy/photutils: 1.8.0*. Version 1.8.0.

Brennan, M. (1982). *The Boyne Valley vision*. Dolmen Press.

Bromm, V., Coppi, P. S., and Larson, R. B. (1999). ApJ 527.1, pp. L5–L8.

Bruzual, G. and Charlot, S. (2003). MNRAS 344.4, pp. 1000–1028.

Bullock, J. S. et al. (2001). ApJ 555.1, pp. 240–257.

Bunker, A. J. et al. (2003). MNRAS 342.3, pp. L47–L51.

Bunker, A. J. et al. (2004). MNRAS 355.2, pp. 374–384.

Bunker, A. J. et al. (2010). MNRAS 409.2, pp. 855–866.

Bunker, A. J. et al. (2023). A&A 677, A88.

Bunker, A. J. et al. (2024). A&A 690, A288.

Burgasser, A. J. (2014). In: *Astronomical Society of India Conference Series*. Vol. 11. Astronomical Society of India Conference Series, pp. 7–16.

Burgasser, A. J. et al. (2024). ApJ 962.2, p. 177.

Bushouse, H. et al. (2023). *JWST Calibration Pipeline*. Version 1.9.4.

Cai, Z.-Y. et al. (2014). ApJ 785.1, p. 65.

Calzetti, D. et al. (2000). *ApJ* 533.2, pp. 682–695.

Cameron, A. J. et al. (2023). A&A 677, A115.

Cameron, A. J. et al. (2024). MNRAS 534.1, pp. 523–543.

Cano-Díaz, M. et al. (2012). A&A 537, p. L8.

Capak, P. et al. (2011). ApJ 730.2, p. 68.

Carnall, A. C. et al. (2018). MNRAS 480.4, pp. 4379–4401.

Carnall, A. C. et al. (2023a). MNRAS 520.3, pp. 3974–3985.

Carnall, A. C. et al. (2023b). Nature 619.7971, pp. 716–719.

Carniani, S. et al. (2024). Nature 633.8029, pp. 318–322.

Casey, C. M. et al. (2023). ApJ 954.1, p. 31.

Castellano, M. et al. (2022). ApJ 938.2, p. L15.

Castellano, M. et al. (2024). ApJ 972.2, p. 143.

Chabrier, G. (2003). PASP 115.809, pp. 763–795.

Charlot, S. and Longhetti, M. (2001). MNRAS 323.4, pp. 887–903.

Chemerynska, I. et al. (2024). MNRAS 531.2, pp. 2615–2625.

Cirasuolo, M. et al. (2020). *The Messenger* 180, pp. 10–17.

Claeyssens, A. et al. (2022). A&A 666, A78.

Conroy, C. (2013). ARA&A 51.1, pp. 393–455.

Conselice, C. J. (2014). ARA&A 52, pp. 291–337.

Conselice, C. J., Bershady, M. A., and Jangren, A. (2000). ApJ 529.2, pp. 886–910.

Costantin, L. et al. (2023). ApJ 946.2, p. 71.

Cowie, L. L. et al. (1996). AJ 112, p. 839.

Cox, T. J. et al. (2008). MNRAS 384.1, pp. 386–409.

Cuillandre, J. .-. et al. (2024). *arXiv e-prints*, arXiv:2405.13496.

Cuillandre, J.-C. J. et al. (2012). In: *Observatory Operations: Strategies, Processes, and Systems IV*. Ed. by A. B. Peck, R. L. Seaman, and F. Comeron. Vol. 8448. Society of Photo-Optical Instrumentation Engineers (SPIE) Conference Series, p. 84480M.

Curti, M. et al. (2023). MNRAS 518.1, pp. 425–438.

Curtis-Lake, E. et al. (2016). MNRAS 457.1, pp. 440–464.

Curtis-Lake, E. et al. (2023). *Nature Astronomy* 7, pp. 622–632.

Cushing, M. C. et al. (2008). ApJ 678.2, pp. 1372–1395.

da Cunha, E., Charlot, S., and Elbaz, D. (2008). MNRAS 388.4, pp. 1595–1617.

Danovich, M. et al. (2015). MNRAS 449.2, pp. 2087–2111.

Davé, R. et al. (2019). MNRAS 486.2, pp. 2827–2849.

Davies, L. J. M. et al. (2018). MNRAS 480.1, pp. 768–799.

Davis, K. et al. (2024). ApJ 974.1, p. 42.

de Jong, R. S. and Lacey, C. (2000). ApJ 545.2, pp. 781–797.

Dekel, A. et al. (2009a). Nature 457.7228, pp. 451–454.

Dekel, A., Sari, R., and Ceverino, D. (2009b). ApJ 703.1, pp. 785–801.

Dekel, A. et al. (2023). MNRAS 523.3, pp. 3201–3218.

Devecchi, B. and Volonteri, M. (2009). ApJ 694.1, pp. 302–313.

Ding, X., Silverman, J. D., and Onoue, M. (2022). *ApJL* 939.2, p. L28.

Donnan, C. T. et al. (2023a). MNRAS 518.4, pp. 6011–6040.

Donnan, C. T. et al. (2024). MNRAS 533.3, pp. 3222–3237.

Donnan, C. T. et al. (2025). *arXiv e-prints*, arXiv:2501.03217.

Donnan, F. R. et al. (2023b). MNRAS 519.3, pp. 3691–3705.

Duncan, K. J. et al. (2024). *arXiv e-prints*, arXiv:2410.09000.

Dunlop, J. S. et al. (2021). *PRIMER: Public Release IMaging for Extragalactic Research*. JWST Proposal. Cycle 1, ID. #1837.

Durkalec, A. et al. (2015). A&A 583, A128.

Dwek, E. (1998). ApJ 501, p. 643.

Egami, E. et al. (2024). *SAPPHIRES: Slitless Areal Pure-Parallel High-Redshift Emission Survey*. JWST Proposal. Cycle 3, ID. #6434.

Eisenstein, D. J. et al. (2023). *arXiv e-prints*, arXiv:2306.02465.

Ellis, R. S. et al. (2013). ApJ 763.1, p. L7.

Endsley, R. et al. (2021a). MNRAS 502.4, pp. 6044–6063.

Endsley, R. et al. (2021b). MNRAS 500.4, pp. 5229–5248.

Endsley, R. et al. (2023). MNRAS 520.3, pp. 4609–4620.

Erben, T. et al. (2009). *A&A* 493.3, pp. 1197–1222.

Euclid Collaboration et al. (2019). A&A 631, A85.

Euclid Collaboration et al. (2022a). A&A 662, A112.

Euclid Collaboration et al. (2022b). A&A 658, A126.

Euclid Collaboration et al. (2024a). *arXiv e-prints*, arXiv:2405.13491.

Euclid Collaboration et al. (2024b). *arXiv e-prints*, arXiv:2405.13492.

Euclid Collaboration et al. (2024c). *arXiv e-prints*, arXiv:2405.13493.

Euclid Collaboration et al. (2025). *arXiv e-prints*, arXiv:2503.15322.

Fall, S. M. and Efstathiou, G. (1980). MNRAS 193, pp. 189–206.

Ferguson, H. C. et al. (2004). ApJ 600.2, pp. L107–L110.

Ferland, G. J. et al. (1998). PASP 110.749, pp. 761–778.

Ferrami, G. and Wyithe, J. S. B. (2023). MNRAS 523.1, pp. L21–L25.

Ferrami, G. and Wyithe, J. S. B. (2024). MNRAS 532.2, pp. 1832–1848.

Ferrara, A., Pallottini, A., and Sommovigo, L. (2024). *arXiv e-prints*, arXiv:2410.19042.

Ferrara, A., Pallottini, A., and Dayal, P. (2023). MNRAS 522.3, pp. 3986–3991.

Ferreira, L. et al. (2023). ApJ 955.2, p. 94.

Finkelstein, S. L. and Bagley, M. B. (2022). ApJ 938.1, p. 25.

Finkelstein, S. L. et al. (2015). ApJ 810.1, p. 71.

Finkelstein, S. L. et al. (2017). *The Cosmic Evolution Early Release Science (CEERS) Survey*. JWST Proposal ID 1345. Cycle 0 Early Release Science.

Finkelstein, S. L. et al. (2022). ApJ 940.2, p. L55.

Fixsen, D. J. (2009). ApJ 707.2, pp. 916–920.

Fujimoto, S. et al. (2022). Nature 604.7905, pp. 261–265.

Fujimoto, S. et al. (2023). ApJ 949.2, p. L25.

Fujimoto, S. et al. (2024). ApJ 977.2, p. 250.

Gaia Collaboration et al. (2018). A&A 616, A1.

Gaia Collaboration et al. (2021). A&A 649, A1.

Gaia Collaboration et al. (2023). A&A 674, A1.

García-Argumánez, Á. et al. (2023). ApJ 944.1, p. 3.

Genzel, R. et al. (2010). MNRAS 407.4, pp. 2091–2108.

Giavalisco, M. et al. (2004). ApJ 600.2, pp. L93–L98.

Governato, F. et al. (2010). Nature 463.7278, pp. 203–206.

Grazian, A. et al. (2012). A&A 547, A51.

Greene, J. E. et al. (2024). ApJ 964.1, p. 39.

Grogin, N. A. et al. (2011). ApJS 197.2, p. 35.

Guhathakurta, P., Tyson, J. A., and Majewski, S. R. (1990). ApJ 357, p. L9.

Gunn, J. E. and Peterson, B. A. (1965). ApJ 142, pp. 1633–1636.

Guth, A. H. (1981). Phys. Rev. D 23.2, pp. 347–356.

Harikane, Y. et al. (2022a). ApJ 929.1, p. 1.

Harikane, Y. et al. (2022b). *ApJS* 259.1, p. 20.

Harikane, Y. et al. (2023a). ApJS 265.1, p. 5.

Harikane, Y. et al. (2023b). ApJ 959.1, p. 39.

Harikane, Y. et al. (2025). ApJ 980.1, p. 138.

Hashimoto, T. et al. (2019). PASJ 71.4, p. 71.

Hatfield, P. W. et al. (2018). MNRAS 477.3, pp. 3760–3774.

Hathi, N. P., Malhotra, S., and Rhoads, J. E. (2008). ApJ 673.2, pp. 686–693.

Hawking, S. (1971). MNRAS 152, p. 75.

Heckman, T. M. et al. (2001). ApJ 558.1, pp. 56–62.

Herschel, W. (1785). *Phil. Trans. R. Soc.*

Hilmi, M. et al. (2024). MNRAS 532.1, pp. 920–931.

Hogg, D. W. et al. (2002). *arXiv e-prints*, astro–ph/0210394.

Holwerda, B. W. et al. (2015). ApJ 808.1, p. 6.

Hopkins, P. F., Quataert, E., and Murray, N. (2012). MNRAS 421.4, pp. 3522–3537.

Hu, W. et al. (2017). ApJ 845.2, p. L16.

Huang, K.-H. et al. (2013). ApJ 765.1, p. 68.

Hubble, E. P. (1925). *The Observatory* 48, pp. 139–142.

Hubble, E. P. (1926). ApJ 64, pp. 321–369.

Hubble, E. (1929). *Proceedings of the National Academy of Science* 15.3, pp. 168–173.

Huertas-Company, M. et al. (2024). A&A 685, A48.

Hutter, A. et al. (2025). A&A 694, A254.

Ilbert, O. et al. (2006). A&A 457.3, pp. 841–856.

Inami, H. et al. (2022). MNRAS 515.3, pp. 3126–3143.

Inoue, A. K. et al. (2014). MNRAS 442.2, pp. 1805–1820.

Ishigaki, M. et al. (2015). ApJ 799.1, p. 12.

Ito, K. et al. (2024). ApJ 964.2, p. 192.

Ivezić, Ž. et al. (2019). ApJ 873.2, 111, p. 111.

Iye, M. et al. (2006). Nature 443.7108, pp. 186–188.

Iyer, K. G. et al. (2025). *arXiv e-prints*, arXiv:2502.17680.

Jacobs, C. et al. (2023). ApJ 948.2, p. L13.

Jarvis, M. J. et al. (2013). MNRAS 428.2, pp. 1281–1295.

Ji, Z. et al. (2024). *arXiv e-prints*, arXiv:2401.00934.

Jones, G. C. et al. (2021). MNRAS 507.3, pp. 3540–3563.

Juodžbalis, I. et al. (2023). MNRAS 525.1, pp. 1353–1364.

Kannan, R. et al. (2022). MNRAS 511.3, pp. 4005–4030.

Kartaltepe, J. S. et al. (2023). ApJ 946.1, p. L15.

Kashikawa, N. et al. (2004). PASJ 56, pp. 1011–1023.

Katz, H. et al. (2023). *The Open Journal of Astrophysics* 6, p. 44.

Kauffmann, O. B. et al. (2022). A&A 667, A65.

Kawamata, R. et al. (2018). ApJ 855.1, p. 4.

Kawinwanichakij, L. et al. (2021). ApJ 921.1, p. 38.

Kennicutt Jr., R. C. (1998). ARA&A 36, pp. 189–232.

Kocevski, D. D. et al. (2023). ApJ 954.1, p. L4.

Koekemoer, A. M. et al. (2011). ApJS 197.2, p. 36.

Koekemoer, A. M. et al. (2013). ApJS 209.1, p. 3.

Kokorev, V. et al. (2024). ApJ 975.2, p. 178.

Kozasa, T., Hasegawa, H., and Nomoto, K. (1989). ApJ 344, p. 325.

Kron, R. G. (1980). ApJS 43, pp. 305–325.

Kroupa, P. (2001). MNRAS 322.2, pp. 231–246.

Labbe, I. et al. (2025). ApJ 978.1, p. 92.

Labbé, I. et al. (2023a). Nature 616.7956, pp. 266–269.

Labbé, I. et al. (2023b). Nature 616.7956, pp. 266–269.

LaChance, P. et al. (2025). *The Open Journal of Astrophysics* 8, p. 20.

Laha, S. et al. (2021). *Nature Astronomy* 5, pp. 13–24.

Laigle, C. et al. (2016). ApJS 224.2, p. 24.

Lange, R. et al. (2015). MNRAS 447.3, pp. 2603–2630.

Langeroodi, D. et al. (2023). ApJ 957.1, p. 39.

Law, D. R. et al. (2012). ApJ 745.1, p. 85.

Lawrence, A. et al. (2007). MNRAS 379.4, pp. 1599–1617.

Leethochawalit, N. et al. (2023a). ApJ 942.2, p. L26.

Leethochawalit, N. et al. (2023b). MNRAS 524.4, pp. 5454–5467.

Legrand, L. et al. (2019). MNRAS 486.4, pp. 5468–5481.

Lewis, J. S. W. et al. (2023). MNRAS 519.4, pp. 5987–6007.

Li, A. and Draine, B. T. (2001). ApJ 554.2, pp. 778–802.

Liddle, A. (2003). *An Introduction to Modern Cosmology, Second Edition*.

Lilly, S. J. et al. (1996). ApJ 460, p. L1.

Lines, N. E. P. et al. (2024). *arXiv e-prints*, arXiv:2409.10963.

Loeb, A. and Furlanetto, S. R. (2013). *The First Galaxies in the Universe*.

Long, A. S. et al. (2024). ApJ 970.1, p. 68.

Lovell, C. C. et al. (2021). MNRAS 500.2, pp. 2127–2145.

Lovell, C. C. et al. (2023). MNRAS 525.4, pp. 5520–5539.

Lu, T.-Y. et al. (2024). *arXiv e-prints*, arXiv:2411.04176.

Luhman, K. L. et al. (2024). ApJ 975.2, p. 162.

Madau, P. (1995). *ApJ* 441, p. 18.

Madau, P. and Dickinson, M. (2014). ARA&A 52, pp. 415–486.

Madau, P., Haardt, F., and Rees, M. J. (1999). ApJ 514.2, pp. 648–659.

Magorrian, J. et al. (1998). AJ 115.6, pp. 2285–2305.

Maiolino, R. et al. (2020). *The Messenger* 180, pp. 24–29.

Marconcini, C. et al. (2024). *arXiv e-prints*, arXiv:2411.08627.

Marley, M. S. et al. (2021). ApJ 920.2, p. 85.

Marshall, M. A. et al. (2022). MNRAS 511.4, pp. 5475–5491.

Mason, C. A., Trenti, M., and Treu, T. (2023). MNRAS 521.1, pp. 497–503.

Matsuoka, Y. et al. (2018). ApJ 869.2, p. 150.

Matsuoka, Y. et al. (2023). ApJ 949.2, p. L42.

Matthee, J. et al. (2023). ApJ 950.1, p. 67.

Matthee, J. et al. (2024). ApJ 963.2, p. 129.

Mauduit, J. .-. et al. (2012). *PASP* 124.917, p. 714.

Mauerhofer, V. and Dayal, P. (2023). MNRAS 526.2, pp. 2196–2209.

McCracken, H. J. et al. (2012). A&A 544, A156.

McKellar, A. (1940). PASP 52.307, p. 187.

McLeod, D. J., McLure, R. J., and Dunlop, J. S. (2016). MNRAS 459.4, pp. 3812–3824.

McLeod, D. J. et al. (2021). MNRAS 503.3, pp. 4413–4435.

McLeod, D. J. et al. (2024). MNRAS 527.3, pp. 5004–5022.

McLure, R. J. et al. (2009). MNRAS 395.4, pp. 2196–2209.

McLure, R. J. et al. (2010). MNRAS 403.2, pp. 960–983.

McLure, R. J. et al. (2013). MNRAS 432.4, pp. 2696–2716.

Merlin, E. et al. (2022). ApJ 938.2, p. L14.

Miyazaki, S. et al. (2002). PASJ 54, pp. 833–853.

Miyazaki, S. et al. (2012). In: *Ground-based and Airborne Instrumentation for Astronomy IV*. Ed. by I. S. McLean, S. K. Ramsay, and H. Takami. Vol. 8446. Society of Photo-Optical Instrumentation Engineers (SPIE) Conference Series, 84460Z.

Mo, H. J., Mao, S., and White, S. D. M. (1998). MNRAS 295.2, pp. 319–336.

Morishita, T. et al. (2023). *arXiv e-prints*, arXiv:2308.05018.

Morishita, T. et al. (2024). ApJ 963.1, p. 9.

Mortlock, D. J. et al. (2011). Nature 474.7353, pp. 616–619.

Mosleh, M. et al. (2011). ApJ 727.1, p. 5.

Moster, B. P. et al. (2010). ApJ 710.2, pp. 903–923.

Naidu, R. P. et al. (2020). ApJ 892.2, p. 109.

Naidu, R. P. et al. (2022). ApJ 940.1, p. L14.

Neistein, E., van den Bosch, F. C., and Dekel, A. (2006). MNRAS 372.2, pp. 933–948.

Nelson, E. J. et al. (2016). ApJ 828.1, p. 27.

Netzer, H. (2015). ARA&A 53, pp. 365–408.

Ni, Q. et al. (2019). *RNAAS* 3.1, p. 5.

Nightingale, J. W. et al. (2023). *J. Open Source Softw.* 8.81, p. 4475.

Niida, M. et al. (2020). ApJ 904.2, p. 89.

Nikopoulos, G. P. and Dayal, P. (2024). *arXiv e-prints*, arXiv:2409.10613.

Oei, M. S. S. L. et al. (2022). A&A 660, A2.

Oesch, P. A. et al. (2007). ApJ 671.2, pp. 1212–1226.

Oesch, P. A. et al. (2010a). ApJ 709.1, pp. L21–L25.

Oesch, P. A. et al. (2010b). ApJ 714.1, pp. L47–L51.

Oesch, P. A. et al. (2012a). ApJ 745.2, p. 110.

Oesch, P. A. et al. (2012b). ApJ 759.2, p. 135.

Oesch, P. A. et al. (2015). ApJ 804.2, p. L30.

Oesch, P. A. et al. (2016). ApJ 819.2, p. 129.

Oesch, P. A. et al. (2018). ApJ 855.2, p. 105.

Oesch, P. A. et al. (2023). MNRAS 525.2, pp. 2864–2874.

Oke, J. B. and Gunn, J. E. (1983). ApJ 266, pp. 713–717.

Ono, Y. et al. (2018). PASJ 70, S10.

Ono, Y. et al. (2023). *ApJ* 951.1, p. 72.

Ono, Y. et al. (2024). PASJ 76.2, pp. 219–250.

Ormerod, K. et al. (2024). MNRAS 527.3, pp. 6110–6125.

Ouchi, M., Ono, Y., and Shibuya, T. (2020). ARA&A 58, pp. 617–659.

Ouchi, M. et al. (2013). ApJ 778.2, p. 102.

Pandya, V. et al. (2024). ApJ 963.1, p. 54.

Papovich, C., Dickinson, M., and Ferguson, H. C. (2001). ApJ 559.2, pp. 620–653.

Papovich, C. et al. (2023). ApJ 949.2, p. L18.

Peebles, P. J. E. (1968). ApJ 153, p. 1.

Peebles, P. J. E. (1969). ApJ 155, p. 393.

Peebles, P. J. E. (1993). *Principles of Physical Cosmology*.

Peng, Y.-j. et al. (2010). ApJ 721.1, pp. 193–221.

Penzias, A. A. and Wilson, R. W. (1965). ApJ 142, pp. 419–421.

Pérez-González, P. G. et al. (2023). ApJ 951.1, p. L1.

Perrin, M. D. et al. (2014). In: *Space Telescopes and Instrumentation 2014: Optical, Infrared, and Millimeter Wave*. Ed. by J. Oschmann Jacobus M. et al. Vol. 9143. Society of Photo-Optical Instrumentation Engineers (SPIE) Conference Series, p. 91433X.

Petrosian, V. (1976). ApJ 210, p. L53.

Pichon, C. et al. (2011). MNRAS 418.4, pp. 2493–2507.

Pillepich, A. et al. (2018). MNRAS 473.3, pp. 4077–4106.

Pillepich, A. et al. (2019). MNRAS 490.3, pp. 3196–3233.

Pirie, C. A. et al. (2024). *arXiv e-prints*, arXiv:2410.11808.

Planck Collaboration et al. (2020). A&A 641, A6.

Pontoppidan, K. M. et al. (2022). ApJ 936.1, p. L14.

Press, W. H. and Schechter, P. (1974). ApJ 187, pp. 425–438.

Rees, M. J. and Ostriker, J. P. (1977). MNRAS 179, pp. 541–559.

Regan, J. A. and Haehnelt, M. G. (2009). MNRAS 396.1, pp. 343–353.

Rieke, M. J. et al. (2023). PASP 135.1044, p. 028001.

Rigby, J. et al. (2023). PASP 135.1046, p. 048001.

Roberts-Borsani, G. W. et al. (2016). ApJ 823.2, p. 143.

Robertson, B. E. (2022). ARA&A 60, pp. 121–158.

Rodighiero, G. et al. (2010). A&A 515, A8.

Rojas-Ruiz, S. et al. (2020). ApJ 891.2, p. 146.

Roper, W. J. et al. (2022). MNRAS 514.2, pp. 1921–1939.

Roper, W. J. et al. (2023). MNRAS 526.4, pp. 6128–6144.

Rubin, V. C. and Ford Jr., W. K. (1970). ApJ 159, p. 379.

Rujopakarn, W. et al. (2023). ApJ 948.1, p. L8.

Ryan Russell E., J. et al. (2017). ApJ 847.1, p. 53.

Ryan, R. E. et al. (2011). ApJ 739.2, p. 83.

Salim, S., Boquien, M., and Lee, J. C. (2018). ApJ 859.1, p. 11.

Salim, S. and Narayanan, D. (2020). ARA&A 58, pp. 529–575.

Salpeter, E. E. (1955). ApJ 121, p. 161.

Schechter, P. (1976). ApJ 203, pp. 297–306.

Schindler, J.-T. et al. (2023). ApJ 943.1, p. 67.

Schmidt, M. (1963). Nature 197.4872, p. 1040.

Schmidt, M. (1959). ApJ 129, p. 243.

Schmidt, M. (1968). ApJ 151, p. 393.

Schneider, R. and Maiolino, R. (2024). A&A Rev. 32.1, p. 2.

Scholtz, J. et al. (2023). *arXiv e-prints*, arXiv:2311.18731.

Scoville, N. et al. (2007). ApJS 172.1, pp. 1–8.

Sérsic, J. L. (1963). *Boletin de la Asociacion Argentina de Astronomia La Plata Argentina* 6, pp. 41–43.

Shen, L. et al. (2024a). ApJ 963.2, p. L49.

Shen, X. et al. (2023). MNRAS 525.3, pp. 3254–3261.

Shen, X. et al. (2024b). MNRAS 534.2, pp. 1433–1458.

Shibuya, T., Ouchi, M., and Harikane, Y. (2015). ApJS 219.2, p. 15.

Shibuya, T. et al. (2016). ApJ 821.2, p. 72.

Shipley, H. V. et al. (2016). ApJ 818.1, p. 60.

Silk, J. (1977). ApJ 211, pp. 638–648.

Smit, R. et al. (2014). *ApJ* 784.1, p. 58.

Smit, R. et al. (2015). ApJ 801.2, p. 122.

Sobral, D. et al. (2015). ApJ 808.2, p. 139.

Sommovigo, L. et al. (2022). MNRAS 513.3, pp. 3122–3135.

Sorahana, S., Nakajima, T., and Matsuoka, Y. (2019). ApJ 870.2, p. 118.

Stanway, E. R. and Eldridge, J. J. (2018). MNRAS 479.1, pp. 75–93.

Stanway, E. R. et al. (2004). ApJ 607.2, pp. 704–720.

Stanway, E. R. et al. (2008). MNRAS 386.1, pp. 370–376.

Stark, D. P. (2016). ARA&A 54, pp. 761–803.

Stark, D. P. et al. (2013). ApJ 763.2, p. 129.

Stark, D. P. et al. (2025). *arXiv e-prints*, arXiv:2501.17078.

Stefanon, M. et al. (2017). ApJ 851.1, p. 43.

Stefanon, M. et al. (2019). *ApJ* 883.1, p. 99.

Steidel, C. C. et al. (1996). ApJ 462, p. L17.

Steidel, C. C. et al. (1999). ApJ 519.1, pp. 1–17.

Stevans, M. L. et al. (2018). ApJ 863.1, p. 63.

Suess, K. A. et al. (2019a). ApJ 877.2, p. 103.

Suess, K. A. et al. (2019b). ApJ 885.1, p. L22.

Suess, K. A. et al. (2022). ApJ 937.2, p. L33.

Sun, G. et al. (2023). MNRAS 526.2, pp. 2665–2672.

Sun, W. et al. (2024). ApJ 960.2, p. 104.

Tacchella, S. et al. (2023). *ApJ* 952.1, p. 74.

Tacconi, L. J. et al. (2013). ApJ 768.1, p. 74.

Tacconi, L. J. et al. (2018). ApJ 853.2, p. 179.

Tamura, N. et al. (2016). In: *Ground-based and Airborne Instrumentation for Astronomy VI*. Ed. by C. J. Evans, L. Simard, and H. Takami. Vol. 9908. Society of Photo-Optical Instrumentation Engineers (SPIE) Conference Series, p. 99081M.

Trenti, M. and Stiavelli, M. (2008). ApJ 676.2, pp. 767–780.

Trujillo, I. et al. (2006). ApJ 650.1, pp. 18–41.

Umeda, H. et al. (2025). ApJS 277.2, p. 37.

Vaccari, M. et al. (2016). In: *The 4th Annual Conference on High Energy Astrophysics in Southern Africa (HEASA 2016)*, p. 26.

Vale, A. and Ostriker, J. P. (2006). MNRAS 371.3, pp. 1173–1187.

van der Burg, R. F. J., Hildebrandt, H., and Erben, T. (2010). A&A 523, A74.

van der Wel, A. et al. (2014). ApJ 788.1, p. 28.

van Mierlo, S. E. et al. (2022). A&A 666, A200.

Ventou, E. et al. (2017). A&A 608, A9.

Vijayan, A. P. et al. (2021). MNRAS 501.3, pp. 3289–3308.

Vijayan, A. P. et al. (2024). MNRAS 527.3, pp. 7337–7354.

Virtanen, P. et al. (2020). *Nature Methods* 17, pp. 261–272.

Vogelsberger, M. et al. (2014). Nature 509.7499, pp. 177–182.

Wald, R. M. (1984). *General Relativity*.

Wang, F. et al. (2021). ApJ 907.1, p. L1.

Ward, E. et al. (2024). ApJ 962.2, p. 176.

Warren, M. S. et al. (1992). ApJ 399, p. 405.

Weaver, J. R. et al. (2022). ApJS 258.1, p. 11.

Weaver, J. R. et al. (2024). *arXiv e-prints*, arXiv:2405.13505.

Wechsler, R. H. and Tinker, J. L. (2018). ARA&A 56, pp. 435–487.

Westcott, L. et al. (2024). *arXiv e-prints*, arXiv:2412.14970.

Whitler, L. et al. (2023). MNRAS 519.4, pp. 5859–5881.

Whitler, L. et al. (2025). *arXiv e-prints*, arXiv:2501.00984.

Whitney, A. et al. (2019). ApJ 887.2, p. 113.

Wilkins, S. M., Stanway, E. R., and Bremer, M. N. (2014). MNRAS 439.1, pp. 1038–1050.

Williams, R. E. et al. (1996). AJ 112, p. 1335.

Willott, C. J. et al. (2024). ApJ 966.1, p. 74.

Windhorst, R. A. et al. (2011). ApJS 193.2, p. 27.

Wolfe, A. M., Gawiser, E., and Prochaska, J. X. (2005). ARA&A 43.1, pp. 861–918.

Worthey, G. (1994). ApJS 95, p. 107.

Wright, G. S. et al. (2023). PASP 135.1046, p. 048003.

Wu, X. et al. (2020). MNRAS 494.4, pp. 5636–5651.

Wuyts, S. et al. (2012). ApJ 753.2, p. 114.

Wyithe, J. S. B. et al. (2010). MNRAS 401.4, pp. 2561–2571.

Wyithe, J. S. B. and Loeb, A. (2003). ApJ 586.2, pp. 693–708.

Wyithe, J. S. B. and Loeb, A. (2011). MNRAS 413.1, pp. L38–L42.

Yang, L. et al. (2022). MNRAS 514.1, pp. 1148–1161.

Yang, X., Mo, H. J., and van den Bosch, F. C. (2009). ApJ 695.2, pp. 900–916.

Yung, L. Y. A. et al. (2020). MNRAS 496.4, pp. 4574–4592.

Zavala, J. A. et al. (2021). ApJ 909.2, p. 165.

Zavala, J. A. et al. (2025). *Nature Astronomy* 9, pp. 155–164.

Zhuang, M.-Y. and Shen, Y. (2024). ApJ 962.2, p. 139.